Understanding the Electronic Structures of First-Row Transition Metal Complexes for Solar Energy Conversion and Catalysis

Thesis by

Gautam Dutta Stroscio

In Partial Fulfillment of the Requirements for
the degree of
Doctor of Philosophy

CALIFORNIA INSTITUTE OF TECHNOLOGY
Pasadena, California

2021
(Defended February 5, 2021)

Gautam Dutta Stroscio
ORCID: 0000-0002-0827-1062

ACKNOWLEDGEMENTS

First and foremost, I would like to thank my thesis advisor Prof. Ryan Hadt. It was an enormous privilege to work with Ryan during these past few years, and I am proud of the research we did together. Since we started working together in summer 2018, I grew a lot as a scientist and I owe much of this growth to Ryan. I am very grateful for all the support he has shown me.

My thesis committee has also been a great source of support. It was a tremendous blessing to have interacted with Prof. Harry Gray during my graduate career. Harry, with his thoughtful guidance and genuine concern for my well-being, was the perfect committee chair (even before he formally had that role). To me, he embodies all that is good about Caltech.

Also on my committee, my first thesis advisor, Prof. Mitchio Okumura recognized that I might have a knack for computational chemistry and all the research presented in this thesis has resulted from that insight; for years to come, I will fondly remember having Thanksgiving dinner with Mitchio, his family, and other graduate students. Prof. Garnet Chan, the most recent addition to my committee, has been exceptionally generous to me despite only having known me for a little while. Thank you all!

It was also a great privilege to work with Dr. Martin Srnec at the Czech Academy of Sciences on the iron porphyrin carbene work. The month I spent in Prague working with Martin and his group was my favorite time of my graduate career. Martin has a great chemical intuition and is a wonderful, kind person.

Within the Hadt lab, I was very fortunate to have talented collaborators and mentors. Ryan Ribson did all the experimental work for the Cu(I) photosensitizer collaboration. Ryan's ability to successfully surmount very difficult challenges in the laboratory has been a continuous source of inspiration; his accomplishments as a graduate student are among the very most impressive of which I know. Regarding the iron porphyrin carbene study, Dr. Alec Follmer and Dr. Mauricio Maldonado-Domínguez both mentored me in critical ways that contributed to my intellectual growth. It was always great fun to learn about bioinorganic chemistry from Alec; his great enthusiasm for science and his high personal standards enriched my graduate experience. In Prague, Mauricio introduced me to many new computational techniques and concepts. For the Ni(II) photoredox catalyst study, David Cagan was an enthusiastic partner and his artistic talents greatly improved the presentation of our data.

Outside these direct collaborators and mentors, I also owe a lot to some of the other founding members of the Hadt lab. Alex Barth was a very thoughtful groupmate who often shared helpful materials for research. Nick Higdon was a great literature meeting partner and a pleasant officemate. Best wishes to all the new members joining the Hadt lab and those who join in the coming years; hope you have as much fun as I did!

I am also very fortunate to have made many cherished personal friends at Caltech. I am a much better human being for knowing Matt Chalkley, William Denman, Javier Fajardo Jr., Alec Follmer, Elizabeth Lunny, Ruben Mirzoyan, Ryan Ribson, and Jaron Tong. These individuals gave me sage advice and brightened my days with laughter; it has been a joy spending time with them. I was also quite fortunate in that my best friends from college, Sam Greene and Andy Nian, were able to make trips to visit me in Pasadena. These visits (and reciprocal meetings in Chicago) are also among my best memories.

This thesis is dedicated to my parents. Their love and support sustained me every step of the way.

ABSTRACT

Chapter 1 discusses the major findings and themes of the studies presented in this thesis. Chapter 2 presents a DFT-based methodology for quantifying entatic states. Here it is applied to Cu-based photosensitizers used for solar electricity generation, solar fuels synthesis, organic light emitting diodes (OLEDs), and photoredox catalysis. The methodology can be used to decouple the steric and electronic contributions to excited state dynamics and, in turn, can be used to guide the design of future photosensitizers. The computed entatic energies in some of the photosensitizers were the largest quantified to date: ~20 kcal mol^{-1} relative to the conformationally flexible $[Cu(phen)_2]^+$. Of course, considering typical chemical barriers and driving forces, these values are significant.

Chapter 3 is an investigation of the ground and excited spin state energetics of a free carbene and several of its iron porphyrin carbene (IPC) analogs. Here it is shown that for the IPC models, multireference *ab initio* wave function methods give results most consistent with experiment. Specifically, the predicted, mixed singlet ground state is mostly dominated by the closed-shell singlet ($Fe(II) \leftarrow \{:C(X)Y\}^0$) configuration, with a small contribution from an $Fe(III)–\{C(X)Y\}^{-\bullet}$ open-shell singlet configuration (hole in d(xz)). This description differs from that obtained by using DFT. Also, using the multireference *ab initio* wave methods, elongation of the IPC Fe–C(carbene) bond increases the weighting of this particular open-shell configuration within the ground state singlet.

Chapter 4 also deals with a system where DFT and multireference *ab initio* results diverge: the light-induced Ni(II)–C homolytic bond dissociation in Ni 2,2’-bipyridine photoredox catalysts. DFT calculations give a barrier of ~30 kcal mol^{-1} while multireference *ab initio* calculations giving a barrier of ~70 kcal mol^{-1}. Thus, within the latter description, a previously proposed mechanism of thermally assisted dissociation from the lowest energy triplet ligand field excited state is unfavorable. Instead, the mechanism given by the multireference description is initial population of a singlet Ni(II)-to-bpy metal-to-ligand charge transfer (^{1}MLCT) excited state followed by intersystem crossing and aryl-to-Ni(III) charge transfer. From accessible repulsive triplet excited states, homolytic bond dissociation can occur.

PUBLISHED CONTENT AND CONTRIBUTIONS

†Co-first author. *Corresponding author.

1. Stroscio, G. D.; Ribson, R. D.; Hadt, R. G.* Quantifying Entatic States in Photophysical Processes: Applications to Copper Photosensitzers. *Inorg. Chem.* **2019**, *58* (24), 16800-16817. https://doi.org/10.1021/acs.inorgchem.9b02976.

   G.D.S. performed all the computations; together with R.D.R. and R.G.H., G.D.S. wrote and edited the paper.

2. Stroscio, G. D.; Srnec, M.*; Hadt, R. G.* Multireference Ground and Excited State Electronic Structures of Free- versus Iron Porphyrin-Carbenes. *Inorg. Chem.* **2020**, *59* (13), 8707–8715. https://doi.org/10.1021/acs.inorgchem.0c00249.

   G.D.S. performed all the computations; together with M.S. and R.G.H., G.D.S. wrote and edited the paper.

3. Cagan, D. A.†; Stroscio, G. D.†; Cusumano, A. Q.; Hadt, R. G.* Multireference Description of Nickel–Aryl Homolytic Bond Dissociation Processes in Photoredox Catalysis. *J. Phys. Chem. A* **2020**, *124* (48), 9915-9922. https://doi.org/10.1021/acs.jpca.0c08646.

   G.D.S. performed all the computations for ‘complex 1’ and performed the multireference calculations for the ‘complex 2’ S = 1 scan; together with D.A.C., A.Q.C., and R.G.H., G.D.S. wrote and edited the paper.

TABLE OF CONTENTS

LIST OF FIGURES

LIST OF TABLES

NOMENCLATURE AND ABBREVIATIONS

Å. Angstrom.

ac. Acetate.

bcp. Bathocuproine or 2,9-dimethyl-4,7-diphenyl-1,10-phenanthroline.

BDE. Bond dissociation energy.

bfp. 2,9-bis(trifluoromethyl)-1,10-phenanthroline.

bis-phen. bis-phenanthroline.

bpy. 2,2’-bipyridine.

BSS. Broken-symmetry singlet.

CASSCF. Complete active space self-consistent field theory.

CPCM. Conductor-like polarizable continuum model.

CSS. Closed-shell singlet.

Cu-Cl. Homoleptic complex containing the 2,9-dichloro-1,10-phenanthroline ligand.

Cz. Carbazolyl.

DCM. Dichloromethane.

dbp. 2,9-dibutyl-1,10-phenanthroline.

dbdmp. 2,9-di-*n*-butyl-4,7-dimethyl-1,10-phenanthroline.

dbtmp. 2,9-di-*n*-butyl-3,4,7,8-tetramethyl-1,10-phenanthroline.

DFT. Density functional theory.

DLPNO. Domain-based local pair natural orbital approximation.

DLPNO-MR-CCSD. Multi-reference coupled cluster with single and double excitations using the DLPNO approximation.

dmp. 2,9-dimethyl-1,10-phenanthroline.

dmpp. 2,9-bis(4-methylphenyl)-1,10-phenanthroline.

DMSO. Dimethyl sulfoxide.

dnpp. 2,9-dineopentyl-1,10-phenanthroline.

dpdmp. 2,9-diphenyl-4,7-dimethyl-1,10-phenanthroline.

dptmp. 2,9-diphenyl-3,4,7,8-dimethyl-1,10-phenanthroline.

dpp. 2,9-diphenyl-1,10-phenanthroline.

dsbp. 2,9-di-*sec*-butyl-1,10-phenanthroline.

dtbp. 2,9-di-*tert*-butyl-1,10-phenanthroline.

E°. Reduction potential.

Entatic/rack-induced state. When transition metal ion and its first coordination sphere are placed into an energized geometric and electronic structure that differs significantly from that of the relaxed form.

EPR. Electron paramagnetic resonance spectroscopy.

FMO. Frontier molecular orbital.

FIC-MRCI. Fully internally contracted multireference configuration interaction.

γ_i. Excited state inner sphere relaxation energy.

HOMO. Highest occupied molecular orbital.

IPC. Iron porphyrin carbene.

λ_i. Inner sphere reorganization energy.

LCT. Linear coupling term.

LUMO. Lowest unoccupied molecular orbital.

MAC. Monoamido-aminocarbene.

MLCT. Metal-to-ligand charge transfer.

mmp. 2-methyl-1,10-phenathroline

NEVPT2. N-electron valence second-order perturbation theory.

N-MeImid. *N*-methylimidazole.

NMR. Nuclear magnetic resonance spectroscopy.

OLED. Organic light emitting diode.

OSS. Open-shell singlet.

PES. Potential energy surface.

ph. Phenyl.

phen. 1,10-phenanthroline.

$[PNP]^-$. bis(2-(diisobutylphosphino)pheny)amide.

POP. bis[*2*-(diphenylphosphino)phenyl]ether.

PPh_3. Triphenylphosphine.

$[PPP]^-$. bis(2-di-*iso*-propylphosphinophenyl)phosphide.

QD-NEVPT2. Quasi-degenerate N-electron valence second-order perturbation theory.

RI. Resolution of identities approximation.

RKS. Restricted Kohn-Sham formalism.

SCF. Self-consistent field.

SET. Single electron transfer.

τ. Excited state lifetime.

TDDFT. Time-dependent density functional theory.

THF. Tetrahydrofuran.

tmbp. 4,4’,6,6’-tetramethyl-2,2’-bipyridine.

tpp. 2,4,7,9-tetraphenyl-1,10-phenanthroline.

TPP. Tetraphenylporphyrin.

UKS. Unrestricted Kohn-Sham formalism.

XAS. X-ray absorption spectroscopy.

Chapter 1

INTRODUCTION

1.1. Opening Remarks

This thesis presents several computational chemistry studies of first-row transition metal complexes with applications for solar energy conversion and catalysis. Chapter 2 (supporting materials in Appendix A) developed an original methodology for quantifying entatic state energetics in molecules. Chapter 3 (supporting materials in Appendix B) characterized the electronic structure of the iron porphyrin carbene (IPC) reactive intermediates relevant to engineered carbene transferase enzymes. This characterization yielded useful insights regarding IPC reactivity. Chapter 4 (supporting materials in Appendix C) examined the homolytic bond dissociation in Ni(II) 2,2'-bipyridine photoredox catalysts; this examination yielded a new description of these complexes and their bond dissociation mechanism: a description involving strong Ni(II)-aryl bonds and ligand noninnocence. These studies utilized density functional theory (DFT) and multireference methods based on complete active space self-consistent field theory (CASSCF); Appendix D contains annotated example scripts for these calculations.

1.2. Chapter Summaries and Core Concepts

The bioinorganic concept of the entatic state involves placing a transition metal ion and its first-coordination sphere into a strained, energized geometric and electronic structure for the tuning of thermodynamic and kinetic parameters.[1] Chapter 2 extended the entatic state concept to copper(I) photosensitizers useful for solar energy conversion.[2] Initially, a series of homoleptic copper(I) bis-phenanthrolines functionalized with alkyl groups at the ligand 2,9-positions were examined (Figure 2.2). For this series, several energetic parameters were found to linearly correlate with the experimental lifetimes (τ) of triplet metal-to-ligand charge transfer (^{3}MLCT) excited states. Of these, the excited state relaxation energy (γ_i; defined in Chapter 2 and Appendix A) was found to most robustly characterize the sterically-induced energization of the transient Cu(II) ion and its first sphere. For a four orders of magnitude increase in τ, this entatic energization had a value of ~20 kcal mol^{-1}; this is the first quantification of entatic energetics in a molecular system, and notably the ~20 kcal mol^{-1} value is significant relative to chemical driving forces and barriers. In light of calculated linear coupling terms, it became clear how the γ_i parameter relates to the shapes of excited state potential energy surfaces across the series of complexes. The obtained methodology was then applied to many additional classes of copper photosensitizers.

The iron porphyrin carbene (IPC) is the reactive intermediate in engineered carbene transferase enzymes capable of catalyzing non-biological chemistry.[3] Chapter 3 uses multireference methods to characterize the electronic structure of models for the IPC reactive intermediates.[4] In contrast to previous broken-symmetry DFT studies[5,6], but in agreement with related experimental studies[3,7–9], the IPC ground state was found to be mixed, but largely dominated by the low-spin d^6 Fe(II)←{:C(X)Y} closed-shell singlet (CSS). During bond dissociation scans of the iron-carbene bond, the open-shell singlet (OSS) Fe(III)–$\{C(X)Y\}^{-\bullet}$ configuration became dominant at lengths relevant to those that could potentially be seen at transition states. This initial foray into understanding the relative electrophilic versus radical character of the IPC carbene center represents a step towards better understanding the reactivity profiles of the enzymes and molecular complexes operating through IPCs.

Ni(II) 2,2’-bipyridine photoredox complexes catalyze organic transformations via the generation of organic radicals and high/low-valence nickel species.[10,11] Chapter 4 presents the use of multireference methods to arrive at an original, potential mechanism for the homolytic bond dissociation in Ni(II) 2,2’-bipyridine photoredox complexes.[12] In addition, the multireference description of the physical and chemical properties of the Ni(II) photoredox catalysts is unique; the description uniquely predicts of strong nickel-aryl bonds and the importance of ligand noninnocence.

REFERENCES

(1) Solomon, E. I.; Hadt, R. G. Recent Advances in Understanding Blue Copper Proteins. *Celebr. Harry B Grays 75th Birthd.* **2011**, *255* (7), 774–789. https://doi.org/10.1016/j.ccr.2010.12.008.

(2) Stroscio, G. D.; Ribson, R. D.; Hadt, R. G. Quantifying Entatic States in Photophysical Processes: Applications to Copper Photosensitizers. *Inorg. Chem.* **2019**, *58* (24), 16800–16817. https://doi.org/10.1021/acs.inorgchem.9b02976.

(3) Lewis, R. D.; Garcia-Borràs, M.; Chalkley, M. J.; Buller, A. R.; Houk, K. N.; Kan, S. B. J.; Arnold, F. H. Catalytic Iron-Carbene Intermediate Revealed in a Cytochrome *c* Carbene Transferase. *Proc. Natl. Acad. Sci.* **2018**, *115* (28), 7308–7313. https://doi.org/10.1073/pnas.1807027115.

(4) Stroscio, G. D.; Srnec, M.; Hadt, R. G. Multireference Ground and Excited State Electronic Structures of Free- versus Iron Porphyrin-Carbenes. *Inorg. Chem.* **2020**, *59* (13), 8707–8715. https://doi.org/10.1021/acs.inorgchem.0c00249.

(5) Sharon, D. A.; Mallick, D.; Wang, B.; Shaik, S. Computation Sheds Insight into Iron Porphyrin Carbenes' Electronic Structure, Formation, and N–H Insertion Reactivity. *J. Am. Chem. Soc.* **2016**, *138* (30), 9597–9610. https://doi.org/10.1021/jacs.6b04636.

(6) Su, H.; Ma, G.; Liu, Y. Theoretical Insights into the Mechanism and Stereoselectivity of Olefin Cyclopropanation Catalyzed by Two Engineered Cytochrome P450 Enzymes. *Inorg. Chem.* **2018**, *57* (18), 11738–11745. https://doi.org/10.1021/acs.inorgchem.8b01875.

(7) Li, Y.; Huang, J.-S.; Zhou, Z.-Y.; Che, C.-M.; You, X.-Z. Remarkably Stable Iron Porphyrins Bearing Nonheteroatom-Stabilized Carbene or (Alkoxycarbonyl)Carbenes: Isolation, X-Ray Crystal Structures, and Carbon Atom Transfer Reactions with Hydrocarbons. *J. Am. Chem. Soc.* **2002**, *124* (44), 13185–13193. https://doi.org/10.1021/ja020391c.

(8) Khade, R. L.; Fan, W.; Ling, Y.; Yang, L.; Oldfield, E.; Zhang, Y. Iron Porphyrin Carbenes as Catalytic Intermediates: Structures, Mössbauer and NMR Spectroscopic Properties, and Bonding. *Angew. Chem. Int. Ed.* **2014**, *53* (29), 7574–7578. https://doi.org/10.1002/anie.201402472.

(9) Liu, Y.; Xu, W.; Zhang, J.; Fuller, W.; Schulz, C. E.; Li, J. Electronic Configuration and Ligand Nature of Five-Coordinate Iron Porphyrin Carbene Complexes: An Experimental Study. *J. Am. Chem. Soc.* **2017**, *139* (14), 5023–5026. https://doi.org/10.1021/jacs.7b01722.

(10) Welin, E. R.; Le, C.; Arias-Rotondo, D. M.; McCusker, J. K.; MacMillan, D. W. C. Photosensitized, Energy Transfer-Mediated Organometallic Catalysis through Electronically Excited Nickel(II). *Science* **2017**, *355* (6323), 380. https://doi.org/10.1126/science.aal2490.

(11) Ting, S. I.; Garakyaraghi, S.; Taliaferro, C. M.; Shields, B. J.; Scholes, G. D.; Castellano, F. N.; Doyle, A. G. 3d-d Excited States of Ni(II) Complexes Relevant to Photoredox Catalysis: Spectroscopic Identification and Mechanistic Implications. *J. Am. Chem. Soc.* **2020**, *142* (12), 5800–5810. https://doi.org/10.1021/jacs.0c00781.

(12) Cagan, D. A.; Stroscio, G. D.; Cusumano, A. Q.; Hadt, R. G. Multireference Description of Nickel–Aryl Homolytic Bond Dissociation Processes in Photoredox Catalysis. *J. Phys. Chem. A* **2020**. https://doi.org/10.1021/acs.jpca.0c08646.

Chapter 2

QUANTIFYING ENTATIC STATES IN PHOTOPHYSICAL PROCESSES: APPLICATIONS TO COPPER PHOTOSENSITIZERS

Adapted with permission from:

Stroscio, G. D.; Ribson, R. D.; Hadt, R. G.* Quantifying Entatic States in Photophysical Processes: Applications to Copper Photosensitzers. *Inorg. Chem.* **2019**, *58* (24), 16800-16817. https://doi.org/10.1021/acs.inorgchem.9b02976.

*Corresponding author.

Abstract

The entatic or rack-induced state is a core concept in bioinorganic chemistry. In its simplest form, it is present when a protein scaffold places a transition metal ion and its first coordination sphere into an energized geometric and electronic structure that differs significantly from that of the relaxed form. This energized complex can exhibit special properties. Under this purview, however, entatic states are hardly unique to bioinorganic chemistry, and their effects can be found throughout a variety of important chemistries and materials science applications. Despite this broad influence, there are only a few examples where entatic effects have been quantified. Here we extend the entatic concept more generally to photophysical processes by developing a combined experimental and computational methodology to quantify entatic states across an entire class of functional molecules, e.g., Cu-based photosensitizers. These metal complexes have a broad range of applications, including solar electricity generation, solar fuels synthesis, organic light emitting diodes (OLEDs), and photoredox catalysis. As a direct consequence of quantifying entatic states, this methodology allows the disentanglement of steric and electronic contributions to excited state dynamics. Thus, before embarking on the syntheses of new Cu-based photosensitizers, the correlations described herein can be used as an estimate of entatic and electronic contributions and thus guide ligand design and the development of next-generation transition metal complexes with improved and/or tailored excited state dynamics. Lastly, entatic energies in some Cu photosensitizers are the largest yet quantified and are found here to approach 20 kcal/mol relative to the conformationally flexible $[Cu(phen)_2]^+$. These energetics are significant relative to typical chemical driving forces and barriers, highlighting the utility in extending entatic state descriptors to new classes of molecules and

materials with interesting functional properties involving the coupling between electron and vibrational dynamics.

2.1. Introduction

Energized states in proteins have been recognized since the 1950s.[1,2] The concept was further developed and applied by a number of researchers, including Vallee, Williams, Malmström, and Gray,[3–7] and was thereafter more colloquially referred to as the entatic[6] or rack-induced[5] (entatic/rack) state. In its simplest description, the entatic state in biology refers to the energy provided by the overall protein fold, inclusive of first and second spheres and long range H-bonding and electrostatics, to distort the ligand field around a transition metal ion. In doing so, the metal is endowed with an activated geometric and electronic structure that can finely tune a variety of functional properties. While a central concept in bioinorganic chemistry, it is still a major challenge to demonstrate the existence of and quantify entatic states, and only a few examples exist in the literature.[8–12]

Classic cases where the entatic state has been discussed include the blue (type 1, T1) and green (perturbed) Cu active sites[7,13] and the ground state redox properties of their related Cu complexes.[14–18] In addition to tuning redox potentials by varying free energies, the entatic state can also significantly affect electron transfer kinetics through a reduction in ground state inner sphere reorganization energies (λ_is). An interesting extension of ground state entatic contributions in Cu active sites and complexes has recently been discussed by Kohler et al.[19] and Dicke et al.,[20] wherein entatic concepts were translated to understanding Cu(I) metal-to-ligand charge transfer (MLCT) excited state dynamics.

Ultrafast spectroscopies have provided a clear picture of the MLCT-triggered geometric and electronic structural dynamics of Cu(I) bis-phenanthroline (bis-phen) complexes.[21–24] As illustrated in Figure 2.1, excitation into the ^{1}MLCT absorption band of a T_d Cu(I) complex induces the transient formation of an oxidized Cu(II) state. This photo-triggered, Cu-centered redox event induces a Jahn-Teller distorting force along a flattening mode in the excited state (Figure 2.1), and, upon intersystem crossing, a metastable ^{3}MLCT state is formed. By introducing steric bulk at the 2,9-positions of the bis-phen ligand, the degree of structural flattening can be mitigated and the lifetime (τ) of the ^{3}MLCT state can be tuned over many orders of magnitude (*vide infra*). Given the transient formation of Cu(II), the excited state structural dynamics mimic those that are relevant for Cu-based electron transfer active sites in biology and related Cu complexes. Thus, for Cu(I) bis-phen complexes, and Cu photosensitizers in general, the same structural contributions are responsible for tuning redox potentials and the potential energy surfaces involved in excited state formation and decay. The entatic state description provides a framework for understanding the important role of structure in tuning the kinetics associated with photophysical processes across Cu(I) photosensitizers. That said, as has been the case for biology, quantifying entatic contributions is not necessarily straightforward and has yet to be accomplished for photochemical dynamics.

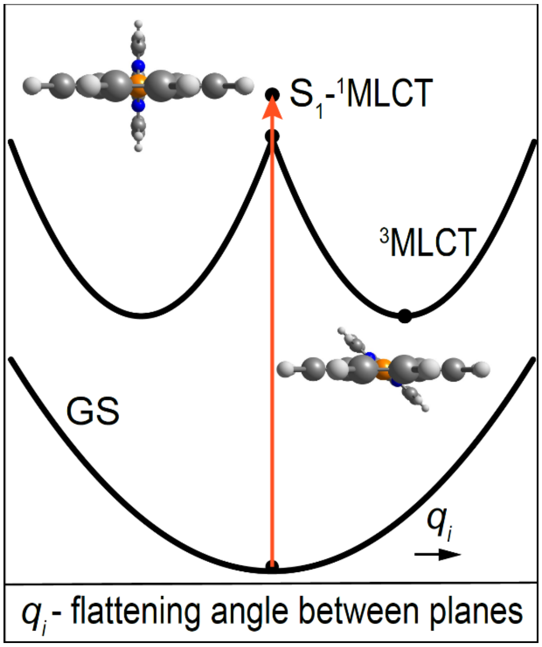

Figure 2.1. ^{3}MLCT excited state structural distortion in Cu(I) bis-phenanthroline complexes and their generalized excited state potential energy surfaces. The entatic state under consideration here inhibits the flattening of the dihedral angle upon formation of the ^{3}MLCT excited state.

It is also enlightening to consider the potential roles entatic states might play in other areas, as they should not be unique to Cu complexes and bioinorganic chemistry. For example, Snyder et al.[25] has invoked an entatic state in heterogeneous catalysis, wherein structural contributions from a zeolite lattice activate a ferryl unit for the oxidation of the strong C–H bond of methane. Similarly, entatic contributions have been shown to tune the relative energies of the important S=1,2 spin states of ferryl complexes, leading to variations in alkane hydroxylation, alkene epoxidation, and phosphine and thioether oxidation.[26] Entatic-like effects, strains and stresses in particular, have also been shown to directly influence thermodynamic and kinetic aspects across a broad range of important chemistries and materials properties, including electrocatalysis,[27–36] battery electrode materials,[37–39] solar energy storage,[40] transition metal-mediated organic synthetic reactions,[41] single molecule magnetism,[42] photomagnetic/spin-crossover materials,[43,44] internal conversion in fluorescent proteins and molecules,[45,46] quantum information processing,[47–49] and colossal magnetoresistance.[50,51]

This wide range of chemical and physical properties where entatic-like effects have been invoked is perhaps not surprising given the general description above. For dynamic and photophysical processes, we would like to highlight the important coupling between molecular vibrations or phonons to key changes in electronic structure (e.g., intersystem crossing). Given the fundamental nature of this coupling, we can expect entatic-like effects to tune this coupling and influence the dynamic properties of interest. For example, ultrafast spectroscopies have highlighted the role of electron-nuclear coupling in photophysical processes, especially through analyses of wavepacket dynamics.[52–55] Another interesting example in a solid state system involves strain-engineering in diamond vacancies for quantum information processing.[47–49,56] Strain-induced distortions of nitrogen vacancies can modify the electron-phonon couplings that mediate intersystem crossings, and thus strain-dependent intersystem crossing rates and/or emission energies represent a means to potentially quantify entatic-like contributions in the solid state.[47] Thus, while analyzing entatic states with thermodynamic quantities and descriptors is attractive, the extension to understanding steric influences in dynamic processes and leveraging ultrafast spectroscopies represents an exciting area of exploration; these quantifications can better guide ligand and materials design, while also pushing forward our fundamental understanding of the key role played by the coupling of molecular vibrations to electron dynamics.

We take a step in this direction by developing a combined experimental and computational methodology to quantify entatic states in photophysical processes and apply this combined approach to an entire class of functional molecules, e.g., Cu-based photosensitizers. These complexes exhibit a broad range of applications, including solar electricity generation,[57–62] solar fuels synthesis (e.g., H_2 generation and CO_2 reduction),[63–70] organic light emitting diodes (OLEDs),[71–78] and photoredox catalysis in organic synthesis.[79–87] The experimental and computational approach outlined here utilizes electrochemical methods, ultrafast transient absorption spectroscopy, and emission spectroscopy and couples these to density functional theory (DFT) calculated redox potentials, ground state reorganization energies, and excited state relaxation energies. This approach gives a detailed picture of the ground and excited state potential energy surfaces involved in redox and the photodynamics of Cu(I)-based photosensitizers, which has provided the first quantification of entatic state contributions to a class of photoactive molecules. Importantly, once entatic contributions are quantified, contributions from sterics and electronics can be disentangled. By defining and quantifying entatic states, we provide a clear framework and picture of their fundamental origins and the role they play in tuning potential energy surfaces and thus spin-vibrational coupling. Here we show that entatic energies in Cu(I) photosensitizers can approach 20 kcal/mol relative to the conformationally flexible $[Cu(phen)_2]^+$. These energetics represent a significant contribution relative to typical chemical driving forces and barriers, further supporting their extension to catalysis, photophysics, and materials science.

2.2. Results

In the following sections, we utilize the observation that the natural logarithms of the ^{3}MLCT excited state lifetimes, ln(τ)s, correlate linearly with a wide variety of thermodynamic and kinetic data on the 2,9-alkyl substituted Cu(I) bis-phenanthroline (bis-phen) complexes. These linear correlations provide slopes and thus quantifications of the complex energization (i.e., entatic state) due to structural constrains. Several approaches to quantifying entatic states using a broad range of experimental and computational data are discussed below. Lastly, while the majority of electrochemical data and lifetimes are gleaned from the literature, the electrochemical and excited state properties of the Cu(I) 2-methyl-1,10-phenanthroline (mmp) complex (bis-mmp) were studied here for the first time. These new data span a previously unavailable yet critical region of the ln(τ) plots given here.

2.2.1. Quantifying Entatic States in 2,9-Alkyl Substituted Copper(I) Bis-Phenanthrolines

The reduction potentials (E°s) and ^{3}MLCT excited state lifetimes (τ) for a variety of Cu(I) bis-phen complexes have been reported in the literature.[21,23,24,88–92] Among these are six homoleptic Cu(I) bis-phen complexes differing only in the alkyl group at the 2,9-position of the phenanthroline ligand (*viz*., 1,10-phenanthroline (phen), 2,9-dimethyl-1,10-phenanthroline (dmp), 2,9-dibutyl-1,10-phenanthroline (dbp), 2,9-dineopentyl-1,10-phenanthroline (dnpp), 2,9-di-*sec*-butyl-1,10-phenanthroline (dsbp), and 2,9-di-*tert*-butyl-1,10-phenanthroline (dtbp)) (Figure 2.2). Solely changing the alkyl group at the 2,9-positions tunes the Cu(I/II) E° over ~600 mV and ^{3}MLCT lifetimes by greater than four orders of magnitude (e.g., from 140 ps (bis-phen) to 3.26 μs (bis-dtbp) in DCM).[21] These systematic structure/function variations thus provide an opportunity to quantify entatic states in photophysical processes for the first time. Indeed, our examination of these complexes demonstrates that tuning the steric bulk of the alkyl chains at the 2,9-positions has a quantifiable effect on τ. In the following sections, we first correlate experimental and computational $E°$s to evaluate potential entatic state contributions. Analyses are then extended to ground state inner sphere reorganization energies (λ_is) for Cu(I/II) redox and, finally, to Cu(I/II) ^{3}MLCT excited state inner sphere relaxation energies (γ_is) and energy gaps. As shown below, entatic energies depend on the model used to quantify them. For Cu-photosensitizers, we have determined that excited state relaxation energies provide a means to quantify purely steric contributions to ^{3}MLCT dynamics (*vide infra*).

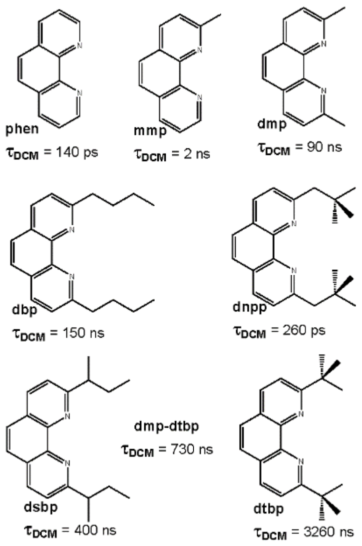

Figure 2.2. Phenanthroline and the 2,9-alkyl substituted ligands of the homoleptic complexes used to quantify entatic contributions to τ.

2.2.1.1. Entatic Contributions and Cu(I/II) Redox Potentials

As pointed out recently for Cu(I) bis-phen complexes,[19] variations in $E°$s and τs reflect the same structural distortion (Figure 2.1); therefore, one can draw a correlation between these experimental observables to quantify entatic contributions to photophysical dynamics. Experimental and calculated $E°$s (see Methods in Appendix A) for Cu(I) bis-phen and the 2,9-alkyl substituted complexes are given in Table 2.1 and Figure 2.3. The best agreement between theory and experimental $E°$s in DCM is observed for the BP86 functional. Thus, if not specified, calculated values correspond to values obtained using the BP86 exchange correlation functional. Within this functional, the best agreement is observed for the bulkier substituents (e.g., bis-dbp, -dsbp, and -dtbp). For bis-phen and -dmp, however, the calculated *E*°s (1.071 and 1.259 V, respectively) are higher than those observed experimentally (0.84 and 0.99 V, respectively). Furthermore, there is a fairly large *E*° difference between bis-phen and bis-dmp complexes relative to the other complexes with *E*°s reported in the literature (Table 2.1). For a more reliable overall comparison across the series, it is useful to fill this gap. Doing so is also important for analyzing ^{3}MLCT lifetimes and relaxation energies (*vide infra*). We therefore synthesized the homoleptic Cu(I) complex with a 2-methyl-1,10-phenanthroline (mmp) ligand (bis-mmp)[93] and measured its *E*° (0.99 V) and photophysical properties for the first time (see Appendix A Figure A.2 and Methods for experimental details). Similarly to bis-phen and -dmp, the calculated *E*° (1.145 V) is higher than that observed experimentally. We return to this difference below (*vide infra*).

Table 2.1. Experimental and Calculated *E*°s (V vs. NHE) for 2,9-Alkyl Substituted Bis-Phen complexes.

Ligand	BP86 (eV)	TPSSh (eV)	B3LYP (eV)	Experiment (V)	BP86 – Exp. (V)
phen	1.071	0.716	0.624	0.84[a]	0.23
phen*	0.769	0.376	0.303	0.84[a]	-0.07
mmp	1.145	0.823	0.740	0.99[a]	0.16
mmp*	1.048	0.702	0.612	0.99[a]	0.06
dmp	1.259	0.978	0.887	1.19[a]	0.07
dmp*	1.201	0.920	0.826	1.19[a]	0.01
dbp	1.318	1.065	0.987	1.31[b]	0.01
dnpp	1.248	0.983	0.909	1.31[b]	-0.06
dsbp	1.341	1.087	1.042	1.38[b]	-0.04
dmp-dtbp	1.459	1.243	1.197		
dtbp	1.401	1.205	1.218	1.40[c]	0.00

*Optimized structure includes a weak H_2O interaction as discussed in the text.

[a] This work

[b] Reference 88

[c] Reference 92

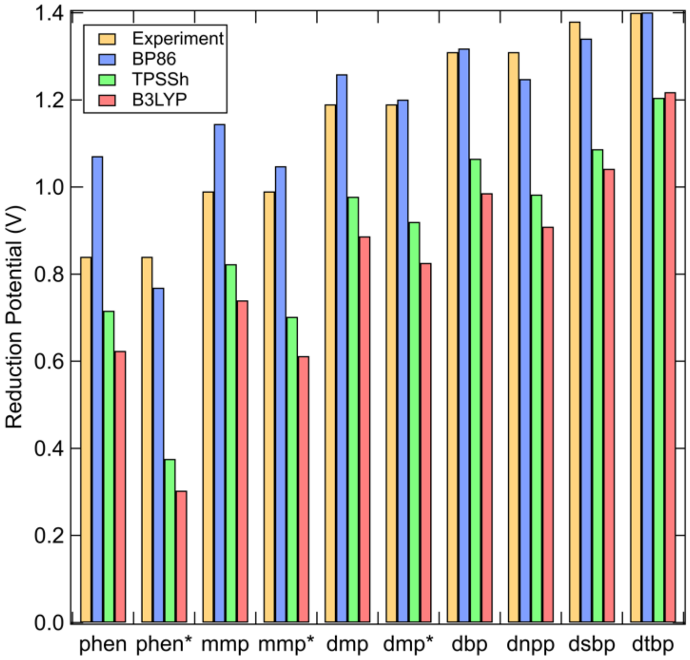

Figure 2.3. Comparison between experimental and calculated *E*°s for phen and 2,9-alkyl substituted complexes. Differences are given in Figure A.3.

As discussed above for *E*°, there is a nearly three order of magnitude gap between the τs of bis-phen and bis-dmp complexes (0.14 vs. 90 ns, respectively). We therefore measured the ^{3}MLCT lifetime of bis-mmp in DCM. The absorption data and corresponding transient absorption data for bis-mmp are given in Figure 2.4 (excitation at 410 nm). Fits to the decay of the excited state absorption at 550 nm give a lifetime of 2 ns. Note that the correlations presented in Figures 2.5 and 2.6 below predicted a similar lifetime for bis-mmp *a priori*; this observation points to the predictive and interpretive power of the correlations addressed herein. The latter in particular is elaborated on through comparisons to other Cu(I)-based photosensitizers in the Discussion section.

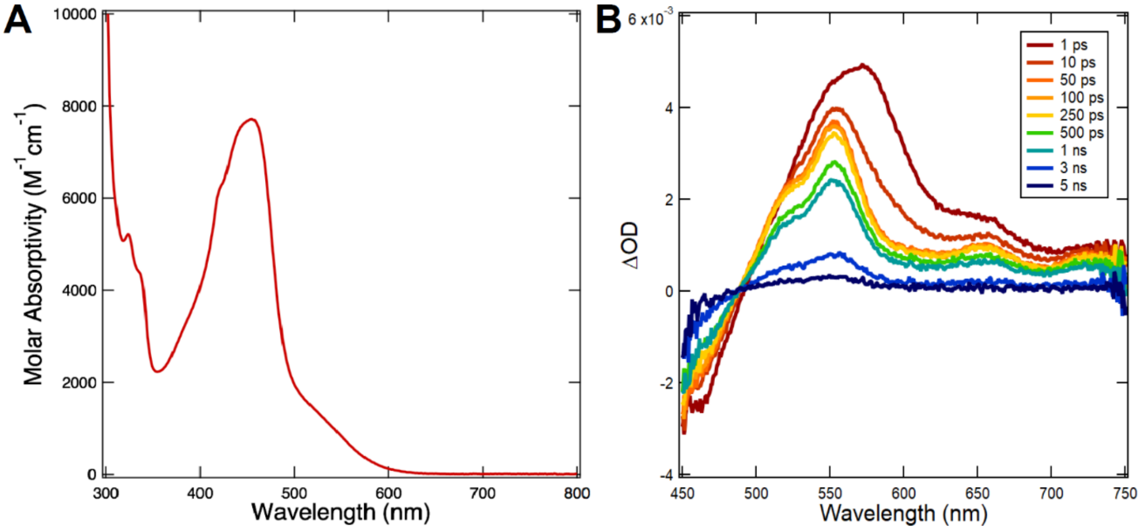

Figure 2.4. Optical data for Cu(I) bis-mmp. (A) UV-vis spectrum and (B) transient absorption data obtained using 410 nm excitation.

Experimental ln(τ)s are correlated to experimental *E*°s for bis-phen and the 2,9-alkyl substituted Cu(I) complexes in Figure 2.5. Given the broad range of structures, *E*°s, and lifetimes over these seven complexes, this linear correlation can provide a means to estimate an entatic energy. The slope and y-intercept of the correlation between ln(τ) and *E*°, along with the corresponding regression analysis at the 95% confidence interval, provides an entatic energy of 3.2 ± 0.7 kcal/mol (0.14 ± 0.03 eV) for one order of magnitude change in τ (see Appendix A Table A.3 for analyses). The experimental τs of the complexes considered in Figure 5 span many orders of magnitude in τ; translating to this experimental window in ^{3}MLCT lifetime equates to an entatic energy of 12.9 ± 2.9 kcal/mol (0.56 ± 0.13 eV) for a four orders of magnitude change in τ. Note that entatic energies for this and all other sections are summarized in Table 2.4 in the Discussion.

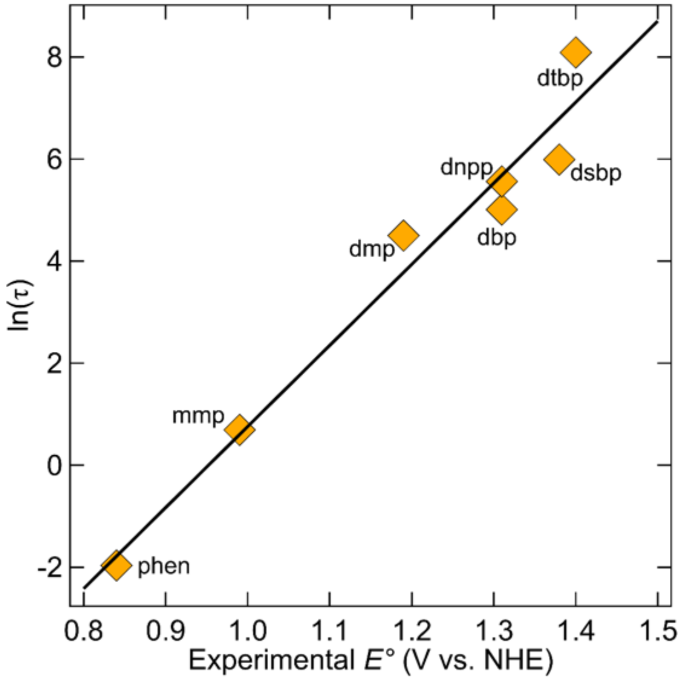

Figure 2.5. The correlation between experimental *E*°s and ln(*τ*)s for bis-phen and 2,9-alkyl substituted Cu(I) complexes. The linear fit has an $R^2 = 0.963$ and $y = (15.89\ V^{-1})x + 15.14$.

While the correlation between *E*° and ln(τ) is a potentially attractive means of determining entatic energies, solvation contributions can affect the Cu(I/II) *E*°. For instance, *E*° for bis-dmp can shift quite dramatically when measured in different coordinating solvents (e.g., a shift of -0.16 or -0.29 V is observed moving from DCM to CH_3CN or DMSO, respectively[94]). This solvent effect was successfully modeled assuming fast, reversible coordination upon oxidation, with little solvent binding to Cu(I).[94] In addition to ground state redox, solvent interactions have also been invoked and discussed for Cu-based excited state ^{3}MLCT formation and decay.[21,95] In the former case, coordination to Cu(II) stabilizes the oxidized state relative to the reduced state; this differential oxidation state stabilization decreases *E*°. Here, however, focusing solely on non-coordinating DCM allows us to effectively reduce contributions from direct solvent coordination to Cu(II) as much as possible and therefore provide a more accurate quantification of entatic contributions to *E*°. Nonetheless, despite being carried out in DCM, the electrochemical data for Cu(I) bis-phen is quasi-reversible, and high scan rates (>600 mV/s) are required (Appendix A Figure A.2). Thus, for the less solvent protected ligand sets, there are likely interactions between the oxidized state and some combination of solvent, electrode surface, and/or counter ion that can potentially contribute to *E*°. However, this selective interaction for Cu(II) is not accounted for using continuum solvation calculations, and we therefore attribute the discrepancies noted above (*vide supra*) between calculated and experimental potentials for bis-phen, -mmp, and -dmp complexes to this differential oxidation state stabilization. Note that the deviations between experiment and theoretical *E*°s are 0.23, 0.16, and 0.07 V for bis-phen, -mmp, and -dmp, respectively, supporting the diminished differential oxidation state stabilization across this series as ligand bulk is increased. Importantly, this observation also suggests that solvent contributions can affect the correlation between *E*° and ln(τ), and thus the quantification of entatic contributions. For example, using the computational values of

E°, which should represent a limit where no differential Cu(II) interactions are present, the correlation between *E*° and ln(τ) gives entatic energies of 1.7 ± 0.5 (0.07 ± 0.02 eV) and 6.8 ± 2.1 kcal/mol (0.29 ± 0.09 eV), respectively, for one and four orders of magnitude change in τ (Appendix A Figure A.3). These values are less than the 3.2 ± 0.7 (0.14 ± 0.03 eV) and 12.9 ± 2.9 kcal/mol (0.56 ± 0.13 eV) using experimental *E*°s (*vide supra*), which further indicates that differential oxidation state stabilization can affect the correlation between *E*° and ln(τ), and thus the entatic energy.

The differential oxidation state interactions can be evaluated by including the effects of a weakly coordinating ligand interaction (H_2O) in Cu bis-phen, -mmp, and -dmp complexes (denoted bis-phen*, -mmp*, and -dmp*). Note that the Cu(II)–OH_2 bond in bis-phen* is weak (~2.4 and ~2.5 Å in the oxidized and ^{3}MLCT states, respectively) and significantly weaker in bis-mmp* (~2.9 and ~3.0 Å in bis-mmp*). Water does not bond to Cu(II) in bis-dmp* (Appendix A Figure A.4). Differential oxidation state stabilization in bis-phen* lowers the calculated *E*° (BP86) from 1.07 to 0.77 V vs. NHE (Table 2.1 and Figure 2.3), in better agreement with experiment. Additionally, including the oxidation state selective interactions in bis-mmp* and -dmp* lowers the calculated *E*°s to 1.048 and 1.201 V, respectively, both improved relative to experiment. Lastly, correlating the calculated *E*°s and ln(τ) using these values for bis-phen*, -mmp*, and -dmp* (Appendix A Figure A.3) gives entatic energies of 3.3 ± 0.9 (0.14 ± 0.04 eV) and 13.1 ± 3.6 kcal/mol (0.57 ± 0.16 eV) for one and four orders of magnitude change in τ, respectively, in excellent agreement with values from purely experimental *E*°s (*vide supra*).

In addition to sterics, the difference in the electron-donating ability of the 2,9-alkyl substituents relative to –H can contribute to *E*° by preferentially stabilizing the oxidized over the reduced state. Here steric vs. electronic contributions can be decomposed using "H–capped" versions of the 2,9-alkyl substituents, which involve replacing the 2,9-alkyl group with an H atom and keeping the geometry completely unperturbed otherwise. The resulting calculated *E*°s for these H–capped structures are given in Appendix A Table A.1; a linear correlation between H–capped and capped structures is given in Appendix A Figure A.5. Indeed, calculated *E*°s are sensitive to H–capping. For example, for bis-dtbp, -dsbp, and -dmp, the difference in calculated *E*° between H–capped and uncapped structures is 0.148, 0.040, and 0.013 V, respectively, showing a systematic decrease with increasing electron-donating ability across the series. These contributions can also affect the correlation between *E*° and ln(τ). Using the calculated H–capped values and correlating with experimental ln(τ)s (Appendix A Figure A.3) results in entatic contributions for one and four orders of magnitude change in τ of 2.2 ± 1.0 (0.10 ± 0.04 eV) and 8.8 ± 4.1 kcal/mol (0.38 ± 0.18 eV), respectively. While the correlation for the H–capped structures is not as tight, these results suggest that the entatic contribution for the H–capped structures is larger than for the uncapped structures and that the electron-donating ability of the alkyl group opposes the entatic state. For a clearer comparison, τ increases from 0.14 to 3260 ns going from bis-phen to bis-dtbp. The calculated *E*°s for these structures vary by 0.330 V (~7.6 kcal/mol) in the uncapped structures. This difference increases to 0.476 V (~11.0 kcal/mol) in the H–capped structures. Therefore, the intrinsic entatic energy from bis-phen to bis-dtbp is opposed by the electron-donating dtbp group, consistent with the analyses using the slope of *E*° vs. ln(τ).

In summary, for this series of Cu photosensitizers, experimental *E*°s correlate linearly with τ over four orders of magnitude in lifetime. The slope of this correlation provides a potential quantitative estimate of the entatic contributions to τ. From experiment, the entatic energy is estimated to be 12.9 ± 2.9 kcal/mol (0.56 ± 0.13 eV) for a four order of magnitude increase in τ. However, differential oxidation state interactions over this series of complexes can affect the correlation and result in an overestimation of the entatic energy. This is exemplified by comparing the entatic energies from calculated *E*°s with and without differential oxidation state interactions (6.8 ± 2.1 kcal/mol (0.29 ± 0.09 eV) and 13.1 ± 3.6 kcal/mol (0.57 ± 0.16 eV), respectively, for a four order of magnitude increase in excited state lifetime). Additionally, steric and electronic contributions to the slope can be decomposed using H–capped vs uncapped structures. Analyses of these structures indicate that the electron-donating ability of the 2,9-alkyl substituents oppose the entatic contributions to the potentials and lifetimes from sterics; this is exemplified by the bis-phen to bis-dtbp comparison described above, for which the entatic energy is opposed by electron-donation by ~3 kcal/mol (~0.1 eV).

Finally, while the correlation between *E*° and ln(τ) is insightful, the entatic energies are estimated solely using thermodynamic parameters. In addition to the effects discussed above, these energies do not fully account for important contributions from the full potential energy surfaces involved in excited state relaxation processes, and are thus not most relevant for analyzing kinetics. The analysis is therefore translated to Cu(I/II) ground state inner sphere reorganization energies, excited state relaxation energies, and energy gaps below.

2.2.1.2. Entatic Contributions and Cu(I/II) Reorganization Energies

Entatic states have been invoked to rationalize the small reorganization energies of biological electron transfer active sites, which for T1 Cu active sites (e.g., plastocyanin, azurin) range from 0.7–1.2 eV.[96,97] This value contains contributions from the outer sphere reorganization as well, and the inner sphere contribution is thought to be ~0.4 eV. Here we use λ_is as an alternative means of quantifying entatic contributions to excited state processes, as they better capture the relative curvatures of the potential energy surfaces involved in redox and photophysical processes.

The approach described by Ryde et al.[98,99] (see Appendix A Figure A.1) has been applied successfully in calculating the λ_is for a wide-range of Cu complexes. Here λ_is have been calculated for a series of bis-phen and 2,9-alkyl Cu(I) complexes (Table 2.2 and Figure 2.2). λ_i for bis-phen is calculated to be 1.06 eV (BP86). For comparison, this value is lower than that reported by Ryde et al. for Cu(I/II)$(NH_3)_4$ (1.40 eV),[98] which reflects the increased steric constraints provided by the phen ligand relative to NH_3. Note that the majority of λ_i for Cu(I/II)$(NH_3)_4$ derives from the tetragonal distortion.[96,98] Beyond $E°$, additional insights regarding entatic contributions, including potential energy surfaces and their curvatures, can be determined from ground state λ_is.

As discussed above, a correlation can be drawn between the calculated ground state λ_is and the experimental ln(τ)s. This correlation, given in Figure 2.6A, is also linear and provides entatic contributions for one and four orders of magnitude change in τ of 4.3 ± 0.6 and 17.3 ± 2.2 kcal/mol. These calculated λ_is are free from differential oxidation state contributions, as was evaluated above for redox potentials. For comparison, using bis-phen*, -mmp*, and -dmp* in the correlation provides entatic contributions for one and four orders of magnitude change in τ of 5.4 ± 0.5 and 21.7 ± 2.0 kcal/mol.

Table 2.2. Comparisons between Excited State Lifetimes and Calculated Ground State Reorganization Energies, Excited State Relaxation Energies, and Energy Gaps for 2,9-Alkyl Substituted Bis-Phen Complexes.[a]

Ligand	**τ (ns)**	**ln(τ)**	**λ (eV)[b]**	**λ (eV)[c]**	**γ (eV)[b]**	**γ (eV)[c]**	**EG (eV)[b]**	**EG (eV)[c]**
phen	0.14	-1.97	0.994 (22.9)	1.064 (24.5)	1.434 (33.1)	1.428 (32.9)	0.778 (17.9)	0.767 (17.7)
phen*			1.067 (24.6)	1.222 (28.2)	1.391 (32.1)	1.411 (32.5)	0.655 (15.1)	0.627 (14.5)
mmp	2[d]	0.69	0.706 (16.3)	0.763 (17.6)	1.114 (25.7)	1.112 (25.6)	1.044 (24.1)	1.029 (23.7)
mmp*			0.802 (18.5)	0.922 (21.3)	1.202 (27.7)	1.202 (27.7)	0.944 (21.8)	0.932 (21.5)
dmp	90	4.50	0.484 (11.2)	0.521 (12.0)	0.910 (21.0)	0.890 (20.5)	1.377 (31.8)	1.360 (31.4)
dmp*			0.481 (11.1)	0.526 (12.1)	0.865 (19.9)	0.867 (20.0)	1.330 (30.7)	1.321 (30.5)
dbp	150	5.01	0.445 (10.3)	0.458 (10.6)	0.747 (17.2)	0.725 (16.7)	1.507 (34.8)	1.507 (34.8)
dnpp	260	5.56	0.388 (9.0)	0.393 (9.1)	0.665 (15.3)	0.664 (15.3)	1.418 (32.7)	1.423 (32.8)
dsbp	400	5.99	0.397 (9.2)	0.407 (9.4)	0.715 (16.5)	0.716 (16.5)	1.511 (34.8)	1.515 (34.9)
dmp-dtbp	730[e]	6.59	0.383 (8.8)	0.381 (8.8)	0.616 (14.2)	0.621 (14.3)	1.658 (38.2)	1.649 (38.0)
dtbp	3260	8.09	0.176 (4.1)	0.183 (4.2)	0.312 (7.2)	0.312 (7.2)	1.896 (43.7)	1.894 (43.7)

*Optimized structure includes a weak H_2O interaction as discussed in the text.

[a] Unless indicated, lifetimes were taken from Table 1 of Ref 21 and references cited therein. Parenthetical values in kcal/mol.

[b] Gas phase.

[c] CPCM corrected.

[d] This work.

[e] Reference 92.

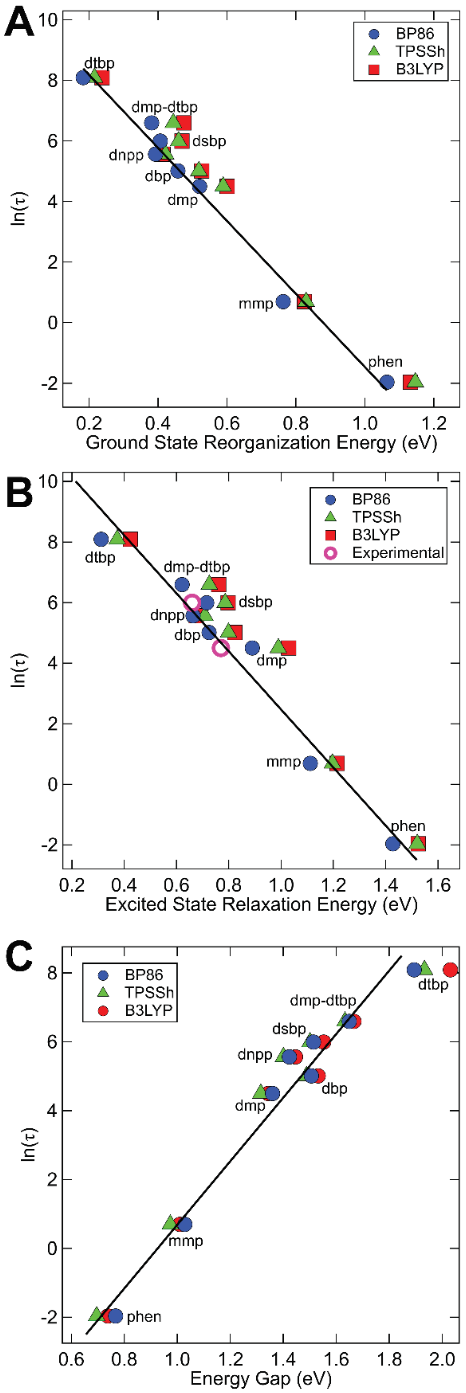

Figure 2.6. Correlations between ln(τ)s and (A) ground state reorganization energies, (B) excited state relaxation energies, and (C) energy gaps for bis-phen and the 2,9-alkyl substituted Cu(I) complexes. The linear fit (black line) is shown for BP86. For A, the fit has $R^2 = 0.984$ and the equation $y = (-12.06\ \text{eV}^{-1})x + 10.59$. For B, $R^2 = 0.956$ and the equation $y = (-9.58\ \text{eV}^{-1})x + 12.05$. For C, $R^2 = 0.965$ and the equation $y = (9.23\ \text{eV}^{-1})x + 8.55$.

As presented above for ground state redox, the λ_is can be corrected for electron-donating effects of the 2,9-alkyl substituents to decompose the steric and electronic contributions to λ_i by analyzing the H-capped structures. The H–capped results provide entatic contributions for one and four orders of magnitude in τ of 4.4 ± 0.7 and 17.7 ± 3.0 kcal/mol (see Appendix A Figure A.6). These values are similar to those obtained from uncapped structures, indicating that, unlike $E°$s, electron-donating effects are minimized in the evaluation of λ_i. Thus, the entatic contributions estimated using λ_i are largely due to sterics and further suggest that sterics play a more significant role in excited state lifetimes than electron-donating contributions. This is corroborated below using excited state relaxation energies.

Lastly, entatic contributions estimated for over four orders of magnitude change in τ are similar between gas phase and CPCM solvation approaches (15.7 ± 2.4 and 17.3 ± 2.2 kcal/mol, respectively). This observation further supports that λ_is moreso reflect geometric/steric contributions as opposed to solvation and/or electron-donating effects.

In summary, for this series of Cu(I) photosensitizers, the calculated λ_is correlate linearly with $\ln(\tau)$ over four orders of magnitude in τ. The slope of this correlation provides a potential quantitative estimate of the entatic contributions to the excited state lifetimes. The entatic energy using this method is estimated to be 17.3 ± 2.2 kcal/mol for a four order of magnitude increase in τ. In contrast to $E°$s, differential oxidation state interactions over this series of complexes have a significantly smaller effect on the correlation between energetics and $\ln(\tau)$. Furthermore, electron-donating effects, estimated using the comparison between H–capped and uncapped structures, are minimized in λ_is, which results in similar estimates of entatic contributions.

2.2.1.3. Entatic Contributions and Cu(I/II) Metal-to-Ligand Charge Transfer Relaxation

In addition to λ_is, the same methodology can be translated to estimate excited state ^{3}MLCT relaxation energies (γ_is). The calculated γ_is (see Methods and Appendix A Figure A.7) are given in Table 2.2 and their correlation with experimental $\ln(\tau)$ is given in Figure 2.6B. This correlation provides entatic contributions of 5.3 ± 1.1 and 21.2 ± 4.5 kcal/mol, respectively, for one and four orders of magnitude change in τ.

To provide an experimental calibration, 77 K emission spectra were collected on $[Cu(dsbp)_2][PF_6]$ and $[Cu(dmp)_2][PF_6]$ complexes (Appendix A Figure A.10) in 1:1 toluene/DCM glasses, and experimental bandwidths and fittings provide γ_is of 0.66 and 0.77 eV, respectively.[100] These values are in fair agreement with those calculated for bis-dsbp and -dmp complexes (0.715 and 0.910 eV, respectively) and are in good agreement with the overall correlation between $\ln(\tau)$ and γ_i for bis-phen and the 2,9-alkyl complexes (Figure 2.6B, pink circles).

As done above, the potential role of differential solvation can be evaluated using the γ_is estimated for bis-phen*, -mmp*, and -dmp*. Using these structures in the correlation, entatic energies for one and four orders of magnitude in τ are estimated to be 5.5 ± 1.0 and 21.8 ± 4.1 kcal/mol, respectively. Furthermore, the role of electron-donation can be evaluated using the H–capped and uncapped structures. Using the H–capped structures gives entatic contributions of 5.2 ± 1.4 and 20.8 ± 5.5 kcal/mol, respectively, for one and four orders of magnitude change in τ. As with λ_is, γ_is provide very similar entatic contributions using H–capped vs. uncapped structures, both suggesting that excited state lifetimes are largely governed by sterics, and electron-donating contributions from the 2,9-alkyl groups are minimal. Furthermore, entatic contributions over four orders of magnitude in τ are similar between gas phase and CPCM solvation approaches (21.3 ± 4.8 and 21.2 ± 4.5 kcal/mol, respectively). This further supports the observation that the calculated γ_is purely reflect geometric and steric contributions to the relaxation energy.

In summary, for this series of Cu photosensitizers, the calculated γ_is correlate linearly with ln(τ) over four orders of magnitude in τ. The slope of this correlation provides a potential quantitative estimate of the entatic contributions. The entatic energy estimated for four orders of magnitude in τ using the uncapped structures (21.2 ± 4.5 kcal/mol) is essentially identical to those determined using H–capped structures (20.8 ± 5.5 kcal/mol) or those accounting for differential oxidation state stabilization (21.8 ± 4.1 kcal/mol). Additionally, gas phase and CPCM corrected calculations provide essentially identical entatic contributions. Thus, correlating γ_is and experimental τs provides a robust means to quantify purely geometric and steric contributions from the entatic state. As discussed below, we therefore use this correlation to provide a comparison to a variety of classes of Cu-based photosensitizers reported in the literature.

2.2.1.4. Entatic Contributions and the Cu(I/II) Metal-to-Ligand Charge Transfer Energy Gap

In addition to λ_is and γ_is, we can apply the same correlation between ln(τ) and the calculated energy gap between the ^{3}MLCT excited state and the reduced ground state in the equilibrium structure of the ^{3}MLCT excited state (Appendix A Figure A.1B). These energies are reported in Table 2.2 and correlated with ln(τ) in Figure 2.6C (also see Appendix A Figure A.8). This correlation provides entatic contributions of 5.6 ± 1.0 and 22.2 ± 4.2 kcal/mol, respectively, for one and four orders of magnitude change in τ. This is in good agreement with entatic estimates using γ_is.

As done above, the potential role of differential solvation can be evaluated using the energy gaps for bis-phen*, -mmp*, and -dmp*. Using these structures in the correlation, entatic energies for one and four orders of magnitude in τ are estimated to be 6.4 ± 0.9 and 25.6 ± 3.8 kcal/mol, respectively. Furthermore, using the H–capped structures gives entatic contributions of 5.5 ± 1.6 and 22.1 ± 6.2 kcal/mol, respectively, for one and four orders of magnitude change in τ. As with λ_is and γ_is, energy gaps provide very similar entatic contributions using H–capped vs. uncapped structures, both suggesting that excited state lifetimes are largely governed by sterics, and electron-donating contributions from the 2,9-alkyl groups are minimal. Furthermore, entatic contributions over four orders of magnitude in τ are similar between gas phase and CPCM solvation approaches (21.9 ± 4.3 and 22.2 ± 4.2 kcal/mol, respectively). This further supports the observation that the calculated λ_is, γ_is, and energy gaps purely reflect geometric and steric contributions to the relaxation energy.

In summary, similarly to λ_is and $E°$s, the entatic energetics from the energy gap are somewhat sensitive to differential solvation, whereas γ_is appear to provide entatic energies that reflect steric contributions over this series of Cu bis-phen-based complexes. From these data, the entatic state can provide a strong influence over dynamics that can be described by the energy gap law.

2.2.1.5. Perturbations to the 2,9-Position: Effects of π-Stacking and Structural Flattening

The data in Figure 2.6B determined the purely steric contributions to the excited state dynamics of Cu(I) bis-phen and 2,9-alkyl complexes, which provides a powerful means to draw insights into excited state dynamics by quantifying and decomposing additional structural and/or electronic-withdrawing/-donating effects. This can be accomplished for any Cu-based photosensitizer for which τ is known experimentally by adding the corresponding point(s) onto the correlation between $\ln(\tau)$ and γ_i. Excellent first examples of this are the Cu(I) bis-phen complexes with aryl substituents at the 2,9-positions (Figure 2.7A). As shown in Figure 2.7B, the homoleptic Cu(I) complex with the 2,9-diphenyl-1,10-phenanthroline (dpp) ligand has a distinctly flattened structure in the Cu(I) ground state relative to those with H– or alkyl groups (e.g., ~90° vs. ~70° for Cu(I) bis-phen and bis-dpp). This flattening is due to the π-stacking between the aryl groups of the dpp ligand. Here, in addition to bis-dpp, we have investigated homoleptic complexes with the ligands 2,4,7,9-tetraphenyl-1,10-phenanthroline (tpp), 2,9-bis(4-methylphenyl)-1,10-phenanthroline (dmpp), 2,9-diphenyl-4,7-dimethyl-1,10-phenanthroline (dpdmp), and 2,9-diphenyl-3,4,7,8-dimethyl-1,10-phenanthroline (dptmp). While τs for these complexes only span ~230 – 480 ns, they exhibit distinctly different structural characteristics relative to the alkyl complexes. Note that in our investigations of the aryl complexes, we encountered a glitch in the CPCM cavity construction in ORCA, which resulted in erroneous SCF energies, specifically for these aryl complexes. We therefore could only obtain gas phase values of γ_i across this series. However, as shown above, gas phase and CPCM calculations yield identical results for correlations between $\ln(\tau)$ and γ_i, and therefore this has essentially no effect on the analysis.

The gas phase derived correlation between ln(τ) and γ_i for the 2,9-alkyl complexes is reproduced in Figure 2.8. The 2,9-aryl complexes (green circles, Figure 2.8) fall in a cluster below the line defined by the 2,9-alkyl complexes. This deviation could be due to either steric or electronic contributions from the phenyl rings. H–capped structures can be used to evaluate this. Upon capping, the γ_i of the 2,9-diphenyl complexes all systematically increase. This increased γ_i would bring the points in for the uncapped structures in Figure 2.8 closer to the correlation generated from the 2,9-alkyl complexes. Thus, electronics do play a role in the differences between the 2,9-aryl and the 2,9-alkyl complexes, albeit a somewhat minor one.

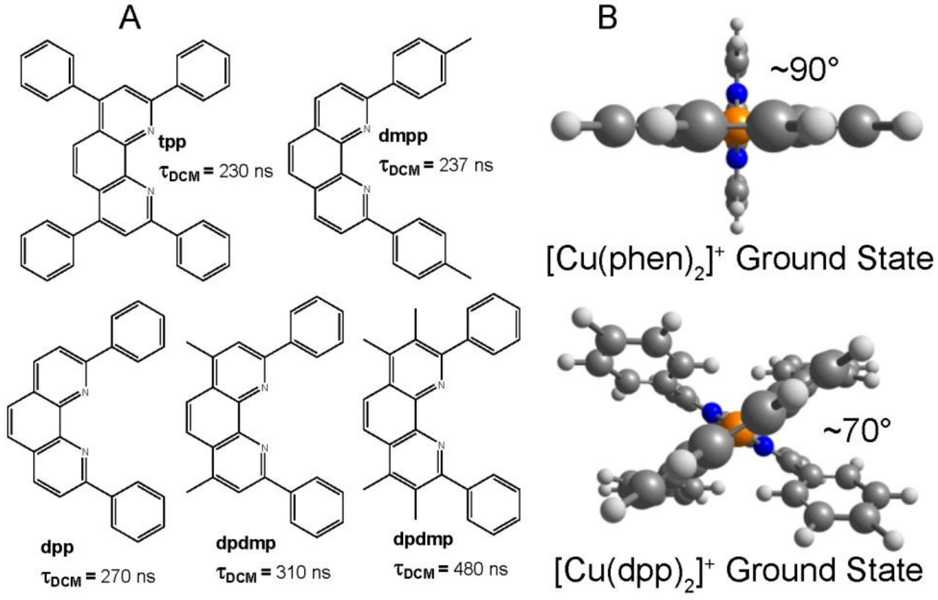

Figure 2.7. 2,9-aryl bis-phens. (A) The 2,9-aryl substituted ligands of the homoleptic complexes used to investigate the effects of π-stacking and structural flattening on τ. (B) Comparison between the flattening angles for the bis-phen and bis-dpp ground states.

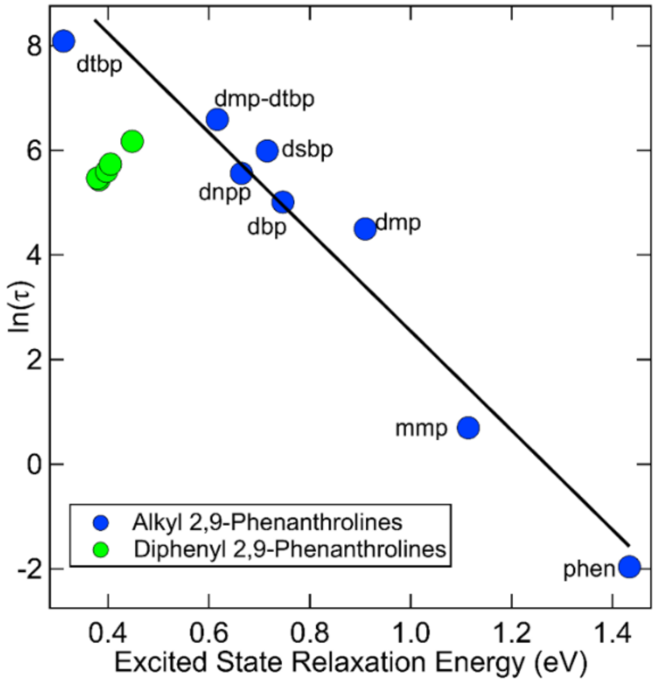

Figure 2.8. ln(τ) vs. γ_i for the bis-phen, 2,9-alkyl, and 2,9-aryl substituted complexes in the gas phase. The gas phase fit for the 2,9-alkyls has an $R^2 = 0.952$ and the equation $y = (-9.50\ eV^{-1})x + 12.04$.

Furthermore, because these complexes are already flattened in the ground state due to π-stacking, minimal structural changes are required to reach the equilibrium ^{3}MLCT states from the corresponding ground states. For bis-dpp, the difference in the ligand plane flattening angle between the ground and ^{3}MLCT states is only 11° compared to 54° for bis-phen. The excited state potential energy surfaces of the 2,9-aryl complexes are also significantly shallower relative to the 2,9-alkyls, which is indicative of a decreased distorting force in the ^{3}MLCT state (*vide infra*).

The calculated γ_i values of bis-tpp, bis-dmpp, bis-dpp, and bis-dpdmp all fall within a <1 kcal/mol range. In the reduced and ^{3}MLCT states, their structures all have ligand plane flattening angles of ~69° and ~58°, respectively. However, bis-dptmp has a γ_i value ~1.0

kcal/mol higher than that for bis-dpdmp, the complex with the next largest γ_i value. bis-dptmp also differs in its ligand flattening angles, 77° for the reduced state and 64° for the ^{3}MLCT state. The methyl-groups at the 3,8-positions are the only possible sources of this difference. A second H-capping at the 3,4,7,8-positions has very little effect on the calculated γ_i value relative to the first H-capping. As might be expected, the 3,8-methyl groups are mostly accounted for by steric bulk rather than electron-donating effects. For bis-tpp, removing the phenyl groups at the 4,7-positions, however, increases γ_i by ~1 kcal/mol relative to the value from the first H-capping. As these rear-facing groups are unable to experience steric clashes, this indicates that there is a small, but noticeable effect on γ_i from the electronics of the 4,7-phenyl groups.

In summary, the 2,9-aryl complexes have significantly diminished γ_is relative to $[Cu(phen)]^+$ due to the structural flattening present in the ground state. This lowered value of γ_i results in a significant increase in the ^{3}MLCT lifetime. Electronics also play a minor role in the 2,9-aryl complexes. The effects result in noticeable shifts from the correlation generated by the 2,9-alkyl complexes, in which γ_i is dominated by sterics.

2.2.1.6. Excited State Linear Coupling Terms

Entatic states can strongly modify the locations and curvatures of potential energy surfaces involved in excited state relaxation processes. The correspondence between γ_i and the curvature of the excited state potential energy surfaces can be directly evaluated through examination of a quantity known as the linear coupling term (LCT), which takes into account the displacement between the ground and excited state potential energy surfaces. This displacement of the excited surface relative to the ground state results in a distorting force along a normal mode, q_i. This distorting force can be quantified by evaluating the effect of electron-nuclear coupling on the total energy of the excited state:[101]

$$E^{e}_{elec-nuc} = \left\langle \psi_e^{elec} \middle| \frac{\partial \boldsymbol{H}_{ES}}{\partial q_i} \middle| \psi_e^{elec} \right\rangle q_i, \qquad \text{(eq 2.1)}$$

For non-zero values of this integral, the excited state will distort along q_i by a value Δq_i; the force present in the excited state can be determined by calculating the energy change in the electronic transition to ψ_e with a change along the coordinate q_i. The resulting line is the LCT (Figure 2.9A), the slope ($\partial E/\partial q_i$) of which corresponds to the excited state distorting force and therefore reflects the relative curvature of the excited state potential energy surface near the ground state equilibrium geometry (i.e., in the vicinity of the Franck-Condon region).

The ^{3}MLCT excited state slopes and LCTs for bis-phen and bis-dmp complexes are given in Figure 2.9B. These were determined by calculating the relative energy separation between the Cu(I) ground state and ^{3}MLCT excited state along q_i, the ground state structure's ligand flattening vibrational mode (see Figure 2.1). This is accomplished by distorting the ground state structure along the ligand flattening normal mode, and then, without further relaxing the geometry, calculating the triplet single point energy. This allows for the evaluation of the ^{3}MLCT excited state slope near the Franck-Condon geometry. For the bis-phen and -dmp complexes, the ^{3}MLCT potential energy surface exhibits the expected 'double-well' shape as a consequence of the Jahn-Teller distortion present along the flattening mode. From Figure 2.9B, the slope (and thus the LCT) is larger for bis-phen than bis-dmp. Linear fits provide quantitative slopes of -0.0182 and -0.0122 eV/° for bis-phen and bis-dmp complexes, respectively. Thus, both γ_i (*vide supra*) and the LCT decrease in going from bis-phen to bis-dmp.

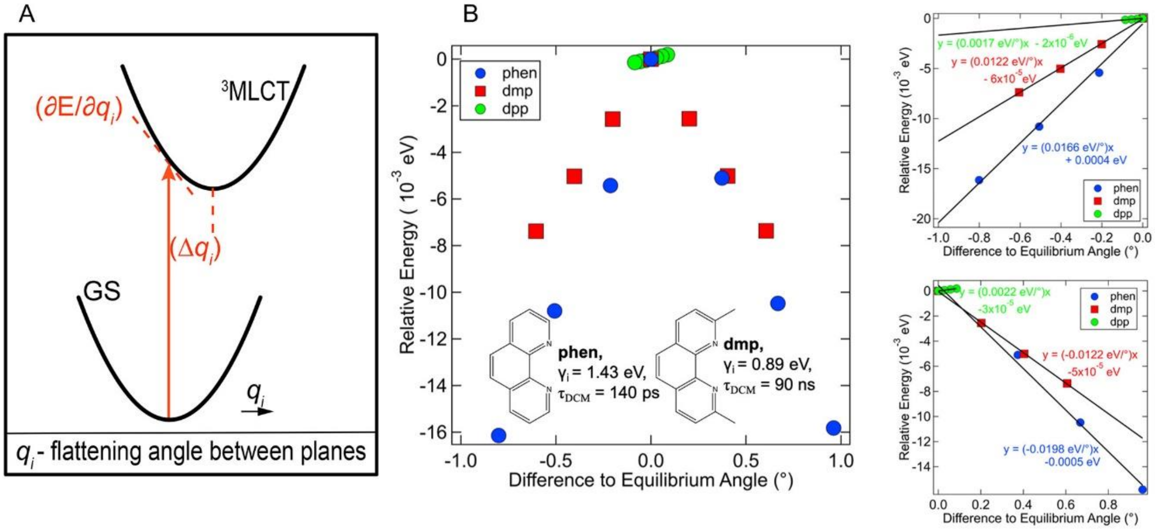

Figure 2.9. Linear Coupling Terms. (A) Origin and depiction of the linear coupling term. (B, left) Calculated linear coupling terms for bis-phen and bis-dmp. (B, right) Linear fits of the linear coupling terms in B, left. All fits have values of $R^2 > 0.99$.

From the LCTs and the results presented above for γ_i (section 2.2.1.3), a general picture of the entatic state can be drawn for these Cu(I)-based photosensitizers (Figure 2.10). The entatic state shifts the ^{3}MLCT excited state to angles closer to 90° (black arrow in Figure 2.10) while concomitantly increasing their curvature (black to blue surfaces in Figure 2.10). Thus, the entatic state changes the point of intersection between the two ‘double-well’ potential energy surfaces and results in a decrease in the LCT, and thus the magnitude of electron-nuclear coupling in the Franck-Condon region (black to blue boxes in Figure 2.10).

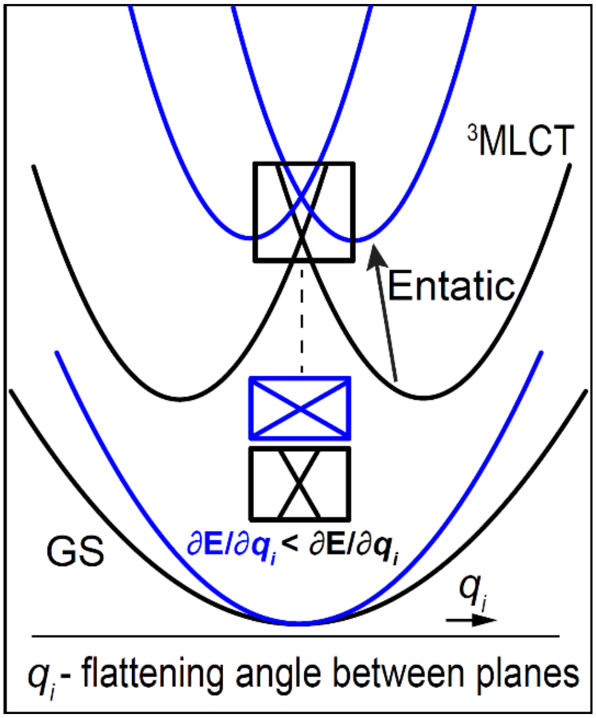

Figure 2.10. Generalized depiction of the entatic state and its effects on the potential energy surfaces for ^{3}MLCT formation and relaxation.

For comparison, the LCTs were also determined for the 2,9-aryl complexes discussed above. Because the Cu(I) ground state is already considerably flattened, there should be no 'double-well' potential energy surfaces for the 2,9-alkyl complexes. This is observed in Figure 2.9, middle, for bis-dpp (green circles). In addition, for this change in the potential energy surface for the 2,9-alkyl vs. -aryl complexes, the resulting LCT is also an order of magnitude smaller for the latter complexes (Table 2.3), indicating an even smaller magnitude of electron-nuclear coupling in the Franck-Condon region for the 2,9-aryl complexes. This is consistent with their significantly reduced γ_is relative to bis-phen and bis-dmp (Table 2.2).

In summary, entatic states result in strongly modified locations, curvatures, and intersections of the potential energy surfaces involved in photochemical dynamics, and γ_is and LCTs provide a detailed picture and quantification of these entatic contributions.

Table 2.3. Comparison Between Calculated Values of γ_i for H–Capped and Uncapped Versions of the 2,9-Aryl Complexes.[a]

Ligand	**τ (ns)**	**ln(τ)**	**γ (eV)[b]**	**γ (eV)[c]**	**γ (eV)[d]**	**$\Delta\gamma$ (eV)[e]**	**Red. Angle (°)**	**Trip. Angle (°)**	**LCT (eV/°)**
phen	0.14	-1.97	1.434 (33.1)	1.434 (33.1)	1.434 (33.1)	0.0 (0.0)	90.0	35.5	0.0198/ 0.0166
dmp	90	4.50	0.910 (21.0)	0.891 (20.5)	0.891 (20.5)	-0.020 (-0.5)	90.0	59.7	0.0122
tpp	230	5.44	0.382 (8.8)	0.489 (11.3)	0.525 (12.1)	0.107 (2.5)	69.4	58.3	0.0023
dmpp	237	5.47	0.379 (8.7)	0.495 (11.4)	0.495 (11.4)	0.116 (2.7)	69.4	58.1	0.0028
dpp	270	5.60	0.397 (9.2)	0.494 (11.4)	0.494 (11.4)	0.097 (2.2)	69.5	58.6	0.0019
dpdmp	310	5.74	0.405 (9.3)	0.504 (11.6)	0.511 (11.8)	0.099 (2.3)	69.7	58.1	0.0068
dptmp	480	6.17	0.448 (10.3)	0.514 (11.9)	0.509 (11.7)	0.066 (1.5)	77.0	63.7	0.0085

[a] Lifetimes were taken from Table 1 of Reference 21. Parenthetical values in kcal/mol.
[b] Uncapped complexes.
[c] H–capped at 2,9-positions.
[d] H–capped at all positions.
[e] Difference between uncapped and H–capped at 2,9-positions.

2.3. Discussion

Photosensitizers have a broad range of applications, including solar electricity generation, solar fuels catalysis, photoredox catalysis, and OLEDs. Their applicability hinges on excited state lifetimes and excited state redox potentials. In terms of the former, much discussion has revolved around sterics and increasing structural rigidity. For Cu-based photosensitizers, the direct correlation between their excited state structural changes and the ground state redox properties of electron transfer active sites of metalloproteins has inspired an extension of the entatic/rack-induced state to photosensitizer dynamics.[19,20] While a core concept in bioinorganic chemistry and a powerful way to inspire new ligand design, the entatic state is difficult to quantify, and there are only a few examples in the literature where this has been accomplished.[8–12] Here we have leveraged correlations between ^{3}MLCT excited state lifetimes of Cu(I) bis-phen complexes and their corresponding $E°$s (Figure 2.5), λ_is, γ_is, and energy gaps (Figures 2.6A/2.6B/2.6C, respectively). These linear correlations are observed for over four orders of magnitude change in τ and provide a direct means to quantify entatic state contributions to the excited state dynamics of a broad range of Cu(I)-based photosensitizers.

There can be differences in the quantified entatic energies, however, depending on which correlation is used. A summary of values for different approaches is given in Table 2.4. When using $E°$s, there can be significant contributions from differential oxidation state stabilization, which, for Cu(I) bis-phen complexes, stabilizes the oxidized over the reduced state and lowers the redox potential. This can affect the correlation between ln(τ) and redox potential. For example, from Table 2.4, the correlation between ln(τ) and experimental redox potential provides an estimate of an entatic contribution of 12.9 ± 2.9 kcal/mol for a four order in magnitude change in τ, while the same correlation using calculated values of redox potentials gives 6.8 ± 2.1 kcal/mol. The difference between these values largely derives from the overestimation of the calculated $E°$s of bis-phen, -mmp, and -dmp complexes. This overestimation decreases the slope of the ln(τ)/$E°$ correlation and gives rise to a lower value of entatic energy. Above, it was shown that accounting for the differential oxidation state stabilization for the three complexes (using bis-phen*, -mmp*, and -dmp*) results in a slope of 13.1 ± 3.6 kcal/mol, in much better agreement with experiment. Lastly, by using H–capped structures, it was demonstrated that the electron donating effects of the 2,9-alkyl substituents can oppose the entatic state contributions (e.g., by ~3 kcal/mol for bis-phen vs. bis-dtbp).

Table 2.4. Entatic state analyses.[a]

Method	**R^2**	**slope (eV)**	**y-int (eV)**	**Entatic (kcal/mol)[b]**	**Entatic (kcal/mol)[c]**
E° (1)[d]	0.963	0.0606	0.9616	3.2 ± 0.7	12.9 ± 2.9
E° (2)[e]	0.935	0.0322	1.1264	1.7 ± 0.5	6.8 ± 2.1
E° (3)[f]	0.946	0.0616	0.9440	3.3 ± 0.9	13.1 ± 3.6
E° (4)[g]	0.857	0.0414	1.1243	2.2 ± 1.0	8.8 ± 4.1
λ_i (1)[h]	0.984	-0.0816	0.0873	4.3 ± 0.6	17.3 ± 2.2
λ_i (2)[i]	0.992	-0.1020	1.0010	5.4 ± 0.5	21.7 ± 2.0
λ_i (3)[j]	0.972	-0.0832	0.8817	4.4 ± 0.7	17.7 ± 3.0
λ_i (4)[k]	0.977	-0.0740	0.8156	3.9 ± 0.6	15.7 ± 2.4
γ_i (1)[h]	0.956	-0.0998	1.2383	5.3 ± 1.1	21.2 ± 4.5
γ_i (2)[i]	0.966	-0.1027	1.2571	5.5 ± 1.0	21.8 ± 4.1
γ_i (3)[j]	0.934	-0.0979	1.2378	5.2 ± 1.4	20.8 ± 5.5
γ_i (4)[k]	0.952	-0.1002	1.2461	5.3 ± 1.2	21.3 ± 4.8
EG (1)[h]	0.965	0.1046	0.9424	5.6 ± 1.0	22.2 ± 4.2
EG (2)[i]	0.978	0.1205	0.8395	6.4 ± 0.9	25.6 ± 3.8
EG (3)[j]	0.926	0.1043	0.9172	5.5 ± 1.6	22.1 ± 6.2
EG (4)[k]	0.962	0.1032	0.9539	5.5 ± 1.1	21.9 ± 4.3

[a] Error analyses conducted at the 95% confidence interval.
[b] One order of magnitude change in τ.
[c] Four orders of magnitude change in τ.
[d] Using experimental *E*°s.
[e] Using calculated *E*°s (uncapped).
[f] Using calculated *E*°s with differential oxidation state stabilization (bis-phen*, -mmp*, and -dmp*). *Optimized structure includes a weak H_2O interaction as discussed in the text.
[g] Using calculated *E*°s (H–capped).
[h] Using calculated energies (uncapped).
[i] Using calculated energies with differential oxidation state stabilization (bis-phen*, -mmp*, and -dmp*).
[j] Using calculated energies (H–capped).
[k] Using calculated energies (uncapped, gas phase).

Overall, the sensitivity to differential oxidation state contributions, largely stemming from the fact that the total oxidation state changes during redox (i.e., Cu(I/II)), in addition to contributions from electron-donating/-withdrawing effects of the 2,9-alkyl groups, suggests that using the correlation between $E°$ and $\ln(\tau)$ is not an ideal way to quantify entatic states in photophysical processes. This is perhaps not surprising given that ground state potentials are thermodynamic quantities and do not take into account important contributions from shifts and changes in the curvature of the excited state potential energy surfaces when an entatic state is present (Figure 2.10).

The extension of the correlation to λ_is alleviates some of the issues presented using $E°$s. The entatic energies estimated using the correlations with calculated λ_is are also given in Table 2.4. Here the correlation provides an entatic energy of 17.3 ± 2.2 kcal/mol, and differential oxidation state stabilization using bis-phen*, -mmp*, and -dmp* provides an entatic energy that varies less relative to the same comparison using redox potentials (21.7 ± 2.0). Additionally, the entatic energy is not sensitive to electron-donating/-withdrawing effects (i.e., H–capped vs. capped, 17.3 ± 2.2 vs. 17.7 ± 3.0 kcal/mol, respectively). These observations are also mirrored by the use of calculated γ_is, which provide an entatic energy of 21.2 ± 4.5 kcal/mol for a four order of magnitude change in τ. This value is similar when incorporating differential oxidation state stabilization, H–capped vs. uncapped structures, or gas phase vs. CPCM calculations (Table 2.4), which indicates that it is a robust, general means to estimate entatic contributions to photophysical processes. This correlation is used below to quantify entatic energies across other types of Cu(I)-based photosensitizers.

2.3.1. Extension to Other Copper(I) Bis-Phenanthrolines

In addition to the 2,9-alkyl and -aryl complexes discussed above, a variety of other copper(I) bis-phen-based complexes have been characterized in the literature. These homoleptic complexes are based on the ligands: 4,4',6,6'-tetramethyl-2,2'-bipyridine (tmbp), 2,9-dimethyl-4,7-diphenyl-1,10-phenanthroline (bathocuproine or bcp), 2,9-di-*n*-butyl-4,7-dimethyl-1,10-phenanthroline (dbdmp), 2,9-bis(trifluoromethyl)-1,10-phenanthroline (bfp), 2,9-dineopentyl-1,10-phenanthroline (dnpp), 2,9-di-*n*-butyl-3,4,7,8-tetramethyl-1,10-phenanthroline (dbtmp), and 2,9-dichloro-1,10-phenanthroline ligand (Cu-Cl, for consistency[102]) (Figure 2.11).[21,102,103] γ_i values were calculated for these complexes and are compared to the ln(τ) vs. γ_i line given by the 2,9-alkyl complexes in Figure 2.12A.

In Figure 2.12A, the non-diphenyl Cu(I) bis-phen-based complexes all fairly closely track the ln(τ) vs. γ_i line given by the 2,9-alkyl complexes. Of these species and those discussed above, the bis-bfp and Cu-Cl complexes are unique due to the presence of electron-withdrawing groups at the 2,9-positions. Using the gas phase correlation between ln(τ) and γ_i, the estimated entatic energies for bis-bfp and Cu-Cl are 16.5 ± 3.4 and 14.3 ± 3.0, respectively. However, we can further investigate the potential role of electronics provided by the –CF_3 and –Cl substituents using the H–capped structures. The gas phase γ_is for the uncapped and H–capped versions of bis-bfp are 0.793 and 0.721 eV (Δ = -0.072 eV, -1.6 kcal/mol), respectively, while the analogous values for Cu-Cl are 0.722 and 0.856 eV (Δ = 0.134 eV, ~3.1 kcal/mol). Consistent with the earlier discussion of λ_is and, especially γ_is, the excited state lifetimes appear to be largely reflecting the steric effects on structure, and the electronic contributions to the lifetimes are relatively minor.

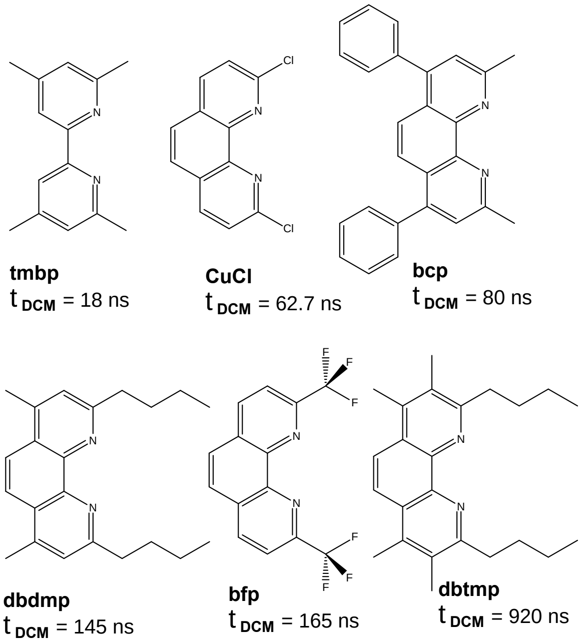

Figure 2.11. Additional ligands for homoleptic Cu(I) bis-phenanthroline complexes of interest.

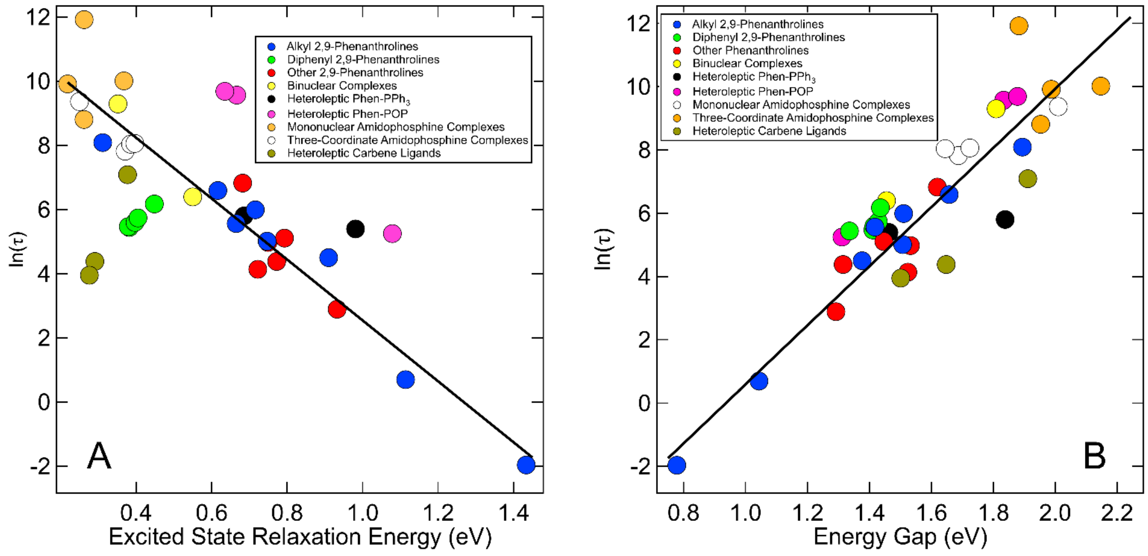

Figure 2.12. Gas phase plots of ln(τ) vs. (A) γ_i and (B) energy gap for all Cu(I) complexes. Linear fits are for the 2,9-alkyl complexes. Deviations from these fits reflect key differences in geometric vs. electronic contributions to excited state dynamics.

Previous discussions in the literature have ascribed the long lifetime of bis-bfp to the electron-withdrawing nature of the $–CF_3$ substituents.[92] The analysis here suggests otherwise. For comparison, the flattening angle of bis-bfp in the Cu(I) ground state and ^{3}MLCT excited states are 89° and 66°, respectively. Interestingly, the same angles for bis-dbp are very similar to bis-bfp at 90° and 65°. Additionally, the γ_is for bis-bfp and bis-dbp are within ~1 kcal/mol, and their respective lifetimes are 165 and 150 ns (Appendix A Table A.4). Thus, the power of the entatic analysis is highlighted here and suggests that the excited state lifetime of bis-bfp is not strongly influenced by electron-withdrawing effects. Rather, steric contributions are dominant.

Cu-Cl provides another interesting comparison. It was shown above that the γ_i of Cu-Cl is reduced by 0.134 eV (~3.1 kcal/mol) by the –Cl substituent. Furthermore, the ligand flattening angles in the reduced and ^{3}MLCT states are 90° and 59°, respectively. For comparison, the same angles for bis-dmp are 90°and 65°. However, bis-dmp has a γ_i of 0.910 eV, which is 0.188 eV higher than Cu-Cl. This higher γ_i is present despite the smaller change in ligand flattening for bis-dmp relative to Cu-Cl. However, despite this reduced γ_i for Cu-Cl relative to bis-dmp, it still has a reduced excited state lifetime (63 ns) relative to bis-dmp (90 ns), which suggests that electronics play a role in the excited state lifetime. This is in agreement with a recent study of the effects of halogen substituents by Pellegrin et al.[102] Thus, the entatic state analyses can be used to disentangle steric and electronic effects across Cu(I)-based photosensitizers, and bis-bfp and Cu-Cl have provided two interesting examples for mononuclear Cu(I) complexes. Similar analyses are extended to binuclear Cu(I) complexes below.

2.3.2. Additional Classes of Copper Complexes

In addition to Cu(I) bis-phen complexes, a wide range of additional Cu(I) complexes with long ^{3}MLCT excited state lifetimes have been reported. Among these are three- and four-coordinate mononuclear amidophosphine complexes[104,105] and binuclear Cu complexes constructed from either $[PPP]^-$ (bis(2-di-*iso*-propylphosphinophenyl)phosphide)[106] ($\{PPP\text{-}Cu(I)\}_2$) or $[PNP]^-$ (bis(2-(diisobutylphosphino)pheny)amide)[107,108] ($\{PNP\text{-}Cu(I)\}_2$) ligands reported by Peters et al. McMillin et al. pioneered insights into two classes of heteroleptic Cu(I) complexes constructed from one 2,9-alkyl substituted 1,10-phenanthroline (phen, dmp, or dbp) and a bulkier phosphine ligand (e.g., POP (bis[*2*-(diphenylphosphino)phenyl]ether) or two triphenylphosphines (PPh_3)).[109] Additionally, Shi et al. has recently developed highly emissive two-coordinate Cu(I) complexes with carbene and carbazolyl ligation.[71] These complexes provide an interesting opportunity to utilize the correlations developed above to gain further insights.

The γ_i values for these complexes were calculated and are compared to the $\ln(\tau)/\gamma_i$ correlation generated by the 2,9-alkyl complexes in Figure 2.12A. We first discuss the results related to the amidophosphine and carbene complexes (orange, white, and beige circles in Figure 2.12A). For $[PN]Cu(PPh_3)_2$, and $(Ph_3P)_2Cu(cbz)$, using the τs of 20,300 and 11,700 ns equates to decreased excited state structural reorganization of 27.5 ± 5.8 and 26.3 ± 5.5 kcal/mol, respectively, relative to $[Cu(I)(phen)_2]^+$. However, the excited states of these mononuclear Cu complexes do not feature pure ^{3}MLCT excited states like the bis-phen-based Cu(I) and the binuclear Cu(I) complexes (*vide infra*) and therefore the reduced structural reorganization energies for these complexes are not ascribed to entatic contributions. Instead, the long lifetimes of these complexes derive from a change in the relevant excited state from ^{3}MLCT-based to intra-[104] or inter-ligand-based.[105] Thus, these complexes achieve intrinsically lower structural reorganization by leveraging a different excited state that delocalizes the electron/hole over the ligand framework.

Shi et al.[71] has developed a series of two-coordinate Cu(I) complexes featuring an N-heterocyclic carbene and carbazolyl (Cz) ligands. For the monoamido-aminocarbene (MAC*) complex, (MAC*)Cu(CzCN), the 1200 ns lifetime equates to a decreased excited state structural reorganization of 21.0 ± 4.4 kcal/mol relative to $[Cu(I)(phen)_2]^+$. Similarly to the amidophosphine complexes considered above, Shi et al.[71] have ascribed the excited state to an interligand charge transfer, albeit with a small Cu contribution, and we therefore do not ascribe these lower structural reorganization energies to entatic contributions. Rather, these are again ascribed to electron/hole delocalization over the ligand framework due to a different excited state. Lastly, the two-coordinate Cu(I) carbene complexes were used to develop new materials for OLEDs. While beyond the scope of this study, in principle one could also use plots similar to those in Figures 2.6A/B/C to develop an entatic description that describes nonradiative vs radiative decay channels, as well as the energy of light emission, which would provide a means to develop new luminescent Cu(I) complexes for applications in OLED technology.

An additional interesting set of points is McMillin's heteroleptic phen-based complexes containing the POP ligand (Figure 2.12A, pink markers). While there are only three data points, it appears that these complexes form a line parallel to the homoleptic 2,9-alkyl substituted complexes. Thus, across this series of three POP complexes, the steric bulk at the 2,9-positions of the phen ligand tunes $\ln(\tau)$ and γ_i in a similar fashion as the bis-phen 2,9-alkyl complexes. The shift in y-intercept between the bis-phen complexes and the heteroleptic phen-POP complexes quantifies the differential effect of the ligand–metal bonding between bis-phen and phen-POP complexes and how this affects γ_i, with the POP ligand actually giving rise to a larger γ_i. For the phen-POP complex, the angle between the phen ligand and the P–Cu–P plane is 87° and 57° in the reduced and ^{3}MLCT states, respectively. Going to the more constrained dmp-POP complex, these angles are 88° and 75°, respectively. These angles are actually similar to those corresponding to the bis-dbp and bis-dtbp 2,9-alkyl complexes (Appendix A Table A.6). These bis-phen complexes would be near to the phen-POP points if the latter were translated to the line made by the 2,9-alkyl complexes in Figure 2.12A. Finally, we note that the Cu–ligand bonding in the ^{3}MLCT excited states is quite different for the bis-phen and phen-POP complexes. For example, in the ^{3}MLCT state of bis-dbp, the Cu Loewdin spin density and population is 0.58 and ~50%, respectively, while in the phen-POP complex, they decrease to 0.46 and ~35%, indicating significantly more covalent ligand–metal bonding. This is expected in going from the Cu–N bonds of the bis-phen complexes to the Cu–P bonds of the phen-POP complexes. Thus, while the phen-POP complexes are constrained due to entatic contributions, which gives rise to their long lifetimes, their γ_is are increased relative to the 2,9-alkyl complexes due to more covalent and stronger Cu–P vs. Cu–N bonds. The comparison between Figures 2.12A and 2.12B is also insightful for these complexes and is touched on briefly below (*vide infra*).

The binuclear Cu complexes (yellow markers, Figure 2.12A) from Peters et al.[106,108] fall particularly close to the correlation generated by the 2,9-alkyl complexes. These binuclear Cu complexes have long lifetimes (10,900 and 600 ns for $\{PNP\text{-}Cu(I)\}_2$ and $\{PPP\text{-}Cu(I)\}_2$, respectively) and small γ_is and λ_is (0.352/0.550 eV and 0.208/0.389 eV for {PNP-

Cu(I)}$_2$ and {PPP-Cu(I)}$_2$, respectively). Harkins et al.[108] ascribed the long lifetime to limited excited state structural reorganization and provided an experimental estimate of γ_i (~0.32 eV), which is in agreement with the calculations presented here. Using the gas phase correlations between ln(τ) and γ_i, the {PNP-Cu(I)}$_2$ and {PPP-Cu(I)}$_2$ complexes have reduced γ_i contributions of 26.1 ± 5.5 and 19.4 ± 4.1 kcal/mol, respectively, relative to the structurally flexible $[Cu(I)(phen)_2]^+$. Using the λ_i correlation gives 15.0 ± 6.3 and 8.3 ± 4.9 kcal/mol. Regardless of method, there is a ~7 kcal/mol difference in λ_i/γ_i between the $[PNP]^-$ and $[PPP]^-$ ligand sets, with $[PNP]^-$ providing reduced energies. Below, we identify the origin of this difference.

In addition to the purely steric constraints provided by the 2,9-alkyl ligand sets, excited state electron delocalization in binuclear assemblies can also contribute to their reduced γ_is relative to a mononuclear Cu complex. Analogous to electron transfer active sites in biology, excited state ^{3}MLCT formation in a binuclear assembly may benefit from excited state mixed valency to reduce reorganization energies.[110] Electron delocalization plays an important role in the inner sphere reorganization energies of class II vs. class III binuclear metal sites and is described by:[110]

$$\lambda_i = k_{dis} n (\Delta r)^2, \qquad \text{(eq 2.2)}$$

where k_{dis} is the force constant of the distortion coordinate, n is the number of distorting bonds, and Δr is the magnitude of bond distortion upon redox. For a valence-localized dimer, n is halved and Δr is doubled (n_{mon}/n_{dim} ~0.5 and $\Delta r_{mon}/\Delta r_{dim}$ ~2). Assuming similar force constants and the absence of more global structural changes during redox, λ_i is roughly twice as large for a localized oxidation. Indeed, electron delocalization in the ^{3}MLCT state of the [PNP]$^-$ complex can be observed in a plot of the excited state β-LUMO reflecting the transient oxidation of the Cu_2N_2 core (Figure 2.13A). As in the Cu_A active site, metal-metal interactions facilitate a class III mixed-valent (e.g., Cu(1.5)/Cu(1.5)) ^{3}MLCT excited state.

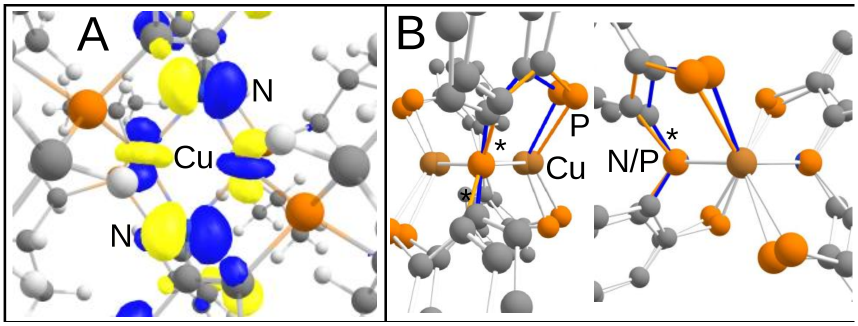

Figure 2.13. Key geometric and electronic structural influences for the excited state dynamics of the binuclear Cu(I) complexes considered here. (A) Delocalized ^{3}MLCT β-LUMO for the [PNP]$^-$ binuclear Cu(I) complex. (B) Comparison between the oxidized structures with [PNP]$^-$ and [PPP]$^-$ ligands. Note that the asterisks highlight the different N/P–C bond distances. Blue and orange lines correspond to structures of [PNP]$^-$ and [PPP]$^-$ ligands, respectively.

The contributions from this class III mixed-valency can be quantified and differentiated from entatic contributions through a series of systematic comparisons. However, in order to make these comparisons we turn to λ_is, as the analysis requires the extraction of the Cu_2X_2 cores, prohibiting the evaluation using the ^{3}MLCT state. For {PNP-Cu(I)}$_2$, the gas phase λ_i is 0.208 eV. Removing the Cu_2N_2 core with the ligating P atoms and capping with Hs gives the neutral $Cu(I)_2(NH_2)_2(PH_3)_4$ analog. Optimizing the Hs and leaving the heavy atoms frozen provides a λ_i of 0.320 eV. Furthermore, a full optimization of the $Cu(I)_2(NH_2)_2(PH_3)_4$ analog in both oxidized and reduced states provides a λ_i of 0.696 eV. Lastly, λ_i for a $Cu(I)Zn(II)(NH_2)_2(PH_3)_4$ analog increases dramatically to 2.152 eV. This increase from 0.696 to 2.152 eV reflects the two times increase in λ_i predicted from eq 2, as well as additional large structural distortions, including the rotation of the P–Cu–P plane into the $CuZnN_2$ plane, upon localized oxidation. Using these values, λ_i of {PNP-Cu(I)}$_2$ is reduced by 1.456 eV (~33.6 kcal/mol) going from a mononuclear to binuclear core. Also, between the frozen and optimized structures, λ_i is reduced by 0.376 eV (~8.7 kcal/mol); this difference corresponds to an estimate of the entatic contribution to the reduction in λ_i. Similarly, for {PPP-Cu(I)}$_2$, removing the Cu_2P_2 core, optimizing the Hs, and leaving the heavy atoms frozen provides a λ_i of 0.519 eV. Carrying out a full optimization, λ_i increases to 0.673 eV. This provides an entatic contribution of ~3.5 kcal/mol. Interestingly, this value is ~5 kcal/mol smaller than that obtained for {PNP-Cu(I)}$_2$. Furthermore, the relative λ_is for the fully optimized cores of {PNP-Cu(I)}$_2$ and {PPP-Cu(I)}$_2$ are 0.696 and 0.673 eV, respectively, indicating that very minimal (<1 kcal/mol) contributions to the reduction of λ_i derives from intrinsic bonding differences. Thus, the greater than one order of magnitude increase in ^{3}MLCT excited state lifetime for {PNP-Cu(I)}$_2$ relative to {PPP-Cu(I)}$_2$ is almost entirely due to an entatic state.

The nature of the relative entatic states present in {PNP-Cu(I)}$_2$ and {PPP-Cu(I)}$_2$ complexes, which gives rise to their order of magnitude difference in lifetime, is likely due to the significant differences in the N/P–C bond distances (~1.40 and ~1.83 Å, respectively) in the ligands (see asterisks in Figure 2.13B). This change in bond distance gives rise to large changes in the flexibility of the Cu_2X_2 core upon redox. Relevant bond distances and angles for redox are given in Table 2.5. As can be seen from the last two columns, there are significant differences between the fully optimized and constrained cores between the [PNP]$^-$

and [PPP]$^-$ ligands. For the [PNP]$^-$ ligand, large differences are observed, mainly associated with the Cu–Cu, Cu–N, and P–Cu–P angles. These structural changes between constrained and optimized structures are not observed for the [PPP]$^-$ ligand, which further supports the observation here that the greater than one order of magnitude increase in ^{3}MLCT excited state lifetime for $\{PNP\text{-}Cu(I)\}_2$ relative to $\{PPP\text{-}Cu(I)\}_2$ is almost entirely due to an entatic state. This entatic state arises from subtle, yet important differences between the [PNP]$^-$ and [PPP]$^-$ ligands (Figure 2.13B). For $\{PNP\text{-}Cu(I)\}_2$, this entatic energy is ~9 kcal/mol.

Table 2.5. Structural Comparisons between $\{PNP\text{-}Cu(I)\}_2$ and $\{PPP\text{-}Cu(I)\}_2$ Complexes in Both Oxidized and Reduced States.

Bond/ Angle[d]	**ox.**[a]	**red.**[a]	**Δ**[a]	**ox.**[b]	**red.**[b]	**Δ**[b]	**Δ**[c] **(ox)**	**Δ**[c] **(red)**
PNP								
Cu–Cu	2.56	2.77	0.21	2.50	2.86	0.36	-0.06	0.09
Cu–N	2.11	2.16	0.05	2.00	2.03	0.03	-0.11	-0.13
Cu–P	2.27	2.23	-0.04	2.28	2.20	-0.09	0.01	-0.03
P–Cu–P	134	137	3	111	106	-5	-23	-31
PPP								
Cu–Cu	3.01	3.37	0.36	2.99	3.39	0.40	-0.02	0.02
Cu–P	2.32	2.35	0.03	2.32	2.36	0.04	0.00	0.01
Cu–P	2.29	2.26	-0.03	2.28	2.25	-0.03	-0.01	-0.01
P–Cu–P	125	127	2	117	112	-5	-8	-15

[a] Hydrogens optimized, heavy atoms frozen.
[b] Full geometry optimization.
[c] Difference between frozen and optimized structures.
[d] Bond distances in Å and angles in °.

We make a final observation in the comparison between Figures 2.12A and 2.12B, which give correlations between ln(τ) and γ_i and the energy gap as calculated in Appendix A Figure A.1B. As discussed above, the phen-POP complexes are displaced from the 2,9-alkyl complexes in Figure 2.12A. This is not the case, however, for Figure 2.12B. Additionally, the 2,9-aryl substituted bis-phen complexes (green circles) exhibit a different clustering in Figures 2.12A and 2.12B. While the entatic contributions across 2,9-alkyl Cu(I) photosensitizers are similar using data in either Figure 2.12A or 2.12B (Table 2.4), there are key geometric and electronic structural insights to be obtained via their direct comparison. Furthermore, from Appendix A Figure A.1B, the ^{3}MLCT energy at the Franck-Condon point is the sum of γ_i and the energy gap. In an entatic state, the excited state potential energy surface shifts to higher relative energy and lower flattening angle (Figure 2.10). This simultaneously lowers γ_i and increases the energy gap. Cancellation of these effects would result in similar ^{3}MLCT energies across a set of complexes. Indeed, the ^{3}MLCT energies are similar for the 2,9-alkyl complexes (50.8 ± 1.4 kcal/mol); for example, bis-phen and bis-dtbp both have ^{3}MLCT energies of ~50.7 kcal/mol. Similar tight groupings of ^{3}MLCT energies are observed in other classes of complexes (e.g., 42.0 ± 1.6 and 57.1 ± 1.2 kcal/mol for the 2,9-diphenyls and phen-POP complexes, respectively). Thus, the offsets of data points from the line formed by the 2,9-alkyl complexes reflect different ^{3}MLCT energies between species and thus different ligand–metal bonding. For example, the phen-POP complexes exhibit different bonding due to substitution of Cu–N with more covalent Cu–P bonds (*vide supra*); furthermore, 2,9-aryl bis-phen complexes achieve lower γ_is due to flattening in the ground state from π-stacking. These geometric and electronic structural contributions to ^{3}MLCT dynamics could not be determined from the correlation between ln(τ) and energy gap alone, and Figure 2.12A further allows for the disentanglement of steric and electronic contributions to photophysical processes.

2.4. Conclusion

This study has developed a combined experimental and computational methodology to quantify entatic contributions to photophysical processes, with specific applications to a broad range of Cu-based photosensitizers and luminescent complexes. This methodology is based on the observation that experimental ^{3}MLCT excited state lifetimes for a range of Cu(I) bis-phen complexes correlate with redox potentials, ground state inner sphere reorganization energies, and excited state relaxation energies and energy gaps over four orders in magnitude in time. These correlations provide a means to directly quantify entatic contributions to the ^{3}MLCT excited state lifetimes over an entire class of photoactive metal complexes. Furthermore, the correlations in Figure 2.6 and 2.12 provide a means to benchmark the potential performance characteristics of new complexes before embarking on their syntheses. Lastly, within Cu(I)-based photosensitizers, entatic states are found here to reach ~20 kcal/mol relative to the conformationally flexible $[Cu(phen)_2]^+$. Being the largest entatic states yet quantified, these energetics are significant relative to typical chemical driving forces and barriers, suggesting that entatic state descriptors will be valuable to extend to new classes of molecules and materials with interesting functional properties involving the coupling between electron and vibrational dynamics. Our laboratory is currently extending these analyses to quantifying entatic states in (photo)catalytic and (photo)magnetic materials.

REFERENCES

(1) Lumry, R.; Eyring, H. Conformation Changes of Proteins. *J. Phys. Chem.* **1954**, *58* (2), 110–120. https://doi.org/10.1021/j150512a005.

(2) Eyring, H.; Lumry, R.; Spikes, J. D. *Mechanism of Enzyme Action*; Johns Hopkins Press, **1956**.

(3) Vallee, B. L.; Williams, R. J. Metalloenzymes: The Entatic Nature of Their Active Sites. *Proc. Natl. Acad. Sci.* **1968**, *59* (2), 498–505. https://doi.org/10.1073/pnas.59.2.498.

(4) Gray, H. B.; Malmström, B. G. On the Relationship between Protein-Forced Ligand Fields and the Properties of Blue Copper Centers. *Comments Inorg. Chem.* **1983**, *2* (5), 203–209. https://doi.org/10.1080/02603598308078118.

(5) Malmström, B. G. Rack-Induced Bonding in Blue-Copper Proteins. *Eur. J. Biochem.* **1994**, *223* (3), 711–718. https://doi.org/10.1111/j.1432-1033.1994.tb19044.x.

(6) Williams, R. J. P. Energised (Entatic) States of Groups and of Secondary Structures in Proteins and Metalloproteins. *Eur. J. Biochem.* **1995**, *234* (2), 363–381. https://doi.org/10.1111/j.1432-1033.1995.363_b.x.

(7) Gray, H. B.; Malmström, B. G.; Williams, R. J. P. Copper Coordination in Blue Proteins. *JBIC J. Biol. Inorg. Chem.* **2000**, *5* (5), 551–559. https://doi.org/10.1007/s007750000146.

(8) Ghosh, S.; Xie, X.; Dey, A.; Sun, Y.; Scholes, C. P.; Solomon, E. I. Thermodynamic Equilibrium between Blue and Green Copper Sites and the Role of the Protein in Controlling Function. *Proc. Natl. Acad. Sci.* **2009**, *106* (13), 4969–4974. https://doi.org/10.1073/pnas.0900995106.

(9) Tsai, M.-L.; Hadt, R. G.; Marshall, N. M.; Wilson, T. D.; Lu, Y.; Solomon, E. I. Axial Interactions in the Mixed-Valent Cu_A Active Site and Role of the Axial Methionine in Electron Transfer. *Proc. Natl. Acad. Sci.* **2013**, *110* (36), 14658–14663. https://doi.org/10.1073/pnas.1314242110.

(10) Mara, M. W.; Hadt, R. G.; Reinhard, M. E.; Kroll, T.; Lim, H.; Hartsock, R. W.; Alonso-Mori, R.; Chollet, M.; Glownia, J. M.; Nelson, S.; et al. Metalloprotein Entatic Control of Ligand-Metal Bonds Quantified by Ultrafast X-ray Spectroscopy. *Science* **2017**, *356* (6344), 1276–1280. https://doi.org/10.1126/science.aam6203.

(11) Metz, M.; Solomon, E. I. Dioxygen Binding to Deoxyhemocyanin: Electronic Structure and Mechanism of the Spin-Forbidden Two-Electron Reduction of O_2. *J. Am. Chem. Soc.* **2001**, *123* (21), 4938–4950. https://doi.org/10.1021/ja004166b.

(12) Hadt, R. G.; Xie, X.; Pauleta, S. R.; Moura, I.; Solomon, E. I. Analysis of Resonance Raman Data on the Blue Copper Site in Pseudoazurin: Excited State π and σ Charge Transfer Distortions and Their Relation to Ground State Reorganization Energy. *J. Inorg. Biochem.* **2012**, *115*, 155–162. https://doi.org/10.1016/j.jinorgbio.2012.03.006.

(13) Solomon, E. I.; Hadt, R. G. Recent Advances in Understanding Blue Copper Proteins. *Coord. Chem. Rev.* **2011**, *255* (7), 774–789. https://doi.org/10.1016/j.ccr.2010.12.008.

(14) Rorabacher, D. B. Electron Transfer by Copper Centers. *Chem. Rev.* **2004**, *104* (2), 651–698. https://doi.org/10.1021/cr020630e.

(15) Chaka, G.; Sonnenberg, J. L.; Schlegel, H. B.; Heeg, M. J.; Jaeger, G.; Nelson, T. J.; Ochrymowycz, L. A.; Rorabacher, D. B. A Definitive Example of a Geometric “Entatic State” Effect: Electron-Transfer Kinetics for a Copper(II/I) Complex Involving A Quinquedentate Macrocyclic Trithiaether−Bipyridine Ligand. *J. Am. Chem. Soc.* **2007**, *129* (16), 5217–5227. https://doi.org/10.1021/ja068960u.

(16) Xie, B.; Elder, T.; Wilson, L. J.; Stanbury, D. M. Internal Reorganization Energies for Copper Redox Couples: The Slow Electron-Transfer Reactions of the $[Cu(II/I)(Bib)_2]^{2+/+}$ Couple. *Inorg. Chem.* **1999**, *38* (1), 12–19. https://doi.org/10.1021/ic980926w.

(17) Comba, P. Coordination Compounds in the Entatic State. *Coord. Chem. Rev.* **2000**, *200–202*, 217–245. https://doi.org/10.1016/S0010-8545(00)00265-4.

(18) Comba, P. Strains and Stresses in Coordination Compounds. *Coord. Chem. Rev.* **1999**, *182* (1), 343–371. https://doi.org/10.1016/S0010-8545(98)00199-4.

(19) Kohler, L.; Hadt, R. G.; Hayes, D.; Chen, L. X.; Mulfort, K. L. Synthesis, Structure, and Excited State Kinetics of Heteroleptic Cu(I) Complexes with a New Sterically Demanding Phenanthroline Ligand. *Dalton Trans.* **2017**, *46* (38), 13088–13100. https://doi.org/10.1039/C7DT02476B.

(20) Dicke, B.; Hoffmann, A.; Stanek, J.; Rampp, M. S.; Grimm-Lebsanft, B.; Biebl, F.; Rukser, D.; Maerz, B.; Göries, D.; Naumova, M.; et al. Transferring the Entatic-State Principle to Copper Photochemistry. *Nat. Chem.* **2018**, *10* (3), 355–362. https://doi.org/10.1038/nchem.2916.

(21) Mara, M. W.; Fransted, K. A.; Chen, L. X. Interplays of Excited State Structures and Dynamics in Copper(I) Diimine Complexes: Implications and Perspectives. *Coord. Chem. Rev.* **2015**, *282–283*, 2–18. https://doi.org/10.1016/j.ccr.2014.06.013.

(22) Iwamura, M.; Takeuchi, S.; Tahara, T. Real-Time Observation of the Photoinduced Structural Change of Bis(2,9-Dimethyl-1,10-Phenanthroline)Copper(I) by Femtosecond Fluorescence Spectroscopy: A Realistic Potential Curve of the Jahn−Teller Distortion. *J. Am. Chem. Soc.* **2007**, *129* (16), 5248–5256. https://doi.org/10.1021/ja069300s.

(23) Lockard, J. V.; Kabehie, S.; Zink, J. I.; Smolentsev, G.; Soldatov, A.; Chen, L. X. Influence of Ligand Substitution on Excited State Structural Dynamics in Cu(I) Bisphenanthroline Complexes. *J. Phys. Chem. B* **2010**, *114* (45), 14521–14527. https://doi.org/10.1021/jp102278u.

(24) Shaw, G. B.; Grant, C. D.; Shirota, H.; Castner, E. W.; Meyer, G. J.; Chen, L. X. Ultrafast Structural Rearrangements in the MLCT Excited State for Copper(I) Bis-Phenanthrolines in Solution. *J. Am. Chem. Soc.* **2007**, *129* (7), 2147–2160. https://doi.org/10.1021/ja067271f.

(25) Snyder, B. E. R.; Vanelderen, P.; Bols, M. L.; Hallaert, S. D.; Böttger, L. H.; Ungur, L.; Pierloot, K.; Schoonheydt, R. A.; Sels, B. F.; Solomon, E. I. The Active Site of Low-Temperature Methane Hydroxylation in Iron-Containing Zeolites. *Nature* **2016**, *536* (7616), 317–321. https://doi.org/10.1038/nature19059.

(26) Comba, P.; Fukuzumi, S.; Koke, C.; Martin, B.; Löhr, A.-M.; Straub, J. A Bispidine Iron(IV)–Oxo Complex in the Entatic State. *Angew. Chem. Int. Ed.* **2016**, *55* (37), 11129–11133. https://doi.org/10.1002/anie.201605099.

(27) Xia, Z.; Guo, S. Strain Engineering of Metal-Based Nanomaterials for Energy Electrocatalysis. *Chem. Soc. Rev.* **2019**, *48* (12), 3265–3278. https://doi.org/10.1039/C8CS00846A.

(28) Stoerzinger, K. A.; Choi, W. S.; Jeen, H.; Lee, H. N.; Shao-Horn, Y. Role of Strain and Conductivity in Oxygen Electrocatalysis on $LaCoO_3$ Thin Films. *J. Phys. Chem. Lett.* **2015**, *6* (3), 487–492. https://doi.org/10.1021/jz502692a.

(29) Petrie, J. R.; Cooper, V. R.; Freeland, J. W.; Meyer, T. L.; Zhang, Z.; Lutterman, D. A.; Lee, H. N. Enhanced Bifunctional Oxygen Catalysis in Strained $LaNiO_3$ Perovskites. *J. Am. Chem. Soc.* **2016**, *138* (8), 2488–2491. https://doi.org/10.1021/jacs.5b11713.

(30) You, B.; Tang, M. T.; Tsai, C.; Abild-Pedersen, F.; Zheng, X.; Li, H. Enhancing Electrocatalytic Water Splitting by Strain Engineering. *Adv. Mater.* **2019**, *31* (17), 1807001. https://doi.org/10.1002/adma.201807001.

(31) Pingel, T. N.; Jørgensen, M.; Yankovich, A. B.; Grönbeck, H.; Olsson, E. Influence of Atomic Site-Specific Strain on Catalytic Activity of Supported Nanoparticles. *Nat. Commun.* **2018**, *9* (1), 1–9. https://doi.org/10.1038/s41467-018-05055-1.

(32) Verdaguer-Casadevall, A.; Li, C. W.; Johansson, T. P.; Scott, S. B.; McKeown, J. T.; Kumar, M.; Stephens, I. E. L.; Kanan, M. W.; Chorkendorff, I. Probing the Active Surface Sites for CO Reduction on Oxide-Derived Copper Electrocatalysts. *J. Am. Chem. Soc.* **2015**, *137* (31), 9808–9811. https://doi.org/10.1021/jacs.5b06227.

(33) Yang, R.; Leisch, J.; Strasser, P.; Toney, M. F. Structure of Dealloyed $PtCu_3$ Thin Films and Catalytic Activity for Oxygen Reduction. *Chem. Mater.* **2010**, *22* (16), 4712–4720. https://doi.org/10.1021/cm101090p.

(34) Johnson, B.; Guduru, P. R.; Peterson, A. A. Strain-Induced Changes to the Methanation Reaction on Thin-Film Nickel Catalysts. *Catal. Sci. Technol.* **2019**, *9* (12), 3279–3286. https://doi.org/10.1039/C9CY00735K.

(35) Yan, K.; Maark, T. A.; Khorshidi, A.; Sethuraman, V. A.; Peterson, A. A.; Guduru, P. R. The Influence of Elastic Strain on Catalytic Activity in the Hydrogen Evolution Reaction. *Angew. Chem. Int. Ed.* **2016**, *55* (21), 6175–6181. https://doi.org/10.1002/anie.201508613.

(36) Chan, Z. M.; Kitchaev, D. A.; Weker, J. N.; Schnedermann, C.; Lim, K.; Ceder, G.; Tumas, W.; Toney, M. F.; Nocera, D. G. Electrochemical Trapping of Metastable Mn^{3+} Ions for Activation of MnO2 Oxygen Evolution Catalysts. *Proc. Natl. Acad. Sci.* **2018**, *115* (23), E5261–E5268. https://doi.org/10.1073/pnas.1722235115.

(37) Koohbor, B.; Sang, L.; Çapraz, Ö. Ö.; Gewirth, A. A.; Nuzzo, R. G.; White, S. R.; Sottos, N. R. In Situ Strain Measurement in Solid-State Li-Ion Batteries. In *Fracture, Fatigue, Failure and Damage Evolution, Volume 6*; Carroll, J., Xia, S., Beese, A. M., Berke, R. B., Pataky, G. J., Eds.; Conference Proceedings of the Society for Experimental Mechanics Series; Springer International Publishing, 2019; pp 1–3.

(38) Wang, H.; Xu, S.; Tsai, C.; Li, Y.; Liu, C.; Zhao, J.; Liu, Y.; Yuan, H.; Abild-Pedersen, F.; Prinz, F. B.; et al. Direct and Continuous Strain Control of Catalysts with Tunable Battery Electrode Materials. *Science* **2016**, *354* (6315), 1031–1036. https://doi.org/10.1126/science.aaf7680.

(39) Tavassol, H.; Jones, E. M. C.; Sottos, N. R.; Gewirth, A. A. Electrochemical Stiffness in Lithium-Ion Batteries. *Nat. Mater.* **2016**, *15* (11), 1182–1187. https://doi.org/10.1038/nmat4708.

(40) Kucharski, T. J.; Ferralis, N.; Kolpak, A. M.; Zheng, J. O.; Nocera, D. G.; Grossman, J. C. Templated Assembly of Photoswitches Significantly Increases the Energy-Storage Capacity of Solar Thermal Fuels. *Nat. Chem.* **2014**, *6* (5), 441–447. https://doi.org/10.1038/nchem.1918.

(41) Ren, Y.; Forte, J.; Cheaib, K.; Vanthuyne, N.; Fensterbank, L.; Vezin, H.; Orio, M.; Blanchard, S.; Desage-El Murr, M. High-Performance Group Transfer Catalysis by Copper Complex with Redox-Active Ligand in an Entatic State. **2019**. https://doi.org/10.26434/chemrxiv.8965475.v1.

(42) Vallejo, J.; Pardo, E.; Viciano-Chumillas, M.; Castro, I.; Amorós, P.; Déniz, M.; Ruiz-Pérez, C.; Yuste-Vivas, C.; Krzystek, J.; Julve, M.; et al. Reversible Solvatomagnetic Switching in a Single-Ion Magnet from an Entatic State. *Chem. Sci.* **2017**, *8* (5), 3694–3702. https://doi.org/10.1039/C6SC05188J.

(43) Verat, A. Y.; Ould-Moussa, N.; Jeanneau, E.; Le Guennic, B.; Bousseksou, A.; Borshch, S. A.; Matouzenko, G. S. Ligand Strain and the Nature of Spin Crossover in Binuclear Complexes: Two-Step Spin Crossover in a 4,4′-Bipyridine-Bridged Iron(II) Complex [{Fe(dpia)(NCS)$_2$}$_2$(4,4′-bpy)] (dpia=di(2-picolyl)amine; 4,4′-bpy=4,4′-bipyridine). *Chem. – Eur. J.* **2009**, *15* (39), 10070–10082. https://doi.org/10.1002/chem.200900921.

(44) Zhou, J.; Wang, Q.; Sun, Q.; Kawazoe, Y.; Jena, P. Strain-Induced Spin Crossover in Phthalocyanine-Based Organometallic Sheets. *J. Phys. Chem. Lett.* **2012**, *3* (21), 3109–3114. https://doi.org/10.1021/jz301303t.

(45) Voityuk, A. A.; Michel-Beyerle, M.-E.; Rösch, N. Structure and Rotation Barriers for Ground and Excited States of the Isolated Chromophore of the Green Fluorescent Protein. *Chem. Phys. Lett.* **1998**, *296* (3), 269–276. https://doi.org/10.1016/S0009-2614(98)01035-5.

(46) Fidder, H.; Rini, M.; Nibbering, E. T. J. The Role of Large Conformational Changes in Efficient Ultrafast Internal Conversion: Deviations from the Energy Gap Law. *J. Am. Chem. Soc.* **2004**, *126* (12), 3789–3794. https://doi.org/10.1021/ja038741y.

(47) Udvarhelyi, P.; Shkolnikov, V. O.; Gali, A.; Burkard, G.; Pályi, A. Spin-Strain Interaction in Nitrogen-Vacancy Centers in Diamond. *Phys. Rev. B* **2018**, *98* (7), 075201. https://doi.org/10.1103/PhysRevB.98.075201.

(48) Goldman, M. L.; Doherty, M. W.; Sipahigil, A.; Yao, N. Y.; Bennett, S. D.; Manson, N. B.; Kubanek, A.; Lukin, M. D. State-Selective Intersystem Crossing in Nitrogen-Vacancy Centers. *Phys. Rev. B* **2015**, *91* (16), 165201. https://doi.org/10.1103/PhysRevB.91.165201.

(49) Sohn, Y.-I.; Meesala, S.; Pingault, B.; Atikian, H. A.; Holzgrafe, J.; Gündoğan, M.; Stavrakas, C.; Stanley, M. J.; Sipahigil, A.; Choi, J.; et al. Controlling the Coherence of a Diamond Spin Qubit through Its Strain Environment. *Nat. Commun.* **2018**, *9* (1), 1–6. https://doi.org/10.1038/s41467-018-04340-3.

(50) Manna, R. S.; Das, P.; de Souza, M.; Schnelle, F.; Lang, M.; Müller, J.; von Molnár, S.; Fisk, Z. Lattice Strain Accompanying the Colossal Magnetoresistance Effect in

EuB_6. *Phys. Rev. Lett.* **2014**, *113* (6), 067202. https://doi.org/10.1103/PhysRevLett.113.067202.

(51) Moshnyaga, V.; Samwer, K. Electron-Lattice Correlations and Phase Transitions in CMR Manganites. *Ann. Phys.* **2011**, *523* (8–9), 652–663. https://doi.org/10.1002/andp.201100040.

(52) Capano, G.; Milne, C. J.; Chergui, M.; Rothlisberger, U.; Tavernelli, I.; Penfold, T. J. Probing Wavepacket Dynamics Using Ultrafast X-Ray Spectroscopy. *J. Phys. B At. Mol. Opt. Phys.* **2015**, *48* (21), 214001. https://doi.org/10.1088/0953-4075/48/21/214001.

(53) Monni, R.; Auböck, G.; Kinschel, D.; Aziz-Lange, K. M.; Gray, H. B.; Vlček, A.; Chergui, M. Conservation of Vibrational Coherence in Ultrafast Electronic Relaxation: The Case of Diplatinum Complexes in Solution. *Chem. Phys. Lett.* **2017**, *683*, 112–120. https://doi.org/10.1016/j.cplett.2017.02.071.

(54) Cammarata, M.; Bertoni, R.; Lorenc, M.; Cailleau, H.; Di Matteo, S.; Mauriac, C.; Matar, S. F.; Lemke, H.; Chollet, M.; Ravy, S.; et al. Sequential Activation of Molecular Breathing and Bending during Spin-Crossover Photoswitching Revealed by Femtosecond Optical and X-Ray Absorption Spectroscopy. *Phys. Rev. Lett.* **2014**, *113* (22), 227402. https://doi.org/10.1103/PhysRevLett.113.227402.

(55) Lemke, H. T.; Kjær, K. S.; Hartsock, R.; van Driel, T. B.; Chollet, M.; Glownia, J. M.; Song, S.; Zhu, D.; Pace, E.; Matar, S. F.; et al. Coherent Structural Trapping through Wave Packet Dispersion during Photoinduced Spin State Switching. *Nat. Commun.* **2017**, *8*, 15342. https://doi.org/10.1038/ncomms15342.

(56) Goldman, M. L.; Sipahigil, A.; Doherty, M. W.; Yao, N. Y.; Bennett, S. D.; Markham, M.; Twitchen, D. J.; Manson, N. B.; Kubanek, A.; Lukin, M. D. Phonon-Induced Population Dynamics and Intersystem Crossing in Nitrogen-Vacancy Centers. *Phys. Rev. Lett.* **2015**, *114* (14), 145502. https://doi.org/10.1103/PhysRevLett.114.145502.

(57) Mara, M. W.; Bowman, D. N.; Buyukcakir, O.; Shelby, M. L.; Haldrup, K.; Huang, J.; Harpham, M. R.; Stickrath, A. B.; Zhang, X.; Stoddart, J. F.; et al. Electron Injection from Copper Diimine Sensitizers into TiO_2: Structural Effects and Their Implications for Solar Energy Conversion Devices. *J. Am. Chem. Soc.* **2015**, *137* (30), 9670–9684. https://doi.org/10.1021/jacs.5b04612.

(58) Alonso-Vante, N.; Nierengarten, J.-F.; Sauvage, J.-P. Spectral Sensitization of Large-Band-Gap Semiconductors (Thin Films and Ceramics) by a Carboxylated Bis(1,10-Phenanthroline)Copper(I) Complex. *J. Chem. Soc. Dalton Trans.* **1994**, No. 11, 1649–1654. https://doi.org/10.1039/DT9940001649.

(59) Huang, J.; Buyukcakir, O.; Mara, M. W.; Coskun, A.; Dimitrijevic, N. M.; Barin, G.; Kokhan, O.; Stickrath, A. B.; Ruppert, R.; Tiede, D. M.; et al. Highly Efficient Ultrafast Electron Injection from the Singlet MLCT Excited State of Copper(I) Diimine Complexes to TiO_2 Nanoparticles. *Angew. Chem. Int. Ed.* **2012**, *51* (51), 12711–12715. https://doi.org/10.1002/anie.201204341.

(60) Sakaki, S.; Kuroki, T.; Hamada, T. Synthesis of a New Copper(I) Complex, $[Cu(Tmdcbpy)_2]^+$ (Tmdcbpy = 4,4′,6,6′-Tetramethyl-2,2′-Bipyridine-5,5′-Dicarboxylic Acid), and Its Application to Solar Cells. *J. Chem. Soc. Dalton Trans.* **2002**, No. 6, 840–842. https://doi.org/10.1039/B109518H.

(61) Bessho, T.; Constable, E. C.; Graetzel, M.; Redondo, A. H.; Housecroft, C. E.; Kylberg, W.; Nazeeruddin, M. K.; Neuburger, M.; Schaffner, S. An Element of Surprise—Efficient Copper-Functionalized Dye-Sensitized Solar Cells. *Chem. Commun.* **2008**, No. 32, 3717–3719. https://doi.org/10.1039/B808491B.

(62) Sandroni, M.; Pellegrin, Y.; Odobel, F. Heteroleptic Bis-Diimine Copper(I) Complexes for Applications in Solar Energy Conversion. *Comptes Rendus Chim.* **2016**, *19* (1), 79–93. https://doi.org/10.1016/j.crci.2015.06.008.

(63) Luo, S.-P.; Mejía, E.; Friedrich, A.; Pazidis, A.; Junge, H.; Surkus, A.-E.; Jackstell, R.; Denurra, S.; Gladiali, S.; Lochbrunner, S.; et al. Photocatalytic Water Reduction with Copper-Based Photosensitizers: A Noble-Metal-Free System. *Angew. Chem. Int. Ed.* **2013**, *52* (1), 419–423. https://doi.org/10.1002/anie.201205915.

(64) Takeda, H.; Ohashi, K.; Sekine, A.; Ishitani, O. Photocatalytic CO_2 Reduction Using Cu(I) Photosensitizers with a Fe(II) Catalyst. *J. Am. Chem. Soc.* **2016**, *138* (13), 4354–4357. https://doi.org/10.1021/jacs.6b01970.

(65) Khnayzer, R. S.; McCusker, C. E.; Olaiya, B. S.; Castellano, F. N. Robust Cuprous Phenanthroline Sensitizer for Solar Hydrogen Photocatalysis. *J. Am. Chem. Soc.* **2013**, *135* (38), 14068–14070. https://doi.org/10.1021/ja407816f.

(66) McCusker, C. E.; Castellano, F. N. Design of a Long-Lifetime, Earth-Abundant, Aqueous Compatible Cu(I) Photosensitizer Using Cooperative Steric Effects. *Inorg. Chem.* **2013**, *52* (14), 8114–8120. https://doi.org/10.1021/ic401213p.

(67) Ruthkosky, M.; Castellano, F. N.; Meyer, G. J. Photodriven Electron and Energy Transfer from Copper Phenanthroline Excited States. *Inorg. Chem.* **1996**, *35* (22), 6406–6412. https://doi.org/10.1021/ic960503z.

(68) McCullough, B. J.; Neyhouse, B. J.; Schrage, B. R.; Reed, D. T.; Osinski, A. J.; Ziegler, C. J.; White, T. A. Visible-Light-Driven Photosystems Using Heteroleptic Cu(I) Photosensitizers and Rh(III) Catalysts To Produce H_2. *Inorg. Chem.* **2018**, *57* (5), 2865–2875. https://doi.org/10.1021/acs.inorgchem.7b03273.

(69) Yuan, Y.-J.; Yu, Z.-T.; Chen, D.-Q.; Zou, Z.-G. Metal-Complex Chromophores for Solar Hydrogen Generation. *Chem. Soc. Rev.* **2017**, *46* (3), 603–631. https://doi.org/10.1039/C6CS00436A.

(70) Lazorski, M. S.; Castellano, F. N. Advances in the Light Conversion Properties of Cu(I)-Based Photosensitizers. *Polyhedron* **2014**, *82*, 57–70. https://doi.org/10.1016/j.poly.2014.04.060.

(71) Shi, S.; Jung, M. C.; Coburn, C.; Tadle, A.; Sylvinson M. R., D.; Djurovich, P. I.; Forrest, S. R.; Thompson, M. E. Highly Efficient Photo- and Electroluminescence from Two-Coordinate Cu(I) Complexes Featuring Nonconventional N-Heterocyclic Carbenes. *J. Am. Chem. Soc.* **2019**, *141* (8), 3576–3588. https://doi.org/10.1021/jacs.8b12397.

(72) Hashimoto, M.; Igawa, S.; Yashima, M.; Kawata, I.; Hoshino, M.; Osawa, M. Highly Efficient Green Organic Light-Emitting Diodes Containing Luminescent Three-Coordinate Copper(I) Complexes. *J. Am. Chem. Soc.* **2011**, *133* (27), 10348–10351. https://doi.org/10.1021/ja202965y.

(73) Igawa, S.; Hashimoto, M.; Kawata, I.; Yashima, M.; Hoshino, M.; Osawa, M. Highly Efficient Green Organic Light-Emitting Diodes Containing Luminescent Tetrahedral

Copper(I) Complexes. *J. Mater. Chem. C* **2013**, *1* (3), 542–551. https://doi.org/10.1039/C2TC00263A.

(74) Zink, D. M.; Volz, D.; Baumann, T.; Mydlak, M.; Flügge, H.; Friedrichs, J.; Nieger, M.; Bräse, S. Heteroleptic, Dinuclear Copper(I) Complexes for Application in Organic Light-Emitting Diodes. *Chem. Mater.* **2013**, *25* (22), 4471–4486. https://doi.org/10.1021/cm4018375.

(75) Zink, D. M.; Bächle, M.; Baumann, T.; Nieger, M.; Kühn, M.; Wang, C.; Klopper, W.; Monkowius, U.; Hofbeck, T.; Yersin, H.; et al. Synthesis, Structure, and Characterization of Dinuclear Copper(I) Halide Complexes with P–N Ligands Featuring Exciting Photoluminescence Properties. *Inorg. Chem.* **2013**, *52* (5), 2292–2305. https://doi.org/10.1021/ic300979c.

(76) Zhang, Q.; Komino, T.; Huang, S.; Matsunami, S.; Goushi, K.; Adachi, C. Triplet Exciton Confinement in Green Organic Light-Emitting Diodes Containing Luminescent Charge-Transfer Cu(I) Complexes. *Adv. Funct. Mater.* **2012**, *22* (11), 2327–2336. https://doi.org/10.1002/adfm.201101907.

(77) Leitl, M. J.; Küchle, F.-R.; Mayer, H. A.; Wesemann, L.; Yersin, H. Brightly Blue and Green Emitting Cu(I) Dimers for Singlet Harvesting in OLEDs. *J. Phys. Chem. A* **2013**, *117* (46), 11823–11836. https://doi.org/10.1021/jp402975d.

(78) Bizzarri, C.; Spuling, E.; Knoll, D. M.; Volz, D.; Bräse, S. Sustainable Metal Complexes for Organic Light-Emitting Diodes (OLEDs). *Coord. Chem. Rev.* **2018**, *373*, 49–82. https://doi.org/10.1016/j.ccr.2017.09.011.

(79) Ahn, B.-T.; McMillin, D. R. Studies of Photoinduced Electron Transfer from Bis(2,9-Dimethyl-1,10-Phenanthroline)Copper(I). *Inorg. Chem.* **1978**, *17* (8), 2253–2258. https://doi.org/10.1021/ic50186a048.

(80) Dietrich-Buchecker, C. O.; Marnot, P. A.; Sauvage, J.-P.; Kirchhoff, J. R.; McMillin, D. R. Bis(2,9-Diphenyl-1,10-Phenanthroline)Copper(I): A Copper Complex with a Long-Lived Charge-Transfer Excited State. *J. Chem. Soc. Chem. Commun.* **1983**, No. 9, 513–515. https://doi.org/10.1039/C39830000513.

(81) Ng, Y. Y.; Tan, L. J.; Ng, S. M.; Chai, Y. T.; Ganguly, R.; Du, Y.; Yeow, E. K. L.; Soo, H. S. Spectroscopic Characterization and Mechanistic Studies on Visible Light Photoredox Carbon–Carbon Bond Formation by Bis(Arylimino)Acenaphthene Copper Photosensitizers. *ACS Catal.* **2018**, *8* (12), 11277–11286. https://doi.org/10.1021/acscatal.8b02502.

(82) Paria, S.; Reiser, O. Visible Light and Copper Complexes: A Promising Match in Photoredox Catalysis. In *Visible Light Photocatalysis in Organic Chemistry*; John Wiley & Sons, Ltd, **2018**; pp 233–251. https://doi.org/10.1002/9783527674145.ch7.

(83) Paria, S.; Reiser, O. Copper in Photocatalysis. *ChemCatChem* **2014**, *6* (9), 2477–2483. https://doi.org/10.1002/cctc.201402237.

(84) Wang, B.; Shelar, D. P.; Han, X.-Z.; Li, T.-T.; Guan, X.; Lu, W.; Liu, K.; Chen, Y.; Fu, W.-F.; Che, C.-M. Long-Lived Excited States of Zwitterionic Copper(I) Complexes for Photoinduced Cross-Dehydrogenative Coupling Reactions. *Chem. – Eur. J.* **2015**, *21* (3), 1184–1190. https://doi.org/10.1002/chem.201405356.

(85) Hernandez-Perez, A. C.; Collins, S. K. Heteroleptic Cu-Based Sensitizers in Photoredox Catalysis. *Acc. Chem. Res.* **2016**, *49* (8), 1557–1565. https://doi.org/10.1021/acs.accounts.6b00250.

(86) Larsen, C. B.; Wenger, O. S. Photoredox Catalysis with Metal Complexes Made from Earth-Abundant Elements. *Chem. – Eur. J.* **2018**, *24* (9), 2039–2058. https://doi.org/10.1002/chem.201703602.

(87) Nicholls, T. P.; Caporale, C.; Massi, M.; Gardiner, M. G.; Bissember, A. C. Synthesis and Characterisation of Homoleptic 2,9-Diaryl-1,10-Phenanthroline Copper(I) Complexes: Influencing Selectivity in Photoredox-Catalysed Atom-Transfer Radical Addition Reactions. *Dalton Trans.* **2019**, *48* (21), 7290–7301. https://doi.org/10.1039/C8DT04116D.

(88) Eggleston, M. K.; McMillin, D. R.; Koenig, K. S.; Pallenberg, A. J. Steric Effects in the Ground and Excited States of $Cu(NN)^{2+}$ Systems. *Inorg. Chem.* **1997**, *36* (2), 172–176. https://doi.org/10.1021/ic960698a.

(89) Cunningham, C. T.; Cunningham, K. L. H.; Michalec, J. F.; McMillin, D. R. Cooperative Substituent Effects on the Excited States of Copper Phenanthrolines. *Inorg. Chem.* **1999**, *38* (20), 4388–4392. https://doi.org/10.1021/ic9906611.

(90) Ichinaga, A. K.; Kirchhoff, J. R.; McMillin, D. R.; Dietrich-Buchecker, C. O.; Marnot, P. A.; Sauvage, J. P. Charge-Transfer Absorption and Emission of $Cu(NN)^{2+}$ Systems. *Inorg. Chem.* **1987**, *26* (25), 4290–4292. https://doi.org/10.1021/ic00272a030.

(91) Vögtle, F.; Lüer, I.; Balzani, V.; Armaroli, N. Endoreceptors with Convergent Phenanthroline Units: A Molecular Cavity for Six Guest Molecules. *Angew. Chem. Int. Ed. Engl.* **1991**, *30* (10), 1333–1336. https://doi.org/10.1002/anie.199113331.

(92) Green, O.; Gandhi, B. A.; Burstyn, J. N. Photophysical Characteristics and Reactivity of Bis(2,9-Di-Tert-Butyl-1,10-Phenanthroline)Copper(I). *Inorg. Chem.* **2009**, *48* (13), 5704–5714. https://doi.org/10.1021/ic802361q.

(93) Desvergnes-Breuil, V.; Hebbe, V.; Dietrich-Buchecker, C.; Sauvage, J.-P.; Lacour, J. NMR Evaluation of the Configurational Stability of Cu(I) Complexes. *Inorg. Chem.* **2003**, *42* (2), 255–257. https://doi.org/10.1021/ic0259890.

(94) Scaltrito, D. V.; Thompson, D. W.; O'Callaghan, J. A.; Meyer, G. J. MLCT Excited States of Cuprous Bis-Phenanthroline Coordination Compounds. *Coord. Chem. Rev.* **2000**, *208* (1), 243–266. https://doi.org/10.1016/S0010-8545(00)00309-X.

(95) Penfold, T. J.; Karlsson, S.; Capano, G.; Lima, F. A.; Rittmann, J.; Reinhard, M.; Rittmann-Frank, M. H.; Braem, O.; Baranoff, E.; Abela, R.; et al. Solvent-Induced Luminescence Quenching: Static and Time-Resolved X-Ray Absorption Spectroscopy of a Copper(I) Phenanthroline Complex. *J. Phys. Chem. A* **2013**, *117* (22), 4591–4601. https://doi.org/10.1021/jp403751m.

(96) Solomon, E. I.; Szilagyi, R. K.; DeBeer George, S.; Basumallick, L. Electronic Structures of Metal Sites in Proteins and Models: Contributions to Function in Blue Copper Proteins. *Chem. Rev.* **2004**, *104* (2), 419–458. https://doi.org/10.1021/cr0206317.

(97) Di Bilio, A. J.; Hill, M. G.; Bonander, N.; Karlsson, B. G.; Villahermosa, R. M.; Malmström, B. G.; Winkler, J. R.; Gray, H. B. Reorganization Energy of Blue Copper: Effects of Temperature and Driving Force on the Rates of Electron Transfer in Ruthenium- and Osmium-Modified Azurins. *J. Am. Chem. Soc.* **1997**, *119* (41), 9921–9922. https://doi.org/10.1021/ja971518e.

(98) Olsson, M. H. M.; Ryde, U.; Roos, B. O. Quantum Chemical Calculations of the Reorganization Energy of Blue-Copper Proteins. *Protein Sci.* **1998**, *7* (12), 2659–2668. https://doi.org/10.1002/pro.5560071220.

(99) Ryde, U.; Olsson, M. H. M. Structure, Strain, and Reorganization Energy of Blue Copper Models in the Protein. *Int. J. Quantum Chem.* **2001**, *81* (5), 335–347. https://doi.org/10.1002/1097-461X(2001)81:5<335::AID-QUA1003>3.0.CO;2-Q.

(100) Murtaza, Z.; Graff, D. K.; Zipp, A. P.; Worl, L. A.; Jones, W. E. Jr.; Bates, W. D.; Meyer, T. J. Energy Transfer in the Inverted Region: Calculation of Relative Rate Constants by Emission Spectral Fitting. *J. Phys. Chem.* **1994**, *98* (41), 10504–10513. https://doi.org/10.1021/j100092a020.

(101) Solomon, E. I. Inorganic Spectroscopy–An Overview. *Comments Inorg. Chem.* **1984**, *3* (5), 225–320. https://doi.org/10.1080/02603598408080072.

(102) Brown-Xu, S.; Fumanal, M.; Gourlaouen, C.; Gimeno, L.; Quatela, A.; Thobie-Gautier, C.; Blart, E.; Planchat, A.; Riobé, F.; Monnereau, C.; et al. Intriguing Effects of Halogen Substitution on the Photophysical Properties of 2,9-(Bis)Halo-Substituted Phenanthrolinecopper(I) Complexes. *Inorg. Chem.* **2019**, *58* (12), 7730–7745. https://doi.org/10.1021/acs.inorgchem.9b00042.

(103) Miller, M. T.; Gantzel, P. K.; Karpishin, T. B. A Photoluminescent Copper(I) Complex with an Exceptionally High CuII/CuI Redox Potential: $[Cu(Bfp)_2]^+$ (Bfp=2,9-Bis(Trifluoromethyl)-1,10-Phenanthroline). *Angew. Chem. Int. Ed.* **1998**, *37* (11), 1556–1558. https://doi.org/10.1002/(SICI)1521-3773(19980619)37:11<1556::AID-ANIE1556>3.0.CO;2-W.

(104) Miller, A. J. M.; Dempsey, J. L.; Peters, J. C. Long-Lived and Efficient Emission from Mononuclear Amidophosphine Complexes of Copper. *Inorg. Chem.* **2007**, *46* (18), 7244–7246. https://doi.org/10.1021/ic7009513.

(105) Lotito, K. J.; Peters, J. C. Efficient Luminescence from Easily Prepared Three-Coordinate Copper(I) Arylamidophosphines. *Chem. Commun.* **2010**, *46* (21), 3690–3692. https://doi.org/10.1039/C000818D.

(106) Mankad, N. P.; Rivard, E.; Harkins, S. B.; Peters, J. C. Structural Snapshots of a Flexible Cu_2P_2 Core That Accommodates the Oxidation States Cu(I)Cu(I), Cu(1.5)Cu(1.5), and Cu(II)Cu(II). *J. Am. Chem. Soc.* **2005**, *127* (46), 16032–16033. https://doi.org/10.1021/ja056071l.

(107) Harkins, S. B.; Peters, J. C. Amido-Bridged Cu_2N_2 Diamond Cores That Minimize Structural Reorganization and Facilitate Reversible Redox Behavior between a Cu(1)Cu(1) and a Class III Delocalized Cu(1.5)Cu(1.5) Species. *J. Am. Chem. Soc.* **2004**, *126* (9), 2885–2893. https://doi.org/10.1021/ja037364m.

(108) Harkins, S. B.; Peters, J. C. A Highly Emissive Cu_2N_2 Diamond Core Complex Supported by a $[PNP]^-$ Ligand. *J. Am. Chem. Soc.* **2005**, *127* (7), 2030–2031. https://doi.org/10.1021/ja043092r.

(109) Cuttell, D. G.; Kuang, S.-M.; Fanwick, P. E.; McMillin, D. R.; Walton, R. A. Simple Cu(I) Complexes with Unprecedented Excited-State Lifetimes. *J. Am. Chem. Soc.* **2002**, *124* (1), 6–7. https://doi.org/10.1021/ja012247h.

(110) Gamelin, D. R.; Randall, D. W.; Hay, M. T.; Houser, R. P.; Mulder, T. C.; Canters, G. W.; de Vries, S.; Tolman, W. B.; Lu, Y.; Solomon, E. I. Spectroscopy of Mixed-Valence Cu_A-Type Centers: Ligand-Field Control of Ground-State Properties

Related to Electron Transfer. *J. Am. Chem. Soc.* **1998**, *120* (21), 5246–5263. https://doi.org/10.1021/ja973161k.

Chapter 3

MULTIREFERENCE GROUND AND EXCITED STATE ELECTRONIC STRUCTURES OF FREE- VERSUS IRON PORPHYRIN-CARBENES

Adapted with permission from:

Stroscio, G. D.; Srnec, M.*; Hadt, R. G.* Multireference Ground and Excited State Electronic Structures of Free- versus Iron Porphyrin-Carbenes. *Inorg. Chem.* **2020**, *59* (13), 8707–8715. https://doi.org/10.1021/acs.inorgchem.0c00249.

*Corresponding author.

Abstract

Iron porphyrin carbenes (IPCs) are important reaction intermediates in engineered carbene transferase enzymes and homogeneous catalysis. However, discrepancies between theory and experiment complicate the understanding of the IPC electronic structure. In the literature, this has been framed as whether the ground state is an open- vs. closed-shell singlet (OSS vs. CSS). Here we investigate the structurally dependent ground and excited spin state energetics of a free carbene and its IPC analogs with variable trans axial ligands. In particular, for IPCs, multireference *ab initio* wave function methods are more consistent with experiment and predict a mixed singlet ground state that is dominated by the CSS (Fe(II)←$\{:\text{C(X)Y}\}^{0}$) configuration (i.e., electrophilic carbene), but that also has a small, non-negligible contribution from an Fe(III)–$\{\text{C(X)Y}\}^{-\bullet}$ configuration (hole in d(xz), i.e., radical carbene). In the multireference approach, the "OSS-like" excited states are metal-to-ligand charge transfer (MLCT) in nature and are energetically well above the CSS-dominated ground state. The first, lowest energy, of these "OSS-like" excited states is predicted to be heavily weighted towards the Fe(III)–$\{\text{C(X)Y}\}^{-\bullet}$ (hole in d(yz)) configuration. As expected from exchange considerations, this state falls energetically above a triplet of the same configuration. Furthermore, potential energy surfaces (PESs) along the IPC Fe–C(carbene) bond elongation coordinate exhibit increasingly strong mixings between CSS/OSS characters, with the Fe(III)–$\{\text{C(X)Y}\}^{-\bullet}$ configuration (hole in d(xz)) growing in weight in the ground state during bond elongation. The relative degree of electrophilic/radical carbene character along this structurally relevant PES can potentially play a role in reactivity and selectivity patterns in catalysis. Future studies on IPC reaction coordinates should evaluate contributions from ground and excited state multireference character.

3.1. Introduction

Iron porphyrin carbenes (IPCs) carry out a variety of important chemistries, including B–H,[1,2] C–H,[3] N–H,[4,5] O–H,[6] Si–H,[7,8] and S–H[9,10] insertion, as well as cyclopropanation,[11–15] cyclopropenation,[16] and carbonyl olefination.[17] This diverse reactivity has spurred interest in defining the electronic structures of IPCs. Relevant electronic structure descriptions include: Fe(IV)=$\{C(X)Y\}^{2-}$, Fe(II)←{:C(X)Y}, or Fe(III)–$\{C(X)Y\}^{-\bullet}$, with X and Y corresponding to different chemical groups. For Fe(III), the metal- and carbene-based electron spins can couple ferro- or anti-ferromagnetically to give the total spin states $S_T = 1$ or 0, respectively. The Fe(II)←{:C(X)Y} form is a closed shell singlet (CSS), differentiated from the antiferromagnetically coupled Fe(III)–$\{C(X)Y\}^{-\bullet}$ open shell singlet (OSS). Experimental data, including nuclear magnetic resonance (NMR),[18,19] electron paramagnetic resonance (EPR),[8] Mössbauer,[8,19,20] and X-ray absorption spectroscopy (XAS),[20] have largely been interpreted as reflecting the CSS Fe(II) state. However, studies utilizing density functional theory (DFT) have suggested the potential importance of an OSS state.[8,21,22] Given the broad array of chemistries that can be accomplished by IPCs, it is important to more clearly align theory and experiment in order to understand their reactivity patterns and ultimately define their mechanisms to tune and/or enhance catalytic capabilities.

Here we study the structurally dependent energetics of the ground and excited state electronic structures of a free carbene and its IPC analogs with several different axial ligands. Multireference *ab initio* methods provide a singlet ground state dominated by a CSS configuration, more consistent with experimental observations. "OSS-like" excited states, dominated by Fe(III)–$\{C(X)Y\}^{-\bullet}$ configurations, are predicted to be a metal-to-ligand charge transfer (MLCT) excited states energetically well isolated from the ground state.

Furthermore, the contributions of CSS/OSS character in the ground state evolve along the Fe–C(carbene) coordinate, which is important for evaluating the transition metal carbene catalysis.

3.2. Computational Methods

All calculations were performed using ORCA[23,24] versions 4.0.1.2, 4.1.2, 4.2.0, and 4.2.1.

3.2.1. Scans of the Free Carbene Dihedral Angle

Initially, geometry optimizations constraining the dihedral angle shown in Figure 3.1 were performed using the BP86[25–27] or B3LYP[26,28] functionals. The 6-311G(d)[29] basis set was used on all atoms. AutoAux[30] was used as an auxiliary basis, so the resolution of identities[31–35] (RI) approximations could be applied. In the BP86 case, Split-RI-J was used; in the B3LYP case, RIJCOSX needed to be used. Fine DFT grids were used (GRID7 NOFINALGRID for BP86, GRID7 NOFINALGRID GRIDX9 for B3LYP). The unrestricted Kohn-Sham formalism (UKS) was used to find the closed-shell singlet, triplet, and broken-symmetry singlet (BSS) states. The former was verified to be the spin-restricted solution by checking that the $<S^2>$ value equaled exactly zero and through orbital inspection. Using the triplet geometry and wavefunction, constrained optimizations were used to find the BSS. Tight SCF convergence criteria, which has a convergence tolerance of 10^{-8} Hartrees, was applied for all calculations. Using the same settings, restricted TDDFT calculations with 5 roots were performed on the spin-restricted solution geometries. Yamaguchi's correction was also applied to the DFT BSS energy.[36]

$$E_{corrected} = \alpha E^{1}_{BSS-geom.} - \beta E^{3}_{BSS-geom.} \qquad \text{(eq 3.1)}$$

$$\alpha = \beta + 1$$

$$\beta = \frac{\langle \hat{S}^2 \rangle_{BSS}}{\langle \hat{S}^2 \rangle_{triplet,BSS-geom.} - \langle \hat{S}^2 \rangle_{BSS}}$$

Quasi-degenerate N-electron valence second-order perturbation theory (QD-NEVPT2)[37] single point calculations using a 2-in-2 active space were performed (active space orbitals for select angles in Figures B.4-B.6) on the free carbene. Using the B3LYP triplet geometries, the triplet manifold was evaluated using a state-specific calculation. Using the B3LYP BSS geometries, two singlet roots were used in a state-averaged calculation (occupancies in Table B.1; CI-Vectors in Tables B.2-3). For DFT calculations, the 6-311G(d) basis was used on all atoms. Tight SCF convergence criteria with an energy tolerance of 10^{-7} Hartrees was applied for all these calculations. While QD-NEVPT2 was used throughout this study, it was found to give identical results to regular NEVPT2[38–42] calculations (Tables B47). In the same manner, fully internally contracted multireference configuration interaction (FIC-MRCI)[43] calculations were performed by reading in the QD-NEVPT2 wavefunctions (.gbw file). Multi-reference coupled cluster with single and double excitations (MR-CCSD) and with the domain-based local pair natural orbital (DLPNO)[44] approximation (denoted in the work as DLPNO-MR-CCSD) were performed using cc-pVTZ[45] and cc-pV6z/c[46] and a 2-in-2 active space (see Figure 3.1) with very tight convergence criteria. Here state-specific calculations needed to be used for all three states and the BSS B3LYP geometry was used.

3.2.2. Scans of the Dihedral Angle in IPC Models and Additional Single Point Calculations

Geometry optimizations constraining the dihedral angle in Figure 3.1 were performed in much the same way for the IPC model complexes as for the free carbene. However, for the IPC model complexes, a split basis was used. 6-311G(d) was on the iron, the ligating nitrogen atoms, and all the atoms in the carbene molecule; 6-31G(d)[47] was used on all the other atoms. The restricted Kohn-Sham formalism (RKS) was used to find the spin-restricted solution. In addition to BP86 and B3LYP, TPSSh[48–50] was also used for the scans. DFT grids sufficiently fine for accurate energies and geometries were used (GRID7 NOFINALGRID for BP86, GRID4 NOFINALGRID GRIDX5 for TPSSh and B3LYP). All other aspects of the DFT calculations were the same as for the free carbene case.

Using the B3LYP RKS geometries, QD-NEVPT2 calculations using a 12-in-12 active space were performed. Two singlet roots, five triplet roots, and one quintet root were used in the state-averaged calculations. For the case of the hydroxide ligated IPC, a two singlets and five triplets state-averaged calculation was also done (energetic comparison in Figure B.2; comparison of configuration weights in Tables B.36-B.37). This was done because the case with the quintet occasionally converged to an excited quintet. The 6-311G(d) basis was again used. Again, tight SCF convergence criteria with an energy tolerance of 10^{-7} Hartrees was applied for all these calculations. The RIJCOSX approximation was used. The Bloch formalism was used throughout this study. The active spaces and occupancies are provided in Appendix B; the CI-vectors and useful Löwdin orbital analyses are provided in Tables B.17-B.43.

For [Fe(TPP)CCl_2], the same procedures were used as for the above; however, single point calculations on the crystal structure[20] were performed (energetics and CI-Vectors tabulated in Tables B.10-14). QD-NEVPT2 calculations were also performed on the BSS structure from Sharon et al.[21] (Tables B.4-S6) and on an “Hs only” optimized crystal structure of an IPC intermediate in an engineered cytochrome *c* protein (PDB ID code: 6CUN; tables B.7-B.9).[8]

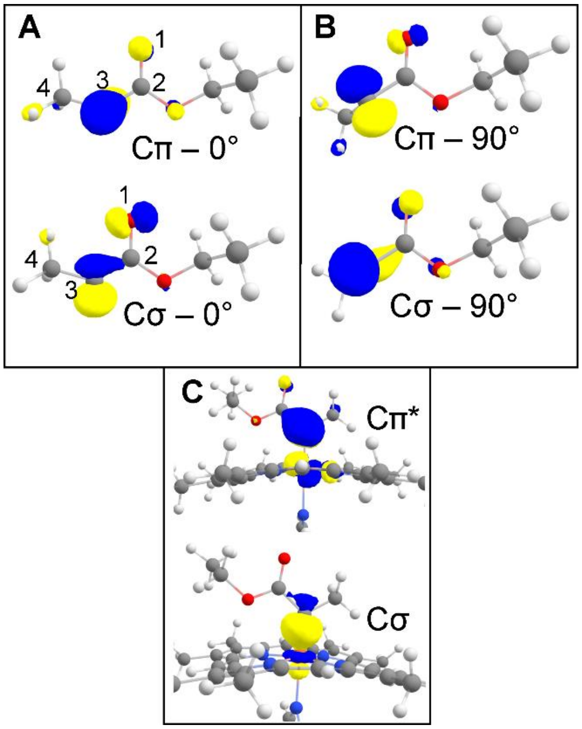

Figure 3.1. Free carbene Cσ and Cπ orbitals from multireference calculations for (A) 0° and (B) 90° conformations and (C) the Cσ and Cπ* orbitals for the IPC. The dihedral angle of interest is numbered in panel A.

3.2.3. Scans of the Fe-C Bond Length in IPCs

Using B3LYP and the same methodology of constrained optimizations as described in Section B.A.2., a relaxed scan of the Fe-C bond length in the IPC model RKS geometries was performed with the B3LYP 90° geometry as the starting point. Using these geometries, B3LYP single point calculations (Figure B.8) and QD-NEVPT2 single point calculations using the same methodology as described above were performed. CI-Vectors are presented in Tables B.44-B.46.

3.3. Results and Discussion

In the following, electronic structure calculations are first carried out on a free carbene to establish differences between DFT and multireference descriptions (Section 3.3.1). These calculations are then extended to a variety of IPC analogs with the same carbene ligand but with variable trans-axial ligation (e.g., *N*-methylimidazole (*N*-MeImid), thiolate, or hydroxide, Section 3.3.2). Additional comparisons are made to IPC analogs where spectroscopic and X-ray crystallographic data exist (see Subsections of Section 3.3.2). Finally, in Section 3.3.3, the multireference approach is used to investigate the IPC Fe–C bond PESs for the trans-axial ligands considered in Section 3.3.2, which allows for the evaluation of catalytically relevant structural contributions to the frontier molecular orbitals (FMOs) of the ground and excited state electronic structures of IPCs.

3.3.1. Free Carbene: DFT/Multireference Comparison

3.3.1.1 DFT Calculations of Ground and Excited States

The Cσ- and Cπ-type FMOs of the free- and IPC-carbene, which are critical for understanding their respective electronic structures, are shown in Figure 3.1. Note, given the antibonding character of the π-type molecular orbital for the IPC, it is referred to throughout as Cπ*. For methylene, the following electronic configurations and states have been previously discussed: $(C\sigma)^2(C\pi)^0$ ($^1A_1$), $(C\sigma)^1(C\pi)^1$ ($^{1,3}B_1$), and $(C\sigma)^0(C\pi)^2$ ($^1A_1$).[51,52] Here, for ethyl 2-diazopropanate (Me-EDA), we have investigated the relative energetics of the spin-restricted singlet, $(C\sigma)^2(C\pi)^0$, the triplet, $(C\sigma)^1(C\pi)^1$, and the BSS as a function of the O–C–C–C dihedral angle given in Figure 3.1. Note that this dihedral was recently discussed in the context of potentially important secondary coordination sphere contributions in a carbene transferase enzyme.[8] Further note, as discussed by Cremer,[53] the DFT-based BSS of methylene is considered an alternative description of the carbene spin-restricted singlet. It does not, in this case, correspond to the formal $^1B_1$ state arising from the $(C\sigma)^1(C\pi)^1$ electronic configuration (*vide infra*).

The DFT (BP86/B3LYP) relaxed PESs from 0–180° along the O–C–C–C dihedral coordinate are given in Figure 3.2A (the 360° angular dependence is a mirror image about 180° (Figure B.1), and thus only the 0–180° scans are considered). Both functionals provide fairly similar descriptions despite the 20% difference in exact exchange. At 0° and 180°, the ground state is predicted to be a triplet (e.g., $(C\sigma)^1(C\pi)^1$, $^3B_1$ of methylene; blue markers in Figure 3.2A, orbitals in Figure B.4). The spin-restricted singlet (red markers in Figure 3.2A, orbitals in Figure B.5) and BSS (green markers in Figure 3.2A, orbitals in Figure B.6A/B) are excited states ~10–20 kcal mol^{-1} above the ground state. Upon rotating to 90°, both the spin-restricted and BSSs provide similar overall descriptions and thus have similar electronic energies (i.e., the BSS state collapses to a restricted-singlet-like description between ~50°–150° in Figure 3.2A). Furthermore, as described in the Computational Methods, upon applying the approximate spin-correction procedure of Yamaguchi,[36] the energies of the BSS calculations outside this angular region become similar to those obtained directly from the restricted-singlet state solution (orange vs. red markers in Figure 3.2A). Also, the canonical molecular orbitals obtained from the BSS do evolve along the O–C–C–C dihedral coordinate (Figure B.6A). The relevant BSS natural orbital occupancies (Figure B.6B) are consistent with the Yamaguchi correction in that, at 90°, the BSS approaches the spin restricted solution and there is more mixing at angles deviating from 90°.

In order to obtain an approximate PES of the $^1B_1$ excited state, time-dependent DFT (TDDFT) calculations were performed along the spin-restricted singlet surface using both BP86 and B3LYP functionals (purple markers in Figure 3.2A). The lowest energy excitation along the PES indeed represents a $C\sigma \rightarrow C\pi$ transition, which provides a formal singlet $(C\sigma)^1(C\pi)^1$ electronic configuration. For the most part, the energy of this singlet excited state mirrors that of the triplet. However, there is a noticeable dip in the TDDFT excited state energies around ~50°. This excited state PES is also a mirror image about 180° (Figure B.1). As discussed below for multireference methods, the energy difference between the singlet TDDFT excited state (which approximates the $^1B_1$ state of methylene) and the lower energy triplet ($^3B_1$ of methylene) is $2K_{\sigma\pi}$, where $K_{\sigma\pi}$ is the exchange integral in electron-electron repulsion.[54] These results are now compared to multireference approaches.

3.3.1.2. Multireference Calculations of Ground and Excited States

PESs along the free carbene dihedral distortion for three multireference *ab initio* methods as implemented in ORCA[23,24] (DLPNO-MR-CCSD, FIC-MRCI, and QD-NEVPT2; acronyms and other computational details provided in the Computational Methods) are presented in Figure 3.2B. In each case, an active space with two electrons and the Cσ- and Cπ-type orbitals was used (2-in-2 active space; orbitals in Figure 3.1). Similarly to DFT, the triplet ((Cσ)^1(Cπ)^1, blue markers in Figure 3.2B, orbitals in Figure B.4) is the ground state at 0°/180°. However, at 90°, the lowest energy singlet (red markers in Figure 3.2B, orbitals in Figure B.5) is similar in energy to the triplet. The QD-NEVPT2 CI vectors of the lowest energy singlet (Table B.2) and the first excited singlet state (green markers in Figure 3.2B, Table B.3, orbitals in Figure B.6A/B) indicates ~89-97 % (Cσ)^2(Cπ)^0 and >99 % (Cσ)^1(Cπ)^1 contributions, respectively. From this, the first excited singlet is therefore similar to the $^1B_1$ state of methylene. The ground state singlet is observed to have some character from the (Cσ)^0(Cπ)^2 configuration, especially approaching 0 and 180°, and a near negligible amount from the (Cσ)^1(Cπ)^1 configuration. The energy difference between the first excited singlet and the lower energy triplet states is thus $2K_{\sigma\pi}$. Ranging from ~29 kcal mol^{-1} (~1.26 eV) at 10° to ~41 kcal mol^{-1} (~1.78 eV) at 100°, these energies can be smaller or larger than the energy splitting between the ^{3}P and ^{1}D states of free carbon (1.3 eV),[55] depending on the O–C–C–C dihedral angle. Thus, overall, the ground and excited state electronic structures and corresponding PESs obtained using DFT/TDDFT and multireference methods are qualitatively similar and both provide a means to analyze and quantify ground and excited states in the free carbene. As shown below, however, this is not the case for IPCs.

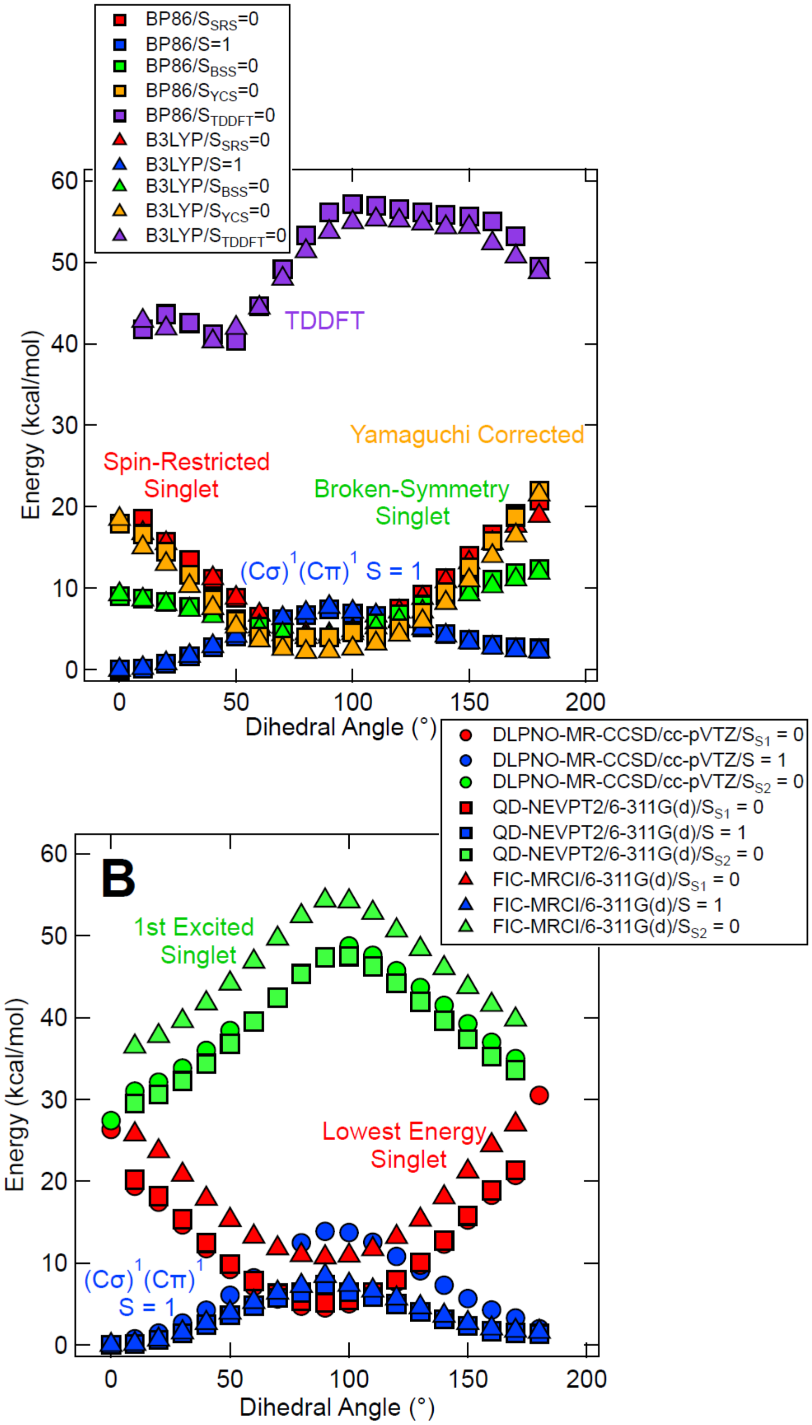

Figure 3.2. Ground and excited state PESs along the free carbene dihedral coordinate from Figure 3.1 using (A) DFT/TDDFT or (B) multireference *ab initio* methods. Acronyms for (B) are given in Section 3.2.

3.3.2. Iron Porphyrin Carbene: DFT/Multireference Comparison

3.3.2.1. DFT Calculations and Axial Ligand Dependence of Ground and Excited States

The ground and excited spin state energetic comparisons were extended to the IPC analogs. Both DFT (Figure B.3 and B.7) and QD-NEVPT2 (Figure 3.3) were used to investigate the energetic dependencies on the dihedral angle. Several axial ligands were studied: *N*-MeImid, methyl thiolate, and hydroxide. DFT relaxed PESs are consistent with existing literature in that the spin-restricted and BSS states are either close in energy or the BSS state is lowest (Figure B.3 and B.7, BSS spin densities given in Table B.48).[8,21,22] For all ligands, the amount of exact exchange has significant effects on the relative energies of the lowest triplet, spin-restricted CSS, and BSS. Note that the triplet from DFT captured here is an Fe(III) d(yz)-based hole ferromagnetically coupled to a carbene anion radical (spin densities in Table B.48). Several other triplet states are captured using the multireference description described below. Increasing exact exchange from 0 to 20 % stabilizes the triplet relative to the BSS and spin-restricted CSS states, as expected. While the energies of the latter are virtually identical with BP86, the BSS is stabilized relative to the spin-restricted CSS state with increasing amounts of exact exchange. Also, going from *N*-MeImid to thiolate to hydroxide, the triplet and the BSS states are stabilized in energy relative to the spin-restricted CSS. This is consistent with the increased stabilization of the formal Fe(III) redox level for these states. Thus, for all levels of theory and different axial ligands, DFT provides a BSS ground state description, and the energy of the BSS state is stabilized further relative to the spin-restricted CSS with anionic ligands and larger amounts of exact exchange.

The BSS results also clearly capture significant Fe(III) d(xz)-based hole character (Table B.48). Likewise, the 0.78 – 0.55 overlaps from corresponding orbital analyses[56] indicate spin-coupled pairs. However, these spin-coupled pairs appear on $(d(xz))^1(C\pi)^1$ bonding corresponding orbitals, with the difference between the two orbitals within each pair being whether the density is mostly on the metal or the carbene. Visually inspecting the corresponding orbitals (Figure B.9), they look qualitatively similar to the d(xz) natural orbital in the QD-NEVPT2 active space (*vide infra*), which experiences some bonding character with the carbene center (Löwdin population analyses in Tables B.17, B.26, and B.35).

3.3.2.1.1. Additional Comparisons to Experiment

XAS and Mössbauer spectroscopies on IPC model complexes have been interpreted as reflecting an Fe(II) CSS ground state.[20] DFT calculations were also performed on the synthetic complex [Fe(TPP)CCl_2] (tpp = tetraphenylporphyrin). Similarly to other IPC complexes, the CSS and BSS states are nearly degenerate using the BP86, TPSSh, or B3LYP functionals (Table B.10). The triplet is ~30 kcal mol^{-1} higher in energy and is also stabilized with increasing exact exchange. Thus, while the IPC analogs have low-lying CSS states, the presence of the BSS (and its Fe(III)-based dominant description) ground state seems inconsistent with the available experimental data. These inconsistencies can be further evaluated using multireference *ab initio* approaches.

3.3.2.2. Multireference Calculations and Axial Ligand Dependence of Ground and Excited States

The QD-NEVPT2 calculated PESs are given in Figures 3.3A-C for *N*-MeImid, thiolate, or hydroxide axial ligands, respectively. Note that the *N*-MeImid and thiolate calculations were carried out using two singlets, five triplets, and one quintet. For clarity, only the two singlets and four lowest energy triplets are shown here. All states are given in Figure B.2. For the hydroxide axial ligand, the data given in Figure 3.3C were obtained using two singlets and five triplets. For the hydroxide, the converged energy of the quintet state was quite sporadic (Figure B.2). Nonetheless, the PESs of the relevant singlet and triplet states considered here are virtually identical with and without this quintet (Figure B.2).

The ground state is a singlet for all angles and axial ligands (red markers and numbers in Figure 3.3, top, bottom, respectively). A global energy minimum exists at ~90°, although the energy profile is shallow. As with the free carbene, the 360° angular dependence of the IPC energetics are a mirror image about 180° (Figure B.2). For *N*-MeImid, the ground state, as described by the QD-NEVPT2 CI vector over the PES, is not particularly sensitive to dihedral angle and is consistently ~60 % CSS, with ~16 % and ~6 % contributions from the OSS, $(d(xz))^1(C\pi^*)^1$, and the $(d(xz))^0(C\pi^*)^2$ Fe(IV)-based configurations (Table B.18). Similarly, for the thiolate, the ground state singlet over the PES is comprised of ~57 % CSS, ~19 % OSS, and ~7 % Fe(IV)-based configurations, and is not particularly sensitive to dihedral angle (Table B.27). Similarly for the hydroxide ligand, the ground state singlet over the PES is comprised of ~61 % CSS, ~13 % OSS, and ~10 % Fe(IV)-based configurations, and is not particularly sensitive to dihedral angle (Table B.36).

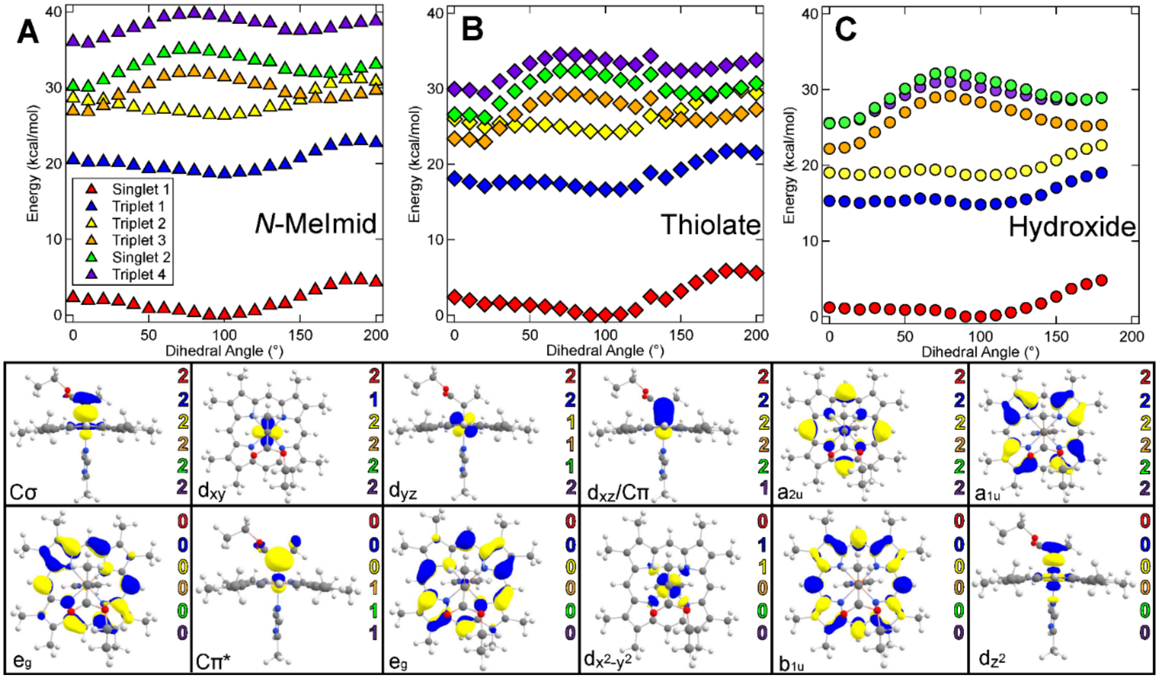

Figure 3.3. IPC PESs and Active Space. (Top) Ground and excited state PESs along the dihedral coordinate calculated with quasi-degenerate *N*-electron valence second order perturbation theory (QD-NEVPT2) for (A) *N*-MeImid, (B) thiolate, and (C) hydroxide axial ligands. (Bottom) The 12 orbital active space for the *N*-MeImid IPC. Formal orbital occupation numbers are provided. The color of the number corresponds to the state given in the top panel. Note that the first two triplets for the IPC (blue and yellow markers) are metal-based spin-forbidden ligand field transitions (i.e., no carbene radical and more CSS-like), while triplets three and four involve the occupation of the Cπ* orbital, with triplet three arising from the d(yz) → Cπ* transition (and always below the singlet of the same configuration) and triplet four arising from the d(xz)/Cπ → Cπ* transition.

While the triplet considered in the DFT description corresponded to the $(d(yz))^1(C\pi^*)^1$ electronic configuration, there are additional ones to consider using the multireference approach. More specifically, there are two metal-based spin-forbidden ligand field excited states arising from transitions between the filled Fe d(xy)/d(yz) and unoccupied d(x^2-y^2) orbitals (Figure 3.3, bottom), which is reflected by their formal occupation numbers given in Figure 3.3, bottom (blue and yellow numbers) (CI vectors given in Tables B.19 and

B.20, respectively for *N*-MeImid). At ~90°, both (d(yz))^1(Cπ*)^1 and (d(xz))^1(Cπ*)^1-based triplets are located higher in energy than the ligand-field based (d(xy))^1(d(x^2-y^2))^1 and (d(yz))^1(d(x^2-y^2))^1 triplets (orange and purple markers in Figure 3.3, top, CI vectors given in Tables B.21 and B.24, respectively for *N*-MeImid), with the (d(yz))^1(Cπ*)^1-based triplet being lower than the (d(xz))^1(Cπ*)^1-based triplet. The lowest energy singlet excited state (green markers in Figure 3.3, CI vector in Table B.22 for *N*-MeImid) is located between these two triplets. Importantly, this singlet falls above the triplet of the same configuration, as one might expect from exchange considerations (triplet 3 relative to singlet 2 in Figure 3.3). For *N*-MeImid, this state is ~66 – 71 % (d(yz))^1(Cπ*)^1 over the entire PES (Table B.22). Interestingly, for *N*-MeImid at 90°, the “OSS-like” singlet dominated by (d(xz))^1(Cπ*)^1, is not observed here, even when increasing the number of singlet states in the QD-NEVPT2 calculation to 30, which represents the highest number of states we can accommodate with current computational power. Note that the highest energy singlet in the QD-NEVPT2 calculation with 30 singlets is at ~41 000 cm^{-1} (~115 kcal mol^{-1}). Thus, while we cannot rule out the (d(xz))^1(Cπ*)^1-based singlet at higher energies, this importantly demonstrates that “OSS-like” excited states represent MLCT transitions at energies significantly higher than the predominantly CSS ground state.

3.3.2.2.1. Comparisons to Additional Iron Porphyrin Carbene Structures

We have further considered two additional IPC structures using the QD-NEVPT2 approach, including the IPC structure from Sharon et al.,[21] as well as the X-ray crystallographic structure of the IPC active site reported by Lewis et al.[8] Note that for the X-ray structure, all heavy atoms were frozen, while the hydrogen atoms were optimized (H-optimized structure). Using the BSS structure from Sharon et al., which features a thiolate axial ligand and a truncated carbene (CH_3 replaced with H), the QD-NEVPT2 ground state is also a singlet (Table B.4) with dominantly CSS character (~45 %), with ~29 % and ~8 % contributions from the OSS and Fe(IV)-based configurations, respectively (Table B.5). The excited state manifold is also similar to the other IPC structures considered here in that the first excited singlet is dominated by a $(d(yz))^1(C\pi^*)^1$ configuration and energetically above a triplet dominated by the same configuration (Table B.6). Furthermore, using the H-optimized IPC active site structure, which is comparable to the *N*-MeImid structure considered here, the ground state is also a singlet and with dominantly CSS character (~46 %), with ~28 % and ~5 % contributions from the OSS and Fe(IV)-based configurations, respectively. Again, the first excited singlet is dominated by a $(d(yz))^1(C\pi^*)^1$ configuration and energetically above a triplet dominated by the same configuration (Tables B.7 and B.9). As shown in the following Section, the relative amounts of CSS and OSS characters are quite sensitive to the Fe–C(carbene) bond distance. Thus, the decreased CSS character and increased OSS character (by ~10 %) for the structures from Sharon et al.[21] and Lewis et al.[8] relative to the structures considered above is likely related to slightly longer Fe–C(carbene) bond distances in the former (by 0.1 Å).

In summary, *ab initio* methods suggest that the IPC ground state has a significant degree of multireference character and is dominated by the CSS description, with smaller contributions from OSS- and Fe(IV)-based configurations. This is the case for all three axial ligands studied here, as well as the IPC from an enzyme active site characterized by X-ray crystallography.[8] Furthermore, the shallowness of the singlet ground state PESs in Figure 3.3 suggests a high degree of carbene conformational flexibility about the O–C–C–C dihedral coordinate, including two minima over the entire PESs (Figure B.2). This preference for the rotated conformation of the IPC is consistent with the ~266° angle found in the active site of the carbene transferase enzyme.[8] However, it is especially interesting to note that, while similar energies are observed here for the ~90° and ~270° IPC structures in the absence of additional interactions (Figure B.2), only the latter conformation is observed in the protein structure, which suggests that second sphere interactions play an important role in stabilizing one or the other conformation, as discussed by Lewis *et al*.[8] Overall, the predominant CSS contribution to the ground state, as described by multireference *ab initio* methods, is more consistent with experimental data.[8,18–20] Lastly, singlet "OSS-like" configurations are thus formal ^{1}MLCT excited states energetically well above the dominantly CSS ground state. Future optical and X-ray spectroscopic studies directed at characterizing the excited state ligand field and MLCT manifolds will be insightful.

3.3.3. Iron Porphyrin Carbene (Fe–C) Potential Energy Surfaces

While the ground states of IPCs are predominantly CSSs in the multireference description, the OSS may become important if structural distortions favoring the OSS occur along reaction coordinates. Indeed, the spin state energetics and ground state characters evolve significantly with Fe–C(carbene) bond elongation (Figure 3.4), an important coordinate to consider for reactivity. Only QD-NEVPT2 PESs are considered here, and the DFT results are given in Figure B.8. While the ground states at the Fe–C(carbene) equilibrium geometries in the QD-NEVPT2 calculated Fe–C PESs are predominantly CSS for all axial ligands, the energy of the $(d(yz))^1(C\pi^*)^1$ OSS approaches the ground CSS state as the Fe–C(carbene) bond is elongated (compare red and green markers in Figures 3.4A-C). Furthermore, from analyses of the multireference ground state wave function (i.e., the CI vector), the amount of CSS character (red markers in Figures 3.4D-F), which is dominant at the Fe–C(carbene) equilibrium distance, decreases significantly upon elongation of the Fe–C bond. This decrease occurs with an increase in the $(d(xz))^1(C\pi^*)^1$ OSS contribution to the ground state (Table B.44-46 and green markers in Figures 3.4D-F). For all structures, the $(d(xz))^1(C\pi^*)^1$ OSS character exceeds that of the CSS character at an Fe–C distance of ~2.1 Å. Overall, these bond distances are quite similar to those of relevant transition states.[8,21] These results suggest that the OSS/CSS state mixing will be important to consider for understanding axial ligand dependent IPC reaction coordinates, which can translate to variations in selectivity and efficiency.[8] For instance, CI-vector analyses of ground state wave functions and related energies will be important for accurately and precisely describing reaction mechanisms.

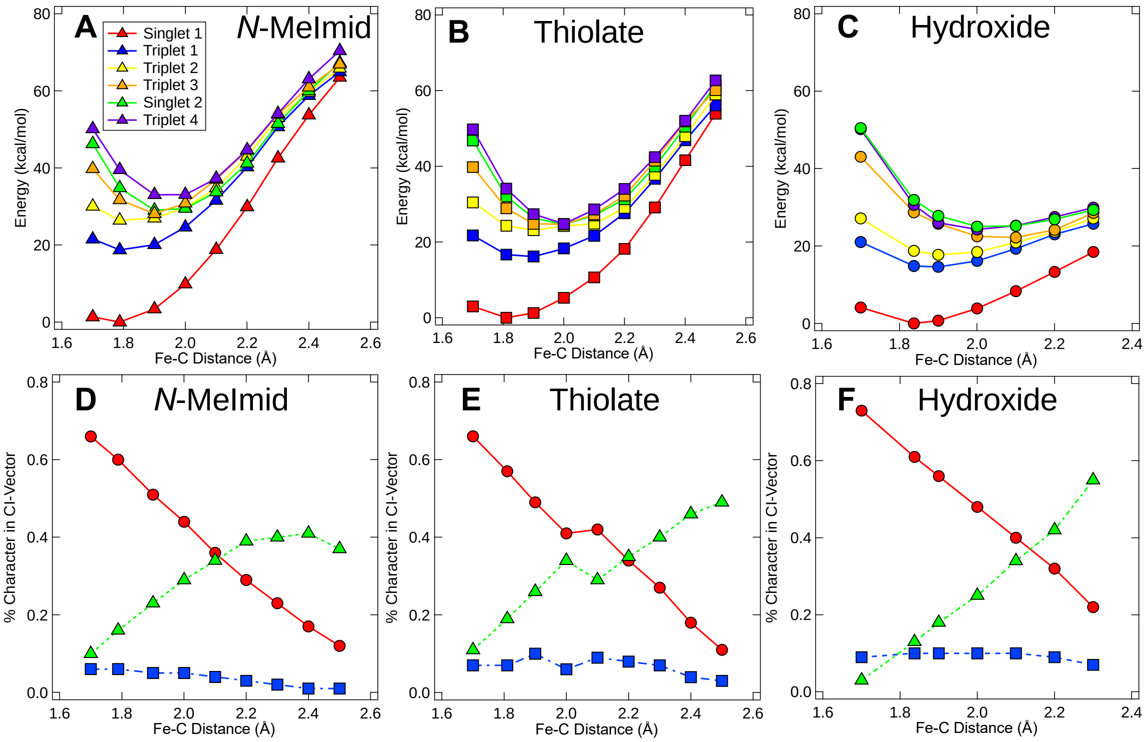

Figure 3.4. QD-NEVPT2 PESs along the Fe–C(carbene) coordinate (top) and associated CI-vectors of the ground state (bottom): (A, D) *N*-MeImid, (B, E) thiolate, and (C, F) hydroxide. Red, CSS; green, OSS; and blue, the first triplet state (top) or the Fe(IV)={C(X)Y}$^{2-}$ singlet (bottom). Note the Fe–C(carbene) PES only extends to 2.3 Å for the hydroxide axial ligand, as CASSCF convergence becomes an issue beyond these bond distances, likely due to the significantly more shallow energy profile relative to the *N*-MeImid and thiolate axial ligands.

3.4. Summary and Conclusions

We have shown that multireference methods provide a predominantly CSS ground state for all IPC conformations and axial ligands investigated here. This ground state description is in agreement with available experimental data.[8,18–20] In contrast, DFT consistently provides a BSS ground state, demonstrating OSS character, for all IPCs studied here. In the multireference calculations, the IPC CSS ground state has a small, but non-negligible amount of $(d(xz))^1(C\pi^*)^1$ OSS character. “OSS-like” excited states are predicted to correspond to high energy MLCT states (i.e., radical carbene) that are somewhat sensitive to the nature of the axial ligand. The lowest energy of these MLCT states is dominated by the $(d(yz))^1(C\pi^*)^1$ configuration and lies energetically above a triplet of the same configuration. Importantly, the IPC CSS ground state corresponds to an electrophilic carbene, which may tend to react as a Fischer-type species. Furthermore, an interesting comparison can be drawn between the findings presented here and those of related Co(II) complexes.[57–63] One electron reduction of the largely CSS Fe(II)–carbene bond would result in formal electron occupation of the $C\pi^*$ FMO (Figure 3.3, bottom) and a low-spin d^6 Fe(II) carbene anion radical. Notably, this FMO is largely ligand-based, with a Löwdin population ranging from ~62 – 69 % carbene character and ~19 – 21 % Fe character over the *N*-MeImid IPC dihedral angle (Table B.17). Thus, this electron configuration would be isoelectronic to the Co carbenes, which have been described as low-spin d^6 Co(III) carbene anion radicals.[57–63]

In addition to IPCs, their nitrene analogs have recently been described as having OSS ground states using DFT and CASSCF, with a calculated reaction coordinate for C–H amination described as H-atom abstraction followed by radical rebound.[64] Notably, here the addition of dynamical correlation in the QD-NEVPT2 approach is largely important for obtaining IPC CSS ground states (one exception being the X-ray crystallographic structure discussed in Section 3.3.2.2.2, which also has a CSS ground state with CASSCF). Thus, results presented here will likely be of general importance for the study of the ground and excited state electronic structures of other metal carbene/nitrene species.

Of final note, while the IPC ground state is dominated by the CSS configuration (i.e., electrophilic carbene), the $(d(xz))^1(C\pi^*)^1$ OSS character (i.e., radical carbene) of the ground state of all IPCs investigated in this study increases significantly upon elongating the Fe–

C(carbene) bond. These changes in CSS/OSS characters emulate those that could occur along a reaction coordinate and increase the radical character of the carbene, which may play a significant role in the reactivity and selectivity patterns of IPCs. Thus, future studies on reaction coordinates and the ground and excited state electronic structures of IPCs and their analogs should evaluate potential multireference contributions to better understand catalytic properties.

REFERENCES

(1) Kan, S. B. J.; Huang, X.; Gumulya, Y.; Chen, K.; Arnold, F. H. Genetically Programmed Chiral Organoborane Synthesis. *Nature* **2017**, *552* (7683), 132–136. https://doi.org/10.1038/nature24996.

(2) Chen, K.; Huang, X.; Zhang, S.-Q.; Zhou, A. Z.; Kan, S. B. J.; Hong, X.; Arnold, F. H. Engineered Cytochrome C-Catalyzed Lactone-Carbene B–H Insertion. *Synlett* **2019**, *30* (04), 378–382. https://doi.org/10.1055/s-0037-1611662.

(3) Mbuvi, H. M.; Woo, L. K. Catalytic C−H Insertions Using Iron(III) Porphyrin Complexes. *Organometallics* **2008**, *27* (4), 637–645. https://doi.org/10.1021/om7007502.

(4) Wang, Z. J.; Peck, N. E.; Renata, H.; Arnold, F. H. Cytochrome P450-Catalyzed Insertion of Carbenoids into N–H Bonds. *Chem. Sci.* **2013**, *5* (2), 598–601. https://doi.org/10.1039/C3SC52535J.

(5) Sreenilayam, G.; Fasan, R. Myoglobin-Catalyzed Intermolecular Carbene N–H Insertion with Arylamine Substrates. *Chem. Commun.* **2015**, *51* (8), 1532–1534. https://doi.org/10.1039/C4CC08753D.

(6) Mbuvi, H. M.; Klobukowski, E. R.; Roberts, G. M.; Woo, L. K. O-H Insertion and Tandem N-H Insertion/Cyclization Reactions Using an Iron Porphyrin as Catalyst with Diazo Compounds as Carbene Sources. *J. Porphyr. Phthalocyanines* **2010**, *14* (03), 284–292. https://doi.org/10.1142/S1088424610001982.

(7) Kan, S. B. J.; Lewis, R. D.; Chen, K.; Arnold, F. H. Directed Evolution of Cytochrome c for Carbon–Silicon Bond Formation: Bringing Silicon to Life. *Science* **2016**, *354* (6315), 1048–1051. https://doi.org/10.1126/science.aah6219.

(8) Lewis, R. D.; Garcia-Borràs, M.; Chalkley, M. J.; Buller, A. R.; Houk, K. N.; Kan, S. B. J.; Arnold, F. H. Catalytic Iron-Carbene Intermediate Revealed in a Cytochrome *c* Carbene Transferase. *Proc. Natl. Acad. Sci.* **2018**, *115* (28), 7308–7313. https://doi.org/10.1073/pnas.1807027115.

(9) Tyagi, V.; Bonn, R. B.; Fasan, R. Intermolecular Carbene S–H Insertion Catalysed by Engineered Myoglobin-Based Catalysts. *Chem. Sci.* **2015**, *6* (4), 2488–2494. https://doi.org/10.1039/C5SC00080G.

(10) Chen, K.; Zhang, S.-Q.; Brandenberg, O. F.; Hong, X.; Arnold, F. H. Alternate Heme Ligation Steers Activity and Selectivity in Engineered Cytochrome P450-Catalyzed Carbene-Transfer Reactions. *J. Am. Chem. Soc.* **2018**, *140* (48), 16402–16407. https://doi.org/10.1021/jacs.8b09613.

(11) Coelho, P. S.; Brustad, E. M.; Kannan, A.; Arnold, F. H. Olefin Cyclopropanation via Carbene Transfer Catalyzed by Engineered Cytochrome P450 Enzymes. *Science* **2013**, *339* (6117), 307–310. https://doi.org/10.1126/science.1231434.

(12) Bordeaux, M.; Tyagi, V.; Fasan, R. Highly Diastereoselective and Enantioselective Olefin Cyclopropanation Using Engineered Myoglobin-Based Catalysts. *Angew. Chem. Int. Ed.* **2015**, *54* (6), 1744–1748. https://doi.org/10.1002/anie.201409928.

(13) Gober, J. G.; Rydeen, A. E.; Gibson-O'Grady, E. J.; Leuthaeuser, J. B.; Fetrow, J. S.; Brustad, E. M. Mutating a Highly Conserved Residue in Diverse Cytochrome P450s Facilitates Diastereoselective Olefin Cyclopropanation. *ChemBioChem* **2016**, *17* (5), 394–397. https://doi.org/10.1002/cbic.201500624.

(14) Knight, A. M.; Kan, S. B. J.; Lewis, R. D.; Brandenberg, O. F.; Chen, K.; Arnold, F. H. Diverse Engineered Heme Proteins Enable Stereodivergent Cyclopropanation of Unactivated Alkenes. *ACS Cent. Sci.* **2018**, *4* (3), 372–377. https://doi.org/10.1021/acscentsci.7b00548.

(15) Carminati, D. M.; Fasan, R. Stereoselective Cyclopropanation of Electron-Deficient Olefins with a Cofactor Redesigned Carbene Transferase Featuring Radical Reactivity. *ACS Catal.* **2019**, *9* (10), 9683–9697. https://doi.org/10.1021/acscatal.9b02272.

(16) Chen, K.; Huang, X.; Kan, S. B. J.; Zhang, R. K.; Arnold, F. H. Enzymatic Construction of Highly Strained Carbocycles. *Science* **2018**, *360* (6384), 71–75. https://doi.org/10.1126/science.aar4239.

(17) Weissenborn, M. J.; Löw, S. A.; Borlinghaus, N.; Kuhn, M.; Kummer, S.; Rami, F.; Plietker, B.; Hauer, B. Enzyme-Catalyzed Carbonyl Olefination by the E. Coli Protein YfeX in the Absence of Phosphines. *ChemCatChem* **2016**, *8* (9), 1636–1640. https://doi.org/10.1002/cctc.201600227.

(18) Li, Y.; Huang, J.-S.; Zhou, Z.-Y.; Che, C.-M.; You, X.-Z. Remarkably Stable Iron Porphyrins Bearing Nonheteroatom-Stabilized Carbene or (Alkoxycarbonyl)Carbenes: Isolation, X-Ray Crystal Structures, and Carbon Atom Transfer Reactions with Hydrocarbons. *J. Am. Chem. Soc.* **2002**, *124* (44), 13185–13193. https://doi.org/10.1021/ja020391c.

(19) Khade, R. L.; Fan, W.; Ling, Y.; Yang, L.; Oldfield, E.; Zhang, Y. Iron Porphyrin Carbenes as Catalytic Intermediates: Structures, Mössbauer and NMR Spectroscopic Properties, and Bonding. *Angew. Chem. Int. Ed.* **2014**, *53* (29), 7574–7578. https://doi.org/10.1002/anie.201402472.

(20) Liu, Y.; Xu, W.; Zhang, J.; Fuller, W.; Schulz, C. E.; Li, J. Electronic Configuration and Ligand Nature of Five-Coordinate Iron Porphyrin Carbene Complexes: An Experimental Study. *J. Am. Chem. Soc.* **2017**, *139* (14), 5023–5026. https://doi.org/10.1021/jacs.7b01722.

(21) Sharon, D. A.; Mallick, D.; Wang, B.; Shaik, S. Computation Sheds Insight into Iron Porphyrin Carbenes' Electronic Structure, Formation, and N–H Insertion Reactivity. *J. Am. Chem. Soc.* **2016**, *138* (30), 9597–9610. https://doi.org/10.1021/jacs.6b04636.

(22) Su, H.; Ma, G.; Liu, Y. Theoretical Insights into the Mechanism and Stereoselectivity of Olefin Cyclopropanation Catalyzed by Two Engineered Cytochrome P450 Enzymes. *Inorg. Chem.* **2018**, *57* (18), 11738–11745. https://doi.org/10.1021/acs.inorgchem.8b01875.

(23) Neese, F. The ORCA Program System. *Wiley Interdiscip. Rev. Comput. Mol. Sci.* **2012**, *2* (1), 73–78. https://doi.org/10.1002/wcms.81.

(24) Neese, F. Software Update: The ORCA Program System, Version 4.0. *Wiley Interdiscip. Rev. Comput. Mol. Sci.* **2018**, *8* (1), e1327. https://doi.org/10.1002/wcms.1327.

(25) Perdew, J. P. Density-Functional Approximation for the Correlation Energy of the Inhomogeneous Electron Gas. *Phys. Rev. B* **1986**, *33* (12), 8822–8824. https://doi.org/10.1103/PhysRevB.33.8822.

(26) Becke, A. D. Density-Functional Exchange-Energy Approximation with Correct Asymptotic Behavior. *Phys. Rev. A* **1988**, *38* (6), 3098–3100. https://doi.org/10.1103/PhysRevA.38.3098.

(27) Becke, A. D. Density-functional Thermochemistry. III. The Role of Exact Exchange. *J. Chem. Phys.* **1993**, *98* (7), 5648–5652. https://doi.org/10.1063/1.464913.

(28) Lee, C.; Yang, W.; Parr, R. G. Development of the Colle-Salvetti Correlation-Energy Formula into a Functional of the Electron Density. *Phys. Rev. B* **1988**, *37* (2), 785–789. https://doi.org/10.1103/PhysRevB.37.785.

(29) Curtiss, L. A.; McGrath, M. P.; Blaudeau, J.; Davis, N. E.; Binning, R. C.; Radom, L. Extension of Gaussian-2 Theory to Molecules Containing Third-row Atoms Ga–Kr. *J. Chem. Phys.* **1995**, *103* (14), 6104–6113. https://doi.org/10.1063/1.470438.

(30) Stoychev, G. L.; Auer, A. A.; Neese, F. Automatic Generation of Auxiliary Basis Sets. *J. Chem. Theory Comput.* **2017**, *13* (2), 554–562. https://doi.org/10.1021/acs.jctc.6b01041.

(31) Neese, F. An Improvement of the Resolution of the Identity Approximation for the Formation of the Coulomb Matrix. *J. Comput. Chem.* **2003**, *24* (14), 1740–1747. https://doi.org/10.1002/jcc.10318.

(32) Kossmann, S.; Neese, F. Comparison of Two Efficient Approximate Hartee–Fock Approaches. *Chem. Phys. Lett.* **2009**, *481* (4), 240–243. https://doi.org/10.1016/j.cplett.2009.09.073.

(33) Kossmann, S.; Neese, F. Efficient Structure Optimization with Second-Order Many-Body Perturbation Theory: The RIJCOSX-MP2 Method. *J. Chem. Theory Comput.* **2010**, *6* (8), 2325–2338. https://doi.org/10.1021/ct100199k.

(34) Izsák, R.; Neese, F. An Overlap Fitted Chain of Spheres Exchange Method. *J. Chem. Phys.* **2011**, *135* (14), 144105. https://doi.org/10.1063/1.3646921.

(35) Izsák, R.; Neese, F. Speeding up Spin-Component-Scaled Third-Order Pertubation Theory with the Chain of Spheres Approximation: The COSX-SCS-MP3 Method. *Mol. Phys.* **2013**, *111* (9–11), 1190–1195. https://doi.org/10.1080/00268976.2013.796071.

(36) Kitagawa, Y.; Saito, T.; Nakanishi, Y.; Kataoka, Y.; Matsui, T.; Kawakami, T.; Okumura, M.; Yamaguchi, K. Spin Contamination Error in Optimized Geometry of Singlet Carbene (^{1} A $_1$) by Broken-Symmetry Method †. *J. Phys. Chem. A* **2009**, *113* (52), 15041–15046. https://doi.org/10.1021/jp905125g.

(37) Angeli, C.; Borini, S.; Cestari, M.; Cimiraglia, R. A Quasidegenerate Formulation of the Second Order N-Electron Valence State Perturbation Theory Approach. *J. Chem. Phys.* **2004**, *121* (9), 4043–4049. https://doi.org/10.1063/1.1778711.

(38) Angeli, C.; Cimiraglia, R.; Evangelisti, S.; Leininger, T.; Malrieu, J.-P. Introduction of N-Electron Valence States for Multireference Perturbation Theory. *J. Chem. Phys.* **2001**, *114* (23), 10252–10264. https://doi.org/10.1063/1.1361246.

(39) Angeli, C.; Cimiraglia, R.; Malrieu, J.-P. N-Electron Valence State Perturbation Theory: A Fast Implementation of the Strongly Contracted Variant. *Chem. Phys. Lett.* **2001**, *350* (3), 297–305. https://doi.org/10.1016/S0009-2614(01)01303-3.

(40) Angeli, C.; Cimiraglia, R.; Malrieu, J.-P. N-Electron Valence State Perturbation Theory: A Spinless Formulation and an Efficient Implementation of the Strongly

Contracted and of the Partially Contracted Variants. *J. Chem. Phys.* **2002**, *117* (20), 9138–9153. https://doi.org/10.1063/1.1515317.

(41) Havenith, R. W. A.; Taylor, P. R.; Angeli, C.; Cimiraglia, R.; Ruud, K. Calibration of the N-Electron Valence State Perturbation Theory Approach. *J. Chem. Phys.* **2004**, *120* (10), 4619–4625. https://doi.org/10.1063/1.1645243.

(42) Schapiro, I.; Sivalingam, K.; Neese, F. Assessment of N-Electron Valence State Perturbation Theory for Vertical Excitation Energies. *J. Chem. Theory Comput.* **2013**, *9* (8), 3567–3580. https://doi.org/10.1021/ct400136y.

(43) Sivalingam, K.; Krupicka, M.; Auer, A. A.; Neese, F. Comparison of Fully Internally and Strongly Contracted Multireference Configuration Interaction Procedures. *J. Chem. Phys.* **2016**, *145* (5), 054104. https://doi.org/10.1063/1.4959029.

(44) Demel, O.; Pittner, J.; Neese, F. A Local Pair Natural Orbital-Based Multireference Mukherjee's Coupled Cluster Method. *J. Chem. Theory Comput.* **2015**, *11* (7), 3104–3114. https://doi.org/10.1021/acs.jctc.5b00334.

(45) Kendall, R. A.; Dunning, T. H.; Harrison, R. J. Electron Affinities of the First-row Atoms Revisited. Systematic Basis Sets and Wave Functions. *J. Chem. Phys.* **1992**, *96* (9), 6796–6806. https://doi.org/10.1063/1.462569.

(46) Weigend, F.; Köhn, A.; Hättig, C. Efficient Use of the Correlation Consistent Basis Sets in Resolution of the Identity MP2 Calculations. *J. Chem. Phys.* **2002**, *116* (8), 3175–3183. https://doi.org/10.1063/1.1445115.

(47) Hehre, W. J.; Ditchfield, R.; Pople, J. A. Self—Consistent Molecular Orbital Methods. XII. Further Extensions of Gaussian—Type Basis Sets for Use in Molecular Orbital Studies of Organic Molecules. *J. Chem. Phys.* **1972**, *56* (5), 2257–2261. https://doi.org/10.1063/1.1677527.

(48) Tao, J.; Perdew, J. P.; Staroverov, V. N.; Scuseria, G. E. Climbing the Density Functional Ladder: Nonempirical Meta--Generalized Gradient Approximation Designed for Molecules and Solids. *Phys. Rev. Lett.* **2003**, *91* (14), 146401. https://doi.org/10.1103/PhysRevLett.91.146401.

(49) Staroverov, V. N.; Scuseria, G. E.; Tao, J.; Perdew, J. P. Comparative Assessment of a New Nonempirical Density Functional: Molecules and Hydrogen-Bonded Complexes. *J. Chem. Phys.* **2003**, *119* (23), 12129–12137. https://doi.org/10.1063/1.1626543.

(50) Staroverov, V. N.; Scuseria, G. E.; Tao, J.; Perdew, J. P. Erratum: "Comparative Assessment of a New Nonempirical Density Functional: Molecules and Hydrogen-Bonded Complexes" [J. Chem. Phys. 119, 12129 (2003)]. *J. Chem. Phys.* **2004**, *121* (22), 11507. https://doi.org/10.1063/1.1795692.

(51) Kirmse, W. *Carbene Chemistry*, 2nd ed.; Academic Press: New York, 1971.

(52) Hoffmann, Roald.; Zeiss, G. D.; Van Dine, G. W. The Electronic Structure of Methylenes. *J. Am. Chem. Soc.* **1968**, *90* (6), 1485–1499. https://doi.org/10.1021/ja01008a017.

(53) Cremer, D. Density Functional Theory: Coverage of Dynamic and Non-Dynamic Electron Correlation Effects. *Mol. Phys.* **2001**, *99* (23), 1899–1940. https://doi.org/10.1080/00268970110083564.

(54) Albright, T. A.; Burdett, J. K.; Whangbo, M.-H. *Orbital Interactions in Chemistry*, 2nd edition.; Wiley-Interscience: Hoboken, New Jersey, 2013.

(55) Moore, C. E. *Atomic Energy Levels as Derived from the Analyses of Optical Spectra: The Spectra of Hydrogen, Deuterium, Tritium, Helium, Lithium, Beryllium, Boron, Carbon, Nitrogen, Oxygen, Flourine, Neon, Sodium, Magnesium, Aluminum, Silicon, Phosphorus, Sulfur, Chlorine, Argon, Potassium, Calcium, Scandium, Titanium, and Vanadium*; US Department of Commerce, National Bureau of Standards, 1949; Vol. 1.

(56) Neese, F. Definition of Corresponding Orbitals and the Diradical Character in Broken Symmetry DFT Calculations on Spin Coupled Systems. *J. Phys. Chem. Solids* **2004**, *65* (4), 781–785. https://doi.org/10.1016/j.jpcs.2003.11.015.

(57) Dzik, W. I.; Xu, X.; Zhang, X. P.; Reek, J. N. H.; de Bruin, B. 'Carbene Radicals' in CoII(Por)-Catalyzed Olefin Cyclopropanation. *J. Am. Chem. Soc.* **2010**, *132* (31), 10891–10902. https://doi.org/10.1021/ja103768r.

(58) Dzik, W. I.; Zhang, X. P.; de Bruin, B. Redox Noninnocence of Carbene Ligands: Carbene Radicals in (Catalytic) C−C Bond Formation. *Inorg. Chem.* **2011**, *50* (20), 9896–9903. https://doi.org/10.1021/ic200043a.

(59) Das, B. G.; Chirila, A.; Tromp, M.; Reek, J. N. H.; de Bruin, B. CoIII–Carbene Radical Approach to Substituted 1H-Indenes. *J. Am. Chem. Soc.* **2016**, *138* (28), 8968–8975. https://doi.org/10.1021/jacs.6b05434.

(60) te Grotenhuis, C.; Das, B. G.; Kuijpers, P. F.; Hageman, W.; Trouwborst, M.; de Bruin, B. Catalytic 1,2-Dihydronaphthalene and E-Aryl-Diene Synthesis via CoIII–Carbene Radical and o-Quinodimethane Intermediates. *Chem. Sci.* **2017**, *8* (12), 8221–8230. https://doi.org/10.1039/C7SC03909C.

(61) te Grotenhuis, C.; de Bruin, B. Radical-Type Reactions Controlled by Cobalt: From Carbene Radical Reactivity to the Catalytic Intermediacy of Reactive o-Quinodimethanes. *Synlett* **2018**, *29* (17), 2238–2250. https://doi.org/10.1055/s-0037-1610204.

(62) te Grotenhuis, C.; van den Heuvel, N.; van der Vlugt, J. I.; de Bruin, B. Catalytic Dibenzocyclooctene Synthesis via Cobalt(III)–Carbene Radical and Ortho-Quinodimethane Intermediates. *Angew. Chem. Int. Ed.* **2018**, *57* (1), 140–145. https://doi.org/10.1002/anie.201711028.

(63) Karns, A. S.; Goswami, M.; de Bruin, B. Catalytic Synthesis of Indolines by Hydrogen Atom Transfer to Cobalt(III)-Carbene Radicals. *Chem. - Eur. J.* **2018**, *24* (20), 5253–5258. https://doi.org/10.1002/chem.201704626.

(64) Li, X.; Dong, L.; Liu, Y. Theoretical Study of Iron Porphyrin Nitrene: Formation Mechanism, Electronic Nature, and Intermolecular C–H Amination. *Inorg. Chem.* **2020**, *59* (3), 1622–1632. https://doi.org/10.1021/acs.inorgchem.9b02216.

Chapter 4

MULTIREFERENCE DESCRIPTION OF NICKEL–ARYL HOMOLYTIC BOND DISSOCIATION PROCESSES IN PHOTOREDOX CATALYSIS

Adapted with permission from:

Cagan, D. A.[†]; Stroscio, G. D.[†]; Cusumano, A. Q.; Hadt, R. G. Multireference Description of Nickel–Aryl Homolytic Bond Dissociation Processes in Photoredox Catalysis. *J. Phys. Chem. A* **2020**, *124* (48), 9915-9922. https://doi.org/10.1021/acs.jpca.0c08646.

[†]Co-first author. *Corresponding author.

Abstract

Multireference electronic structure calculations consistent with known experimental data have elucidated a novel mechanism for photo-triggered Ni(II)–C homolytic bond dissociation in Ni 2,2’-bipyridine (bpy) photoredox catalysts. Previously, a thermally assisted dissociation from the lowest energy triplet ligand field excited state was proposed and supported by density functional theory (DFT) calculations that reveal a barrier of ~30 kcal mol^{-1}. In contrast, multireference *ab initio* calculations suggest this process is disfavored, with barrier heights of ~70 kcal mol^{-1}, and highlight important ligand noninnocent and multiconfigurational contributions to excited state relaxation and bond dissociation processes that are not captured with DFT. In the multireference description, photo-triggered Ni(II)–C homolytic bond dissociation occurs via initial population of a singlet Ni(II)-to-bpy metal-to-ligand charge transfer (^{1}MLCT) excited state followed by intersystem crossing and aryl-to-Ni(III) charge transfer, overall a formal two-electron transfer process driven by a single photon. This results in repulsive triplet excited states from which spontaneous homolytic bond dissociation can occur, effectively competing with relaxation to the lowest energy, nondissociative triplet Ni(II) ligand field excited state. These findings guide important electronic structure considerations for the experimental and computational elucidation of the mechanisms of ground and excited state cross-coupling catalysis mediated by Ni heteroaromatic complexes.

4.1. Introduction

Merging thermal catalysis with photochemistry (i.e., photoredox catalysis) has provided new, more sustainable routes to bond activations and coupling reactions in organic synthesis.[1–10] An extension of solar energy conversion, photoredox catalysis utilizes photosensitizers to harvest photon energy and transform it into chemical potential to drive single electron transfer (SET) processes to generate reactive high- and/or low-valent species and important organic radicals. However, photoredox reactions feature complex mechanisms that are challenging to elucidate, and our understanding of how photon energy drives organic transformations is therefore still growing.

Beyond SET, photosensitized energy transfer can form photocatalyst excited states that can be uniquely reactive relative to ground states.[11–16] The photocatalyst can also potentially act as both the light-absorbing and catalytic unit through direct excitation.[17,18] In direct excitation and energy transfer mediated catalysis, the ultrafast photophysical processes of transition metal excited state relaxation can also contribute to reactivity.[9] Notably, Ni(II) complexes of 2,2’-bipyridine (bpy) exhibit photocatalytic activity for coupling reactions using either energy transfer[11,19] or direct excitation.[20] Several mechanistic hypotheses have been discussed and are summarized in Figure 4.1. In one scenario, energy transfer to a Ni(II)-bpy aryl acetate complex induces reductive elimination from a triplet excited state of Ni(II) (Figure 4.1A, bottom), originally proposed to be ligand field in nature.[11] Ni(II)-to-bpy metal-to-ligand charge transfer (MLCT) excited states have also been suggested to: (1) mediate bimolecular electron transfer to generate Ni(I) and Ni(III) species for catalysis,[17] or (2) directly mediate reductive elimination.[21] The latter consideration encompasses the one-electron oxidatively induced ground state formal Ni(III) reactivity discovered by Hillhouse and co-workers.[22,23]

Thermally assisted homolytic Ni(II)–C bond dissociation from photochemically formed triplet ligand field excited states in Ni(II)-bpy aryl halide complexes has also been proposed.[18] This process results in the formation of formal Ni(I) and aryl radicals (Figure 4.1A, top). While it is unclear whether these species initiate a subsequent Ni(I)/Ni(III) catalytic cycle, this represents an intriguing means to photochemically generate reduced Ni species and organic radicals for ground state thermal catalysis.[18,20] Overall, more detailed experimental and theoretical descriptions of the ground state bonding and excited state relaxation processes in Ni-bpy complexes (and other Ni heteroaromatic complexes[24]) are critical for developing synthetic applications.

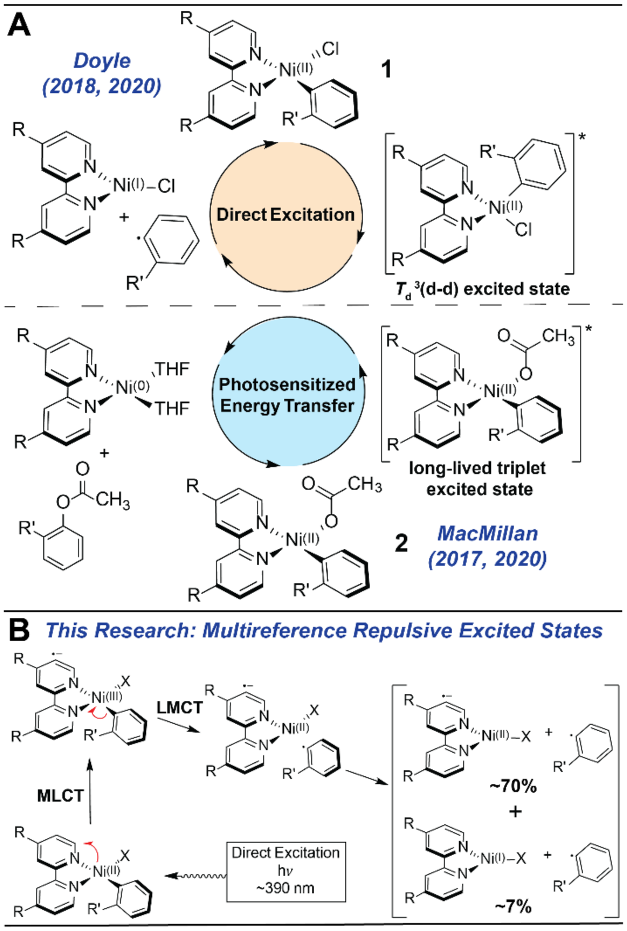

Figure 4.1. Proposed Mechanisms. (A) Two previous mechanistic hypotheses related to Ni-bpy photoredox catalysis and (B) findings in this study. Complex **1** = Ni(II)($^{\text{t-Bu}}$bpy)(*o*-tolyl)Cl; Complex **2** = Ni(II)(bpy)(ph)(ac) (ph = phenyl, ac = acetate).

Here we describe a new electronic structural framework to interpret experimental data on Ni(II)-bpy complexes of relevance to photoredox catalysis. Of particular importance is the multireference description (relative to density functional theory (DFT)), which manifests in multiconfigurational ground and excited state wave functions and potential energy surfaces (PESs) in Ni(II)–C homolytic bond dissociation. Intractable barriers are found for thermal bond dissociation from the lowest energy triplet ligand field excited state within the multireference framework. However, higher energy repulsive triplet excited states are found here and are proposed to be responsible for homolytic bond dissociation. These triplet excited states feature a high-spin Ni(II) coupled to anionic bpy and neutral aryl radicals and can be generated from initial ^{1}MLCT excitation (Ni(II)-to-bpy) followed by intersystem crossing and intramolecular charge transfer (aryl-to-Ni(III)) (Figure 4.1B).

4.2. Computational Methods

Calculations were performed using ORCA[25,26] version 4.2.1. The BP86[27–29] functional was used for geometry optimizations and frequency calculations, including both full geometry optimizations and constrained optimizations where the Ni–C bond length was systematically varied. The 6-311G(d)[30] basis set was used on all atoms, and AutoAux[31] was used as the auxiliary basis set. Split-RI-J, the default and recommended version of resolution of identities[32–35] (RI) approximation was used. The finest available DFT grids were used (GRID7 NOFINALGRID). Very tight SCF convergence criteria, which has a convergence tolerance of 10^{-9} Hartrees, was applied for all DFT calculations. The restricted Kohn-Sham formalism (RKS) was used for the singlet ground state optimizations; the unrestricted Kohn-Sham formalism (UKS) was used for the triplet optimizations. Additional single point calculations using the B3LYP[28,36] functional, the def2-TZVP[37] basis, and implicit solvation by tetrahydrofuran (THF) modeled by the conductor-like polarizable continuum model[38] (CPCM) were performed on optimized structures. Here the RIJCOSX[39] approximation was used with fine DFT grids (GRID7 NOFINALGRID GRIDX9). At this level of theory, broken-symmetry singlet (BSS) and unrestricted triplet single point calculations were performed on the S=0 and S=1 optimized geometries, respectively. Likewise, TDDFT calculations were performed using these same settings. Applying a Yamaguchi spin correction[40,41] did not significantly affect the BSS dissociations energies of **1** and **2**. It lowered the dissociation energy of **1** from 43.3 kcal mol^{-1} to 41.7 kcal mol^{-1} (Table C.1P); it barely changed the dissociation energy of **2** from 44.9 kcal mol^{-1} to 45.1 kcal mol^{-1} (Table C.2L). Sample input DFT and TDDFT parameters are given in Appendix C.

Quasidegenerate N-electron valence state second-order perturbation theory[42] (QD-NEVPT2) corrected complete active space self-consistent field (CASSCF) single point calculations were performed on DFT optimized geometries. Tight SCF convergence criteria with an energy tolerance of 10^{-7} Hartrees were applied. The def2-TZVP basis set was used on all atoms, and the RIJCOSX approximation was employed. Note that the number of states averaged was varied (see Tables C.1G-1 – C.1G-3), and it was found that a state-averaging with fifteen singlets and twenty-five triplets yielded a thorough description of the ground and excited states of interest while maintaining reasonable computational costs. Therefore, state-averaged CASSCF/QD-NEVPT2 single point calculations utilized fifteen singlets and twenty-five triplets throughout. The recommended Nakano formalism was used, and the corresponding CI-vectors are tabulated in Appendix C. A comparison between gas phase and solvent corrected CASSCF/QD-NEVPT2 single point calculations yielded qualitatively similar results at both the singlet equilibrium geometry and at longer Ni–C distances (3.2 Å for **1** and 3.1 Å for **2**); therefore, gas phase calculations were conducted on all structures (comparisons are tabulated in Appendix C). Sample input files for CASSCF/QD-NEVPT2 calculations are given in Appendix C.

The size of the active space was varied until a thorough description of **1** and **2** was reached (comparisons between active space sizes are tabulated in Appendix C). Active spaces are shown in Figures C.1C and C.1E for **1** (S=0 and S=1) and Figure C.2C and C.2E for **2** (S=0 and S=1). The first 10-20 lowest energy roots, CI vectors, transitions, and oscillator strengths are tabulated in Appendix C. An active space consisting of nine orbitals filled with ten electrons (9o/10e): d(xy), d(z^2), d(xz), d(yz), a pair of bonding and antibonding orbitals from the d(x^2-y^2) and the C(sp^2) orbital on the dissociating phenyl group, and three π* orbitals on the bipyridine ligand, were found to be thorough descriptors of the S=0 equilibrium geometry of **1**, while an additional orbital was added for **2**. The additional orbital in **2** is a bonding d(xy)/C(π) orbital (see Figure C.2C), which was kept in the active space due to its partially unfilled occupancy of 1.93 (for compound **1**, this orbital has occupancy of ~2 (1.99), and thus was not needed to generate a complete active space). However, as can be seen in Table C.2C1-3, the additional orbital in **2** was not involved in any critical transitions. At all other Ni–C bond lengths, the third bpy π* orbital exhibited very low occupancy and was removed to aid convergence. For example, the ten electrons in nine orbitals CASSCF calculation using the 3.6 Å geometry of **1**, the third π* orbital had an extremely low active space occupancy value of 0.00004.

As the Ni–C bond was elongated and eventually cleaved, the molecular geometry along the singlet surface approached that of the optimized triplet surface. This observation is particularly clear for **2**. The active space for the triplet scan of **1** again consisted of the ten electrons in eight orbitals (active space with the third π* removed, Figure C.1E). Here the third bpy π* again had very low active space occupancy values (~0.0001). This was true in geometries ranging from 2.0 Å to 3.6 Å. For triplet structures of **1** with a short Ni–C bond (between 1.6-2.0 Å), the second π* orbital was similarly removed to aid convergence. For the triplet scan of **2**, it was possible to use an active space of ten electrons in nine orbitals active space for the entire scan (Figure C.2E).

4.3. Results and Discussion

Homolytic bond dissociation is an inherently multiconfigurational process that can pose difficulties for DFT.[43,44] Analyses therefore began by comparing the ground state wave functions of Ni(II)($^{t\text{-}Bu}$bpy)(*o*-tolyl)Cl (**1**) and Ni(II)(bpy)(ph)(ac) (ph = phenyl, ac = acetate) (**2**), as well as their lowest energy singlet and triplet bond dissociation energies (BDEs) using both DFT and multireference *ab initio* calculations (i.e., CASSCF/QD-NEVPT2[42]) within ORCA.[25,26]

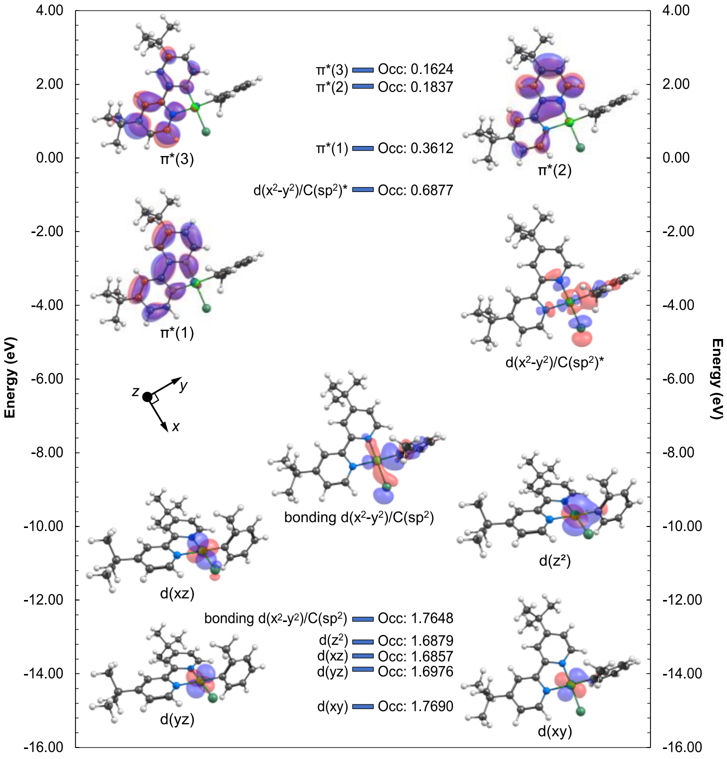

Figure 4.2. Simplified MO diagram of **1** as calculated by CASSCF/QD-NEVPT2 using a nine orbital, ten electron active space. Natural orbitals energies are plotted; orbital occupancies are labeled.

CASSCF/QD-NEVPT2 calculations on **1** and **2** exhibit appreciable ground state multiconfigurational character (Figures C.1C/C.2C and Tables C.1C/C.2C-1). Using a nine orbital, ten electron active space (Figure 4.2, C.1C), the dominant contributions to the configuration interaction (CI) vector of the singlet ground state of **1** are ~58 % low-spin d^8 (closed shell singlet, CSS) and ~22 % ^{1}MLCT (Table C.1E). Similar values are obtained for **2** (~57% CSS and ~23 % ^{1}MLCT) (Table C.2D-2). With only an eight electron, five 3d-orbital active space, the low-spin d^8 character increases to ~95 % in both **1** and **2** (Table C.1A-2/C.2B-2). Thus, the unoccupied bpy π* orbitals, which have relatively large active space occupancies (Figure 4.2), play a critical role in the degree of multiconfigurational ground state bonding.

It is interesting to consider the multireference data in the context of the DFT bonding description. The low-spin $d(x^2-y^2)$ ground states of **1** and **2** are highly covalent (~56/57 % Ni(II) and ~11/13 % bpy character), with some back-bonding (~7-8 % occupied Ni(II) character in the bpy-based unoccupied π* orbitals of both **1** and **2**) (Figure C.1B/C.2B). This highly covalent bonding framework is not particularly amenable to formal redox state assignment and is more consistent with a multiconfigurational bonding description.[45,46]

PESs for Ni(II)–C bond dissociations from **1** and **2** are given in Figures 4.3A and C.2G, respectively. The DFT BDEs are ~43 kcal mol^{-1} and ~31 kcal mol^{-1} starting from the relaxed, lowest energy singlet and triplet structures of **1**, respectively, consistent with the ~32 kcal mol^{-1} from a study invoking thermal homolysis on the triplet PES.[18] Values for **2** are similar (~45 kcal mol^{-1} and ~38 kcal mol^{-1}). The multireference bond dissociation is fundamentally different than DFT, with significantly higher BDEs (~87/65 kcal mol^{-1} and

73/70 kcal mol^{-1} from the lowest energy singlet and triplet states of **1**/**2**), suggesting that the Ni(II)–C bonds are stronger than in DFT and will not be thermally cleaved, even upon formation of the relaxed lowest energy triplet ligand field excited state. This difference is important, as the ~30 kcal mol^{-1} barrier was used to rationalize photochemical formation of radicals and reduced Ni species from **1**.[18]

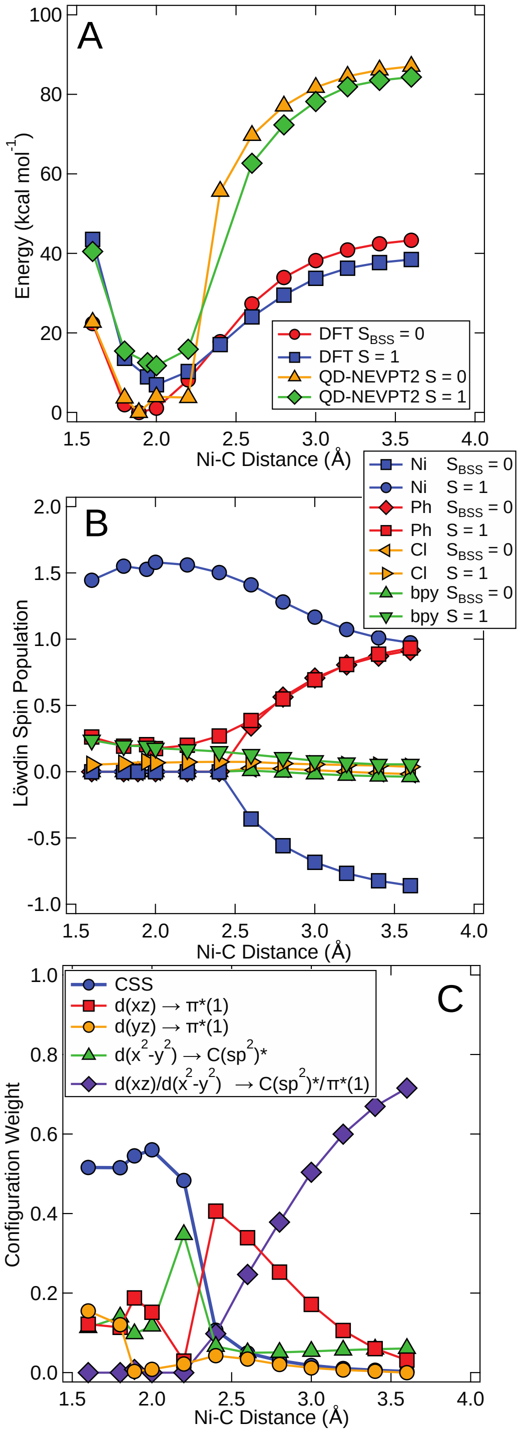

Figure 4.3. Ni(II)–C bond dissociation from the lowest energy singlet and triplet states in **1**. (A) Relaxed DFT vs CASSCF/QD-NEVPT2 PESs and (B) DFT Löwdin spin densities for both the singlet (BSS) and triplet states and (C) the CASSCF/QD-NEVPT2 lowest energy singlet CI vector.

From Löwdin spin density plots in Figures 4.3B and C.2H, the DFT-based homolytic bond dissociation results in the formation of Ni(I) and neutral aryl radicals for **1** and **2**. The compositions of the multiconfigurational ground state CI vectors of **1** and **2** upon bond dissociation from the singlet ground state are given in Figures 4.3C and C.2I, respectively, and describe the nature of bond homolysis. Upon initial elongation of the Ni–C bond, the amount of low-spin d^8 character (CSS) decreases significantly, with a concomitant increase in the weighting of ^{1}MLCT character at 2.4 Å, beyond which the CI vector becomes dominantly $d(xz)/d(x^2\text{-}y^2) \rightarrow C(sp^2)^*/\pi^*$, formally corresponding to a high-spin Ni(II) coupled to anionic bpy and neutral aryl radicals. Some additional formal Ni(I) character is also present (~7 %). Independent DFT vs multireference calculations on the formal Ni(I) species after homolytic bond dissociation (Figure 4.4) further support this description. Notably, similar ligand redox has been observed for reduced formal Ni(I) species in ground state cross-coupling reactions.[24,47]

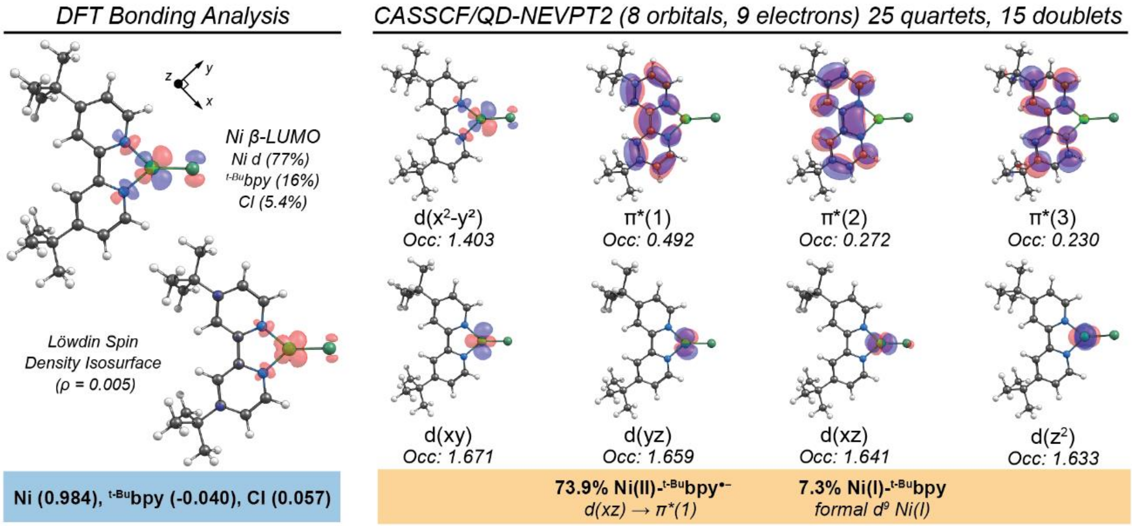

Figure 4.4. DFT (left) vs CASSCF/QD-NEVPT2 (right) description of the formal Ni(I) species formed upon homolytic Ni–C bond cleavage.

Given the intractability of thermally assisted Ni(II)–C homolysis and radical formation from the lowest energy triplet ligand field excited states, we now further describe the excited state PESs/manifolds of **1** and **2** to develop new understanding of the mechanism of homolytic bond dissociation. TDDFT and CASSCF/QD-NEVPT2 calculated excited state manifolds at the ground state singlet relaxed structures of **1** and **2** are given in Figure C.1G and Tables C.1I-K, C.2A, and C.2C. Both methods predict a set of lower and higher energy ^{1,3}MLCTs. However, their relative oscillator strengths differ somewhat from one another and, for **1**, the experimental spectrum.

The CASSCF/QD-NEVPT2 ground and excited state PESs along the Ni(II)–C coordinate of **1** and **2** are given in Figure 4.5 and C.2J, respectively, while the analogous TDDFT PESs are given in Figure C.1F and C.2K, respectively. From Figure 4.5, repulsive excited states are present (left panel: black, red, and yellow lines). The higher energy MLCT excited states (**A** in Figure 4.5, left) cross the repulsive surfaces at Ni–C bond distances of ~2.3–2.4 Å (circled in Figure 4.5) in both **1** and **2** with an activation energy from the Franck-Condon point of ~25 kcal mol^{-1}. Thus, the multireference approach predicts that homolytic bond dissociation occurs via population of a ^{1}MLCT excited state (Ni(II)-to-bpy) followed by an intersystem crossing and intramolecular charge transfer (aryl-to-Ni(III)) (Figure 4.1B), where the intersystem crossing could occur between the ^{1,3}MLCT states or the ^{1}MLCT and dissociative triplet state. The resulting multiconfigurational species can be described as a high-spin Ni(II) with antiferromagnetically coupled electrons on the bpy and phenyl ligands (see Appendix C Tables C.1Q-R and C.2M-N for more details). Interestingly, this description of excited state bond homolysis is conceptually similar to that given for the mixed

MLCT/σπ* (sigma bond to ligand charge transfer) photoinduced radical formation in Re(I) and Ru(II) complexes.[48–57] Overall, this represents a novel homolytic bond dissociation mechanism in nickel catalysis, which we propose derives from the redox noninnocent and multiconfigurational ground and excited state bonding in Ni(II)-bpy complexes.

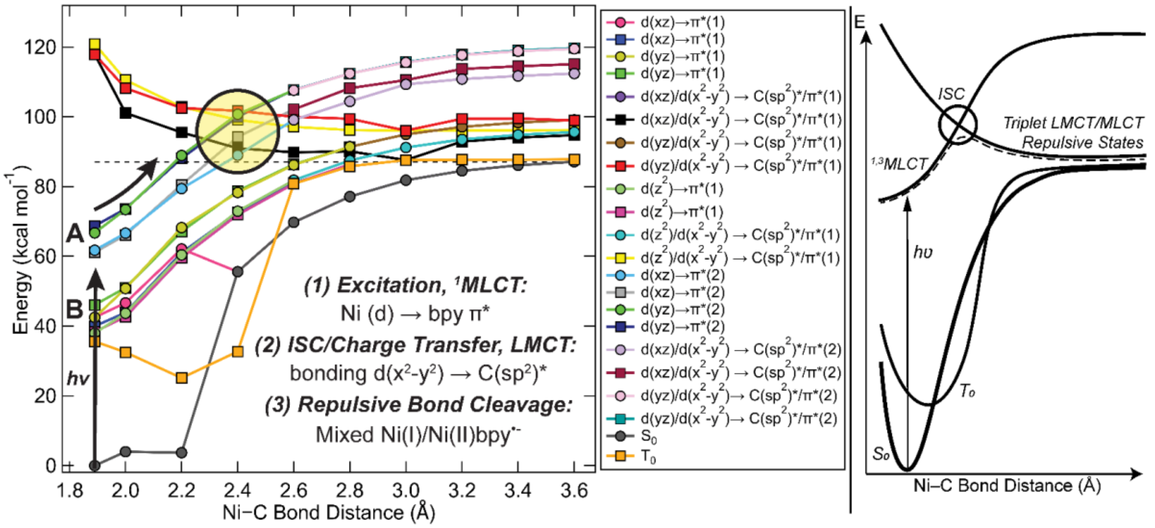

Figure 4.5. CASSCF/QD-NEVPT2 relaxed ground and excited state PESs along the Ni–C coordinate of **1**. Left: Vertical excitation (black vertical arrow), the higher (A) and lower energy (B) manifolds of MLCTs, and the crossings between the higher energy MLCTs and repulsive triplets (circled) are depicted. Singlet states, circles; triplets, squares. Right: Simplified depiction of the UV light photoinduced Ni–C bond homolysis process.

Experimentally, the lowest energy triplet ligand field excited states of Ni(II)-bpy aryl halide complexes are populated in ~5-10 ps.[18] Given an estimated Ni(II)–C frequency of ~250 cm^{-1}, ~40-80 vibrational periods could occur to drive intersystem and surface crossings that could compete with a population of the lowest energy triplet ligand field state. A higher energy aryl vibration (~650 cm^{-1}; Figures C.1I/C.2L for **1** and **2**, respectively) exhibiting significant changes in Ni–C bond distance may also provide ~100-200 vibrational periods to drive these processes.

The yield of the cross-coupled product obtained from direct excitation of **1** is incident light dependent; high yields are only observed with UV light (390-395 nm or ~70 kcal mol^{-1}),[20] corresponding to excitation into the higher energy manifold of MLCT states (Figure 4.5). Of particular relevance to compound **2**, variations in the energy of the photosensitizer triplet state demonstrated C–O coupling occurs when ~40-45 kcal mol^{-1} is transferred to the Ni catalyst.[11] This energy would excite complexes to the lower energy manifold of MLCT states (Figure 4.5, C.2J), resulting in thermodynamically unfavorable radical formation (~45 kcal mol^{-1}) for both **1** and **2**. Thus, an alternative relaxation pathway and mechanism may exist for photosensitized cross-coupling. In fact, triplet ligand field excited state formation, reductive elimination, and homolytic bond dissociation may all be possible for a given Ni(II)-bpy complex. We believe the ligands in addition to bpy will be of particular importance in determining the relative propensity for specific relaxation pathways. For example, reductive elimination is disfavored for the aryl halide (**1**) relative to the aryl carboxylate (**2**). This may preferentially lead to excited state processes that favor the formation of radicals and ligand field excited states over an intractable photosensitized or direct excitation induced reductive elimination.

4.4. Conclusions

In summary, we have provided a new electronic structural framework to interpret UV light-induced homolytic bond dissociation in Ni(II)-bpy complexes of relevance for photoredox catalysis. Compared to DFT, multireference *ab initio* calculations predict: (1) thermal homolysis from the lowest energy triplet ligand field excited state is not energetically favorable (barriers: DFT ~30 kcal mol^{-1}, CASSCF/QD-NEVPT2 ~70 kcal mol^{-1}), (2) initial population of a Ni(II)-to-bpy ^{1}MLCT excited state can be followed by intersystem crossing and aryl-to-Ni(III) intramolecular charge transfer, resulting in the formation of repulsive triplet excited states described as a high-spin Ni(II) coupled to anionic bpy and neutral aryl radicals. Formally, this represents an overall two-electron transfer process driven by a single photon. The formation of repulsive excited states likely also competes with relaxation to the experimentally observed triplet ligand field excited state, which further relaxes to the ground state without radical formation. (3) The immediate products of homolytic bond dissociation are not Ni(I)-bpy and an aryl radical as described by DFT, but rather a multiconfigurational species with a dominantly high-spin Ni(II) coupled to a redox active bpy anion radical ligand, similar to descriptions for formal Ni(I) intermediates in ground state thermal cross-coupling catalysis.[24,47]

REFERENCES

(1) Nicewicz, D. A.; MacMillan, D. W. C. Merging Photoredox Catalysis with Organocatalysis: The Direct Asymmetric Alkylation of Aldehydes. *Science* **2008**, *322* (5898), 77–80. https://doi.org/10.1126/science.1161976.

(2) Prier, C. K.; Rankic, D. A.; MacMillan, D. W. C. Visible Light Photoredox Catalysis with Transition Metal Complexes: Applications in Organic Synthesis. *Chem. Rev.* **2013**, *113* (7), 5322–5363. https://doi.org/10.1021/cr300503r.

(3) Shaw, M. H.; Twilton, J.; MacMillan, D. W. C. Photoredox Catalysis in Organic Chemistry. *J. Org. Chem.* **2016**, *81* (16), 6898–6926. https://doi.org/10.1021/acs.joc.6b01449.

(4) Twilton, J.; Le, C. (Chip); Zhang, P.; Shaw, M. H.; Evans, R. W.; MacMillan, D. W. C. The Merger of Transition Metal and Photocatalysis. *Nat. Rev. Chem.* **2017**, *1* (7), 0052. https://doi.org/10.1038/s41570-017-0052.

(5) Cavalcanti, L. N.; Molander, G. A. Photoredox Catalysis in Nickel-Catalyzed Cross-Coupling. *Top. Curr. Chem.* **2016**, *374* (4), 39. https://doi.org/10.1007/s41061-016-0037-z.

(6) Milligan, J. A.; Phelan, J. P.; Badir, S. O.; Molander, G. A. Alkyl Carbon–Carbon Bond Formation by Nickel/Photoredox Cross-Coupling. *Angew. Chem. Int. Ed.* **2019**, *58* (19), 6152–6163. https://doi.org/10.1002/anie.201809431.

(7) Larsen, C. B.; Wenger, O. S. Photoredox Catalysis with Metal Complexes Made from Earth-Abundant Elements. *Chem. – Eur. J.* **2018**, *24* (9), 2039–2058. https://doi.org/10.1002/chem.201703602.

(8) Schultz, D. M.; Yoon, T. P. Solar Synthesis: Prospects in Visible Light Photocatalysis. *Science* **2014**, *343* (6174), 1239176. https://doi.org/10.1126/science.1239176.

(9) Arias-Rotondo, D. M.; McCusker, J. K. The Photophysics of Photoredox Catalysis: A Roadmap for Catalyst Design. *Chem. Soc. Rev.* **2016**, *45* (21), 5803–5820. https://doi.org/10.1039/C6CS00526H.

(10) Yoon, T. P.; Ischay, M. A.; Du, J. Visible Light Photocatalysis as a Greener Approach to Photochemical Synthesis. *Nat. Chem.* **2010**, *2* (7), 527–532. https://doi.org/10.1038/nchem.687.

(11) Welin, E. R.; Le, C.; Arias-Rotondo, D. M.; McCusker, J. K.; MacMillan, D. W. C. Photosensitized, Energy Transfer-Mediated Organometallic Catalysis through Electronically Excited Nickel(II). *Science* **2017**, *355* (6323), 380–385. https://doi.org/10.1126/science.aal2490.

(12) Ischay, M. A.; Anzovino, M. E.; Du, J.; Yoon, T. P. Efficient Visible Light Photocatalysis of [2+2] Enone Cycloadditions. *J. Am. Chem. Soc.* **2008**, *130* (39), 12886–12887. https://doi.org/10.1021/ja805387f.

(13) Lu, Z.; Yoon, T. P. Visible Light Photocatalysis of [2+2] Styrene Cycloadditions by Energy Transfer. *Angew. Chem. Int. Ed.* **2012**, *51* (41), 10329–10332. https://doi.org/10.1002/anie.201204835.

(14) Zhang, Z.; Rogers, C. R.; Weiss, E. A. Energy Transfer from CdS QDs to a Photogenerated Pd Complex Enhances the Rate and Selectivity of a Pd-Photocatalyzed Heck Reaction. *J. Am. Chem. Soc.* **2020**, *142* (1), 495–501. https://doi.org/10.1021/jacs.9b11278.

(15) Strieth-Kalthoff, F.; Glorius, F. Triplet Energy Transfer Photocatalysis: Unlocking the Next Level. *Chem* **2020**, *6* (8), 1888–1903. https://doi.org/10.1016/j.chempr.2020.07.010.

(16) Strieth-Kalthoff, F.; J. James, M.; Teders, M.; Pitzer, L.; Glorius, F. Energy Transfer Catalysis Mediated by Visible Light: Principles, Applications, Directions. *Chem. Soc. Rev.* **2018**, *47* (19), 7190–7202. https://doi.org/10.1039/C8CS00054A.

(17) Shields, B. J.; Kudisch, B.; Scholes, G. D.; Doyle, A. G. Long-Lived Charge-Transfer States of Nickel(II) Aryl Halide Complexes Facilitate Bimolecular Photoinduced Electron Transfer. *J. Am. Chem. Soc.* **2018**, *140* (8), 3035–3039. https://doi.org/10.1021/jacs.7b13281.

(18) Ting, S. I.; Garakyaraghi, S.; Taliaferro, C. M.; Shields, B. J.; Scholes, G. D.; Castellano, F. N.; Doyle, A. G. ^{3}d-d Excited States of Ni(II) Complexes Relevant to Photoredox Catalysis: Spectroscopic Identification and Mechanistic Implications. *J. Am. Chem. Soc.* **2020**, *142* (12), 5800–5810. https://doi.org/10.1021/jacs.0c00781.

(19) Kim, T.; McCarver, S. J.; Lee, C.; MacMillan, D. W. C. Sulfonamidation of Aryl and Heteroaryl Halides through Photosensitized Nickel Catalysis. *Angew. Chem. Int. Ed.* **2018**, *57* (13), 3488–3492. https://doi.org/10.1002/anie.201800699.

(20) Yang, L.; Lu, H.-H.; Lai, C.-H.; Li, G.; Zhang, W.; Cao, R.; Liu, F.; Wang, C.; Xiao, J.; Xue, D. Light-Promoted Nickel Catalysis: Etherification of Aryl Electrophiles with Alcohols Catalyzed by a NiII-Aryl Complex. *Angew. Chem. Int. Ed.* **2020**, *59* (31), 12714–12719. https://doi.org/10.1002/anie.202003359.

(21) Ma, P.; Wang, S.; Chen, H. Reactivity of Transition-Metal Complexes in Excited States: C–O Bond Coupling Reductive Elimination of a Ni(II) Complex Is Elicited by the Metal-to-Ligand Charge Transfer State. *ACS Catal.* **2020**, *10* (1), 1–6. https://doi.org/10.1021/acscatal.9b03827.

(22) Koo, K.; Hillhouse, G. L. Carbon-Nitrogen Bond Formation by Reductive Elimination from Nickel(II) Amido Alkyl Complexes. *Organometallics* **1995**, *14* (9), 4421–4423. https://doi.org/10.1021/om00009a054.

(23) Han, R.; Hillhouse, G. L. Carbon−Oxygen Reductive-Elimination from Nickel(II) Oxametallacycles and Factors That Control Formation of Ether, Aldehyde, Alcohol, or Ester Products. *J. Am. Chem. Soc.* **1997**, *119* (34), 8135–8136. https://doi.org/10.1021/ja9714999.

(24) Jones, G. D.; Martin, J. L.; McFarland, C.; Allen, O. R.; Hall, R. E.; Haley, A. D.; Brandon, R. J.; Konovalova, T.; Desrochers, P. J.; Pulay, P.; Vicic, D. A. Ligand Redox Effects in the Synthesis, Electronic Structure, and Reactivity of an Alkyl−Alkyl Cross-Coupling Catalyst. *J. Am. Chem. Soc.* **2006**, *128* (40), 13175–13183. https://doi.org/10.1021/ja063334i.

(25) Neese, F. The ORCA Program System. *Wiley Interdiscip. Rev. Comput. Mol. Sci.* **2012**, *2* (1), 73–78. https://doi.org/10.1002/wcms.81.

(26) Neese, F. Software Update: The ORCA Program System, Version 4.0. *Wiley Interdiscip. Rev. Comput. Mol. Sci.* **2018**, *8* (1), e1327. https://doi.org/10.1002/wcms.1327.

(27) Perdew, J. P. Density-Functional Approximation for the Correlation Energy of the Inhomogeneous Electron Gas. *Phys. Rev. B* **1986**, *33* (12), 8822–8824. https://doi.org/10.1103/PhysRevB.33.8822.

(28) Becke, A. D. Density-Functional Exchange-Energy Approximation with Correct Asymptotic Behavior. *Phys. Rev. A* **1988**, *38* (6), 3098–3100. https://doi.org/10.1103/PhysRevA.38.3098.

(29) Becke, A. D. Density-functional Thermochemistry. III. The Role of Exact Exchange. *J. Chem. Phys.* **1993**, *98* (7), 5648–5652. https://doi.org/10.1063/1.464913.

(30) Curtiss, L. A.; McGrath, M. P.; Blaudeau, J.; Davis, N. E.; Binning, R. C.; Radom, L. Extension of Gaussian-2 Theory to Molecules Containing Third-row Atoms Ga–Kr. *J. Chem. Phys.* **1995**, *103* (14), 6104–6113. https://doi.org/10.1063/1.470438.

(31) Stoychev, G. L.; Auer, A. A.; Neese, F. Automatic Generation of Auxiliary Basis Sets. *J. Chem. Theory Comput.* **2017**, *13* (2), 554–562. https://doi.org/10.1021/acs.jctc.6b01041.

(32) Neese, F. An Improvement of the Resolution of the Identity Approximation for the Formation of the Coulomb Matrix. *J. Comput. Chem.* **2003**, *24* (14), 1740–1747. https://doi.org/10.1002/jcc.10318.

(33) Kossmann, S.; Neese, F. Comparison of Two Efficient Approximate Hartee–Fock Approaches. *Chem. Phys. Lett.* **2009**, *481* (4), 240–243. https://doi.org/10.1016/j.cplett.2009.09.073.

(34) Izsák, R.; Neese, F. An Overlap Fitted Chain of Spheres Exchange Method. *J. Chem. Phys.* **2011**, *135* (14), 144105. https://doi.org/10.1063/1.3646921.

(35) Izsák, R.; Neese, F. Speeding up Spin-Component-Scaled Third-Order Pertubation Theory with the Chain of Spheres Approximation: The COSX-SCS-MP3 Method. *Mol. Phys.* **2013**, *111* (9–11), 1190–1195. https://doi.org/10.1080/00268976.2013.796071.

(36) Lee, C.; Yang, W.; Parr, R. G. Development of the Colle-Salvetti Correlation-Energy Formula into a Functional of the Electron Density. *Phys. Rev. B* **1988**, *37* (2), 785–789. https://doi.org/10.1103/PhysRevB.37.785.

(37) Weigend, F.; Ahlrichs, R. Balanced Basis Sets of Split Valence, Triple Zeta Valence and Quadruple Zeta Valence Quality for H to Rn: Design and Assessment of Accuracy. *Phys. Chem. Chem. Phys.* **2005**, *7* (18), 3297–3305. https://doi.org/10.1039/B508541A.

(38) Barone, V.; Cossi, M. Quantum Calculation of Molecular Energies and Energy Gradients in Solution by a Conductor Solvent Model. *J. Phys. Chem. A* **1998**, *102* (11), 1995–2001. https://doi.org/10.1021/jp9716997.

(39) Kossmann, S.; Neese, F. Efficient Structure Optimization with Second-Order Many-Body Perturbation Theory: The RIJCOSX-MP2 Method. *J. Chem. Theory Comput.* **2010**, *6* (8), 2325–2338. https://doi.org/10.1021/ct100199k.

(40) Yamaguchi, K.; Takahara, Y.; Fueno, T.; Houk, K. N. Extended Hartree-Fock (EHF) Theory of Chemical Reactions. *Theor. Chim. Acta* **1988**, *73* (5), 337–364. https://doi.org/10.1007/BF00527740.

(41) Kitagawa, Y.; Saito, T.; Nakanishi, Y.; Kataoka, Y.; Matsui, T.; Kawakami, T.; Okumura, M.; Yamaguchi, K. Spin Contamination Error in Optimized Geometry of Singlet Carbene (^{1} A $_1$) by Broken-Symmetry Method. *J. Phys. Chem. A* **2009**, *113* (52), 15041–15046. https://doi.org/10.1021/jp905125g.

(42) Angeli, C.; Borini, S.; Cestari, M.; Cimiraglia, R. A Quasidegenerate Formulation of the Second Order N-Electron Valence State Perturbation Theory Approach. *J. Chem. Phys.* **2004**, *121* (9), 4043–4049. https://doi.org/10.1063/1.1778711.

(43) Bao, J. L.; Odoh, S. O.; Gagliardi, L.; Truhlar, D. G. Predicting Bond Dissociation Energies of Transition-Metal Compounds by Multiconfiguration Pair-Density Functional Theory and Second-Order Perturbation Theory Based on Correlated Participating Orbitals and Separated Pairs. *J. Chem. Theory Comput.* **2017**, *13* (2), 616–626. https://doi.org/10.1021/acs.jctc.6b01102.

(44) Cramer, C. J.; Truhlar, D. G. Density Functional Theory for Transition Metals and Transition Metal Chemistry. *Phys. Chem. Chem. Phys.* **2009**, *11* (46), 10757–10816. https://doi.org/10.1039/B907148B.

(45) Wilson, S. A.; Kroll, T.; Decreau, R. A.; Hocking, R. K.; Lundberg, M.; Hedman, B.; Hodgson, K. O.; Solomon, E. I. Iron L-Edge X-Ray Absorption Spectroscopy of Oxy-Picket Fence Porphyrin: Experimental Insight into Fe–O_2 Bonding. *J. Am. Chem. Soc.* **2013**, *135* (3), 1124–1136. https://doi.org/10.1021/ja3103583.

(46) Yan, J. J.; Kroll, T.; Baker, M. L.; Wilson, S. A.; Decréau, R.; Lundberg, M.; Sokaras, D.; Glatzel, P.; Hedman, B.; Hodgson, K. O.; Solomon, E. I. Resonant Inelastic X-Ray Scattering Determination of the Electronic Structure of Oxyhemoglobin and Its Model Complex. *Proc. Natl. Acad. Sci.* **2019**, *116* (8), 2854–2859. https://doi.org/10.1073/pnas.1815981116.

(47) Diccianni, J. B.; Diao, T. Mechanisms of Nickel-Catalyzed Cross-Coupling Reactions. *Trends Chem.* **2019**, *1* (9), 830–844. https://doi.org/10.1016/j.trechm.2019.08.004.

(48) Rossenaar, B. D.; Kleverlaan, C. J.; Stufkens, D. J.; Oskam, A. Photochemistry of $ReR(CO)_3(Pr^i\text{-Dab})$(R = Me, Et, Bn; Dab = 1,4-Diazabuta-1,3-Diene): Homolysis of the Re–R Bond, Its Dependence on R and Evidence for the Reactive $\sigma_b\pi^*$ State from Transient Absorption Spectra. *J. Chem. Soc. Chem. Commun.* **1994**, *1*, 63–64. https://doi.org/10.1039/C39940000063.

(49) Nieuwenhuis, H. A.; van de Ven, M. C. E.; Stufkens, D. J.; Oskam, A.; Goubitz, K. Photochemistry of $[Ru(I)(iPr)(CO)_2(iPr\text{-DAB})]$ (iPr-DAB = N,N’-Diisopropyl-1,4-Diaza-1,3-Butadiene): Homolysis of the Metal-Alkyl Bond from the σ_b(Ru-iPr) π^* State. Crystal Structure of the Photoproduct $[Ru(I)_2(CO)_2(iPr\text{-DAB})]$. *Organometallics* **1995**, *14* (2), 780–788. https://doi.org/10.1021/om00002a027.

(50) Rossenaar, B. D.; George, M. W.; Johnson, F. P. A.; Stufkens, D. J.; Turner, J. J.; Vlcek, A. First Direct Structural Information on a Reactive $\sigma_b\pi^*$ Excited State: Time-Resolved UV-Vis and IR Spectroscopic Study of $Re(Benzyl)(CO)_3(IPr\text{-DAB})$. *J. Am. Chem. Soc.* **1995**, *117* (46), 11582–11583. https://doi.org/10.1021/ja00151a025.

(51) Rossenaar, B. D.; Lindsay, E.; Stufkens, D. J.; Vlček, A. Properties and Dynamics of the σ(M′-Re) π* Excited State of Photoreactive Dinuclear $L_nM'\text{-}Re(CO)_3$(α-Diimine) (L_nM' = Ph_3Sn, $(CO)_5Mn$, $(CO)_5Re$; α-Diimine = Bpy′, iPr-PyCa, iPr-DAB) Complexes Studied by Time-Resolved Emission and Absorption Spectroscopies. *Inorganica Chim. Acta* **1996**, *250* (1), 5–14. https://doi.org/10.1016/S0020-1693(96)05203-6.

(52) Aarnts, M. P.; Wilms, M. P.; Stufkens, D. J.; Baerends, E. J.; Vlček, A. σ–π* Electronic Transition of the Di- and Trinuclear Complexes Ru(E)(E‘)$(CO)_2$(iPr-DAB): Resonance Raman, Electronic Absorption, Emission, and Density Functional Study (E = Me, $SnPh_3$, $M(CO)_5$; E‘ = $M(CO)_5$; M = Mn, Re; iPr-DAB = N,N‘-Diisopropyl-1,4-Diaza-1,3-Butadiene). *Organometallics* **1997**, *16* (10), 2055–2062. https://doi.org/10.1021/om9608667.

(53) Stufkens, D. J.; Aarnts, M. P.; Rossenaar, B. D.; Vlcek, A. A New Series of Re- and Ru-Complexes Having a Lowest $\sigma_b\pi^*$ Excited State That Varies from Reactive to Stable and Long Lived. *Pure Appl. Chem.* **1997**, *69* (4), 831–836. https://doi.org/10.1351/pac199769040831.

(54) Kleverlaan, C. J.; Martino, D. M.; van Slageren, J.; van Willigen, H.; Stufkens, D. J.; Oskam, A. FT-EPR Study of Alkyl Radicals Formed in the Photochemical Reaction of Re(Alkyl)(α-Diimine) and Ru(Alkyl)(α-Diimine) Complexes. *Appl. Magn. Reson.* **1998**, *15* (2), 203–214. https://doi.org/10.1007/BF03161872.

(55) Kleverlaan, C. J.; Stufkens, D. J.; Clark, I. P.; George, M. W.; Turner, J. J.; Martino, D. M.; van Willigen, H.; Vlček, A. Photoinduced Radical Formation from the Complexes [Re(R)$(CO)_3$(4,4‘-Me_2-Bpy)] (R = CH_3, CD_3, Et, ^{i}Pr, Bz): A Nanosecond Time-Resolved Emission, UV−Vis and IR Absorption, and FT-EPR Study. *J. Am. Chem. Soc.* **1998**, *120* (42), 10871–10879. https://doi.org/10.1021/ja980540k.

(56) Weinstein, J. A.; Slageren, J. van; Stufkens, D. J.; Záliš, S.; George, M. W. A Time-Resolved Infrared Spectroscopic Study of [M$(SnR_3)_2(CO)_2$(α-Diimine)] (M = Ru, Os; R = Ph, Me): Evidence of Charge Redistribution in the Lowest-Excited State. *J. Chem. Soc. Dalton Trans.* **2001**, No. 18, 2587–2592. https://doi.org/10.1039/B102450G.

(57) Stufkens, D. J.; Vlček, A. Ligand-Dependent Excited State Behaviour of Re(I) and Ru(II) Carbonyl–Diimine Complexes. *Coord. Chem. Rev.* **1998**, *177* (1), 127–179. https://doi.org/10.1016/S0010-8545(98)00132-5.

Appendix A

SUPPORTING INFORMATION FOR CHAPTER 2: QUANTIFYING ENTATIC STATES IN PHOTOPHYSICAL PROCESSES: APPLICATIONS TO COPPER PHOTOSENSITIZERS

Adapted with permission from:

Stroscio, G. D.; Ribson, R. D.; Hadt, R. G.* Quantifying Entatic States in Photophysical Processes: Applications to Copper Photosensitzers. *Inorg. Chem.* **2019**, *58* (24), 16800-16817. https://doi.org/10.1021/acs.inorgchem.9b02976.

*Corresponding author.

A.A. Methods

A.A.1. Synthesis and Electrochemistry

All syntheses were carried out at room temperature in a $N_{2(g)}$ atmosphere M. Braun glovebox. 1,10-phenanthroline and 2,9-dimethyl-1,10-phenanthroline were purchased from Combi-Blocks Inc. and used without further purification. $CDCl_3$ was purchased from Cambridge Isotope Laboratories. 2,9-di-*sec*-butyl-1,10-phenathroline[1], $[Cu(MeCN)_4][PF_6]$[2], $[Cu(phen)_2][PF_6]$, $[Cu(dmp)_2][PF_6]$, and $[Cu(dsbp)_2][PF_6]$[3] were synthesized according to literature procedures. Acetonitrile and diethyl ether were degassed by sparging with nitrogen for 15 minutes and then dried on a column of activated A2 alumina under positive nitrogen pressure. ^1H and ^{13}C NMR spectra were recorded on a Varian 400 MHz spectrometer.

$[Cu(mmp)_2][PF_6]$ was synthesized according to a modified literature procedure.[4] A solution of 2-methyl-1,10-phenanthroline (194.2 mg, 1.0 mmol) in MeCN (3 mL) was added to $[Cu(MeCN)_4][PF_6]$ (186.4 mg, 0.5 mmol) under $N_{2(g)}$ atmosphere. The deep red solution was then stirred for fifteen minutes and Et_2O (~20 mL) was added to precipitate the product, which was then recrystallized via slow vapor diffusion of Et_2O into a concentrated DCM solution of the product. The resulting crystals were collected and washed with Et_2O, yielding the product (% yield). ^1H NMR (400 MHz, $CDCl_3$): δ 2.48 (s, 6H), 7.81 (d, 2H), 7.88 (dd, 2H), 8.06 (m, 4H), 8.50 (d, 2H), 8.57 (d, 2H), 8.86 (d, 2H) ppm. ^{13}C NMR (400 MHz, $CDCl_3$) δ 25.99, 125.29, 125.94, 126.16, 127.06, 127.46, 129.59, 137.03, 137.24, 143.31, 143.71, 148.81, 158.02 ppm.

Cyclic Voltammetry was carried out with a Pine Instrument Company AFCBP1 biopotentiostat with the AfterMath software package. Measurements were performed in a three electrode cell, consisting of a glassy carbon working electrode (ø = 3.0 mm), a silver wire counter electrode, and a platinum wire reference electrode under a $N_{2(g)}$ atmosphere at room temperature in an M. Braun glovebox. Cyclic voltammograms were taken of 2 mM solutions of copper bis-phenanthroline complex and 0.1 M $[Bu_4N][PF_6]$ electrolyte in dry dichloromethane. The ferrocene/ferrocenium (Fc/Fc^+) redox couple or alternatively the decamethylferrocene/decamethylferrocinium (Fc^*/Fc^{*+}) were used as internal reference standards for all measurements. Those redox potentials referenced to Fc^*/Fc^{*+} could then be converted to potentials vs Fc/Fc^+ by using the measured difference in redox potentials of Fc^*/Fc^{*+} and Fc/Fc^+ under our conditions.

A.A.2. Spectroscopic Methods

A.A.2.1. Emission Spectra

Corrected 77 K Emission spectra were collected in the Beckman Institute Laser Resource Center using a modified Jobin Yvon Spec Fluorolog-3 instrument employing two Ocean Optics EQDPro CCD spectrometers spanning 300 to 930 nm for detection. Samples were excited with a xenon arc lamp, employing a monochromator for wavelength selection. 90

° emission spectra were detected with a photodiode array. Samples were prepared as 1 mM solutions in 1:1 Toluene/DCM and were degassed by sparging with $N_{2(g)}$ for 10 minutes prior to being added to an EPR tube and glassed at 77 K in liquid N_2 for the experiment. The glassed samples were then transferred to a vacuum-sealed double walled glass Dewar containing liquid $N_{2(g)}$. The sample compartment of the fluorimeter was purged with $N_{2(g)}$ for 10 min prior to introduction of the 77 K sample and $N_{2(g)}$ flow was maintained throughout the experiment to avoid condensation of moisture. The sample was positioned in the compartment such that the detected emission intensity was maximized.

A.A.2.2. 77 K Emission Spectra Gaussian Fitting

Emission spectra were fit to a minimum of three Gaussian peaks of equal full-width half-maximum using nonlinear least squares estimation of the coefficients with the non-linear regression fitting package in MATLAB. Reorganization energy was then calculated from the fitted full-width half-maximum values.[5]

A.A.2.2. Steady State and Transient Absorption Spectroscopy

Steady state absorption spectra were collected using a Varian Cary 500 Scan spectrophotometer with Varian Cary WinUV software (version 5.10(464)). Transient absorption spectra were collected using a setup consisting of the following three components: 1) a 1 kHz amplified Ti:sapphire system lasing at 800 nm (5 W, 35 fs, Astrella, Coherent), 2) an OPerA Solo optical parametric amplifier (OPA) tuned to 410 nm, and 3) a HELIOS FIRE automated femtosecond transient absorption spectrometer. Samples (purged with $N_{2(g)}$) were stirred in 2 mm pathlength quartz cuvettes during data acquisition to minimize any photodegradation. However, no photodegradation was observed over the course of three scans.

A.A.3. Computational Methods

All DFT calculations were carried out using ORCA[6,7], versions 4.0.0.2, 4.0.1.2, and 4.1.2. Geometry optimizations for reduced, oxidized, and ^{3}MLCT states were carried out using the BP86[8–10] functional (spin unrestricted formalism for oxidized and ^{3}MLCT states), in combination with split basis set: a 6-311G(d)[11] basis set on Cu and ligating atoms and 6-31G(d)[12] on all other atoms. Frequency calculations were carried out to ensure geometries and wavefunctions represented minima. For additional computational benchmarking, the TPSSh[13–15] and B3LYP[9,16] functionals were used, which allowed for benchmarking at HF exchange levels of 0 (BP86), 10 (TPSSh), and 20% (B3LYP). Single point energy calculations were carried out using the functionals mentioned above, but with a higher split basis set (6-311+G(d) for Cu and ligating atoms, and 6-311G(d) for all other atoms). Solvation effects were included using ORCA's conductor-like polarizable continuum model[17] (CPCM). These values are reported when there was not an apparent occurrence of ORCA's CPCM glich, which is possibly due to a problem in cavity-construction. All reported final single point energies were carried out on DFT grid 4; the resolutions of identities[18–23] (RI) approximation was used; Split-RI-J, the default and recommended implementation of RI for generalized gradient approximation functionals was used for BP86 and RIJCOSX, the recommended approximation for hybrid functionals, was used for TPSSh and B3LYP (GRIDX5). AutoAux[24] was used as the auxiliary basis set. All optimization and frequency calculations were carried out on at least DFT grid 4. All thermodynamic quantities have been obtained using the same numerical precision (same grid size). For all calculations, tight SCF convergence criteria were used, corresponding to a convergence tolerance in the energy change of 10^{-8} Hartree. SCF stability analyses showed that the obtained wavefunctions were stable. Also, $<S^2>$ data for the 2,9-alkyl triplets are tabulated below:

Species	**$<S^2>$**
bis-phen	2.002743
bis-mmp	2.002924
bis-dmp	2.002848
bis-dbp	2.002743
bis-dsbp	2.002774
bis-dnpp	2.002918
dmp-dtbp	2.002924
bis-dtbp	2.002783

For each species, the adiabatic ionization energy (IE) was found by taking the energy difference between the reduced (singlet) and oxidized (doublet) states in their equilibrium geometries. Calculated IEs were converted to *E*°s versus the Normal Hydrogen Electrode (NHE) by subtracting 4.44 eV from the IE.[25] This methodology has been employed elsewhere for calculating *E*°s.[26-28] Note that alternative approaches to using NHE have been reported, including referencing to the calculated value of the ferrocene (Fc/Fc+) couple.[29] As we are most interested in reproducing relative *E*°s, we have chosen to use the NHE corrected values instead of calculated values for the ferrocene (Fc/Fc+) couple, as this would correspond to a linear offset. Additionally, calibration against the bis-phen complex was not employed here due to experimental complications regarding *E*° from differential oxidation state stabilization, as described in Section 2.2.1.1 in Chapter 2. Given electronic energies have been used here to calculate potentials, entropic contributions have been neglected. However, these are likely to be relatively constant across this series of complexes. Beyond IE and *E*°, the ground state reorganization energy (λ_i) and excited state relaxation energy (γ_i) parameters were calculated. These metrics contain information regarding the curvature of PESs along a reaction coordinate. The λ_i value was obtained by taking $\lambda_{ox} + \lambda r_{ed}$ (where λ_{ox} = ox(red)-ox(ox), λ_{red} = red(ox)-red(red), where the notation is oxidation state(geometry) with "red" denoting the reduced (singlet) state and "ox" denoting the oxidized (doublet) state) (Figure A.1A). The γ_i value was likewise obtained by taking $\gamma_{trip} + \gamma_{red}$ (where γ_{trip} = trip(red)- trip(trip), γ_{red} = red(trip)-red(red), where the notation is spin state(geometry) with "trip" denoting the triplet state) (Figure A.1B).

A.B. Tables

Table A.1. Calculated *E*° (V vs. NHE) for capped 2,9-alkyl substituted bis-phen complexes.[a]

Ligand	**BP86 (V)**	**TPSSh (V)**	**B3LYP (V)**	**Experiment (V)**
phen	1.071	0.716	0.624	0.84
phen*	0.769	0.376	0.303	0.84
mmp	1.166	0.832	0.760	0.99
mmp*	1.037	0.681	0.604	0.99
dmp	1.272	0.968	0.892	1.19
dmp*	1.219	0.912	0.832	1.19
dbp	1.328	1.030	0.960	1.31
dnpp	1.255	0.951	0.872	1.31
dsbp	1.381	1.086	1.022	1.38
dmp-dtbp	1.454	1.183	1.153	
dtbp	1.549	1.308	1.309	1.40

[a] References are provided in Table 2.1 of Chapter 2.

Table A.2. Comparisons between excited state lifetimes and calculated ground state reorganization energies and excited state relaxation energies for capped 2,9-alkyl substituted bis-phen complexes.[a]

Ligand	**τ (ns)**	**ln(τ)**	**λ (eV)[b]**	**λ (eV)[c]**	**γ (eV)[b]**	**γ (eV)[c]**
phen	0.14	-1.97	0.994 (22.9)	1.064 (24.5)	1.434 (33.1)	1.428 (32.9)
phen*			1.067 (24.6)	1.222 (28.2)	1.391 (32.1)	1.411 (32.5)
mmp	2[d]	0.69	0.714 (16.5)	0.764 (17.6)	1.098 (25.3)	1.094 (25.2)
mmp*			0.812 (18.7)	0.920 (21.2)	1.169 (27.0)	1.169 (27.0)
dmp	90	4.50	0.509 (11.7)	0.551 (12.7)	0.891 (20.5)	0.893 (20.6)
dmp*			0.527 (12.2)	0.558 (12.9)	0.871 (20.1)	0.862 (19.9)
dbp	150	5.01	0.454 (10.5)	0.489 (11.3)	0.792 (18.3)	0.771 (17.8)
dnpp	260	5.56	0.345 (7.96)	0.371 (8.56)	0.646 (14.9)	0.644 (14.9)
dsbp	400	5.99	0.407 (9.39)	0.444 (10.2)	0.761 (17.5)	0.765 (17.6)
dmp-dtbp	730[e]	6.59	0.321 (7.40)	0.345 (7.96)	0.623 (14.4)	0.630 (14.5)
dtbp	3260	8.09	0.134 (3.09)	0.157 (3.62)	0.318 (7.33)	0.304 (7.01)

[a] Unless indicated, lifetimes were taken from Table 1 of ref. 21 in Chapter 2 and references cited therein. Parenthetical values in kcal/mol.

[b] Gas phase

[c] CPCM corrected

[d] This work

[e] Reference 92 of Chapter 2.

Table A.3. Regression analyses (95% CI) for the correlation with experimental ln(τ).

		Coefficients	Standard Error	Lower 95%	Upper 95%
ln(τ) vs. $E^{\circ a}$	y-int.	0.9616	0.0271	0.8919	1.0313
	slope	0.0606	0.0053	0.0469	0.0743
ln(τ) vs. $E^{\circ b}$	y-int.	1.1264	0.0194	1.0767	1.1762
	slope	0.0322	0.0038	0.0225	0.0420
ln(τ) vs. $E^{\circ c}$	y-int.	0.9440	0.0335	0.8579	1.0301
	slope	0.0616	0.0066	0.0447	0.0785
ln(τ) vs. $E^{\circ d}$	y-int.	1.1243	0.0386	1.0251	1.2235
	slope	0.0414	0.0076	0.0219	0.0608
ln(τ) vs. λ_i^e	y-int.	0.0873	0.0225	0.8180	0.9280
	slope	-0.0816	0.0042	-0.0920	-0.0713
ln(τ) vs. λ_i^f	y-int.	1.0010	0.0200	0.9521	1.0500
	slope	-0.1020	0.0038	-0.1112	-0.0928
ln(τ) vs. λ_i^g	y-int.	0.8817	0.0305	0.8070	0.8224
	slope	-0.0832	0.0058	-0.0973	-0.0691
ln(τ) vs. λ_i^h	y-int.	0.8156	0.0248	0.7549	0.8764
	slope	-0.0740	0.0047	-0.0855	-0.0626
ln (τ) vs. γ_i^e	y-int.	1.2383	0.0466	1.1243	1.3523
	slope	-0.0998	0.0088	-0.1212	-0.0783
ln (τ) vs. γ_i^f	y-int.	1.2571	0.0419	1.1545	1.3597
	slope	-0.1027	0.0079	-0.1220	-0.0833
ln (τ) vs. γ_i^g	y-int.	1.2378	0.0567	1.0993	1.3763
	slope	-0.0979	0.0107	-0.1239	-0.0718
ln (τ) vs. γ_i^h	y-int.	1.2461	0.0487	1.1270	1.3651
	slope	-0.1002	0.0092	-0.1227	-0.0778
ln (τ) vs. EG^e	y-int.	0.9424	0.0429	0.8375	1.0474
	slope	0.1046	0.0081	0.0848	0.1243
ln (τ) vs. EG^f	y-int.	0.8395	0.0388	0.7445	0.9344
	slope	0.1205	0.0073	0.1026	0.1383
ln (τ) vs. EG^g	y-int.	0.9172	0.0636	0.7614	1.0729
	slope	0.1043	0.0120	0.0749	0.1336
ln (τ) vs. EG^h	y-int.	0.9539	0.0442	0.8459	1.0620
	slope	0.1032	0.0083	0.0828	0.1236

[a] Using experimental $E°$s.

[b] Using calculated $E°$s (uncapped).

[c] Using calculated $E°$s with differential oxidation state stabilization (bis-phen*, -mmp*, and -dmp*).

[d] Using calculated $E°$s (H–capped).

[e] Using calculated energies (uncapped).

[f] Using calculated energies with differential oxidation state stabilization (bis-phen*, -mmp*, and -dmp*).

[g] Using calculated energies (H–capped).

[h] Using calculated energies (uncapped, gas phase).

[i] Using calculated values of energy gap (uncapped, CPCM).

Table A.4. Calculated inner sphere reorganization and excited state relaxation energies for all complexes considered in Chapter 2 Figure 2.12A. Gas phase.

Alkyl 2,9-Phenanthrolines	**τ**	**ln(τ)**	**λ (eV)**	**λ (kcal/mol)**	**γ (eV)**	**γ (kcal/mol)**
phen	0.14	-1.966	0.994	22.9	1.434	33.1
*phen**			1.067	24.6	1.391	32.1
mmp	2	0.693	0.706	16.3	1.114	25.7
*mmp**			0.802	18.5	1.202	27.7
dmp	90	4.5	0.484	11.2	0.910	21.0
*dmp**			0.481	11.1	0.865	19.9
dbp	150	5.011	0.445	10.3	0.747	17.2
dnpp	260	5.561	0.388	8.95	0.665	15.3
dsbp	400	5.991	0.397	9.15	0.715	16.5
dmp-dtbp	730	6.593	0.383	8.83	0.616	14.2
dtbp	3260	8.089	0.176	4.06	0.312	7.19
Other 2,9-Phenanthrolines	**τ**	**ln(τ)**	**λ (eV)**	**λ (kcal/mol)**	**γ (eV)**	**γ (kcal/mol)**
tmbp	18	2.89	0.621	14.3	0.932	21.5
CuCl	62.7	4.138	0.433	9.98	0.722	16.7
bcp	80	4.382	0.352	8.12	0.772	17.8
dbdmp	145	4.977	0.430	9.91	0.749	17.3
bfp	165	5.106	0.606	14.0	0.793	18.3
dbtmp	920	6.824	0.360	8.31	0.682	15.7
Diphenyl 2,9-Phenanthrolines	**τ**	**ln(τ)**	**λ (eV)**	**λ (kcal/mol)**	**γ (eV)**	**γ (kcal/mol)**
tpp	230	5.438	0.208	4.81	0.382	8.81
dmpp	237	5.468	0.196	4.53	0.379	8.75
dpp	270	5.598	0.212	4.90	0.397	9.15
dpdmp	310	5.737	0.233	5.38	0.405	9.34
dptmp	480	6.174	0.227	5.24	0.448	10.3
Heteroleptic Phen-POPs	**τ**	**ln(τ)**	**λ (eV)**	**λ (kcal/mol)**	**γ (eV)**	**γ (kcal/mol)**
phen-POP	190	5.247	0.580	13.4	1.079	24.9
dmp-POP	14300	9.568	0.370	8.54	0.666	15.4
dbp-POP	16100	9.687	0.362	8.36	0.635	14.6
Tricoordinate Amidophosphines	**τ**	**ln(τ)**	**λ (eV)**	**λ (kcal/mol)**	**γ (eV)**	**γ (kcal/mol)**
$(Ph_3P)_2Cu(N(p\text{-}FPh)_2)$	2500	7.824	0.217	5.01	0.371	8.55
$(Ph_3P)_2Cu(NTol_2)$	3100	8.039	0.162	3.73	0.385	8.88
$(Ph_3P)_2Cu(NPh_2)$	3170	8.061	0.191	4.40	0.397	9.15
$(Ph_3P)_2Cu(cbz)$	11700	9.367	0.178	4.09	0.250	5.77
Mononuclear Amidophosphines	**τ**	**ln(τ)**	**λ (eV)**	**λ (kcal/mol)**	**γ (eV)**	**γ (kcal/mol)**
$[MePN]Cu(PPh_3)_2$	6700	8.81	0.149	3.43	0.262	6.04

[PN]Cu(PPh$_3$)$_2$	20200	9.913	0.152	3.52	0.218	5.03
[PN]Cu(PMe$_3$)$_2$	22300	10.012	0.168	3.87	0.368	8.48
[CF$_3$PN]Cu(PPh$_3$)$_2$	150000	11.918	0.168	3.88	0.262	6.05
Heteroleptic Phen-PPh$_3$	**τ**	**ln(τ)**	**λ (eV)**	**λ (kcal/mol)**	**γ (eV)**	**γ (kcal/mol)**
phen-PPh$_3$	220	5.394	0.496	11.4	0.981	22.6
dmp-PPh$_3$	330	5.799	0.404	9.32	0.686	15.8
Binuclear Complexes	**τ**	**ln(τ)**	**λ (eV)**	**λ (kcal/mol)**	**γ (eV)**	**γ (kcal/mol)**
{PNP-Cu(I)}$_2$	10900	9.297	0.208	4.81	0.352	8.11
{PPP-Cu(I)}$_2$	600	6.397	0.389	8.97	0.550	12.7
Carbene Complexes	**τ**	**ln(τ)**	**λ (eV)**	**λ (kcal/mol)**	**γ (eV)**	**γ (kcal/mol)**
(DAC*)Cu(CzCN$_2$)	80	4.382	0.110	2.55	0.291	6.71
(DAC*)Cu(CzCN)	52	3.951	0.127	2.94	0.276	6.36
(MAC*)Cu(CzCN)	1200	7.090	0.106	2.45	0.377	8.69

Table A.5. Calculated inner sphere reorganization and excited state relaxation energies for all complexes considered in Chapter 2 Figure 2.12A. CPCM.

Alkyl 2,9-Phenanthrolines	**τ**	**ln(τ)**	**λ (eV)**	**λ (kcal/mol)**	**γ (eV)**	**γ (kcal/mol)**
phen	0.14	-1.966	1.06	24.4	1.43	33.0
*phen**			1.222	28.2	1.411	32.5
mmp	2	0.693	0.763	17.7	1.112	25.6
*mmp**			0.922	21.3	1.202	27.7
dmp	90	4.5	0.521	12.0	0.890	20.5
*dmp**			0.526	12.1	0.867	20.0
dbp	150	5.011	0.458	10.6	0.724	16.7
dnpp	260	5.561	0.393	9.06	0.664	15.3
dsbp	400	5.991	0.407	9.39	0.716	16.5
dmp-dtbp	730	6.593	0.381	8.79	0.621	14.3
dtbp	3260	8.089	0.183	4.22	0.312	7.19
Other 2,9-Phenanthrolines	**τ**	**ln(τ)**	**λ (eV)**	**λ (kcal/mol)**	**γ (eV)**	**γ (kcal/mol)**
tmbp	18	2.89	0.659	15.2	0.934	21.5
bcp	80	4.382	0.401	9.25	0.790	18.2
dbdmp	145	4.977	0.441	10.2	0.725	16.7
dbtmp	920	6.824	0.367	8.46	0.659	15.2
Diphenyl 2,9-Phenanthrolines	**τ**	**ln(τ)**	**λ (eV)**	**λ (kcal/mol)**	**γ (eV)**	**γ (kcal/mol)**
tpp	230	5.438	0.220	5.07	0.387	8.92
dptmp	480	6.174	0.232	5.35	0.463	10.7
Heteroleptic Phen-POPs	**τ**	**ln(τ)**	**λ (eV)**	**λ (kcal/mol)**	**γ (eV)**	**γ (kcal/mol)**
phen-POP	190	5.247	0.604	13.9	1.10	25.4
dmp-POP	14300	9.568	0.380	8.76	0.690	15.9
dbp-POP	16100	9.687	0.361	8.32	0.654	15.1
Tricoordinate Amidophosphines	**τ**	**ln(τ)**	**λ (eV)**	**λ (kcal/mol)**	**γ (eV)**	**γ (kcal/mol)**
$(Ph_3P)_2Cu(N(p\text{-}FPh)_2)$	2500	7.824	0.189	4.36	0.336	7.75
$(Ph_3P)_2Cu(NTol_2)$	3100	8.039	0.140	3.23	0.343	7.91
$(Ph_3P)_2Cu(NPh_2)$	3170	8.061	0.167	3.85	0.356	8.21
$(Ph_3P)_2Cu(cbz)$	11700	9.367	0.161	3.71	0.237	5.47
Mononuclear Amidophosphines	**τ**	**ln(τ)**	**λ (eV)**	**λ (kcal/mol)**	**γ (eV)**	**γ (kcal/mol)**
$[MePN]Cu(PPh_3)_2$	6700	8.81	0.137	3.16	0.251	5.79
$[PN]Cu(PPh_3)_2$	20200	9.913	0.137	3.16	0.219	5.05
$[PN]Cu(PMe_3)_2$	22300	10.012	0.156	3.60	0.408	9.41
$[CF_3PN]Cu(PPh_3)_2$	150000	11.918	0.134	3.09	0.284	6.55

Heteroleptic Phen-PPh_3	**τ**	**ln(τ)**	**λ (eV)**	**λ (kcal/mol)**	**γ (eV)**	**γ (kcal/mol)**
phen-PPh_3	220	5.394	0.545	12.6	1.02	23.5
dmp-PPh_3	330	5.799	0.417	9.62	0.694	16.0
Binuclear Complexes	**τ**	**ln(τ)**	**λ (eV)**	**λ (kcal/mol)**	**γ (eV)**	**γ (kcal/mol)**
$\{PNP\text{-}Cu(I)\}_2$	10900	9.297	0.208	4.80	0.351	8.09
$\{PPP\text{-}Cu(I)\}_2$	600	6.397	0.393	9.06	0.532	12.3
Carbene Complexes	**τ**	**ln(τ)**	**λ (eV)**	**λ (kcal/mol**	**γ (eV)**	**γ (kcal/mol)**
$(DAC^*)Cu(CzCN_2)$	80	4.382	0.089	2.05	0.310	7.15

Table A.6. Calculated energy gaps for all complexes considered in Chapter 2 Figure 2.12B. Gas phase.

Baseline 2,9-Phenanthrolines	**τ**	**ln(τ)**	**Energy Gap (eV)**	**Energy Gap (kcal/mol)**	**Red. Angle**	**Ox. Angle**	**Trip. Angle**
phen	0.14	-1.966	0.778	17.9	90.0	38.5	35.5
*phen**			0.655	15.1	82.8	43.5	37.4
mmp	2	0.693	1.044	24.1	86.8	50.9	74.5
*mmp**			0.944	21.8	87.0	48.8	47.0
dmp	90	4.5	1.377	31.8	90.0	64.6	65.0
*dmp**			1.330	30.7	87.5	64.3	59.9
dbp	150	5.011	1.507	34.8	90.0	68.0	65.0
dnpp	260	5.561	1.418	32.7	77.1	61.1	59.4
dsbp	400	5.991	1.511	34.8	89.8	69.7	64.6
dmp-dtbp	730	6.593	1.658	38.2	89.9	72.4	70.0
dtbp	3260	8.089	1.896	43.7	81.8	77.7	70.1
Other 2,9-Phenanthrolines	**τ**	**ln(τ)**	**Energy Gap (eV)**	**Energy Gap (kcal/mol)**	**Red. Angle**	**Ox. Angle**	**Trip. Angle**
tmbp	18	2.89	1.292	29.8	89.9	66.1	64.1
CuCl	62.7	4.138	1.524	35.1	90.0	61.8	59.1
bcp	80	4.382	1.315	30.3	89.5	67.1	61.0
dbdmp	145	4.977	1.533	35.4	90.0	68.5	64.9
bfp	165	5.106	1.446	33.3	89.2	68.5	66.2
dbtmp	920	6.824	1.620	37.4	90.0	72.4	69.4
Diphenyl 2,9-Phenanthrolines	**τ**	**ln(τ)**	**Energy Gap (eV)**	**Energy Gap (kcal/mol)**	**Red. Angle**	**Ox. Angle**	**Trip. Angle**
tpp	230	5.438	1.336	30.8	69.4	60.9	58.3
dmpp	237	5.468	1.411	32.5	69.4	60.4	58.1
dpp	270	5.598	1.415	32.6	69.5	60.7	58.6
dpdmp	310	5.737	1.429	33.0	69.7	60.3	58.1
dptmp	480	6.174	1.436	33.1	77.0	66.4	63.7
Heteroleptic Phen-POPs	**τ**	**ln(τ)**	**Energy Gap (eV)**	**Energy Gap (kcal/mol)**	**Red. Angle**	**Ox. Angle**	**Trip. Angle**
phen-POP	190	5.247	1.312	30.3	87.4	66.8	56.8
dmp-POP	14300	9.568	1.834	42.3	87.7	82.1	74.5
dbp-POP	16100	9.687	1.878	43.3	86.8	82.6	72.1
Tricoordinate Amidophosphines	**τ**	**ln(τ)**	**Energy Gap (eV)**	**Energy Gap (kcal/mol)**	**Red. Angle**	**Ox. Angle**	**Trip. Angle**
$(Ph_3P)_2Cu(N(p\text{-}FPh)_2)$	2500	7.824	1.688	38.9			

$(Ph_3P)_2Cu(NTol_2)$	3100	8.039	1.645	37.9			
$(Ph_3P)_2Cu(NPh_2)$	3170	8.061	1.724	39.8			
$(Ph_3P)_2Cu(cbz)$	11700	9.367	2.010	46.4			
Mononuclear Amidophosphines	**τ**	**ln(τ)**	**Energy Gap (eV)**	**Energy Gap (kcal/mol)**	**Red. Angle**	**Ox. Angle**	**Trip. Angle**
$[MePN]Cu(PPh_3)_2$	6700	8.81	1.953	45.0	82.7	84.1	84.4
$[PN]Cu(PPh_3)_2$	20200	9.913	1.987	45.8	82.7	84.2	85.4
$[PN]Cu(PMe_3)_2$	22300	10.012	2.147	49.5	81.5	86.2	89.5
$[CF_3PN]Cu(PPh_3)_2$	150000	11.918	1.883	43.4	82.8	84.1	84.5
Heteroleptic Phen-PPh_3	**τ**	**ln(τ)**	**Energy Gap (eV)**	**Energy Gap (kcal/mol)**	**Red. Angle**	**Ox. Angle**	**Trip. Angle**
phen-PPh_3	220	5.394	1.464	33.8	89.0	65.9	59.1
dmp-PPh_3	330	5.799	1.839	42.4	86.2	80.8	75.3
Binuclear Complexes	**τ**	**ln(τ)**	**Energy Gap (eV)**	**Energy Gap (kcal/mol)**	**Red. Angle**	**Ox. Angle**	**Trip. Angle**
$\{PNP\text{-}Cu(I)\}_2$	10900	9.297	1.810	41.7	69.4	64.6	69.0
					69.8	70.1	69.9
$\{PPP\text{-}Cu(I)\}_2$	600	6.397	1.455	33.6	57.6	59.3	59.5
					57.7	59.5	59.9
Carbene Complexes	**τ**	**ln(τ)**	**Energy Gap (eV)**	**Energy Gap (kcal/mol)**	**Red. Angle**	**Ox. Angle**	**Trip. Angle**
(DAC*)Cu($CzCN_2$)	80	4.382	1.648	38.0			
(DAC*)Cu(CzCN)	52	3.951	1.501	34.6			
(MAC*)Cu(CzCN)	1200	7.090	1.912	44.1			

Table A.7. Calculated energy gaps for all complexes considered in Chapter 2 Figure 2.12B. CPCM.

Baseline 2,9-Phenanthrolines	**τ**	**ln(τ)**	**Energy Gap (eV)**	**Energy Gap (kcal/mol)**	**Red. Angle**	**Ox. Angle**	**Trip. Angle**
phen	0.14	-1.966	0.767	17.7	90.0	38.5	35.5
*phen**			0.627	14.5	82.8	43.5	37.4
mmp	2	0.693	1.029	23.7	86.8	50.9	74.5
*mmp**			0.932	21.5	87.0	48.8	47.0
dmp	90	4.5	1.360	31.4	90.0	64.6	65.0
*dmp**			1.321	30.5	87.5	64.3	59.9
dbp	150	5.011	1.507	34.8	90.0	68.0	65.0
dnpp	260	5.561	1.423	32.8	77.1	61.1	59.4
dsbp	400	5.991	1.515	34.9	89.8	69.7	64.6
dmp-dtbp	730	6.593	1.649	38.0	89.9	72.4	70.0
dtbp	3260	8.089	1.894	43.7	81.8	77.7	70.1
Other 2,9-Phenanthrolines	**τ**	**ln(τ)**	**Energy Gap (eV)**	**Energy Gap (kcal/mol)**	**Red. Angle**	**Ox. Angle**	**Trip. Angle**
tmbp	18	2.89	1.273	29.4	89.9	66.1	64.1
CuCl	62.7	4.138	1.545	35.6	90.0	61.8	59.1
bcp	80	4.382	1.283	29.6	89.5	67.1	61.0
dbdmp	145	4.977	1.532	35.3	90.0	68.5	64.9
bfp	165	5.106	1.475	34.0	89.2	68.5	66.2
dbtmp	920	6.824	1.620	37.4	90.0	72.4	69.4
Diphenyl 2,9-Phenanthrolines	**τ**	**ln(τ)**	**Energy Gap (eV)**	**Energy Gap (kcal/mol)**	**Red. Angle**	**Ox. Angle**	**Trip. Angle**
tpp	230	5.438	1.324	30.5	69.4	60.9	58.3
dmpp	237	5.468	1.396	32.2	69.4	60.4	58.1
dpp	270	5.598	1.416	32.7	69.5	60.7	58.6
dpdmp	310	5.737	1.429	33.0	69.7	60.3	58.1
dptmp	480	6.174	1.437	33.1	77.0	66.4	63.7
Heteroleptic Phen-POPs	**τ**	**ln(τ)**	**Energy Gap (eV)**	**Energy Gap (kcal/mol)**	**Red. Angle**	**Ox. Angle**	**Trip. Angle**
phen-POP	190	5.247	1.320	30.4	87.4	66.8	56.8
dmp-POP	14300	9.568	1.816	41.9	87.7	82.1	74.5
dbp-POP	16100	9.687	1.856	42.8	86.8	82.6	72.1
Tricoordinate Amidophosphines	**τ**	**ln(τ)**	**Energy Gap (eV)**	**Energy Gap (kcal/mol)**	**Red. Angle**	**Ox. Angle**	**Trip. Angle**
$(Ph_3P)_2Cu(N(p\text{-}FPh)_2)$	2500	7.824	1.783	41.1			

(Ph$_3$P)$_2$Cu(NTol$_2$)	3100	8.039	1.716	39.6			
(Ph$_3$P)$_2$Cu(NPh$_2$)	3170	8.061	1.816	41.9			
(Ph$_3$P)$_2$Cu(cbz)	11700	9.367	2.163	49.9			
Mononuclear Amidophosphines	**τ**	**ln(τ)**	**Energy Gap (eV)**	**Energy Gap (kcal/mol)**	**Red. Angle**	**Ox. Angle**	**Trip. Angle**
[MePN]Cu(PPh$_3$)$_2$	6700	8.81	1.994	46.0	82.7	84.1	84.4
[PN]Cu(PPh$_3$)$_2$	20200	9.913	2.027	46.7	82.7	84.2	85.4
[PN]Cu(PMe$_3$)$_2$	22300	10.012	2.109	48.6	81.5	86.2	89.5
[CF$_3$PN]Cu(PPh$_3$)$_2$	150000	11.918	1.893	43.7	82.8	84.1	84.5
Heteroleptic Phen-PPh$_3$	**τ**	**ln(τ)**	**Energy Gap (eV)**	**Energy Gap (kcal/mol)**	**Red. Angle**	**Ox. Angle**	**Trip. Angle**
phen-PPh$_3$	220	5.394	1.484	34.2	89.0	65.9	59.1
dmp-PPh$_3$	330	5.799	1.860	42.9	86.2	80.8	75.3
Binuclear Complexes	**τ**	**ln(τ)**	**Energy Gap (eV)**	**Energy Gap (kcal/mol)**	**Red. Angle**	**Ox. Angle**	**Trip. Angle**
{PNP-Cu(I)}$_2$	10900	9.297	1.792	41.3	69.4	64.6	69.0
					69.8	70.1	69.9
{PPP-Cu(I)}$_2$	600	6.397	1.424	32.8	57.6	59.3	59.5
					57.7	59.5	59.9
Carbene Complexes	**τ**	**ln(τ)**	**Energy Gap (eV)**	**Energy Gap (kcal/mol)**	**Red. Angle**	**Ox. Angle**	**Trip. Angle**
(DAC*)Cu(CzCN$_2$)	80	4.382	1.746	40.3			

Table A.8. Calculated energy gaps for capped structures. Gas Phase.

Alkyl 2,9-Phenanthrolines	**τ**	**ln(τ)**	**Energy Gap (eV)**	**Energy Gap (kcal/mol)**	**Reduced Angle**	**Oxidized Angle**	**Triplet Angle**
phen	0.14	-1.966	0.778	17.9	90.0	38.5	35.5
*phen**			0.655	15.1	82.8	43.5	37.4
mmp	2	0.693	1.031	23.8	86.8	50.9	74.5
*mmp**			0.948	21.9	87.0	48.8	47.0
dmp	90	4.5	1.328	30.6	90.0	64.6	65.0
*dmp**			1.285	29.6	87.5	64.3	59.9
dbp	150	5.011	1.451	33.5	90.0	68.0	65.0
dnpp	260	5.561	1.415	32.6	77.1	61.1	59.4
dsbp	400	5.991	1.459	33.6	89.8	69.7	64.6
dmp-dtbp	730	6.593	1.643	37.9	89.9	72.4	70.0
dtbp	3260	8.089	1.963	45.3	81.8	77.7	70.1
CuCl	62.7	4.138	1.395	32.2	90.0	61.8	59.1
bfp	165	5.106	1.502	34.6	89.2	68.5	66.2
tpp	230	5.438	1.339	30.9	69.4	60.9	58.3
dmpp	237	5.468	1.425	32.9	69.4	60.4	58.1
dpp	270	5.598	1.422	32.8	69.5	60.7	58.6
dpdmp	310	5.737	1.434	33.1	69.7	60.3	58.1
dptmp	480	6.174	1.479	34.1	77.0	66.4	63.7

Table A.9. Calculated energy gaps for capped structures. CPCM.

Alkyl 2,9-Phenanthrolines	**τ**	**ln(τ)**	**Energy Gap (eV)**	**Energy Gap (kcal/mol)**	**Reduced Angle**	**Oxidized Angle**	**Triplet Angle**
phen	0.14	-1.966	0.767	17.7	90.0	38.5	35.5
*phen**			0.627	14.5	82.8	43.5	37.4
mmp	2	0.693	1.016	23.4	86.8	50.9	74.5
*mmp**			0.936	21.6	87.0	48.8	47.0
dmp	90	4.5	1.308	30.2	90.0	64.6	65.0
*dmp**			1.286	29.7	87.5	64.3	59.9
dbp	150	5.011	1.430	33.0	90.0	68.0	65.0
dnpp	260	5.561	1.399	32.3	77.1	61.1	59.4
dsbp	400	5.991	1.439	33.2	89.8	69.7	64.6
dmp-dtbp	730	6.593	1.623	37.4	89.9	72.4	70.0
dtbp	3260	8.089	1.950	45.0	81.8	77.7	70.1
tpp	230	5.438	1.314	30.3	69.4	60.9	58.3
dmpp	237	5.468	1.409	32.5	69.4	60.4	58.1
dpp	270	5.598	1.407	32.4	69.5	60.7	58.6
dpdmp	310	5.737	1.425	32.9	69.7	60.3	58.1
dptmp	480	6.174	1.474	34.0	77.0	66.4	63.7

A.C. Figures

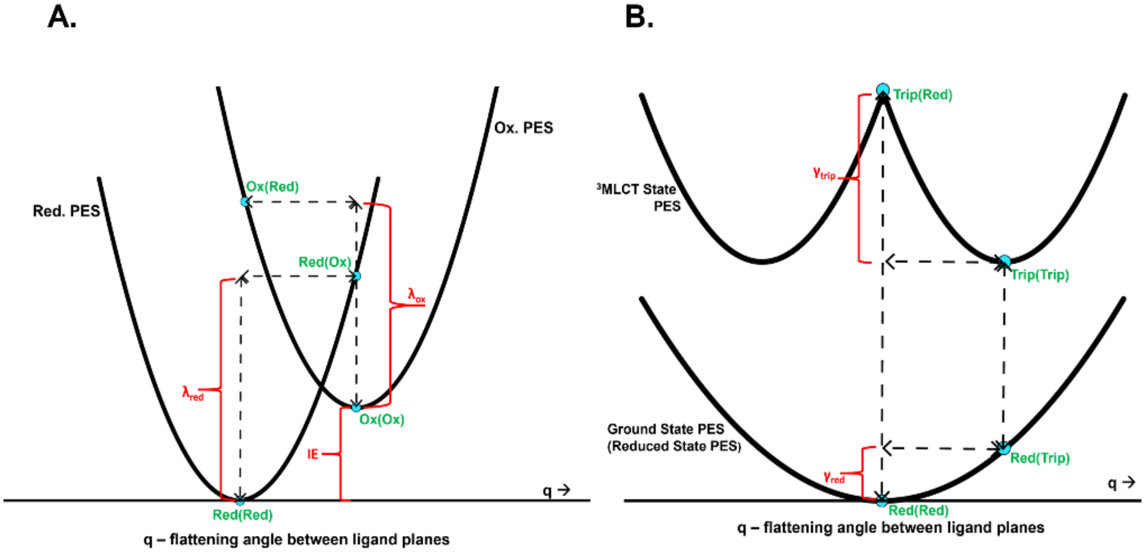

Figure A.1. Potential energy surfaces for calculating (A) ground state reorganization energy (λ_i) and (B) excited state relaxation energy (γ_i).

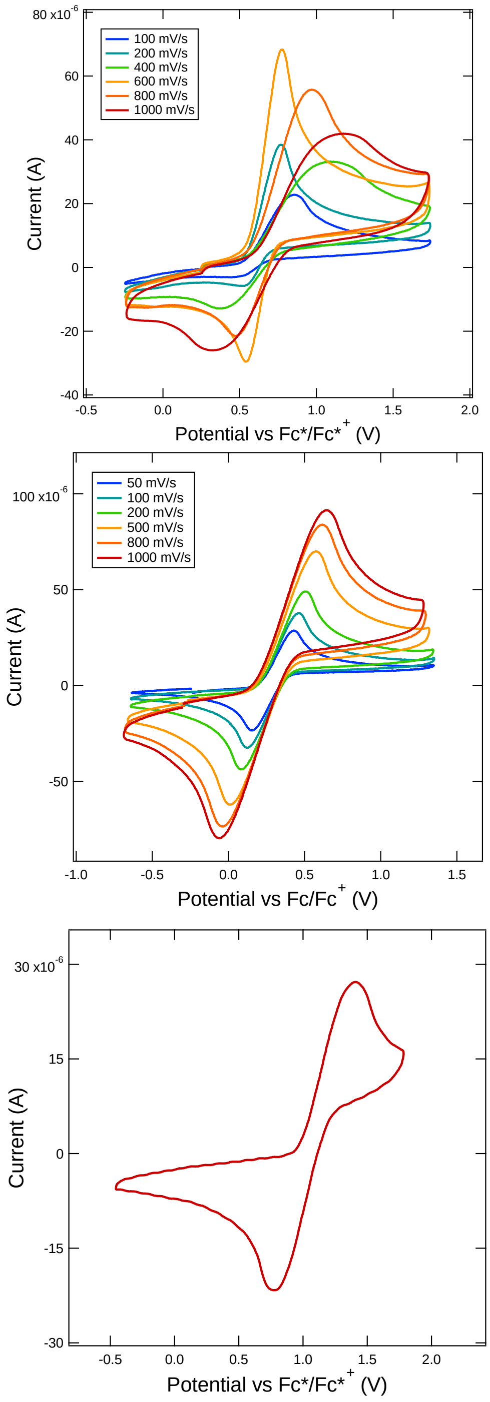

Figure A.2. Electrochemical data (CVs) for a variety of Cu(I) bis-phen complexes. (Top) scan rate dependence of Cu(I) bis-phen; (Middle) scan rate dependence for Cu(I) bis-mmp; and (Bottom) data for Cu(I) bis-dmp. See above for more experimental details.

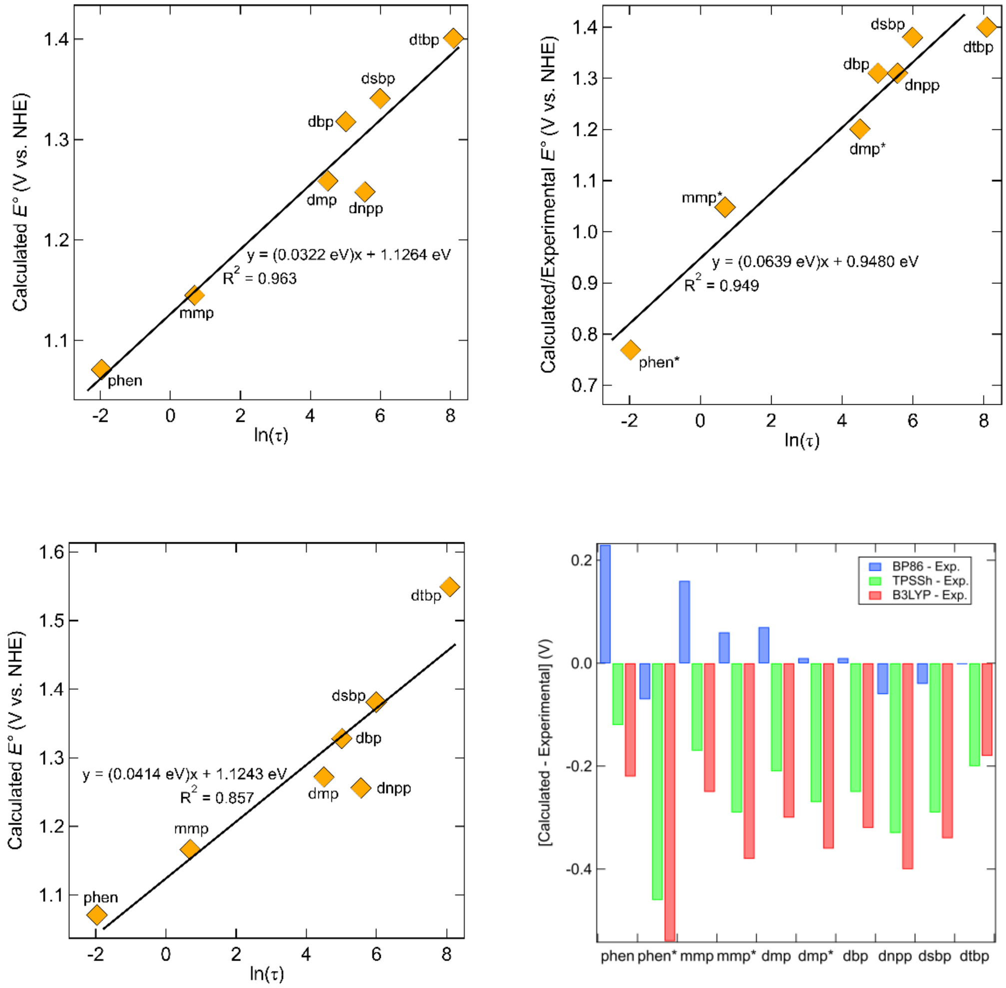

Figure A.3. Correlations between experimental and computational *E*°s and ln(*τ*) for bis-phen and 2,9-alkyl substituted Cu(I) complexes. (Top left) Calculated (uncapped) *E*° vs. ln(*τ*); (Top right) Calculated (for bis-phen*, -mmp*, and dmp*) and experimental (for the rest of the complexes) *E*° vs. ln(*τ*); (Bottom left) Calculated (H–capped) *E*° vs. ln(*τ*); (Bottom right) difference between calculated and experimental reduction potentials for Cu(I) bis-phen complexes (data in Table 2.1).

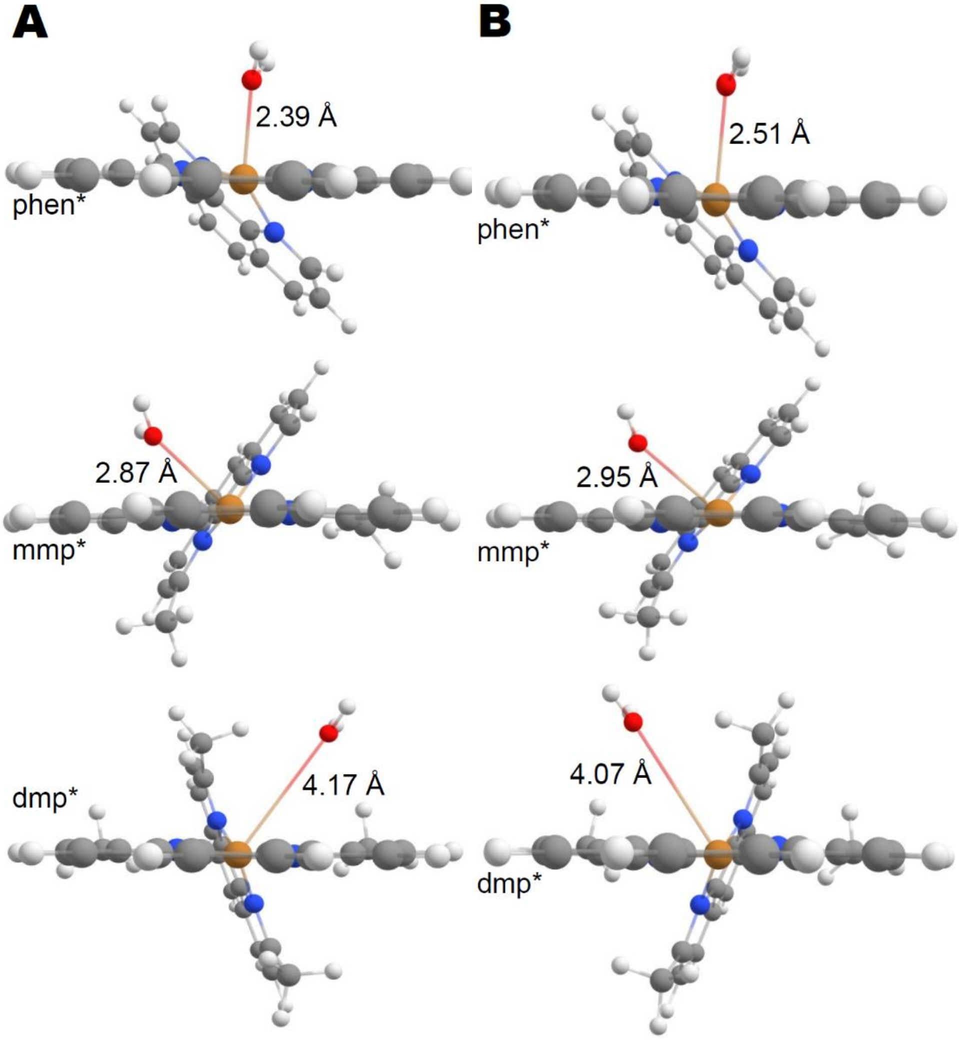

Figure A.4. Structures of the Cu(II)–OH_2 (A) and ^{3}MLCT Cu(II)–OH_2 (B) geometries of bis-phen*, -mmp*, and -dmp* and their corresponding Cu(II)–OH_2 bond distances.

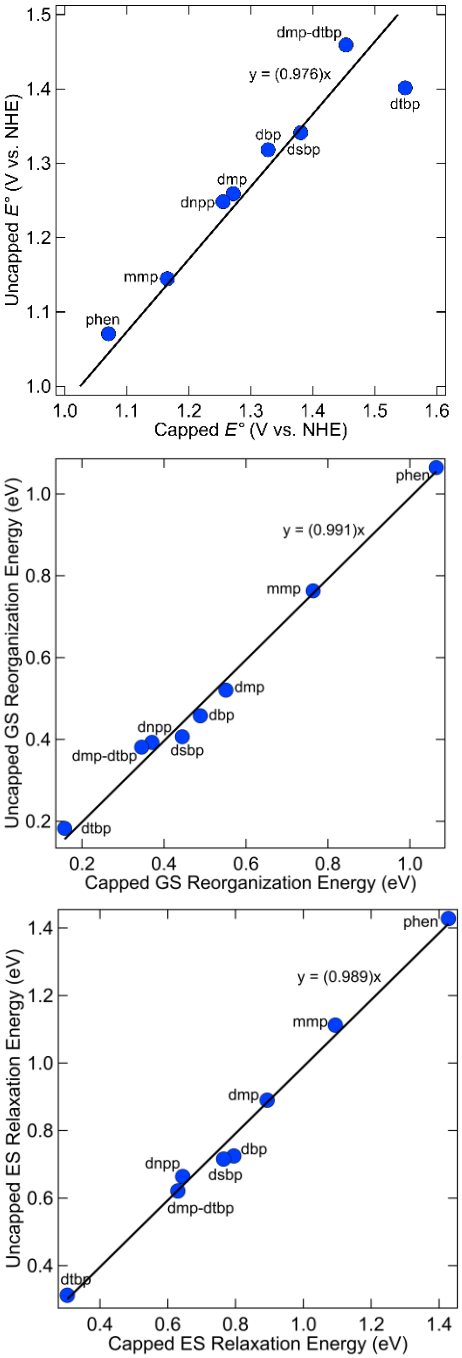

Figure A.5. Correlations between H–capped and uncapped calculated values of (top) *E*°, (middle), λ_i, and (bottom) γ_i.

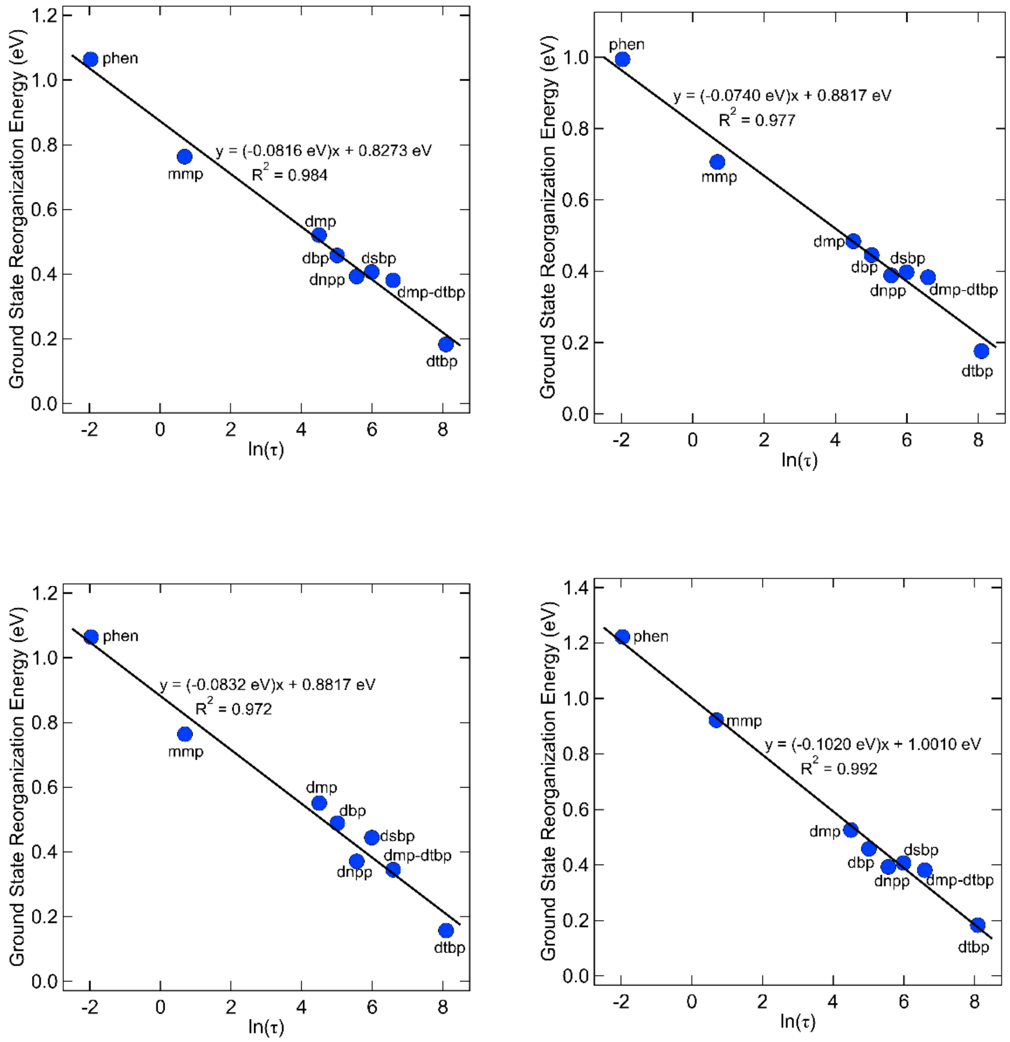

Figure A.6. Plots for the correlations in Table 2.4: ln(τ) vs. λ_i.

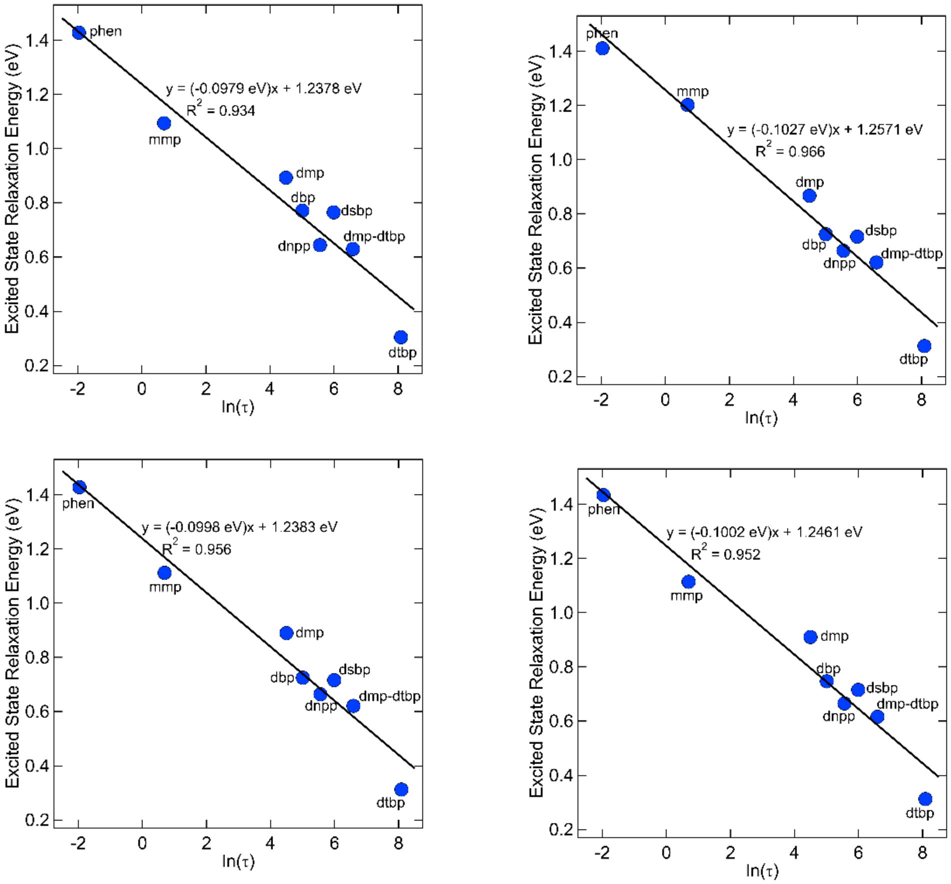

Figure A.7. Plots for the correlations in Table 2.4: ln(τ) vs. γ_i.

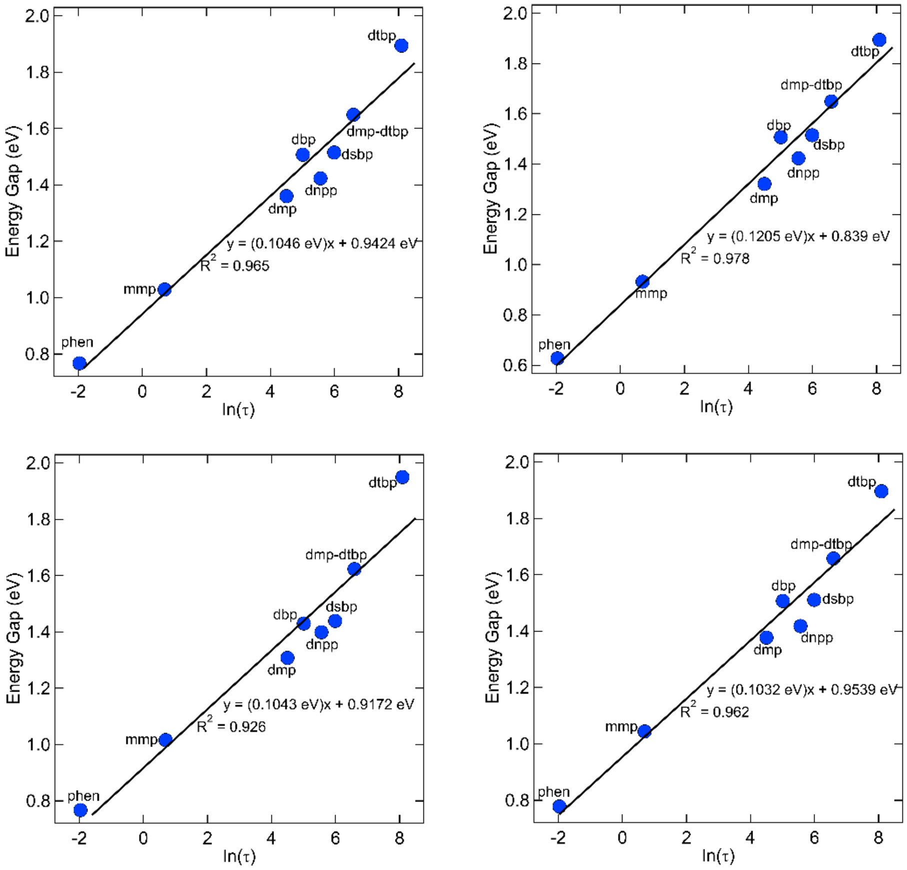

Figure A.8. Plots for the correlations in Table 2.4: ln(τ) vs. energy gap.

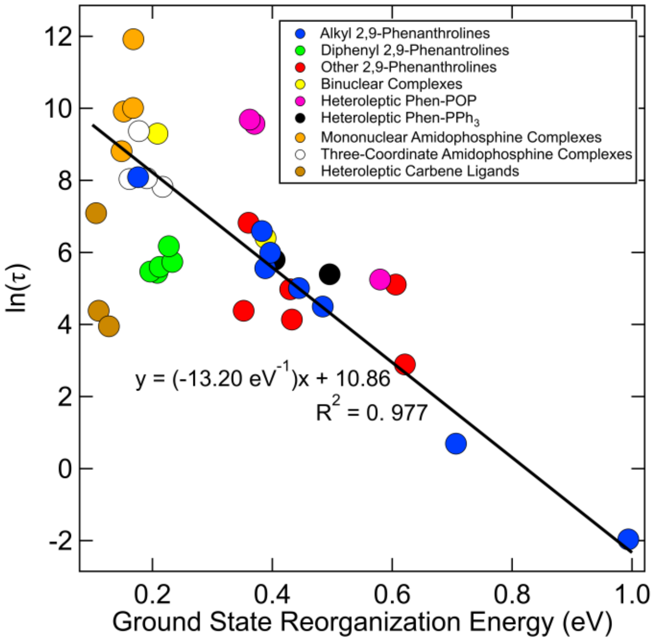

Figure A.9. Ground state reorganization energy (gas phase).

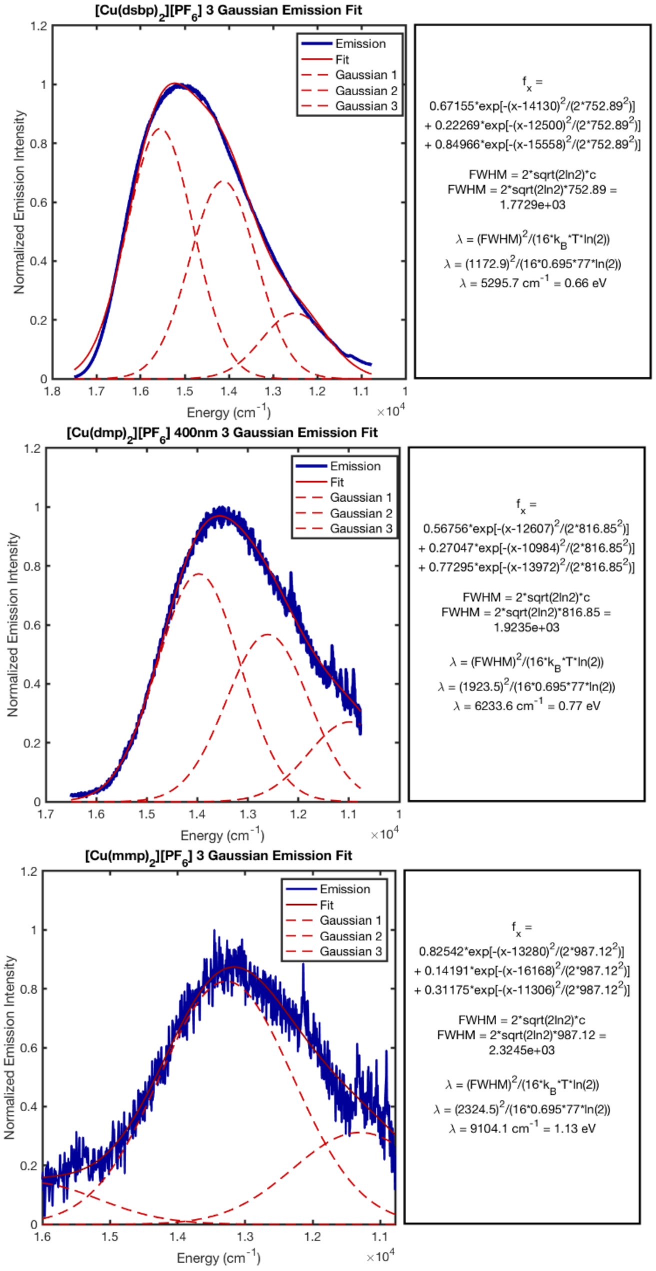

Figure A.10. Low temperature (77 K) emission spectra and fitting for (Top) Cu bis-dsbp and (Middle) Cu bis-dmp. Emission data for bis-mmp (Bottom) are especially weak and structured differently than the bis-dsbp and -dmp complexes. While the fitting provides an estimate of γ_i (1.13 eV) that agrees well with the calculated value (1.114 eV), the low signal-to-noise and different spectral structure precludes a confident determination of γ_i. See above for additional experimental details.

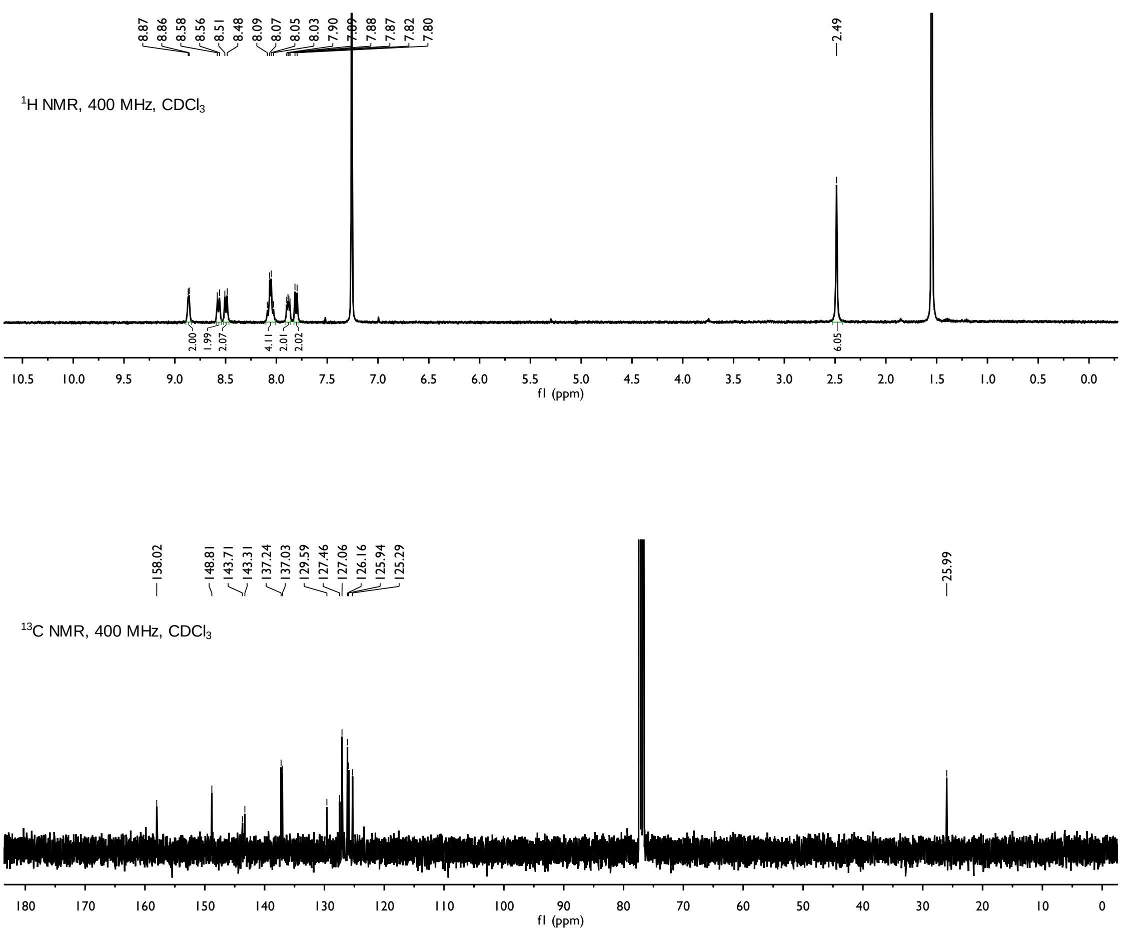

Figure A.11. NMR spectra of Cu(I) bis-mmp.

REFERENCES

(1) Pallenberg, A. J.; Koenig, K. S.; Barnhart, D. M. Synthesis and Characterization of Some Copper(I) Phenanthroline Complexes. *Inorg. Chem.* **1995**, *34* (11), 2833–2840. https://doi.org/10.1021/ic00115a009.

(2) Kubas, G. J.; Monzyk, B.; Crumbliss, A. L. Tetrakis(Acetonitrile)Copper(I) Hexafluorophosphate. In *Inorganic Syntheses*; John Wiley & Sons, Ltd, **2007**; pp 90–92. https://doi.org/10.1002/9780470132500.ch18.

(3) Ruthkosky, M.; Castellano, F. N.; Meyer, G. J. Photodriven Electron and Energy Transfer from Copper Phenanthroline Excited States. *Inorg. Chem.* **1996**, *35* (22), 6406–6412. https://doi.org/10.1021/ic960503z.

(4) Desvergnes-Breuil, V.; Hebbe, V.; Dietrich-Buchecker, C.; Sauvage, J.-P.; Lacour, J. NMR Evaluation of the Configurational Stability of Cu(I) Complexes. *Inorg. Chem.* **2003**, *42* (2), 255–257. https://doi.org/10.1021/ic0259890.

(5) Scaltrito, D. V.; Thompson, D. W.; O'Callaghan, J. A.; Meyer, G. J. MLCT Excited States of Cuprous Bis-Phenanthroline Coordination Compounds. *Coord. Chem. Rev.* **2000**, *208* (1), 243–266.

(6) Neese, F. The ORCA Program System. *Wiley Interdiscip. Rev. Comput. Mol. Sci.* **2012**, *2* (1), 73–78. https://doi.org/10.1002/wcms.81.

(7) Neese, F. Software Update: The ORCA Program System, Version 4.0. *Wiley Interdiscip. Rev. Comput. Mol. Sci.* **2018**, *8* (1), e1327. https://doi.org/10.1002/wcms.1327.

(8) Perdew, J. P. Density-Functional Approximation for the Correlation Energy of the Inhomogeneous Electron Gas. *Phys. Rev. B* **1986**, *33* (12), 8822–8824. https://doi.org/10.1103/PhysRevB.33.8822.

(9) Becke, A. D. Density-Functional Exchange-Energy Approximation with Correct Asymptotic Behavior. *Phys. Rev. A* **1988**, *38* (6), 3098–3100. https://doi.org/10.1103/PhysRevA.38.3098.

(10) Becke, A. D. Density-functional Thermochemistry. III. The Role of Exact Exchange. *J. Chem. Phys.* **1993**, *98* (7), 5648–5652. https://doi.org/10.1063/1.464913.

(11) Curtiss, L. A.; McGrath, M. P.; Blaudeau, J.; Davis, N. E.; Binning, R. C.; Radom, L. Extension of Gaussian-2 Theory to Molecules Containing Third-row Atoms Ga–Kr. *J. Chem. Phys.* **1995**, *103* (14), 6104–6113. https://doi.org/10.1063/1.470438.

(12) Hehre, W. J.; Ditchfield, R.; Pople, J. A. Self—Consistent Molecular Orbital Methods. XII. Further Extensions of Gaussian—Type Basis Sets for Use in Molecular Orbital Studies of Organic Molecules. *J. Chem. Phys.* **1972**, *56* (5), 2257–2261. https://doi.org/10.1063/1.1677527.

(13) Tao, J.; Perdew, J. P.; Staroverov, V. N.; Scuseria, G. E. Climbing the Density Functional Ladder: Nonempirical Meta--Generalized Gradient Approximation Designed for Molecules and Solids. *Phys. Rev. Lett.* **2003**, *91* (14), 146401. https://doi.org/10.1103/PhysRevLett.91.146401.

(14) Staroverov, V. N.; Scuseria, G. E.; Tao, J.; Perdew, J. P. Comparative Assessment of a New Nonempirical Density Functional: Molecules and Hydrogen-Bonded Complexes. *J. Chem. Phys.* **2003**, *119* (23), 12129–12137. https://doi.org/10.1063/1.1626543.

(15) Staroverov, V. N.; Scuseria, G. E.; Tao, J.; Perdew, J. P. Erratum: “Comparative Assessment of a New Nonempirical Density Functional: Molecules and Hydrogen-Bonded Complexes” [J. Chem. Phys. 119, 12129 (2003)]. *J. Chem. Phys.* **2004**, *121* (22), 11507. https://doi.org/10.1063/1.1795692.

(16) Lee, C.; Yang, W.; Parr, R. G. Development of the Colle-Salvetti Correlation-Energy Formula into a Functional of the Electron Density. *Phys. Rev. B* **1988**, *37* (2), 785–789. https://doi.org/10.1103/PhysRevB.37.785.

(17) Barone, V.; Cossi, M. Quantum Calculation of Molecular Energies and Energy Gradients in Solution by a Conductor Solvent Model. *J. Phys. Chem. A* **1998**, *102* (11), 1995–2001. https://doi.org/10.1021/jp9716997.

(18) Kossmann, S.; Neese, F. Efficient Structure Optimization with Second-Order Many-Body Perturbation Theory: The RIJCOSX-MP2 Method. *J. Chem. Theory Comput.* **2010**, *6* (8), 2325–2338. https://doi.org/10.1021/ct100199k.

(19) Kossmann, S.; Neese, F. Comparison of Two Efficient Approximate Hartee–Fock Approaches. *Chem. Phys. Lett.* **2009**, *481* (4), 240–243. https://doi.org/10.1016/j.cplett.2009.09.073.

(20) Izsák, R.; Neese, F. Speeding up Spin-Component-Scaled Third-Order Pertubation Theory with the Chain of Spheres Approximation: The COSX-SCS-MP3 Method. *Mol. Phys.* **2013**, *111* (9–11), 1190–1195. https://doi.org/10.1080/00268976.2013.796071.

(21) Izsák, R.; Neese, F. An Overlap Fitted Chain of Spheres Exchange Method. *J. Chem. Phys.* **2011**, *135* (14), 144105. https://doi.org/10.1063/1.3646921.

(22) Neese, F.; Wennmohs, F.; Hansen, A.; Becker, U. Efficient, Approximate and Parallel Hartree–Fock and Hybrid DFT Calculations. A ‘Chain-of-Spheres’ Algorithm for the Hartree–Fock Exchange. *Chem. Phys.* **2009**, *356*, 98–109. https://doi.org/10.1016/j.chemphys.2008.10.036.

(23) Neese, F. An Improvement of the Resolution of the Identity Approximation for the Formation of the Coulomb Matrix. *J. Comput. Chem.* **2003**, *24* (14), 1740–1747. https://doi.org/10.1002/jcc.10318.

(24) Stoychev, G. L.; Auer, A. A.; Neese, F. Automatic Generation of Auxiliary Basis Sets. *J. Chem. Theory Comput.* **2017**, *13* (2), 554–562. https://doi.org/10.1021/acs.jctc.6b01041.

(25) Trasatti, S. The Absolute Electrode Potential: An Explanatory Note: (Recommendations 1986). https://doi.org/10.1515/iupac.58.0011.

(26) Marenich, A. V.; Ho, J.; Coote, M. L.; Cramer, C. J.; Truhlar, D. G. Computational Electrochemistry: Prediction of Liquid-Phase Reduction Potentials. *Phys. Chem. Chem. Phys.* **2014**, *16* (29), 15068–15106. https://doi.org/10.1039/C4CP01572J.

(27) Yan, L.; Lu, Y.; Li, X. A density functional theory protocol for the calculation of redox potentials of copper complexes. *Phys. Chem. Chem. Phys.*, **2016**, *18*, 5529–5536. https://doi.org/10.1039/C5CP06638G.

(28) Solomon, E. I.; Szilagyi, R. K.; DeBeer George, S.; Basumallick, L. Electronic Structures of Metal Sites in Proteins and Models: Contributions to Function in Blue Copper Proteins. *Chem. Rev.* **2004**, *104*, 419–458. https://doi.org/10.1021/cr0206317.

(29) Roy, L. E.; Jakubikova, E.; Guthrie, M. G.; Batista, E. R. Calculation of One-Electron Redox Potentials Revisited. Is It Possible to Calculate Accurate Potentials with Density Functional Methods? *J. Phys. Chem. A* **2009**, *113* (24), 6745–6750. https://doi.org/10.1021/jp811388w.

Appendix B

SUPPORTING INFORMATION FOR CHAPTER 3: MULTIREFERENCE GROUND AND EXCITED STATE ELECTRONIC STRUCTURES OF FREE- VERSUS IRON PORPHYRIN-CARBENES

Adapted with permission from:

Stroscio, G. D.; Srnec, M.*; Hadt, R. G.* Multireference Ground and Excited State Electronic Structures of Free- versus Iron Porphyrin-Carbenes. *Inorg. Chem.* **2020**, *59* (13), 8707–8715. https://doi.org/10.1021/acs.inorgchem.0c00249.

*Corresponding author.

B.A. Additional Computational Details

B.A.1. Example ORCA Input for DLPNO-MR-CCSD

```
!uhf cc-pvtz cc-pv6z/c dlpno-ccsd(t)
%base "S20_2"
! moread noiter
%moinp "S20.gbw"

%scf
end

%method frozencore
FC_NONE
end

%MaxCore 6000

%scf
Convergence VeryTight
end


%mdci
inname "S20"
mrcc on
mrcctype mkcc
n_docc 26
root -1
#USERHFINTS on
root_overlap "1.0,-1.0"
refs "20,02"
STol 1e-7
end

%coords
Ctyp xyz
Charge 0
Mult 1
Units Angs
```

The above input is given for the closed-shell singlet case. For the triplet case, refs in the %mdci block input was changed to “ab,ba” and the multiplicity is of course changed to 3. For the OSS case, refs in the %mdci block input is changed to “ab,ba” and root overlap was changed to “1.0,1.0”. For all three cases, a DLPNO-NEVPT2 jobs was run first (example input on next page) and the orbitals (.gbw files) from this job were input into the DLPNO-MR-CCSD.

B.A.2. Example ORCA Input for Initial DLPNO-NEVPT2

```
!cc-pvtz cc-pv6z/c
%base "S10c"

%scf
end

%casscf
nel 2
norb 2
mult 1
nroots 2
nevpt2 3  #DLPNO-NEVPT2=3, PC-NEVPT2=2, SC-NEVPT2=1
trafostep ri   # using RI approximation
nevpt
d4tpre 1e-14  # for nevpt2 you'd better use accurate D4 and D3 density matrix
d3tpre 1e-14
end
DoDumpForMRCC 1
end

%method frozencore
FC_NONE
end

%MaxCore 6000

%scf
Convergence VeryTight
end



%coords
Ctyp xyz
Charge 0
Mult 1
Units Angs
```

B.A.3. Discussion of <S^2> and Spin Contamination Relating to DFT BSS Results:

For the DFT BSS calculations, the <S^2> values are comparable to previously published studies. Another work reported an <S^2> value of 0.33 for an imidazole ligated IPC.[1] That imidazole-ligated IPC featured the same carbene studied here and has a dihedral angle near 270° (273.7°). Likewise, a <S^2> value of 0.80 was reported for a $^-$SH ligated IPC.[2] This model also features the $CHCO_2Et$ carbene. The values for the free carbene are also presented.

BSS <S^2> values for all three IPC models at 90°, 180°, 270°, and 350°:

	***N*-MeImid.**	**Thiolate**	**Hydroxide**
0°	0.67	0.83	0.85
90°	0.40	0.64	0.72
180°	0.68	0.83	0.86
270°	0.41	0.65	0.72
350°	0.67	0.83	0.85

BSS <S^2> values for the free carbene datasets at 90°, 180°, 270°, and 350°:

	B3LYP	**BP86**
0°	1.01	1.00
90°	0.27	0.00
180°	1.01	1.00
270°	0.28	0.00
350°	0.94	0.98

B.B. Tables

The free carbene active space occupancies for the singlet calculation are included below. The Cσ orbital occupancy is ~0.5 smaller than 2 and the Cπ occupancy is ~0.5 larger than 0; these occupancy values are indictive of a reasonable active space. For the triplet calculation, the occupancies for both orbitals was exactly 1; this is expected for the 2-in-2 triplet, a single reference situation.

Table B.1. Free carbene QD-NEVPT2 active space occupancies for the 2-in-2 state-averaged calculation used to find the ground state singlet and 1st excited singlet.

Dihedral Angle (°)	**Cσ (Orbital 26) Occupancy**	**Cπ (Orbital 27) Occupancy**
10	1.39	0.61
20	1.41	0.59
30	1.43	0.57
40	1.45	0.56
50	1.46	0.54
60	1.46	0.54
70	1.47	0.53
80	1.47	0.53
90	1.47	0.53
100	1.47	0.53
110	1.47	0.53
120	1.47	0.53
130	1.46	0.54
140	1.45	0.55
150	1.43	0.57
160	1.42	0.58
170	1.40	0.60

In the below two tables, the fractional character of the dominant term from the CI-vector from the roots in the singlet QD-NEVPT2 calculation for the free carbene is given.

Table B.2. Free carbene QD-NEVPT2 CI-vector leading term for the first root in the 2-in-2 state-averaged calculation used to find the ground state singlet and 1st excited singlet.

Dihedral Angle (°)	**CFG[20] Fractional Character**	**CFG[02] Fractional Character**	**CFG[11] Fractional Character**
10	0.891	0.105	0.004
20	0.905	0.090	0.005
30	0.927	0.070	0.003
40	0.944	0.055	0.001
50	0.956	0.044	<0.001
60	0.963	0.037	<0.001
70	0.968	0.031	<0.001
80	0.971	0.028	0.001
90	0.972	0.026	0.002
100	0.970	0.027	0.003
110	0.967	0.029	0.004
120	0.962	0.034	0.005
130	0.955	0.040	0.004
140	0.947	0.050	0.003
150	0.934	0.065	0.001
160	0.916	0.084	<0.001
170	0.898	0.100	0.002

Table B.3. Free carbene QD-NEVPT2 CI-vector leading term for the second root in the 2-in-2 state-averaged calculation used to find the ground state singlet and 1st excited singlet. N/A is used in situations where both components are too small for printing.

Dihedral Angle (°)	**CFG[11] Fractional Character**	**CFG[20] Fractional Character**	**CFG[02] Fractional Character**
10	0.996	0.004	<0.001
20	0.995	0.004	<0.001
30	0.997	N/A	N/A
40	0.999	N/A	N/A
50	> 0.999	N/A	N/A
60	> 0.999	N/A	N/A
70	> 0.999	N/A	N/A
80	0.999	N/A	N/A
90	0.998	N/A	N/A
100	0.997	0.003	<0.001
110	0.996	0.004	<0.001
120	0.995	0.005	<0.001
130	0.995	0.005	<0.001
140	0.997	0.003	<0.001
150	0.999	N/A	N/A
160	> 0.999	N/A	N/A
170	0.998	N/A	N/A

Table B.4. QD-NEVPT2 Results Using the BSS Structure from Sharon et. al.

	Sing. 1	**Trip. 1**	**Trip. 2**	**Sing. 2**	**Quin. 1**	**Trip. 3**	**Trip. 4**	**Trip. 5**
Energy (kcal/mol)	0.0	12.4	14.8	16.3	17.0	18.3	19.7	23.9

Table B.5. QD-NEVPT2 Ground State Character Using the BSS Structure from Sharon et. al.

	CFG 1 $(d_{xz})^2(C\pi^*)^0$	**Wt. CFG 1**	**CFG 2** $(d_{xz})^1(C\pi^*)^1$	**Wt. CFG 2**	**CFG 3** $(d_{xz})^0(C\pi^*)^2$	**Wt. CFG 3**
Singlet 1	222222000000	0.45	222122100000	0.29	222022200000	0.08

Table B.6. Dominant Configurations in QD-NEVPT2 Excited States Using the BSS Structure from Sharon et. al.

	CFG	**CFG Assignment**	**Wt.**
Triplet 1	222221100000	$(d_{yz})^1(C\pi^*)^1$	0.34
Triplet 2	222221100000	$(d_{yz})^1(C\pi^*)^1$	0.42
Singlet 1	222221100000	$(d_{yz})^1(C\pi^*)^1$	0.75
Quintet 1	222211110000	$(a_{2u})^2(a_{1u})^2(\sigma_{z2})^2(d_{xz})^2(d_{xy})^1(d_{yz})^1(C\pi^*)^1(d_{x2-y2})^1$	0.81
Triplet 3	222122100000	$(d_{yz})^1(C\pi^*)^1$	0.82
Triplet 4	222121110000	$(d_{xz})^1(d_{xy})^2(d_{yz})^1(C\pi^*)^1(d_{x2-y2})^1$	0.43
Triplet 5	222211110000	$(a_{2u})^2(a_{1u})^2(\sigma_{z2})^2(d_{xz})^2(d_{xy})^1(d_{yz})^1(C\pi^*)^1(d_{x2-y2})^1$	0.76

Table B.7. QD-NEVPT2 Results Using Hs Only Optimized PDB:6CUN.

	Sing. 1	**Trip. 1**	**Sing. 2**	**Trip. 2**	**Trip. 3**	**Trip. 4**	**Quin.1**	**Trip.5**
Energy (kcal/mol)	0.0	19.0	20.0	22.6	23.7	29.6	33.3	34.7

Table B.8. QD-NEVPT2 Ground State Character Using Hs Only Optimized PDB:6CUN.

	CFG 1 $(d_{xz})^2(C\pi^*)^0$	**Wt. CFG 1**	**CFG 2 $(d_{xz})^1(C\pi^*)^1$**	**Wt. CFG 2**	**CFG 3 $(d_{xz})^0(C\pi^*)^2$**	**Wt. CFG 3**
Singlet 1	222222000000	0.46	222122100000	0.28	222022200000	0.05

Table B.9. Dominant Configurations in QD-NEVPT2 Excited States Using Hs Only Optimized PDB:6CUN.

	CFG	**CFG Assignment**	**Wt.**
Triplet 1	222221100000	$(d_{yz})^1(C\pi^*)^1$	0.71
Singlet 2	222221100000	$(d_{yz})^1(C\pi^*)^1$	0.76
Triplet 2	222112110000	$(d_{xz})^1(d_{xy})^1(d_{yz})^2$ $(C\pi^*)^1(d_{x2-y2})^1$	0.39
Triplet 3	222122100000	$(d_{xz})^1(C\pi^*)^1$	0.69
Triplet 4	222121110000	$(a_{2u})^2(a_{1u})^2(\sigma_{z2})^2(d_{xz})^1$ $(d_{xy})^2(d_{yz})^1(C\pi^*)^1(d_{x2-y2})^1$	0.45
Quintet 1	222211110000	$(a_{2u})^2(a_{1u})^2(\sigma_{z2})^2(d_{xz})^2$ $(d_{xy})^1(d_{yz})^1(C\pi^*)^1(d_{x2-y2})^1$	0.79
Triplet 5	222211110000	$(a_{2u})^2(a_{1u})^2(\sigma_{z2})^2(d_{xz})^2$ $(d_{xy})^1(d_{yz})^1(C\pi^*)^1(d_{x2-y2})^1$	0.73

Table B.10. [Fe(TPP)CCl_2] DFT Single Point Energies.

	BSS (kcal/mol)	**RKS (kcal/mol)**	**Triplet (kcal/mol)**
BP86	0.00	0.00	34.9
TPSSh	0.00	0.00	31.7
B3LYP	0.00	0.28	28.9

Table B.11. [Fe(TPP)CCl_2] Loewdin BSS Spin Populations.

	Fe	**Carbene C**
BP86	0.02	-0.01
TPSSh	0.13	-0.10
B3LYP	0.43	-0.32

Table B.12. QD-NEVPT2 Results Using the [Fe(TPP)CCl_2] Model.

	Sing. 1	**Trip. 1**	**Quin. 1**	**Trip. 2**	**Trip. 3**	**Sing. 2**	**Trip. 4**	**Trip. 5**
Energy (kcal/mol)	0.0	36.5	38.2	38.6	47.6	49.0	49.5	54.8

Table B.13. QD-NEVPT2 Ground State Character Using the [Fe(TPP)CCl_2] Model.

	CFG 1 $(d_{xz})^2(C\pi^*)^0$	**Wt. CFG 1**	**CFG 2 $(d_{xz})^1(C\pi^*)^1$**	**Wt. CFG 2**	**CFG 3 $(d_{xz})^0(C\pi^*)^2$**	**Wt. CFG 3**
Singlet 1	222222000000	0.64	222122100000	0.05	222022200000	0.14

Table B.14. Dominant Configurations in QD-NEVPT2 Excited States Using the [Fe(TPP)CCl$_2$] Model.

	CFG	**CFG Assignment**	**Wt.**
Triplet 1	222212010000	$(d_{xy})^1(d_{x2-y2})^1$	0.50
Quintet 1	222211011000	$(d_{xy})^1 (d_{yz})^1(C\pi^*)^0(d_{x2-y2})^1(\sigma^*)^1$	0.53
Triplet 2	222221001000	$(d_{yz})^1(\sigma^*)^1$	0.53
Triplet 3	222221100000	$(d_{yz})^1(C\pi^*)^1$	0.57
Singlet 2	222221100000	$(d_{yz})^1(C\pi^*)^1$	0.62
Triplet 4	222221010000	$(d_{yz})^1(d_{x2-y2})^1$	0.42
Triplet 5	222212001000	$(d_{xz})^1(\sigma^*)^1$	0.37

Table B.15. Examples of Changes in Weight of Configuration Upon Addition of Roots. Example is Thiolate at 180°. The $(d_{yz})^1(C\pi^*)^1$ configuration was too small to print (e.g. 0.003).

Number of Roots	**Weight of Closed-Shell CFG**	**Weight of $(d_{xz})^1(C\pi^*)^1$ CFG**	**Weight $(d_{xz})^0(C\pi^*)^2$ CFG**
2 singlets, 2 triplets	0.71	0.01	0.10
2 singlets, 5 triplets	0.59	0.15	0.10
20 singlets, 5 triplets	0.59	0.14	0.10
2 singlets, 5 triplets, 1 quintet	0.55	0.19	0.08

Table B.16. IPC Models: QD-NEVPT2 energy relative to the minimum (90° for MeImid.; 100° for Thiolate) at select angles. (Using the 2 singlet, 5 triplet calculation for hydroxide.)

0° Dihedral Angle:						
	Singlet 1 (kcal/mol)	**Triplet 1 (kcal/mol)**	**Triplet 2 (kcal/mol)**	**Triplet 3 (kcal/mol)**	**Singlet 2 (kcal/mol)**	**Triplet 4 (kcal/mol)**
Hydroxide	1.2	15.3	19.0	22.2	25.5	25.6
Thiolate	2.4	18.1	26.0	23.3	26.6	30.0
***N*-MeImid**	2.3	20.5	28.6	26.9	30.2	36.1
90° Dihedral Angle:						
	Singlet 1 (kcal/mol)	**Triplet 1 (kcal/mol)**	**Triplet 2 (kcal/mol)**	**Triplet 3 (kcal/mol)**	**Singlet 2 (kcal/mol)**	**Triplet 4 (kcal/mol)**
Hydroxide	0.0	14.9	18.7	28.7	31.9	30.6
Thiolate	0.0	16.7	24.3	29.0	32.1	34.2
***N*-MeImid**	0.0	18.7	26.4	31.7	34.8	39.5
180° Dihedral Angle:						
	Singlet 1 (kcal/mol)	**Triplet 1 (kcal/mol)**	**Triplet 2 (kcal/mol)**	**Triplet 3 (kcal/mol)**	**Singlet 2 (kcal/mol)**	**Triplet 4 (kcal/mol)**
Hydroxide	4.8	19.0	22.7	25.3	28.9	28.9
Thiolate	5.9	21.7	29.8	26.3	29.7	33.0
***N*-MeImid**	4.6	22.9	31.1	28.8	32.2	38.4

Table B.17. QD-NEVPT2 Loewdin orbital compositions helpful for assigning orbitals in the *N*-MeImid IPC model.

Dihedral Angle	**% Fe of d_{xz} (171)**	**% Carbene Character d_{xz} (171)**	**174 Fe % of $C\pi^*$ (174)**	**% Carbene Character $C\pi^*$ (174)**
0	78.0	16.6	20.9	62.5
10	78.2	16.4	20.8	62.9
20	78.7	16.2	20.4	63.8
30	79.2	15.9	19.9	65.3
40	79.6	15.6	19.6	66.7
50	80.0	15.4	19.5	67.6
60	80.1	15.4	19.1	67.6
70	80.2	15.3	19.1	69.0
80	80.2	15.4	18.8	69.5
90	80.1	15.4	18.9	69.4
100	80.0	15.5	18.9	69.2
110	79.8	15.7	17.4	68.6
120	79.5	15.7	17.4	67.9
130	79.3	16.0	18.5	66.8
140	79.0	16.1	18.4	65.8
150	78.6	16.3	18.9	64.3
160	78.0	16.7	21.0	62.9
170	77.7	16.8	21.3	62.0
180	77.4	16.9	21.3	61.6

Table B.18. *N*-MeImid. Lowest Energy Singlet State CI-vector.

Dihedral Angle	**CFG 1 $(d_{xz})^2(C\pi^*)^0$**	**Wt. CFG 1**	**CFG 2 $(d_{xz})^1(C\pi^*)^1$**	**Wt. CFG 2**	**CFG 3 $(d_{xz})^0(C\pi^*)^2$**	**Wt. CFG 3**
0	222222000000	0.58	222122100000	0.17	222022200000	0.06
10	222222000000	0.58	222122100000	0.17	222022200000	0.06
20	222222000000	0.58	222122100000	0.17	222022200000	0.06
30	222222000000	0.58	222122100000	0.17	222022200000	0.06
40	222222000000	0.58	222122100000	0.17	222022200000	0.06
50	222222000000	0.59	222122100000	0.16	222022200000	0.06
60	222222000000	0.59	222122100000	0.16	222022200000	0.06
70	222222000000	0.60	222122100000	0.16	222022200000	0.05
80	222222000000	0.60	222122100000	0.16	222022200000	0.06
90	222222000000	0.60	222122100000	0.16	222022200000	0.06
100	222222000000	0.59	222122100000	0.16	222022200000	0.06
110	222222000000	0.59	222122100000	0.16	222022200000	0.06
120	222222000000	0.59	222122100000	0.17	222022200000	0.06
130	222222000000	0.59	222122100000	0.17	222022200000	0.06
140	222222000000	0.59	222122100000	0.17	222022200000	0.06
150	222222000000	0.58	222122100000	0.17	222022200000	0.06
160	222222000000	0.58	222122100000	0.17	222022200000	0.06
170	222222000000	0.58	222122100000	0.17	222022200000	0.06
180	222222000000	0.58	222122100000	0.17	222022200000	0.06

Table B.19. *N*-MeImid. Triplet 1 CI-vector. Approaching 90°, CFG 3 becomes slightly less heavily weighted than some more complicated configurations.

Dihedral Angle	**CFG 1 $(d_{xy})^1(d_{x2-y2})^1$**	**Wt. CFG 1**	**CFG 2 $(d_{xz})^1(d_{xy})^1(C\pi^*)^1(d_{x2-y2})^1$**	**Wt. CFG 2**	**CFG 3 $(d_{yz})^1 (C\pi^*)^1$**	**Wt. CFG 3**
0	222212010000	0.42	222112110000	0.24	222221100000	0.08
10	222212010000	0.42	222112110000	0.25	222221100000	0.07
20	222212010000	0.43	222112110000	0.25	222221100000	0.06
30	222212010000	0.44	222112110000	0.26	222221100000	0.04
40	222212010000	0.45	222112110000	0.26	222221100000	0.03
50	222212010000	0.45	222112110000	0.26	222221100000	0.03
60	222212010000	0.46	222112110000	0.26	222221100000	0.02
70	222212010000	0.47	222112110000	0.26	222221100000	0.02
80	222212010000	0.48	222112110000	0.26	222221100000	0.02
90	222212010000	0.48	222112110000	0.26	222221100000	0.02
100	222212010000	0.48	222112110000	0.26	222221100000	0.02
110	222212010000	0.47	222112110000	0.26	222221100000	0.02
120	222212010000	0.47	222112110000	0.26	222221100000	0.02
130	222212010000	0.46	222112110000	0.26	222221100000	0.03
140	222212010000	0.45	222112110000	0.26	222221100000	0.04
150	222212010000	0.44	222112110000	0.25	222221100000	0.05
160	222212010000	0.43	222112110000	0.25	222221100000	0.07
170	222212010000	0.42	222112110000	0.24	222221100000	0.09
180	222212010000	0.41	222112110000	0.23	222221100000	0.10

Table B.20. *N*-MeImid. Triplet 2 state CI-vector.

Dihedral Angle	**CFG 1 $(d_{yz})^1(d_{x2-y2})^1$**	**Wt. CFG 1**	**CFG 2 $(d_{xz})^1(d_{yz})^1$ $(C\pi^*)^1(d_{x2-y2})^1$**	**Wt. CFG 2**	**CFG for $(d_{yz})^1(C\pi^*)^1$**	**Wt. CFG**
0	222221010000	0.44	222121110000	0.29	222221100000	0.01
10	222221010000	0.44	222121110000	0.28	222221100000	0.02
20	222221010000	0.35	222121110000	0.22	222221100000	0.18
30	222221010000	0.38	222121110000	0.26	222221100000	0.10
40	222221010000	0.43	222121110000	0.29	222221100000	0.03
50	222221010000	0.45	222121110000	0.29	222221100000	0.01
60	222221010000	0.46	222121110000	0.30	222221100000	0.00
70	222221010000	0.46	222121110000	0.29	222221100000	0.00
80	222221010000	0.47	222121110000	0.30	222221100000	0.00
90	222221010000	0.47	222121110000	0.30	222221100000	0.00
100	222221010000	0.47	222121110000	0.30	222221100000	0.00
110	222221010000	0.47	222121110000	0.30	222221100000	0.00
120	222221010000	0.47	222121110000	0.30	222221100000	0.00
130	222221010000	0.45	222121110000	0.29	222221100000	0.01
140	222221010000	0.42	222121110000	0.28	222221100000	0.04
150	222221010000	0.27	222121110000	0.19	222221100000	0.27
160	222221010000	0.43	222121110000	0.27	222221100000	0.04
170	222221010000	0.44	222121110000	0.28	222221100000	0.01
180	222221010000	0.44	222121110000	0.28	222221100000	0.00

Table B.21. *N*-MeImid. Triplet 3 state CI-vector.

Dihedral Angle	**CFG 1 $(d_{yz})^1(C\pi^*)^1$**	**Wt. CFG 1**	**CFG 2 $(d_{xz})^1(d_{xy})^1$ $(C\pi^*)^1(d_{x2-y2})^1$**	**Wt. CFG 2**	**CFG for $(d_{yz})^1(d_{x2-y2})^1$**	**Wt. CFG**
0	222221100000	0.68	222112110000	0.07	222221010000	0.01
10	222221100000	0.68	222112110000	0.06	222221010000	0.01
20	222221100000	0.52	222112110000	0.05	222221010000	0.10
30	222221100000	0.63	222112110000	0.03	222221010000	0.08
40	222221100000	0.72	222112110000	0.04	222221010000	0.02
50	222221100000	0.74	222112110000	0.04	222221010000	0.01
60	222221100000	0.75	222112110000	0.04	222221010000	0.00
70	222221100000	0.76	222112110000	0.03	222221010000	0.00
80	222221100000	0.76	222112110000	0.04	222221010000	0.01
90	222221100000	0.76	222112110000	0.04	222221010000	0.01
100	222221100000	0.76	222112110000	0.04	222221010000	0.01
110	222221100000	0.76	222112110000	0.04	222221010000	0.01
120	222221100000	0.75	222112110000	0.04	222221010000	0.00
130	222221100000	0.74	222112110000	0.04	222221010000	0.01
140	222221100000	0.70	222112110000	0.03	222221010000	0.04
150	222221100000	0.44	222112110000	0.02	222221010000	0.20
160	222221100000	0.66	222112110000	0.06	222221010000	0.02
170	222221100000	0.68	222112110000	0.07	222221010000	0.00
180	222221100000	0.67	222112110000	0.07	222221010000	0.00

Table B.22. *N*-MeImid 1st Excited Singlet State CI-vector.

Dihedral Angle	**CFG 1 $(d_{yz})^1(C\pi^*)^1$**	**Wt. CFG 1**	**CFG 2 $(d_{xy})^1(d_{x2-y2})^1$**	**Wt. CFG 2**	**CFG 3 $(d_{xz})^1(d_{yz})^1(C\pi^*)^2$**	**Wt. CFG 3**
0	222221100000	0.71	222212010000	0.05	222121200000	0.05
10	222221100000	0.71	222212010000	0.05	222121200000	0.05
20	222221100000	0.71	222212010000	0.05	222121200000	0.05
30	222221100000	0.70	222212010000	0.06	222121200000	0.05
40	222221100000	0.69	222212010000	0.06	222121200000	0.05
50	222221100000	0.68	222212010000	0.07	222121200000	0.05
60	222221100000	0.67	222212010000	0.08	222121200000	0.04
70	222221100000	0.66	222212010000	0.09	222121200000	0.04
80	222221100000	0.66	222212010000	0.09	222121200000	0.04
90	222221100000	0.66	222212010000	0.09	222121200000	0.04
100	222221100000	0.66	222212010000	0.09	222121200000	0.04
110	222221100000	0.66	222212010000	0.08	222121200000	0.05
120	222221100000	0.67	222212010000	0.08	222121200000	0.05
130	222221100000	0.68	222212010000	0.07	222121200000	0.05
140	222221100000	0.69	222212010000	0.06	222121200000	0.05
150	222221100000	0.69	222212010000	0.05	222121200000	0.05
160	222221100000	0.71	222212010000	0.05	222121200000	0.05
170	222221100000	0.71	222212010000	0.05	222121200000	0.05
180	222221100000	0.71	222212010000	0.04	222121200000	0.05

Table B.23. *N*-MeImid. Quintet: $(a_{2u})^2(a_{1u})^2(\sigma_{z2})^2(d_{xz})^2(d_{xy})^1(d_{yz})^1(C\pi^*)^1(d_{x2-y2})^1$

Dihedral Angle	**CFG 1**	**Wt. CFG 1**
0	222211110000	0.80
10	222211110000	0.80
20	222211110000	0.80
30	222211110000	0.80
40	222211110000	0.80
50	222211110000	0.80
60	222211110000	0.80
70	222211110000	0.80
80	222211110000	0.80
90	222211110000	0.81
100	222211110000	0.81
110	222211110000	0.81
120	222211110000	0.81
130	222211110000	0.81
140	222211110000	0.80
150	222211110000	0.80
160	222211110000	0.80
170	222211110000	0.80
180	222211110000	0.80

Table B.24. *N*-MeImid. Fourth Triplet.
CFG 3 is $(a_{2u})^2(a_{1u})^2(\sigma_{z2})^2(d_{xz})^2(d_{xy})^1(d_{yz})^1(C\pi^*)^1(d_{x2-y2})^1$

Dihedral Angle	**CFG 1 $(d_{xz})^1(C\pi^*)^1$**	**Wt. CFG 1**	**CFG 2 $(d_{xy})^1 (C\pi^*)^1$**	**Wt. CFG 2**	**CFG 3**	**Wt. CFG 3**
0	222122100000	0.69	222212100000	0.11	222211110000	0.03
10	222122100000	0.63	222212100000	0.16	222211110000	0.03
20	222122100000	0.63	222212100000	0.16	222211110000	0.03
30	222122100000	0.63	222212100000	0.16	222211110000	0.03
40	222122100000	0.63	222212100000	0.16	222211110000	0.03
50	222122100000	0.63	222212100000	0.17	222211110000	0.03
60	222122100000	0.71	222212100000	0.09	222211110000	0.03
70	222122100000	0.69	222212100000	0.10	222211110000	0.03
80	222122100000	0.77	222212100000	0.03	222211110000	0.03
90	222122100000	0.79	222212100000	0.01	222211110000	0.03
100	222122100000	0.80	222212100000	0.00	222211110000	0.03
110	222122100000	0.80	222212100000	0.01	222211110000	0.03
120	222122100000	0.77	222212100000	0.03	222211110000	0.03
130	222122100000	0.73	222212100000	0.07	222211110000	0.03
140	222122100000	0.63	222212100000	0.03	222211110000	0.03
150	222122100000	0.58	222212100000	0.20	222211110000	0.03
160	222122100000	0.50	222212100000	0.27	222211110000	0.02
170	222122100000	0.41	222212100000	0.35	222211110000	0.02
180	222122100000	0.37	222212100000	0.39	222211110000	0.02

Table B.25. *N*-MeImid Fifth Triplet: $(a_{2u})^2(a_{1u})^2(\sigma_{z2})^2(d_{xz})^2(d_{xy})^1(d_{yz})^1(C\pi^*)^1(d_{x2-y2})^1$

Dihedral Angle	**CFG 1**	**Wt. CFG 1**
0	222211110000	0.74
10	222211110000	0.74
20	222211110000	0.74
30	222211110000	0.74
40	222211110000	0.74
50	222211110000	0.74
60	222211110000	0.75
70	222211110000	0.74
80	222211110000	0.75
90	222211110000	0.75
100	222211110000	0.75
110	222211110000	0.75
120	222211110000	0.75
130	222211110000	0.75
140	222211110000	0.74
150	222211110000	0.74
160	222211110000	0.74
170	222211110000	0.74
180	222211110000	0.74

Table B.26. QD-NEVPT2 Loewdin orbital compositions helpful for assigning orbitals in the thiolate IPC model.

Dihedral Angle	**% Fe of d_{xz} (162)**	**% Carbene Character d_{xz} (162)**	**Fe % of $C\pi^*$ (165)**	**% Carbene Character $C\pi^*$ (165)**
0	77.5	17.0	21.0	61.1
10	77.8	16.5	20.8	61.4
20	77.9	16.5	20.9	61.0
30	79.0	16.0	19.7	64.2
40	79.4	15.8	19.5	65.9
50	79.7	15.6	19.2	67.2
60	79.8	15.5	18.9	68.2
70	79.8	15.6	19.4	68.5
80	80.0	15.5	19.0	69.1
90	79.9	15.7	19.0	69.0
100	79.8	15.6	19.0	68.8
110	79.6	15.7	19.2	68.3
120	79.4	15.8	19.4	67.3
130	79.2	15.9	19.7	66.6
140	78.6	16.3	20.1	64.8
150	78.0	16.6	20.7	63.1
160	77.3	16.9	21.4	61.1
170	76.8	17.2	21.8	60.0
180	76.6	17.3	21.7	59.6

Table B.27. Thiolate Lowest Energy Singlet State CI-vector.

Dihedral Angle	**CFG 1 $(d_{xz})^2(C\pi^*)^0$**	**Wt. CFG 1**	**CFG 2 $(d_{xz})^1(C\pi^*)^1$**	**Wt. CFG 2**	**CFG 3 $(d_{xz})^0(C\pi^*)^2$**	**Wt. CFG 3**
0	222222000000	0.55	222122100000	0.20	222022200000	0.08
10	222222000000	0.55	222122100000	0.20	222022200000	0.08
20	222222000000	0.55	222122100000	0.19	222022200000	0.08
30	222222000000	0.55	222122100000	0.20	222022200000	0.07
40	222222000000	0.56	222122100000	0.20	222022200000	0.07
50	222222000000	0.56	222122100000	0.20	222022200000	0.07
60	222222000000	0.56	222122100000	0.19	222022200000	0.07
70	222222000000	0.57	222122100000	0.19	222022200000	0.06
80	222222000000	0.57	222122100000	0.19	222022200000	0.06
90	222222000000	0.57	222122100000	0.19	222022200000	0.07
100	222222000000	0.57	222122100000	0.19	222022200000	0.07
110	222222000000	0.57	222122100000	0.19	222022200000	0.07
120	222222000000	0.56	222122100000	0.19	222022200000	0.07
130	222222000000	0.56	222122100000	0.19	222022200000	0.07
140	222222000000	0.56	222122100000	0.19	222022200000	0.07
150	222222000000	0.56	222122100000	0.19	222022200000	0.07
160	222222000000	0.55	222122100000	0.19	222022200000	0.08
170	222222000000	0.55	222122100000	0.19	222022200000	0.08
180	222222000000	0.55	222122100000	0.19	222022200000	0.08

Table B.28. Thiolate Triplet 1 CI-vector.

Dihedral Angle	**CFG 1 $(d_{xy})^1(d_{x2-y2})^1$**	**Wt. CFG 1**	**CFG 2 $(d_{xz})^1(d_{xy})^1(C\pi^*)^1(d_{x2-y2})^1$**	**Wt. CFG 2**	**CFG 3 $(d_{yz})^1(C\pi^*)^1$**	**Wt. CFG 3**
0	222212010000	0.39	222112110000	0.27	222221100000	0.10
10	222212010000	0.39	222112110000	0.27	222221100000	0.09
20	222212010000	0.40	222112110000	0.27	222221100000	0.08
30	222212010000	0.41	222112110000	0.29	222221100000	0.05
40	222212010000	0.42	222112110000	0.29	222221100000	0.03
50	222212010000	0.43	222112110000	0.30	222221100000	0.03
60	222212010000	0.44	222112110000	0.30	222221100000	0.02
70	222212010000	0.44	222112110000	0.29	222221100000	0.02
80	222212010000	0.45	222112110000	0.29	222221100000	0.02
90	222212010000	0.45	222112110000	0.29	222221100000	0.02
100	222212010000	0.45	222112110000	0.29	222221100000	0.02
110	222212010000	0.45	222112110000	0.30	222221100000	0.02
120	222212010000	0.44	222112110000	0.29	222221100000	0.03
130	222212010000	0.43	222112110000	0.29	222221100000	0.03
140	222212010000	0.43	222112110000	0.29	222221100000	0.04
150	222212010000	0.41	222112110000	0.28	222221100000	0.06
160	222212010000	0.40	222112110000	0.27	222221100000	0.09
170	222212010000	0.39	222112110000	0.25	222221100000	0.12
180	222212010000	0.38	222112110000	0.25	222221100000	0.13

Table B.29. Thiolate Triplet 2 CI-vector.

Dihedral Angle	**CFG 1 $(d_{yz})^1(d_{x2-y2})^1$**	**Wt. CFG 1**	**CFG 2 $(d_{xz})^1(d_{yz})^1$ $(C\pi^*)^1(d_{x2-y2})^1$**	**Wt. CFG 2**	**CFG for $(d_{yz})^1(C\pi^*)^1$**	**Wt. CFG**
0	222221010000	0.42	222121110000	0.33	222221100000	0.00
10	222221010000	0.42	222121110000	0.33	222221100000	0.00
20	222221010000	0.42	222121110000	0.33	222221100000	0.01
30	222221010000	0.31	222121110000	0.24	222221100000	0.21
40	222221010000	0.40	222121110000	0.32	222221100000	0.03
50	222221010000	0.42	222121110000	0.33	222221100000	0.01
60	222221010000	0.43	222121110000	0.33	222221100000	0.00
70	222221010000	0.44	222121110000	0.32	222221100000	0.00
80	222221010000	0.44	222121110000	0.33	222221100000	0.00
90	222221010000	0.44	222121110000	0.33	222221100000	0.00
100	222221010000	0.44	222121110000	0.33	222221100000	0.00
110	222221010000	0.44	222121110000	0.33	222221100000	0.00
120	222221010000	0.43	222121110000	0.33	222221100000	0.00
130	222221010000	0.42	222121110000	0.32	222221100000	0.02
140	222221010000	0.34	222121110000	0.27	222221100000	0.14
150	222221010000	0.40	222121110000	0.39	222221100000	0.07
160	222221010000	0.42	222121110000	0.32	222221100000	0.01
170	222221010000	0.43	222121110000	0.33	222221100000	0.00
180	222221010000	0.43	222121110000	0.33	222221100000	0.00

Table B.30. Thiolate Triplet 3 CI-vector.

Dihedral Angle	**CFG 1 $(d_{yz})^1(C\pi^*)^1$**	**Wt. CFG 1**	**CFG 2 $(d_{xz})^1(d_{xy})^1$ $(C\pi^*)^1(d_{x2-y2})^1$**	**Wt. CFG 2**	**CFG for $(d_{yz})^1(d_{x2-y2})^1$**	**Wt. CFG**
0	222221100000	0.68	222112110000	0.08	222221010000	0.00
10	222221100000	0.69	222112110000	0.08	222221010000	0.01
20	222221100000	0.70	222112110000	0.07	222221010000	0.00
30	222221100000	0.50	222112110000	0.05	222221010000	0.11
40	222221100000	0.72	222112110000	0.04	222221010000	0.03
50	222221100000	0.75	222112110000	0.04	222221010000	0.01
60	222221100000	0.76	222112110000	0.04	222221010000	0.00
70	222221100000	0.76	222112110000	0.04	222221010000	0.00
80	222221100000	0.78	222112110000	0.04	222221010000	0.00
90	222221100000	0.77	222112110000	0.04	222221010000	0.00
100	222221100000	0.78	222112110000	0.04	222221010000	0.00
110	222221100000	0.76	222112110000	0.04	222221010000	0.00
120	222221100000	0.76	222112110000	0.04	222221010000	0.00
130	222221100000	0.73	222112110000	0.04	222221010000	0.02
140	222221100000	0.60	222112110000	0.03	222221010000	0.10
150	222221100000	0.65	222112110000	0.06	222221010000	0.04
160	222221100000	0.68	222112110000	0.08	222221010000	0.00
170	222221100000	0.65	222112110000	0.09	222221010000	0.00
180	222221100000	0.64	222112110000	0.10	222221010000	0.00

Table B.31. Thiolate 1st Excited Singlet State CI-vector.

Dihedral Angle	**CFG 1 $(d_{yz})^1(C\pi^*)^1$**	**Wt. CFG 1**	**CFG 2 $(d_{xy})^1(d_{x2-y2})^1$**	**Wt. CFG 2**	**CFG 3 $(d_{xz})^1(d_{yz})^1(C\pi^*)^2$**	**Wt. CFG 3**
0	222221100000	0.72	222212010000	0.04	222121200000	0.06
10	222221100000	0.72	222212010000	0.04	222121200000	0.06
20	222221100000	0.72	222212010000	0.04	222121200000	0.06
30	222221100000	0.72	222212010000	0.04	222121200000	0.05
40	222221100000	0.71	222212010000	0.05	222121200000	0.05
50	222221100000	0.70	222212010000	0.06	222121200000	0.05
60	222221100000	0.69	222212010000	0.06	222121200000	0.05
70	222221100000	0.68	222212010000	0.07	222121200000	0.05
80	222221100000	0.68	222212010000	0.07	222121200000	0.05
90	222221100000	0.68	222212010000	0.08	222121200000	0.05
100	222221100000	0.68	222212010000	0.07	222121200000	0.05
110	222221100000	0.69	222212010000	0.07	222121200000	0.05
120	222221100000	0.69	222212010000	0.06	222121200000	0.05
130	222221100000	0.70	222212010000	0.06	222121200000	0.05
140	222221100000	0.71	222212010000	0.05	222121200000	0.05
150	222221100000	0.71	222212010000	0.04	222121200000	0.05
160	222221100000	0.72	222212010000	0.04	222121200000	0.06
170	222221100000	0.72	222212010000	0.04	222121200000	0.06
180	222221100000	0.72	222212010000	0.04	222121200000	0.06

Table B.32. Thiolate Quintet: $(a_{2u})^2(a_{1u})^2(\sigma_{z2})^2(d_{xz})^2(d_{xy})^1(d_{yz})^1(C\pi^*)^1(d_{x2-y2})^1$

Dihedral Angle	**CFG 1**	**Wt. CFG 1**
0	222211110000	0.82
10	222211110000	0.82
20	222211110000	0.81
30	222211110000	0.82
40	222211110000	0.82
50	222211110000	0.82
60	222211110000	0.82
70	222211110000	0.81
80	222211110000	0.82
90	222211110000	0.82
100	222211110000	0.82
110	222211110000	0.82
120	222211110000	0.82
130	222211110000	0.82
140	222211110000	0.82
150	222211110000	0.82
160	222211110000	0.81
170	222211110000	0.81
180	222211110000	0.82

Table B.33. Thiolate Triplet 4: CFG 3 is $(a_{2u})^2(a_{1u})^2(\sigma_{z2})^2(d_{xz})^2(d_{xy})^1(d_{yz})^1(C\pi^*)^1(d_{x2-y2})^1$

Dihedral Angle	**CFG 1** $(d_{xz})^1(C\pi^*)^1$	**Wt. CFG 1**	**CFG 2** $(d_{xy})^1 (C\pi^*)^1$	**Wt. CFG 2**	**CFG 3**	**Wt. CFG 3**
0	222122100000	0.82	222212100000	0.00	222211110000	0.03
10	222122100000	0.80	222212100000	0.02	222211110000	0.03
20	222122100000	0.79	222212100000	0.03	222211110000	0.03
30	222122100000	0.78	222212100000	0.04	222211110000	0.03
40	222122100000	0.76	222212100000	0.03	222211110000	0.03
50	222122100000	0.78	222212100000	0.04	222211110000	0.03
60	222122100000	0.80	222212100000	0.01	222211110000	0.03
70	222122100000	0.76	222212100000	0.05	222211110000	0.03
80	222122100000	0.81	222212100000	0.00	222211110000	0.03
90	222122100000	0.82	222212100000	0.00	222211110000	0.03
100	222122100000	0.82	222212100000	0.00	222211110000	0.03
110	222122100000	0.82	222212100000	0.00	222211110000	0.03
120	222122100000	0.82	222212100000	0.00	222211110000	0.03
130	222122100000	0.75	222212100000	0.07	222211110000	0.03
140	222122100000	0.80	222212100000	0.02	222211110000	0.03
150	222122100000	0.78	222212100000	0.04	222211110000	0.03
160	222122100000	0.78	222212100000	0.03	222211110000	0.03
170	222122100000	0.80	222212100000	0.02	222211110000	0.03
180	222122100000	0.82	222212100000	0.00	222211110000	0.03

Table B.34. Thiolate Triplet 5: $(a_{2u})^2(a_{1u})^2(\sigma_{z2})^2(d_{xz})^2(d_{xy})^1(d_{yz})^1(C\pi^*)^1(d_{x2-y2})^1$

Dihedral Angle	**CFG 1**	**Wt. CFG 1**
0	222211110000	0.76
10	222211110000	0.76
20	222211110000	0.75
30	222211110000	0.76
40	222211110000	0.76
50	222211110000	0.76
60	222211110000	0.76
70	222211110000	0.76
80	222211110000	0.76
90	222211110000	0.77
100	222211110000	0.77
110	222211110000	0.77
120	222211110000	0.77
130	222211110000	0.76
140	222211110000	0.76
150	222211110000	0.76
160	222211110000	0.76
170	222211110000	0.75
180	222211110000	0.76

Table B.35. QD-NEVPT2 Loewdin Orbital Compositions Helpful for Assigning Orbitals in the Hydroxide IPC Model. State-Averaged Calculation: Two Singlets, Five Triplets.

Dihedral Angle	**% Fe of d_{xz} (155)**	**% Carbene Character d_{xz} (155)**	**Fe % of $C\pi^*$ (157)**	**% Carbene Character $C\pi^*$ (157)**
0	75.0	18.4	23.1	58.9
10	75.0	18.4	23.0	59.1
20	75.0	18.4	23.1	59.5
30	75.1	18.7	23.2	60.7
40	75.0	19.1	23.2	61.4
50	75.0	19.4	23.4	62.3
60	68.7	19.4	23.5	63.7
70	75.0	19.6	23.5	62.6
80	74.8	19.8	23.8	64.8
90	74.6	19.9	23.7	64.9
100	74.7	19.8	23.7	64.7
110	74.7	19.7	23.6	64.2
120	74.8	19.6	23.7	63.7
130	74.8	19.3	23.7	62.7
140	74.8	19.2	23.5	61.6
150	74.7	18.9	23.4	60.4
160	74.6	18.7	23.4	59.3
170	74.5	18.6	23.5	58.3
180	74.5	18.6	23.5	58.0

Table B.36. Hydroxide Lowest Energy Singlet State CI-Vector. State-Averaged Calculation: Two Singlets, Five Triplets.

Dihedral Angle	**CFG 1 $(d_{xz})^2(C\pi^*)^0$**	**Wt. CFG 1**	**CFG 2 $(d_{xz})^1(C\pi^*)^1$**	**Wt. CFG 2**	**CFG 3 $(d_{xz})^0(C\pi^*)^2$**	**Wt. CFG 3**
0	222222000000	0.56	222212100000	0.18	222202200000	0.11
10	222222000000	0.56	222212100000	0.18	222202200000	0.11
20	222222000000	0.57	222212100000	0.17	222202200000	0.10
30	222222000000	0.58	222212100000	0.17	222202200000	0.10
40	222222000000	0.58	222212100000	0.16	222202200000	0.10
50	222222000000	0.59	222212100000	0.15	222202200000	0.10
60	222222000000	0.60	222212100000	0.14	222202200000	0.10
70	222222000000	0.61	222212100000	0.14	222202200000	0.10
80	222222000000	0.61	222212100000	0.13	222202200000	0.10
90	222222000000	0.61	222212100000	0.13	222202200000	0.10
100	222222000000	0.61	222212100000	0.14	222202200000	0.10
110	222222000000	0.60	222212100000	0.14	222202200000	0.10
120	222222000000	0.60	222212100000	0.14	222202200000	0.10
130	222222000000	0.59	222212100000	0.15	222202200000	0.10
140	222222000000	0.58	222212100000	0.16	222202200000	0.10
150	222222000000	0.58	222212100000	0.16	222202200000	0.10
160	222222000000	0.57	222212100000	0.17	222202200000	0.10
170	222222000000	0.56	222212100000	0.18	222202200000	0.11
180	222222000000	0.56	222212100000	0.18	222202200000	0.11

Table B.37. Hydroxide Lowest Energy Singlet State CI-Vector. State-Averaged Calculation: Two Singlets, Five Triplets, 1 Quintet. Yellow marks state-averaged calculations with Lower Quintet; these especially agree well with the 2 singlet, 5 triplet calculation results.

Dihedral Angle	**CFG 1 $(d_{xz})^2(C\pi^*)^0$**	**Wt. CFG 1**	**CFG 2 $(d_{xz})^1(C\pi^*)^1$**	**Wt. CFG 2**	**CFG 3 $(d_{xz})^0(C\pi^*)^2$**	**Wt. CFG 3**
0	222222000000	0.54	222122100000	0.21	222022200000	0.09
10	222222000000	0.61	222212100000	0.07	222202200000	0.07
20	222222000000	0.61	222122100000	0.08	222022200000	0.10
30	222222000000	0.62	222122100000	0.09	222022200000	0.13
40	222222000000	0.53	222122100000	0.22	222022200000	0.08
50	222222000000	0.53	222122100000	0.23	222022200000	0.08
60	222222000000	0.54	222122100000	0.22	222022200000	0.08
70	222222000000	0.64	222122100000	0.07	222022200000	0.12
80	222222000000	0.54	222122100000	0.22	222022200000	0.07
90	222222000000	0.55	222122100000	0.22	222022200000	0.08
100	222222000000	0.64	222122100000	0.07	222022200000	0.13
110	222222000000	0.64	222122100000	0.08	222022200000	0.13
120	222222000000	0.64	222122100000	0.08	222022200000	0.13
130	222222000000	0.63	222122100000	0.08	222022200000	0.13
140	222222000000	0.63	222122100000	0.08	222022200000	0.12
150	222222000000	0.62	222122100000	0.08	222022200000	0.11
160	222222000000	0.61	222122100000	0.07	222022200000	0.07
170	222222000000	0.61	222212100000	0.07	222202200000	0.07
180	222222000000	0.55	222122100000	0.20	222022200000	0.10

Table B.38. Hydroxide Triplet 1 State CI-Vector. State-Averaged Calculation: Two Singlets, Five Triplets.

Dihedral Angle	**CFG 1 $(d_{xy})^1(d_{x2-y2})^1$**	**Wt. CFG 1**	**CFG 2 $(d_{xy})^1(d_{xz})^1(C\pi^*)^1(d_{x2-y2})^1$**	**Wt. CFG 2**	**CFG 3 $(d_{xy})^1(d_{xz})^0(d_{yz})^2(C\pi^*)^2(d_{x2-y2})^1$**	**Wt. CFG 3**
0	222122010000	0.42	222112110000	0.29	222102210000	0.09
10	222122010000	0.42	222112110000	0.29	222102210000	0.09
20	222122010000	0.43	222112110000	0.29	222102210000	0.09
30	222122010000	0.44	222112110000	0.28	222102210000	0.09
40	222122010000	0.45	222112110000	0.28	222102210000	0.09
50	222122010000	0.47	222112110000	0.27	222102210000	0.09
60	222122010000	0.48	222112110000	0.27	222102210000	0.09
70	222122010000	0.48	222112110000	0.26	222102210000	0.09
80	222122010000	0.49	222112110000	0.26	222102210000	0.09
90	222122010000	0.49	222112110000	0.26	222102210000	0.09
100	222122010000	0.49	222112110000	0.26	222102210000	0.09
110	222122010000	0.48	222112110000	0.27	222102210000	0.09
120	222122010000	0.48	222112110000	0.27	222102210000	0.09
130	222122010000	0.47	222112110000	0.27	222102210000	0.09
140	222122010000	0.45	222112110000	0.28	222102210000	0.09
150	222122010000	0.44	222112110000	0.28	222102210000	0.09
160	222122010000	0.43	222112110000	0.28	222102210000	0.09
170	222122010000	0.42	222112110000	0.28	222102210000	0.09
180	222122010000	0.42	222112110000	0.28	222102210000	0.09

Table B.39. Hydroxide Triplet 2 State CI-Vector. State-Averaged Calculation: Two Singlets, Five Triplets.

Dihedral Angle	**CFG 1 $(d_{yz})^1(d_{x2-y2})^1$**	**Wt. CFG 1**	**CFG 2 $(d_{xz})^1(d_{yz})^1$ $(C\pi^*)^1(d_{x2-y2})^1$**	**Wt. CFG 2**	**CFG for $(d_{yz})^1(C\pi^*)^1$**	**Wt. CFG**
0	222221010000	0.42	222211110000	0.32	222221100000	0.01
10	222221010000	0.42	222211110000	0.32	222221100000	0.01
20	222221010000	0.43	222211110000	0.32	222221100000	0.01
30	222221010000	0.44	222211110000	0.32	222221100000	0.00
40	222221010000	0.45	222211110000	0.31	222221100000	0.00
50	222221010000	0.46	222211110000	0.30	222221100000	0.00
60	222221010000	0.47	222211110000	0.30	222221100000	0.00
70	222221010000	0.47	222211110000	0.29	222221100000	0.00
80	222221010000	0.48	222211110000	0.29	222221100000	0.00
90	222221010000	0.48	222211110000	0.29	222221100000	0.00
100	222221010000	0.48	222211110000	0.29	222221100000	0.00
110	222221010000	0.47	222211110000	0.29	222221100000	0.00
120	222221010000	0.47	222211110000	0.30	222221100000	0.00
130	222221010000	0.46	222211110000	0.30	222221100000	0.00
140	222221010000	0.45	222211110000	0.31	222221100000	0.01
150	222221010000	0.43	222211110000	0.31	222221100000	0.01
160	222221010000	0.42	222211110000	0.32	222221100000	0.01
170	222221010000	0.42	222211110000	0.32	222221100000	0.01
180	222221010000	0.42	222211110000	0.32	222221100000	0.01

Table B.40. Hydroxide Triplet 3 State CI-Vector. State-Averaged Calculation: Two Singlets, Five Triplets.

Dihedral Angle	**CFG 1** $(d_{yz})^1(C\pi^*)^1$	**Wt. CFG 1**	**CFG 2** $(d_{xz})^1(d_{yz})^1(C\pi^*)^2$	**Wt. CFG 2**	**CFG 3** $(d_{xy})^1(d_{xz})^1(C\pi^*)^1(d_{x2-y2})^1$	**Wt. CFG 3**
0	222221100000	0.72	222211200000	0.05	222112110000	0.06
10	222221100000	0.72	222211200000	0.05	222112110000	0.06
20	222221100000	0.73	222211200000	0.05	222112110000	0.05
30	222221100000	0.74	222211200000	0.06	222112110000	0.05
40	222221100000	0.74	222211200000	0.06	222112110000	0.05
50	222221100000	0.74	222211200000	0.06	222112110000	0.04
60	222221100000	0.75	222211200000	0.06	222112110000	0.04
70	222221100000	0.75	222211200000	0.06	222112110000	0.04
80	222221100000	0.75	222211200000	0.06	222112110000	0.04
90	222221100000	0.75	222211200000	0.06	222112110000	0.04
100	222221100000	0.75	222211200000	0.06	222112110000	0.04
110	222221100000	0.75	222211200000	0.06	222112110000	0.04
120	222221100000	0.75	222211200000	0.06	222112110000	0.04
130	222221100000	0.74	222211200000	0.06	222112110000	0.04
140	222221100000	0.74	222211200000	0.06	222112110000	0.05
150	222221100000	0.73	222211200000	0.05	222112110000	0.05
160	222221100000	0.72	222211200000	0.05	222112110000	0.06
170	222221100000	0.71	222211200000	0.05	222112110000	0.06
180	222221100000	0.70	222211200000	0.05	222112110000	0.06

Table B.41. Hydroxide 1st Excited Singlet State CI-Vector. State-Averaged Calculation: Two Singlets, Five Triplets.

Dihedral Angle	**CFG 1 $(d_{yz})^1(C\pi^*)^1$**	**Wt. CFG 1**	**CFG 2 $(d_{xy})^1(d_{x2-y2})^1$**	**Wt. CFG 2**	**CFG 3 $(d_{xz})^1(d_{yz})^1(C\pi^*)^2$**	**Wt. CFG 3**
0	222221100000	0.70	222122010000	0.04	222211200000	0.08
10	222221100000	0.70	222122010000	0.04	222211200000	0.08
20	222221100000	0.70	222122010000	0.05	222211200000	0.08
30	222221100000	0.69	222122010000	0.05	222211200000	0.08
40	222221100000	0.68	222122010000	0.06	222211200000	0.08
50	222221100000	0.67	222122010000	0.07	222211200000	0.08
60	222221100000	0.66	222122010000	0.08	222211200000	0.08
70	222221100000	0.65	222122010000	0.09	222211200000	0.08
80	222221100000	0.64	222122010000	0.09	222211200000	0.08
90	222221100000	0.64	222122010000	0.09	222211200000	0.08
100	222221100000	0.64	222122010000	0.09	222211200000	0.08
110	222221100000	0.65	222122010000	0.08	222211200000	0.08
120	222221100000	0.66	222122010000	0.08	222211200000	0.08
130	222221100000	0.67	222122010000	0.07	222211200000	0.08
140	222221100000	0.68	222122010000	0.06	222211200000	0.08
150	222221100000	0.69	222122010000	0.05	222211200000	0.08
160	222221100000	0.70	222122010000	0.05	222211200000	0.08
170	222221100000	0.70	222122010000	0.04	222211200000	0.08
180	222221100000	0.71	222122010000	0.04	222211200000	0.08

Table B.42. Hydroxide 4th Triplet CI-Vector.
CFG2: $(a_{2u})^2(a_{1u})^2(\sigma_{z2})^2(d_{xz})^2(d_{xy})^1(d_{yz})^1(C\pi^*)^1(d_{x2-y2})^1$.
CFG 3 involves the porphyrin.

Dihedral Angle	**CFG 1 $(d_{xz})^1(C\pi^*)^1$**	**Wt. CFG 1**	**CFG 2**	**Wt. CFG 2**	**CFG 3**	**Wt. CFG 3**
0	222212100000	0.85	222121110000	0.03	211212101100	0.03
10	222212100000	0.85	222121110000	0.03	211212101100	0.02
20	222212100000	0.85	222121110000	0.03	211212101100	0.02
30	222212100000	0.84	222121110000	0.03	211212101100	0.02
40	222212100000	0.84	222121110000	0.03	211212101010	0.02
50	222212100000	0.84	222121110000	0.03	211212101010	0.02
60	222212100000	0.84	222121110000	0.03	211212101010	0.02
70	222212100000	0.84	222121110000	0.03	211212101010	0.01
80	222212100000	0.84	222121110000	0.03	211212101010	0.01
90	222212100000	0.84	222121110000	0.03	211212101010	0.02
100	222212100000	0.84	222121110000	0.03	211212101010	0.02
110	222212100000	0.84	222121110000	0.03	211212101010	0.02
120	222212100000	0.84	222121110000	0.03	211212101010	0.02
130	222212100000	0.84	222121110000	0.03	211212101010	0.02
140	222212100000	0.84	222121110000	0.03	211212101100	0.02
150	222212100000	0.84	222121110000	0.03	211212101100	0.02
160	222212100000	0.85	222121110000	0.03	211212101100	0.03
170	222212100000	0.85	222121110000	0.03	211212101100	0.03
180	222212100000	0.85	222121110000	0.03	211212101100	0.03

Table B.43. Hydroxide Triplet 5: $(a_{2u})^2(a_{1u})^2(\sigma_{z2})^2(d_{xy})^1$ $(d_{xz})^2(d_{yz})^1(C\pi^*)^1(d_{x2-y2})^1$

Dihedral Angle	**CFG 1**	**Wt. CFG 1**
0	222121110000	0.76
10	222121110000	0.76
20	222121110000	0.76
30	222121110000	0.76
40	222121110000	0.76
50	222121110000	0.75
60	222121110000	0.75
70	222121110000	0.75
80	222121110000	0.75
90	222121110000	0.75
100	222121110000	0.75
110	222121110000	0.75
120	222121110000	0.75
130	222121110000	0.76
140	222121110000	0.76
150	222121110000	0.76
160	222121110000	0.76
170	222121110000	0.76
180	222121110000	0.76

Table B.44. Evolution of *N*-MeImid IPC model ground state CI-vector during Fe-C bond elongation using relaxed geometries. The $(d_{xz})^2(C\pi^*)^0$ and $(d_{xz})^1(C\pi^*)^1$ are the two dominant configurations throughout the 1.7-2.5 Å. Until 2.1 Å, the $(d_{xz})^0(C\pi^*)^2$ is third most dominant.

Fe-C Length (Å)	**CFG $(d_{xz})^2(C\pi^*)^0$**	**Frac. Char.**	**CFG $(d_{xz})^1(C\pi^*)^1$**	**Frac. Char.**	**CFG $(d_{xz})^0(C\pi^*)^2$**	**Frac. Char.**
1.70	222222000000	0.66	222122100000	0.10	222022200000	0.06
1.79	222222000000	0.60	222122100000	0.16	222022200000	0.06
1.90	222222000000	0.51	222122100000	0.23	222022200000	0.05
2.00	222222000000	0.44	222122100000	0.29	222022200000	0.05
2.10	222222000000	0.36	222122100000	0.34	222022200000	0.04
2.20	222222000000	0.29	221222100000	0.39	220222200000	0.03
2.30	222222000000	0.23	221222100000	0.40	220222200000	0.02
2.40	222222000000	0.17	221222100000	0.41	220222200000	0.01
2.50	222222000000	0.12	221222100000	0.37	220222200000	0.01

Table B.45. Evolution of thiolate IPC model ground state CI-vector during Fe-C bond elongation using relaxed geometries. The $(d_{xz})^2(C\pi^*)^0$ and $(d_{xz})^1(C\pi^*)^1$ are the two dominant configurations throughout the 1.7-2.5 Å. Until 2.4 Å, the $(d_{xz})^0(C\pi^*)^2$ is third most dominant.

Fe-C Length (Å)	**CFG 1 $(d_{xz})^2(C\pi^*)^0$**	**Frac. Char.**	**CFG 2 $(d_{xz})^1(C\pi^*)^1$**	**Frac. Char.**	**CFG 3 $(d_{xz})^0(C\pi^*)^2$**	**Frac. Char.**
1.70	222222000000	0.66	222122100000	0.11	222022200000	0.07
1.80	222222000000	0.57	222122100000	0.19	222022200000	0.07
1.90	222222000000	0.49	222122100000	0.26	222022200000	0.10
2.00	222222000000	0.41	222122100000	0.34	222022200000	0.06
2.10	222222000000	0.42	222221100000	0.29	222220200000	0.09
2.20	222222000000	0.34	222221100000	0.35	222220200000	0.08
2.30	222222000000	0.27	222221100000	0.40	222220200000	0.07
2.40	222222000000	0.18	222221100000	0.46	222220200000	0.04
2.50	222222000000	0.11	222221100000	0.49	222220200000	0.03

Table B.46. Evolution of hydroxide IPC model ground state CI-vector during Fe-C bond elongation. Using relaxed geometries. (2 singlets, 5 triplets state-averaged calculation).

Fe-C Length (Å)	**CFG 1 $(d_{xz})^2(C\pi^*)^0$**	**Frac. Char.**	**CFG 2 $(d_{xz})^1(C\pi^*)^1$**	**Frac. Char.**	**CFG 3 $(d_{xz})^0(C\pi^*)^2$**	**Frac. Char.**
1.70	222222000000	0.73	222122100000	0.03	222022200000	0.09
1.84	222222000000	0.61	222212100000	0.13	222202200000	0.10
1.90	222222000000	0.56	222212100000	0.18	222202200000	0.10
2.00	222222000000	0.48	222212100000	0.25	222202200000	0.10
2.10	222222000000	0.40	222212100000	0.34	222202200000	0.10
2.20	222222000000	0.32	222212100000	0.42	222202200000	0.09
2.30	222222000000	0.22	222212100000	0.55	222202200000	0.07

Table B.47. Difference in energetics for free carbene between the QD-NEVPT2 and NEVPT2 methods.

Dihedral Angle	**Difference in Lowest Singlet Energy (kcal/mol)**	**Difference in 1st Excited Singlet Energy (kcal/mol)**	**Difference in Triplet Energy (kcal/mol)**
10	1.3×10^{-4}	-1.3×10^{-4}	0.0
20	1.9×10^{-3}	-1.9×10^{-3}	0.0
30	1.3×10^{-2}	-1.3×10^{-2}	0.0
40	2.6×10^{-2}	-2.6×10^{-2}	0.0
50	3.7×10^{-2}	-3.7×10^{-2}	0.0
60	4.3×10^{-2}	-4.3×10^{-2}	0.0
70	4.5×10^{-2}	-4.5×10^{-2}	0.0
80	4.0×10^{-2}	-4.0×10^{-2}	0.0
90	3.0×10^{-2}	-3.0×10^{-2}	0.0
100	2.1×10^{-2}	-2.1×10^{-2}	0.0
110	1.4×10^{-2}	-1.4×10^{-2}	0.0
120	1.0×10^{-2}	-1.0×10^{-2}	0.0
130	7.6×10^{-3}	-7.6×10^{-3}	0.0
140	7.2×10^{-3}	-7.2×10^{-3}	0.0
150	9.1×10^{-3}	-9.1×10^{-3}	0.0
160	1.5×10^{-2}	-1.5×10^{-2}	0.0
170	2.0×10^{-2}	-2.0×10^{-2}	0.0

Table B.48. Loewdin Atomic Spin Populations for the B3LYP *N*-MeImid in triplet and BSS states and their dependence on dihedral angle.

B3LYP Methyl-Imidazole Triplet		
Dihedral Angle	***Fe Spin Pop.***	***Carbene C Spin Pop.***
0	1.13	0.61
10	1.13	0.61
20	1.12	0.62
30	1.13	0.63
40	1.12	0.65
50	1.12	0.67
60	1.10	0.77
70	1.11	0.77
80	1.10	0.77
90	1.12	0.75
100	1.12	0.73
110	1.09	0.76
120	1.09	0.72
130	1.10	0.69
140	1.10	0.67
150	1.12	0.64
160	1.12	0.62
170	1.13	0.61
180	1.13	0.60
B3LYP Methyl-Imidazole BSS		
Dihedral Angle	***Fe Spin Pop.***	***Carbene C Spin Pop.***
0	0.89	-0.64
10	0.89	-0.63
20	0.86	-0.62
30	0.83	-0.61
40	0.78	-0.59
50	0.74	-0.56

60	0.70	-0.54
70	0.67	-0.52
80	0.66	-0.52
90	0.66	-0.52
100	0.68	-0.53
110	0.71	-0.55
120	0.74	-0.57
130	0.78	-0.59
140	0.82	-0.61
150	0.86	-0.62
160	0.88	-0.63
170	0.90	-0.64
180	0.90	-0.64

B.C. Figures

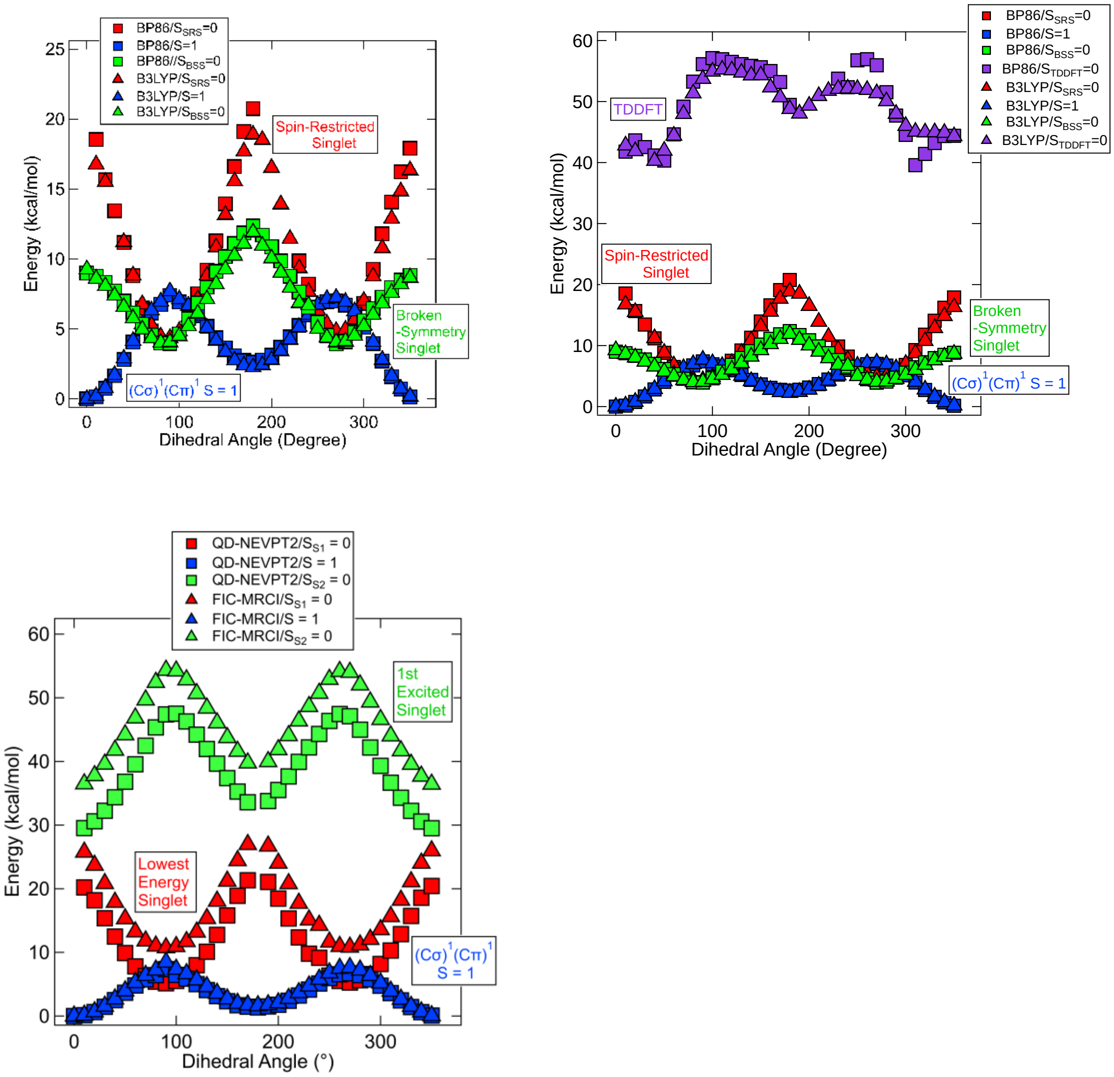

Figure B.1. Top Left: DFT scan for free carbene extending to 350°. Top Right: DFT and TDDFT scans over the same range. Bottom Left: QD-NEVPT2 and FIC-MRCI free carbene scans extending to 350°.

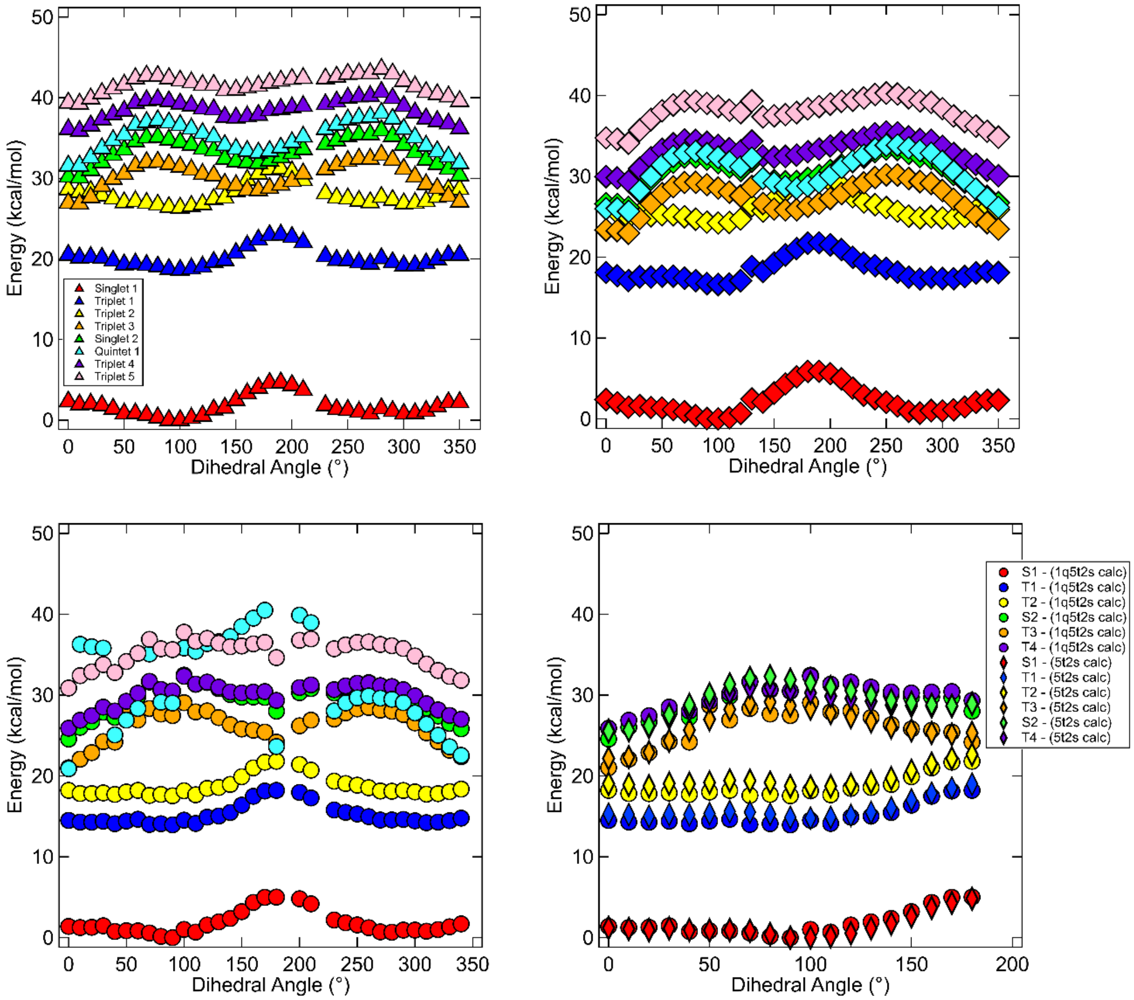

Figure B.2. QD-NEVPT2 Scans for IPC models extending to 350°. Top Left: *N*-MeImid. Top Right: Thiolate. Bottom Left: Hydroxide. Bottom Right: Hydroxide, comparison of energetics with different numbers of roots in state-averaged calculation (i.e. 1 quintet, 5 triplets, and 2 singlets compared to 5 triplets and 2 singlets).

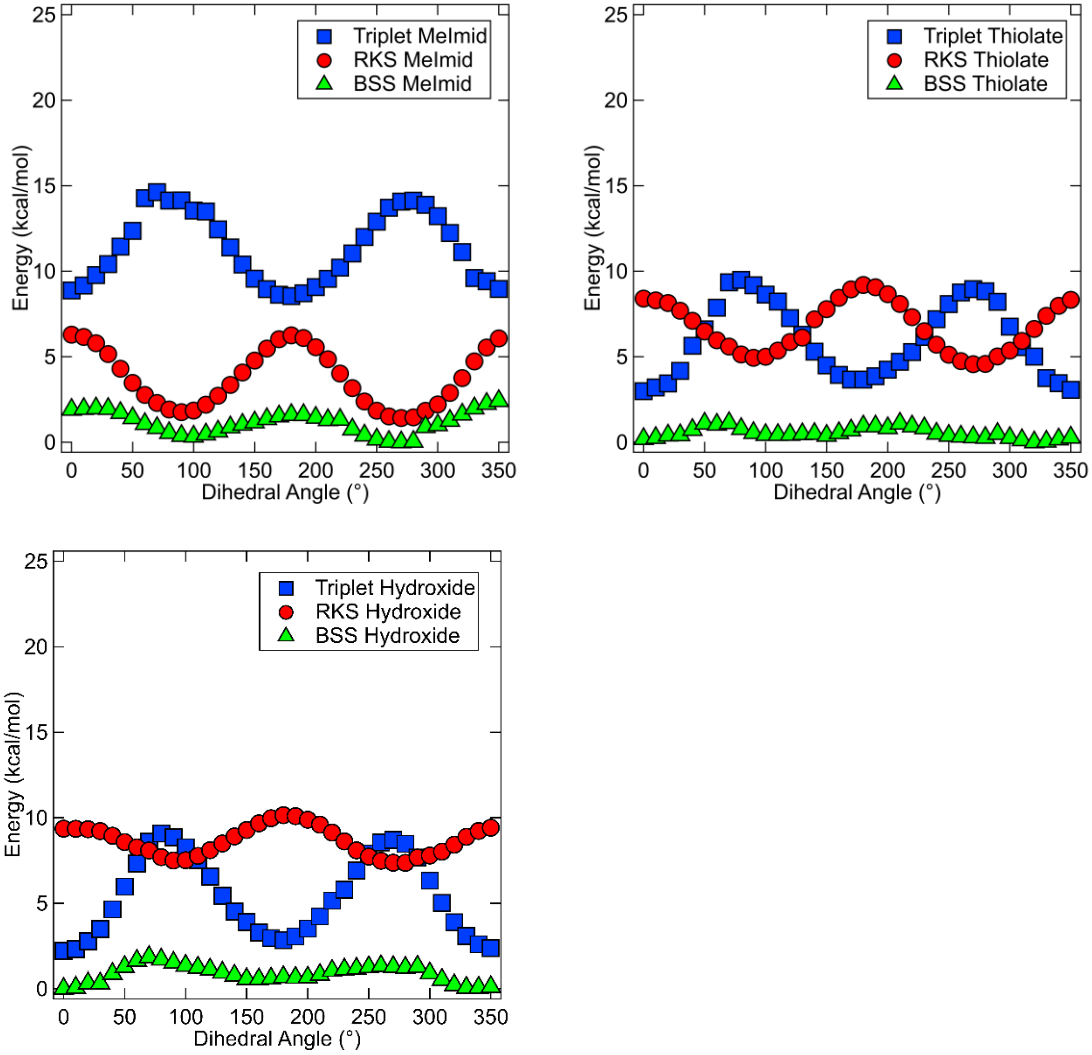

Figure B.3. DFT (B3LYP) scan for IPC models extending to 350°. Top Left: N-methylimidazole. Top Right: Thiolate. Bottom Left: Hydroxide.

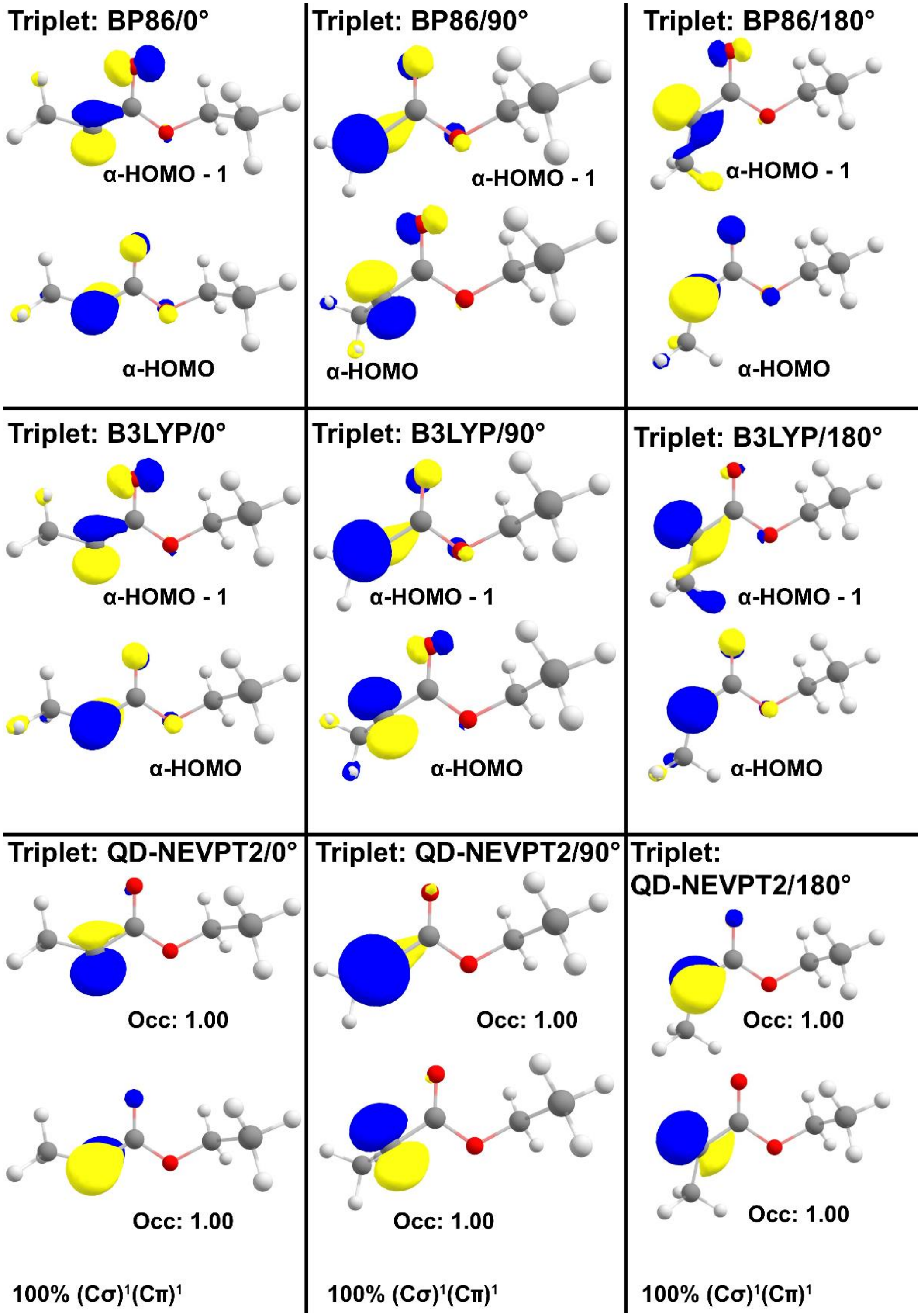

Figure B.4. Orbitals for the free carbene in the triplet state at 0°, 90°, and 180° dihedral angles.

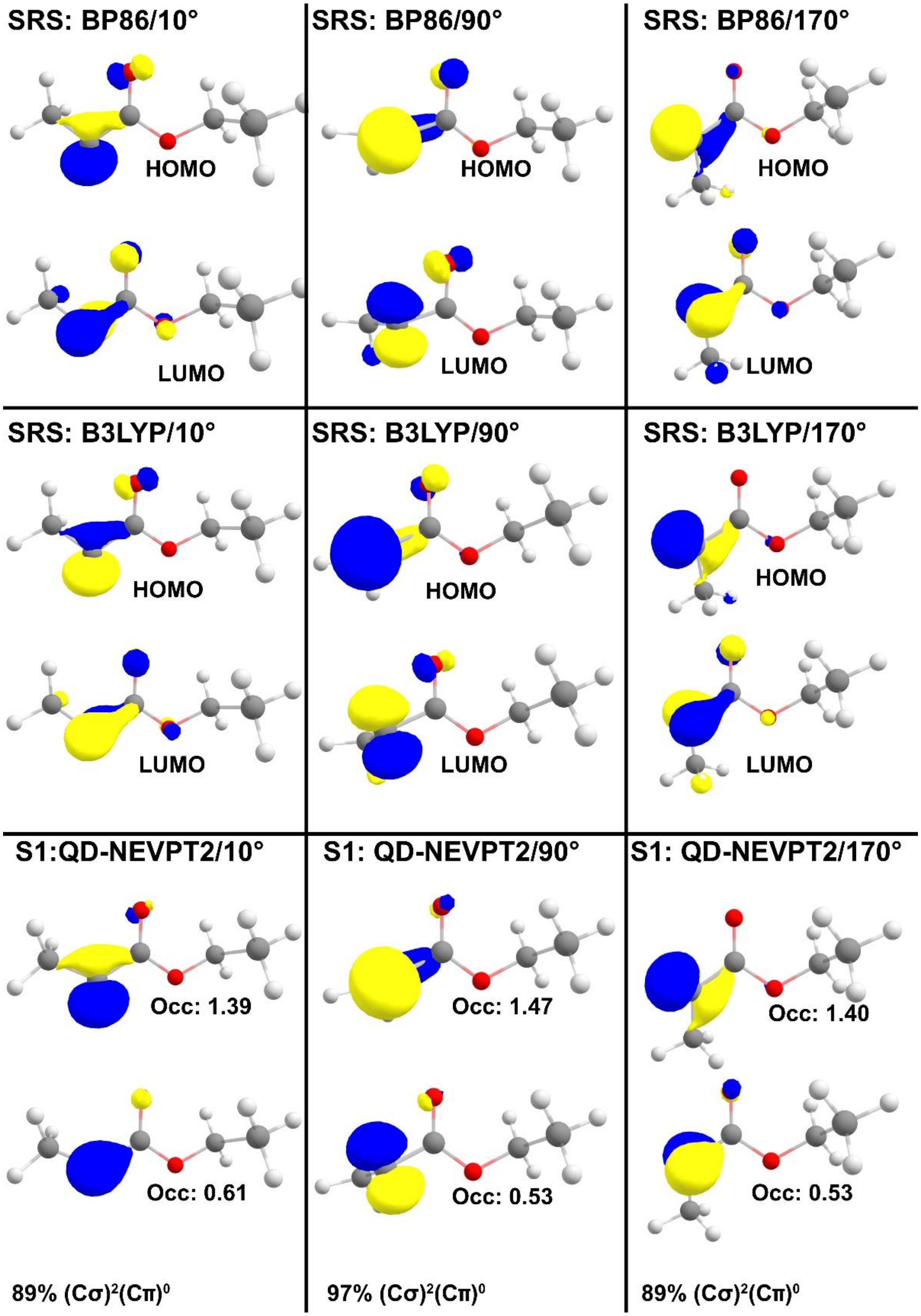

Figure B.5. Orbitals for the free carbene in the spin-restricted singlet state at 10°, 90°, and 170° dihedral angles. Bottom panel: QD-NEVPT2 state-averaged active space orbitals and occs. and weight of the leading term in ground singlet state (S1) for comparison to DFT.

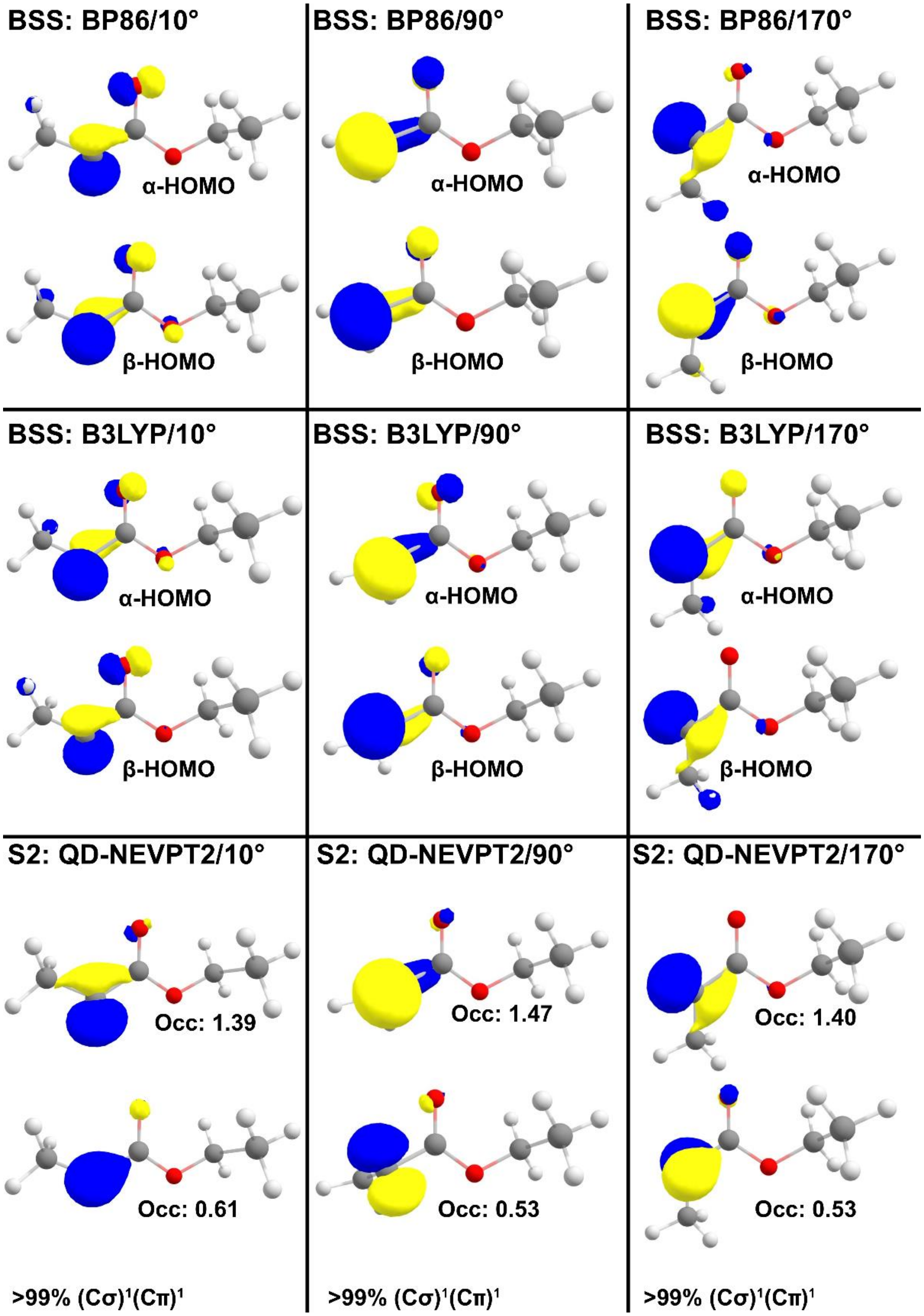

Figure B.6A. Orbitals for the free carbene in the broken-symmetry singlet state at 10°, 90°, and 170° dihedral angles. Bottom panel: QD-NEVPT2 state-averaged active space orbitals and occs. and the weight of leading term in 1st excited singlet state (S2) for comparison to DFT.

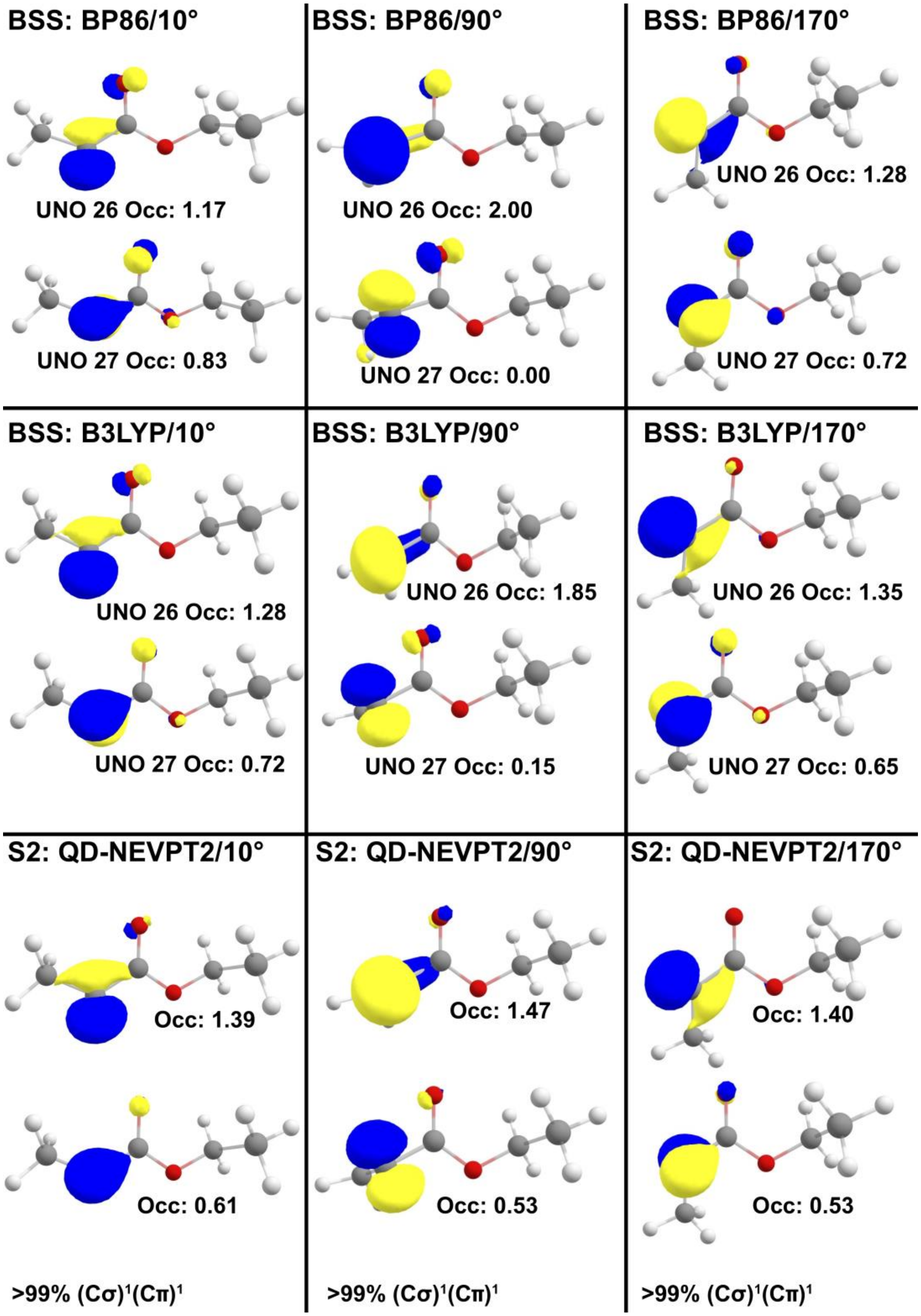

Figure B.6B. Natural orbitals for the free carbene in the broken-symmetry singlet state at 10°, 90°, and 170°. Bottom panel: QD-NEVPT2 state-averaged active space orbitals and occs. and the weight of leading term in 1st excited singlet state (S2) for comparison to DFT.

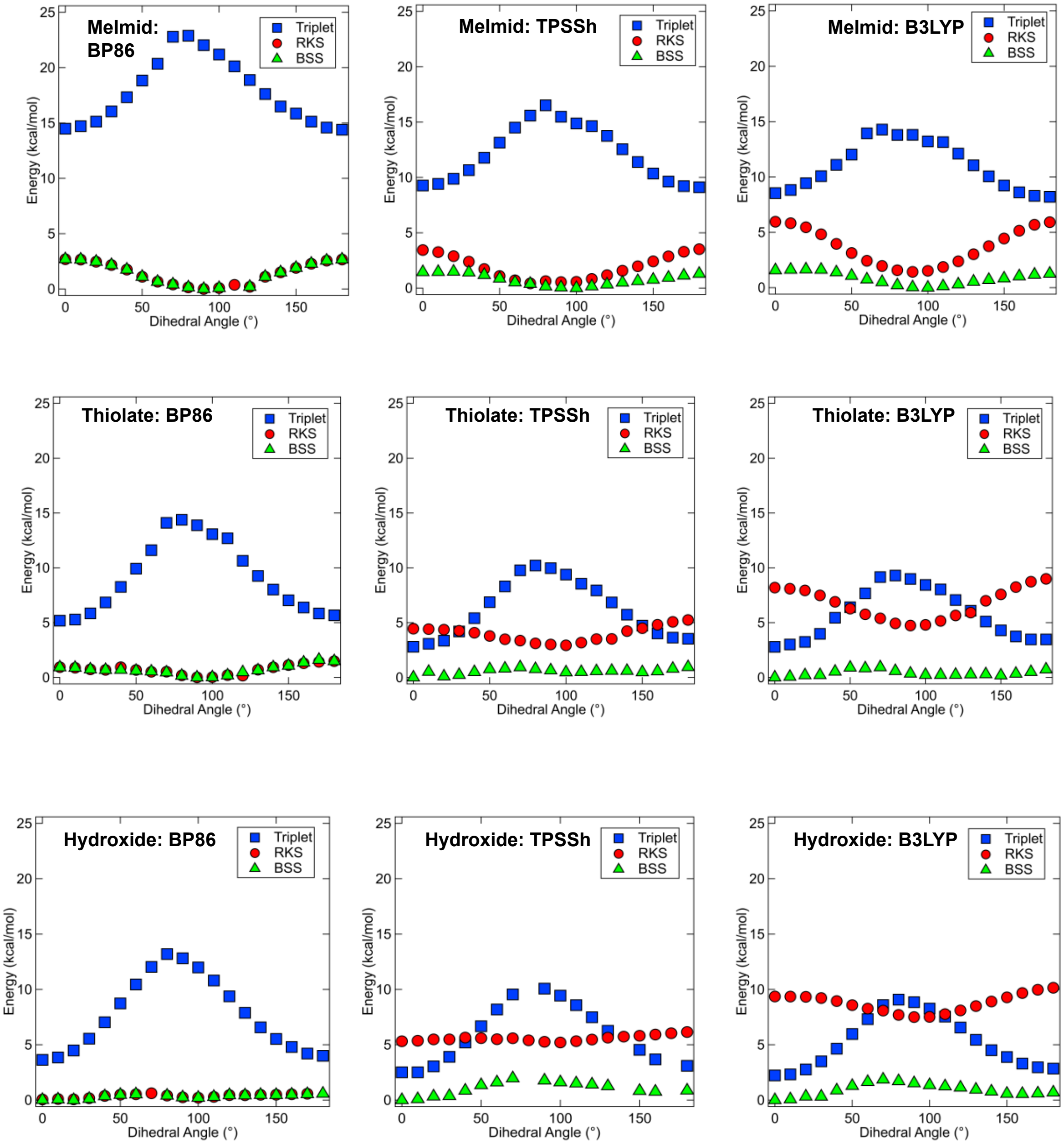

Figure B.7. DFT relaxed scans of IPC model complexes using the BP86, TPSSh, and B3LYP functionals.

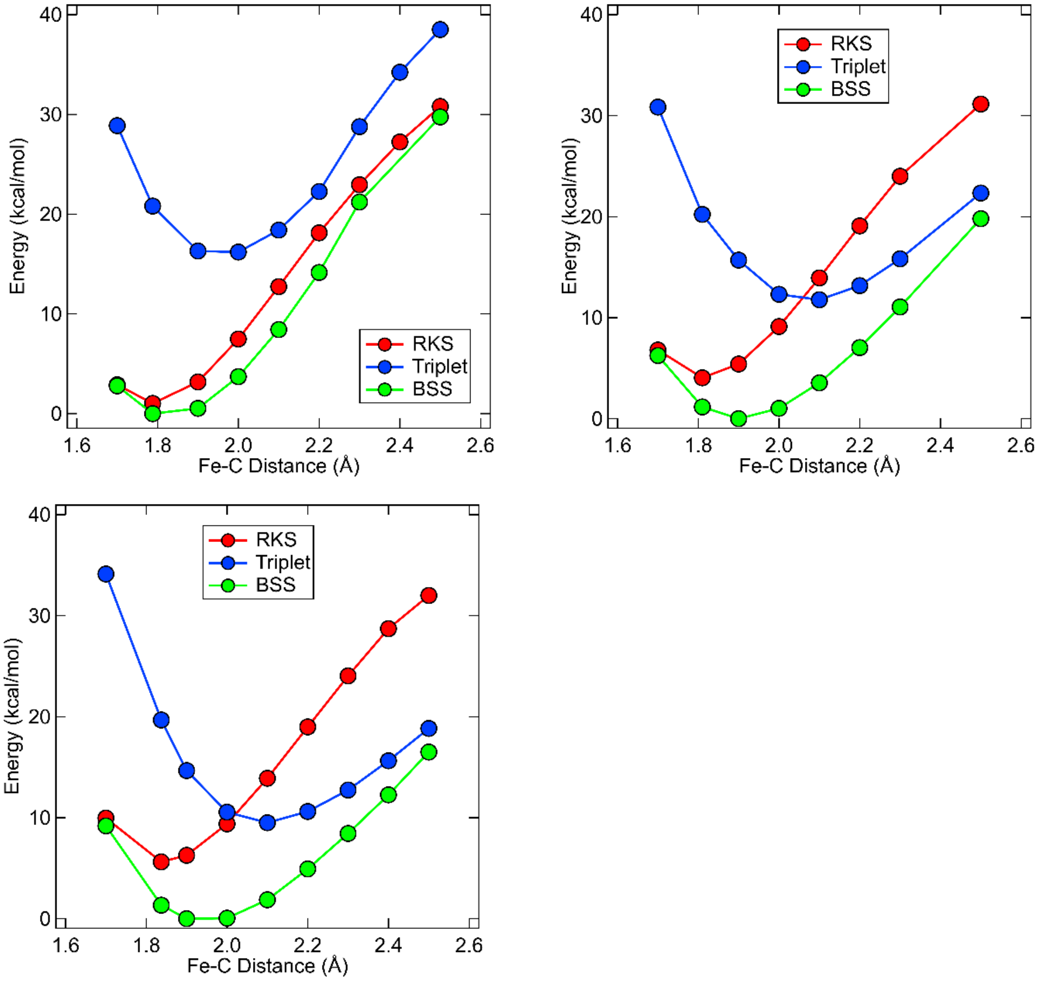

Figure B.8. DFT (B3LYP) relaxed scan of the Fe-C bond length in the RKS geometry (blue). Optimizations started from the 90 ° geometry from the B3LYP dihedral angle relaxed scan. Vertical energies to the triplet and BSS states were found with single point calculations (red and orange). Top Left: *N*-MeImid; Top Right: Thiolate; Bottom Left: Hydroxide.

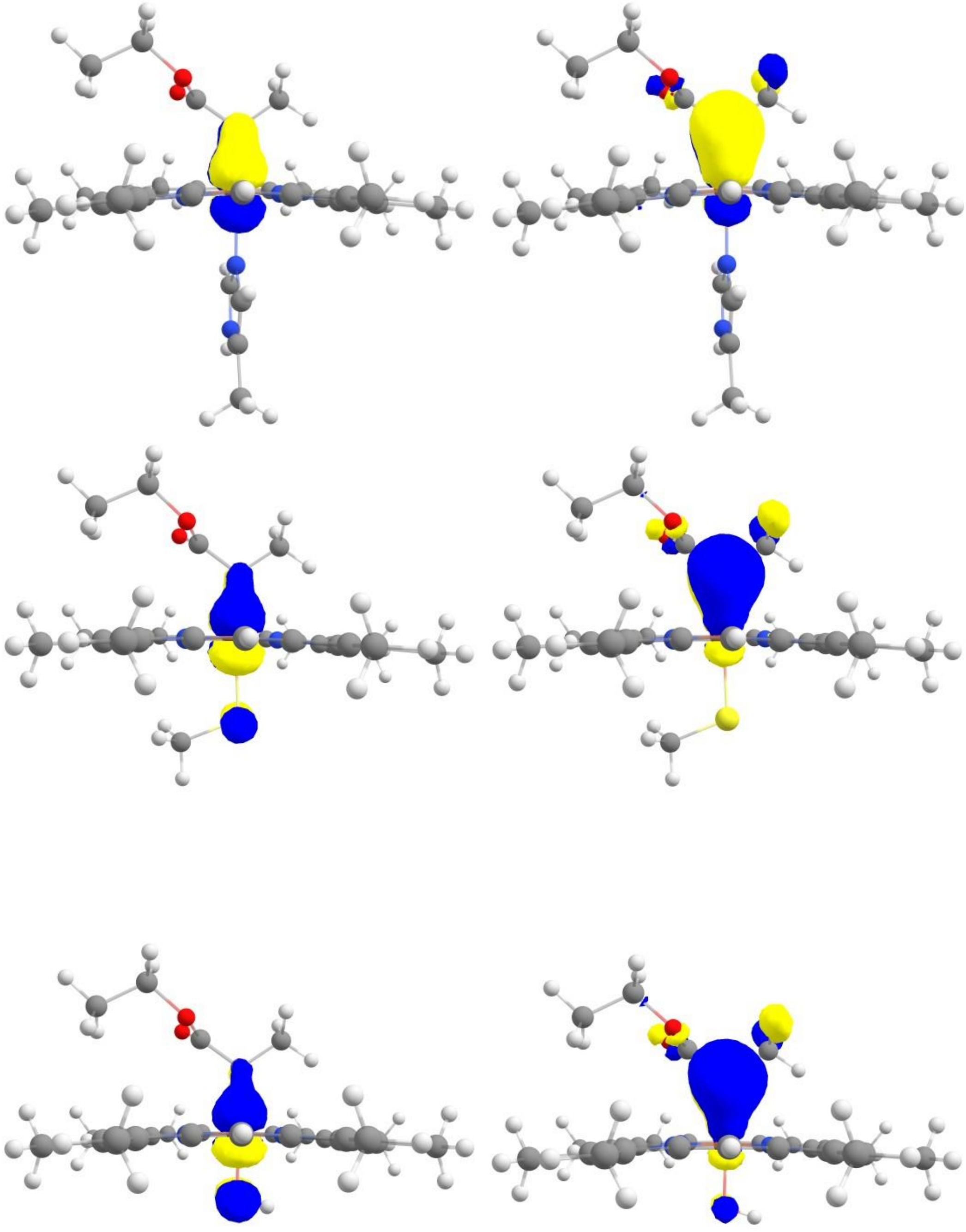

Figure B.9. Corresponding Orbitals for IPC BSS DFT Results. Top: *N*-MeImid. Overlap of 0.78. Middle: Thiolate. Overlap of 0.61. Bottom: Hydroxide: Overlap of 0.55

REFERENCES

(1) Lewis, R. D.; Garcia-Borràs, M.; Chalkley, M. J.; Buller, A. R.; Houk, K. N.; Kan, S. B. J.; Arnold, F. H. Catalytic Iron-Carbene Intermediate Revealed in a Cytochrome *c* Carbene Transferase. *Proc. Natl. Acad. Sci.* **2018**, *115* (28), 7308–7313. https://doi.org/10.1073/pnas.1807027115.

(2) Sharon, D. A.; Mallick, D.; Wang, B.; Shaik, S. Computation Sheds Insight into Iron Porphyrin Carbenes' Electronic Structure, Formation, and N–H Insertion Reactivity. *J. Am. Chem. Soc.* **2016**, *138* (30), 9597–9610. https://doi.org/10.1021/jacs.6b04636.

Appendix C

SUPPORTING INFORMATION FOR CHAPTER 4: MULTIREFERENCE DESCRIPTION OF NICKEL–ARYL HOMOLYTIC BOND DISSOCIATION PROCESSES IN PHOTOREDOX CATALYSIS

Adapted with permission from:

Cagan, D. A.[†]; Stroscio, G. D.[†]; Cusumano, A. Q.; Hadt, R. G. Multireference Description of Nickel–Aryl Homolytic Bond Dissociation Processes in Photoredox Catalysis. *J. Phys. Chem. A* **2020**, *124* (48), 9915-9922. https://doi.org/10.1021/acs.jpca.0c08646.

[†]Co-first author. *Corresponding author.

C.A. Computational Methods

C.A.1. Example DFT Input

```
! RKS BP86 6-311G(d) AutoAux
! TIGHTOPT FREQ
! RI VeryTightSCF GRID7 NOFINALGRID
! SlowConv PrintBasis LargePrint

%pal nprocs 16
end
%maxcore 9000

%method
  Z_solver DIIS
  Z_shift 0.5
end

*xyzfile 0 1 File.xyz
```

C.A.2. Example TDDFT Input

```
! UKS B3LYP def2-tzvp AutoAux SP RIJCOSX
! VeryTightSCF GRID7 NOFINALGRID GRIDX9
! SlowConv PrintBasis LargePrint CPCM(THF)
! MORead
%moinp "File.gbw"

%pal nprocs 16
end
%maxcore 9000

%tddft
  nroots 50
  maxdim 5
end

*xyzfile 0 3 File.xyz
```

C.A.3. Example CASSCF/QD-NEVPT2 Input

```
! def2-TZVP AutoAux RIJCOSX TightSCF CPCM(THF)
! LargePrint MOREAD
%moinp "File.gbw"

%casscf
  norb     9
  nel      10
  mult     3,1
  nroots   25,15
  TrafoStep RI
  MaxIter 400
  etol 1e-7
  printwf det
  orbstep SuperCI
  switchstep DIIS
  ShiftUp 2.0
  ShiftDn 2.0
  ptmethod sc_nevpt2
  ptsettings
  qdtype qd_vanvleck
  end
rel
  dosoc true
  gtensor true
  dtensor true
  end
end

%pal
  nprocs 16
end
%maxcore 9000

* xyzfile 0 1 File.xyz
```

C.B. Tables Part 1: Compound *1*

Table C.1A-1. Compound **1** – CASSCF/QD-NEVPT2 lowest transition energies in the gas phase (5o, 8e Active Space) – 10 triplet roots, 10 singlet roots. Active Space Orbitals (in order for CI vector notation below): d(z^2), d(xz), d(yz), d(xy), d(x^2-y^2).

State	Root	Multiplicity	ΔE/nm	ΔE/kcal mol^{-1}	CI Vector	f_{osc}	Contribution
0	0	1	---	---	22220	---	0.95128
					02222	---	0.02052
1	0	3	1090.8	26.2	12221	---	0.99927
					---	---	---
2	1	3	1009.0	28.3	21221	---	0.75971
					22121	---	0.21841
3	2	3	884.4	32.3	22121	---	0.75325
					21221	---	0.21711
4	3	3	614.5	46.5	22211	---	0.93594
					21122	---	0.06344
5	1	1	420.1	68.1	21221	0.0000024	0.77158
					22122	---	0.20180
6	2	1	414.9	68.9	12221	0.0000399	0.97842
					22022	---	0.00639
7	3	1	395.1	72.4	22121	0.0001334	0.77021
					21221	---	0.20266
8	4	1	382.6	74.7	22211	0.0001352	0.99872
					---	---	---
9	4	3	292.0	97.9	21212	---	0.45857
					22112	---	0.37735
10	5	3	288.9	98.9	12212	---	0.99393
					21122	---	0.00338

Table C.1A-2. Compound **1** – CASSCF/QD-NEVPT2 lowest transition energies with CPCM(THF) (5o, 8e Active Space) – 10 triplet roots, 10 singlet roots. Active Space Orbitals (in order for CI vector notation below): d(z^2), d(xz), d(yz), d(xy), d(x^2-y^2).

State	Root	Multiplicity	ΔE/nm	ΔE/kcal mol^{-1}	CI Vector	f_{osc}	Contribution
0	0	1	---	---	22220	---	0.94984
					02222	---	0.02128
1	0	3	1224.5	23.4	12221	---	0.99185
					---	---	---
2	1	3	1089.4	26.2	21221	---	0.94767
					22121	---	0.03109
3	2	3	973.7	29.4	22121	---	0.93700
					21221	---	0.03119
4	3	3	633.7	45.1	22211	---	0.92979
					21122	---	0.06922
5	1	1	431.4	66.3	21221	0.0000031	0.86047
					12221		0.09338
6	2	1	431.3	66.3	12221	0.0000287	0.88620
					20222		0.00722
7	3	1	410.5	69.6	22121	0.0001197	0.94493
					21221		0.02702
8	4	1	387.8	73.7	22211	0.0001278	0.99747
					---		---
9	4	3	301.8	94.8	21212	---	0.59108
					22112	---	0.23535
10	5	3	299.7	95.4	12212	---	0.99260
					21122	---	0.00415

Table C.1B. Compound **1** – CASSCF/QD-NEVPT2 lowest transition energies in the gas phase. 9o, 10e Active Space – 25 triplet roots, 15 singlet roots. Orbitals (in order for CI vector notation below): d(xy), d(x^2-y^2)/C(sp^2), d(yz), d(z^2), d(xz), d(x^2-y^2)/C(sp^2)*, π*(1), π*(2), π*(3).

State	Root	Multiplicity	ΔE/nm	ΔE/kcal mol^{-1}	CI Vector	f_{osc}	Contribution
0	0	1	---	---	222220000	---	0.5455
					222210100	---	0.1876
					212221000	---	0.0977
1	0	3	802.3	35.6	222121000	---	0.4035
					222210100	---	0.1917
2	1	3	774.8	36.9	222120100	---	0.6406
					222210100	---	0.1186
3	1	1	752.5	38.0	222120100	0.0006862	0.8166
					202122100	---	0.0850
4	2	3	733.8	39.0	221221000	---	0.2244
					222210100	---	0.2117
5	3	3	715.5	40.0	221221000	---	0.2533
					222210100	---	0.2197
6	2	1	672.0	42.5	221220100	0.0649528	0.4507
					222210100	---	0.2848
7	4	3	668.3	42.8	222211000	---	0.4913
					221221000	---	0.2821
8	5	3	620.8	46.1	221220100	---	0.7066
					222210100	---	0.0871
9	3	1	604.1	47.3	221220100	0.1224866	0.3511
					222210100	---	0.2756
10	6	3	551.6	51.8	122221000	---	0.6719
					221212000	---	0.0803
11	7	3	480.7	59.5	222120010	---	0.7737
					202122010	---	0.0829
12	4	1	479.5	59.6	222120010	0.0003566	0.7222
					202122010	---	0.0773
13	5	1	472.4	60.5	122220100	0.0001327	0.7056
					221211100	---	0.0791
14	8	3	468.1	61.1	222210010	---	0.7214
					221220010	---	0.0877
15	6	1	463.2	61.7	222210010	0.0858212	0.3931
					221220010	---	0.2037
16	9	3	463.0	61.8	122220100	---	0.7507
					221211100	---	0.0792
17	7	1	439.3	65.1	222120001	0.0000514	0.7108
					202122001	---	0.0744
18	8	1	428.4	66.7	221220010	0.0799110	0.3735
					222210001	---	0.3188
19	10	3	424.0	67.4	222120001	---	0.7783
					202122001	---	0.0812
20	11	3	416.1	68.7	221220010	---	0.6613
					222210010	---	0.0772

Table C.1C. Compound **1** – CASSCF/QD-NEVPT2 Lowest transition energies with CPCM(THF) 9o, 10e Active Space – 25 triplet roots, 15 singlet roots. Orbital (in order for CI vector notation below): d(xy), bonding d(x^2-y^2)/C(sp^2), d(yz), d(xz), d(z^2), d(x^2-y^2)/C(sp^2)*, π*(1), π*(2), π*(3).

State	Root	Multiplicity	ΔE/nm	ΔE/kcal mol^{-1}	CI Vector	f_{osc}	Contribution
0	0	1	---	---	222220000	---	0.5752
					222120100	---	0.1521
1	0	3	832.8	34.3	222211000	---	0.7672
					212212000	---	0.1435
2	1	3	758.1	37.7	222121000	---	0.4011
					221221000	---	0.3532
3	2	3	712.3	40.1	222210100	---	0.3289
					221221000	---	0.3246
4	3	3	678.4	42.2	222210100	---	0.4433
					222121000	---	0.2503
5	1	1	671.4	42.6	222210100	0.0008408	0.8161
					202212100	---	0.0876
6	4	3	647.1	44.2	222120100	---	0.7582
					202122100	---	0.0850
7	2	1	604.2	47.3	221220100	0.0622469	0.4193
					222120100	---	0.3382
8	5	3	574.3	49.8	221220100	---	0.5752
					122221000	---	0.1682
9	6	3	551.4	51.9	122221000	---	0.5491
					221220100	---	0.1783
10	3	1	546.6	52.3	221220100	0.1520657	0.3722
					222120100	---	0.2674
11	4	1	444.6	64.3	222120010	0.1043472	0.5270
					221220010	---	0.1267
12	7	3	441.9	64.7	222210010	---	0.7193
					222210001	---	0.0917
13	5	1	440.4	64.9	122220100	0.0001963	0.4135
					222210010	---	0.3424
14	6	1	437.3	65.4	222210010	0.0003333	0.4320
					122220100	---	0.3239
15	8	3	424.8	67.3	222120010	---	0.7541
					202122010	---	0.0870
16	9	3	423.2	67.5	122220100	---	0.7670
					221121100	---	0.0820
17	10	3	410.6	69.6	222210001	---	0.7193
					222210010	---	0.0922
18	7	1	407.1	70.2	222121000	0.0002537	0.6733
					221221000	---	0.1149
19	8	1	401.3	71.3	222211000	0.0305023	0.2808
					221220010	---	0.2155
20	9	1	399.9	71.5	122221000	0.0329884	0.4648

222211000	---	0.1385

Table C.1D. Compound **1** – CASSCF/QD-NEVPT2 composition of the singlet equilibrium ground state in gas phase. 9o, 10e Active Space – 25 triplet roots, 15 singlet roots. Orbitals: d(xy), bonding d(x^2-y^2)/C(sp^2), d(yz), d(z^2), d(xz), d(x^2-y^2)/C(sp^2)*, π*(1), π*(2), π*(3).

CI Vector	Transition	Contribution
222220000	Closed shell singlet (CSS) d^8	0.5455
222210100	d(xz) → π*(1)	0.1876
212221000	bonding d(x^2-y^2)/C(sp^2) → d(x^2-y^2)/C(sp^2)*	0.0977
221220001	d(yz) → π*(3)	0.0400
222210010	d(xz) → π*(2)	0.0312
202212100	2x[bonding d(x^2-y^2)/C(sp^2)] + d(xz) → 2x[d(x^2-y^2)/C(sp^2)*] + π*(1)	0.0224
222121000	d(z^2) → d(x^2-y^2)/C(sp^2)*	0.0090
212211100	bonding d(x^2-y^2)/C(sp^2) + d(xz) → d(x^2-y^2)/C(sp^2)* + π*(1)	0.0083
222022000	2x[d(z^2)] → 2x[d(x^2-y^2)/C(sp^2)*]	0.0079
220222000	2x[d(yz)] → 2x[d(x^2-y^2)/C(sp^2)*]	0.0056
222202000	2x[d(xz)] → 2x[d(x^2-y^2)/C(sp^2)*]	0.0055
201222001	2x[bonding d(x^2-y^2)/C(sp^2)] + d(yz) → 2x[d(x^2-y^2)/C(sp^2)*] + π*(3)	0.0042
202212010	2x[bonding d(x^2-y^2)/C(sp^2)] + d(xz) → 2x[d(x^2-y^2)/C(sp^2)*] + π*(2)	0.0040
122221000	d(xy) → d(x^2-y^2)/C(sp^2)*	0.0029
221220100	d(yz) → π*(1)	0.0029
Sum of CSS		**55%**
Sum of all MLCT		**26%**
Sum of all d-d		**13%**
Sum of mixed MLCT + d-d		**3.9%**

Table C.1E. Compound **1** – CASSCF/QD-NEVPT2 composition of the singlet equilibrium ground state with CPCM(THF). 9o, 10e Active Space – 25 triplet roots, 15 singlet roots. Orbitals: d(xy), bonding d(x^2-y^2)/C(sp^2), d(yz), d(xz), d(z^2), d(x^2-y^2)/C(sp^2)*, π*(1), π*(2), π*(3).

CI Vector	**Transition**	**Contribution**
222220000	Closed shell singlet (CSS) d^8	0.5752
222120100	d(xz) → π*(1)	0.1521
212221000	bonding d(x^2-y^2)/C(sp^2) → d(x^2-y^2)/C(sp^2)*	0.1097
221220001	d(yz) → π*(3)	0.0383
222120010	d(xz) → π*(2)	0.0256
202122100	2x[bonding d(x^2-y^2)/C(sp^2)] + d(xz) → 2x[d(x^2-y^2)/C(sp^2)*] + π*(1)	0.0192
222211000	d(z^2) → d(x^2-y^2)/C(sp^2)*	0.0101
221220100	d(yz) → π*(1)	0.0090
222202000	2x[d(z^2)] → 2x[d(x^2-y^2)/C(sp^2)*]	0.0090
212121100	bonding d(x^2-y^2)/C(sp^2) + d(xz) → d(x^2-y^2)/C(sp^2)* + π*(1)	0.0073
220222000	2x[d(yz)] → 2x[d(x^2-y^2)/C(sp^2)*]	0.0063
222022000	2x[d(xz)] → 2x[d(x^2-y^2)/C(sp^2)*]	0.0063
201222001	2x[bonding d(x^2-y^2)/C(sp^2)] + d(yz) → 2x[d(x^2-y^2)/C(sp^2)*] + π*(3)	0.0041
202122010	2x[bonding d(x^2-y^2)/C(sp^2)] + d(xz) → 2x[d(x^2-y^2)/C(sp^2)*] + π*(2)	0.0034
Sum of CSS		**58%**
Sum of all MLCT		**22%**
Sum of all d-d		**14%**
Sum of mixed MLCT + d-d		**3.4%**

Table C.1F. Compound **1** with Ni–C distance of 3.20 Å – CASSCF/QD-NEVPT2 lowest transition energies in gas phase. 8o,10e Active Space – 25 triplet roots, 15 singlet roots. Orbitals: d(xy), d(yz), d(z^2), d(xz), bonding d(x^2-y^2)/C(sp^2), d(x^2-y^2)/C(sp^2)*, π*(1), π*(2).

State	**Root**	**Multiplicity**	**ΔE/nm**	**ΔE/kcal mol^{-1}**	**CI Vector**	f_{osc}	**Contribution**
0	0	3	---	---	22211110	---	0.5998
					22212010	---	0.1057
					22221100	---	0.0567
1	0	3	9086.0	3.1	22211110	---	0.7446
					22112110	---	0.0600
2	1	3	3630.2	7.9	22121110	---	0.8144
					22122010	---	0.1216
3	2	3	3417.1	8.4	22211110	---	0.7561
					22212010	---	0.0919
4	1	1	3189.5	9.0	22121110	0.0000059	0.8124
					22122010	---	0.1225
5	3	3	2489.9	11.5	22121110	---	0.9789
					12221110	---	0.0509
6	4	3	2304.7	12.4	21221110	---	0.7601
					21222010	---	0.1103
7	2	1	2285.4	12.5	21221110	0.0000005	0.6956
					21222010	---	0.1058
8	5	3	1919.3	14.9	21221110	---	0.8607
					22211110	---	0.0484
9	6	3	1172.8	24.4	22220110	---	0.7851
					22221010	---	0.0762
10	3	1	1170.0	24.4	22220110	0.0000682	0.7229
					22221010	---	0.0724
11	4	1	1097.4	26.1	22211101	0.0222545	0.2581
					12221110	---	0.2436
12	5	1	1090.0	26.2	22211101	0.0361406	0.4130
					21212110	---	0.1455
13	7	3	1061.0	27.0	12221110	---	0.4604
					21212110	---	0.4285
14	8	3	1030.4	27.7	22211101	---	0.7389
					22212001	---	0.0804
15	9	3	1003.5	28.5	12221110	---	0.4832
					21212110	---	0.4057
16	10	3	994.6	28.8	22121101	---	0.8005
					22122001	---	0.1199
17	6	1	993.3	28.8	22121101	0.0000753	0.8085
					22122001	---	0.1212
18	11	3	979.4	29.2	22211101	---	0.8202
					22112101	---	0.0673
19	12	3	911.0	31.4	22121101	---	0.9880
					12221101	---	0.0051

20	7	1	863.0	33.1	21221101	0.0022399	0.7256
					21222001	---	0.1076

Table C.1G-1. Compound **1** – CASSCF/QD-NEVPT2 composition of the singlet equilibrium ground state while varying number of singlet roots. 9o, 10e Active Space – 25 triplet roots, *X* singlet roots (where *X* ranged from 15 to 40). Orbitals: bonding d(x^2-y^2)/C(sp^2), d(xy), d(xz), d(yz), d(z^2), d(x^2-y^2)/C(sp^2)*, π*(1), π*(2), π*(3).

Weights of Three Most Dominant Terms in CI-Vector (# Triplets / # Singlets)							
Configuration	**25/15 CPCM**	**25/15 Gas**	**25/20 Gas**	**25/25 Gas**	**25/30 Gas**	**25/35 Gas**	**25/40 Gas**
CSS	0.5752	0.5455	0.5346	0.5202	0.5029	0.4853	0.4733
d(xz) → π*(1)	0.1521	0.1876	0.1149	0.1321	0.1224	0.1316	0.1198
bonding d(x^2-y^2)/C(sp^2) → d(x^2-y^2)/C(sp^2)*	0.1097	0.0977	0.1101	0.0853	0.0971	0.1276	0.1430
Sums of Weights							
Configuration	**25/15 CPCM**	**25/15 Gas**	**25/20 Gas**	**25/25 Gas**	**25/30 Gas**	**25/35 Gas**	**25/40 Gas**
CSS	58%	55%	53%	52%	50%	49%	47%
Sum of MLCT	23%	26%	25%	24%	23%	26%	25%
Sum of d-d	14%	13%	16%	19%	21%	21%	23%
Sum of MLCT+ d-d	3.4%	3.9%	2.6%	1.9%	1.7%	2.8%	2.8%
Singlet → Singlet Transition Energies (kcal mol^{-1})							
Transition	**25/15 CPCM**	**25/15 Gas**	**25/20 Gas**	**25/25 Gas**	**25/30 Gas**	**25/35 Gas**	**25/40 Gas**
$S_0 \rightarrow S_1$	42.6	38.0	39.3	40.1	40.6	39.3	39.8
$S_0 \rightarrow S_2$	47.3	42.5	43.3	43.7	43.9	43.2	43.4
$S_0 \rightarrow S_3$	52.3	47.3	48.0	48.9	49.5	48.2	48.3
$S_0 \rightarrow S_4$	64.3	59.6	60.9	62.1	62.6	61.2	61.7
$S_0 \rightarrow S_5$	64.9	60.5	61.9	62.5	63.0	61.8	62.1
$S_0 \rightarrow S_6$	65.4	61.7	62.3	63.4	63.4	63.2	63.0
$S_0 \rightarrow S_7$	70.2	65.1	67.7	67.7	67.3	68.0	67.9
$S_0 \rightarrow S_8$	71.3	66.7	68.6	69.2	69.0	68.4	68.1
$S_0 \rightarrow S_9$	71.5	69.4	68.8	70.1	70.3	69.4	69.7
$S_0 \rightarrow S_{10}$	72.3	72.2	71.1	70.6	70.7	71.3	71.7
$S_0 \rightarrow S_{11}$	73.3	73.4	71.8	72.0	72.5	72.0	72.0
$S_0 \rightarrow S_{12}$	77.0	75.0	73.0	72.1	73.4	72.2	72.7
$S_0 \rightarrow S_{13}$	78.2	76.2	74.5	74.5	75.2	75.7	74.2
$S_0 \rightarrow S_{14}$	85.6	81.2	80.9	81.5	81.7	81.7	81.4

Table C.1G-2. Compound **1** – CASSCF/QD-NEVPT2 composition of the singlet 3.20 Å ground state while varying number of singlet roots. 9o, 10e Active Space – 25 triplet roots, *X* singlet roots (where *X* ranged from 15 to 45). Orbitals: bonding d(x^2-y^2)/C(sp^2), d(xy), d(xz), d(yz), d(z^2), d(x^2-y^2)/C(sp^2)*, π*(1), π*(2), π*(3).

CI-Vector Weights (# Triplets/# Singlets)

Transition	**25/15 CPCM**	**25/15 Gas**	**25/25 Gas**	**25/35 Gas**
d(xz) + bonding d(x^2-y^2)/C(sp^2) → d(x^2-y^2)/C(sp^2)* + π*(1)	0.5994	0.5998	0.6929	0.7298
d(xz) → π*(1)	0.1042	0.1057	0.0796	0.0626
bonding d(x^2-y^2)/C(sp^2) → d(x^2-y^2)/C(sp^2)*	0.0560	0.0567	0.0631	0.0663
d(z^2) + d(xz) → C(sp^2) + π*(1)	0.0579	0.0549	0.0195	0.0387

Singlet → Singlet Transition Energies (kcal mol^{-1})

Transition	**25/15 CPCM**	**25/15 Gas**	**25/25 Gas**	**25/35 Gas**
$S_0 \rightarrow S_1$	42.6	38.0	40.1	39.3
$S_0 \rightarrow S_2$	47.3	42.5	43.7	43.2
$S_0 \rightarrow S_3$	52.3	47.3	48.9	48.2
$S_0 \rightarrow S_4$	64.3	59.6	62.1	61.2
$S_0 \rightarrow S_5$	64.9	60.5	62.5	61.8
$S_0 \rightarrow S_6$	65.4	61.7	63.4	63.2
$S_0 \rightarrow S_7$	70.2	65.1	67.7	68.0
$S_0 \rightarrow S_8$	71.3	66.7	69.2	68.4
$S_0 \rightarrow S_9$	71.5	69.4	70.1	69.4
$S_0 \rightarrow S_{10}$	72.3	72.2	70.6	71.3
$S_0 \rightarrow S_{11}$	73.3	73.4	72.0	72.0
$S_0 \rightarrow S_{12}$	77.0	75.0	72.1	72.2
$S_0 \rightarrow S_{13}$	78.2	76.2	74.5	75.7
$S_0 \rightarrow S_{14}$	85.6	81.2	81.5	81.7

Table C.1G-3. Compound **1** – CASSCF/QD-NEVPT2 composition of the formal Ni(I) ground state while varying number of doublet roots. 8o, 9e Active Space – 25 quartet roots, *X* doublet roots (where *X* ranged from 15 to 45).

CI-Vector Weights (# Quartets / # Doublets)

Transition	**25/15 CPCM**	**25/15 Gas**	**25/25 Gas**	**25/35 Gas**	**25/45 Gas**
d(xz) → π*(1)	0.7390	0.7363	0.7382	0.7701	0.7631
d(xz) → π*(2)	0.0761	0.0755	0.0746	0.0710	0.0719
formal Ni(I)	0.0733	0.0727	0.0724	0.0716	0.0748
d(yz) → π*(3)	0.0428	0.0455	0.0474	0.0443	0.0467

Doublet→Doublet Transition Energies (kcal mol^{-1})

Transition	**25/15 CPCM**	**25/15 Gas**	**25/25 Gas**	**25/35 Gas**	**25/45 Gas**
1	8.3	9.4	9.4	9.6	9.8
2	11.9	12.7	12.7	12.9	13.1
3	22.5	23.0	22.3	22.5	22.7
4	26.5	26.6	26.6	26.9	27.0
5	27.6	28.2	26.8	27.2	27.5
6	29.4	30.3	30.4	30.1	30.1
7	31.0	31.0	30.6	30.6	30.8
8	33.7	34.3	34.3	34.5	34.9
9	35.2	36.0	36.2	36.4	36.7
10	36.5	37.7	37.4	37.7	37.9
11	36.7	38.1	37.6	37.7	38.0
12	37.8	38.3	38.0	38.4	38.8
13	37.9	38.4	38.3	38.6	39.0
14	49.3	48.1	45.7	46.1	45.9

Table C.1H. Compound **1** – CASSCF/QD-NEVPT2. Transitions for the gas phase spectrum. 9o, 10e Active Space – 25 triplet roots, 15 singlet roots. Orbitals (in order for CI vector notation below): d(xy), bonding d(x^2-y^2)/C(sp^2), d(yz), d(z^2), d(xz), d(x^2-y^2)/C(sp^2)*, π*(1), π*(2), π*(3).

Transition	**ΔE/nm**	**ΔE/kcal mol^{-1}**	**CI Vector**	f_{osc}	**Contribution**
$S_0 \rightarrow S_1$	752.5	38.0	222120100	0.0006862	0.8166
			202122100	---	0.0850
$S_0 \rightarrow S_2$	672.0	42.5	221220100	0.0649528	0.4507
			222210100	---	0.2848
$S_0 \rightarrow S_3$	604.1	47.3	221220100	0.1224866	0.3511
			222210100	---	0.2756
$S_0 \rightarrow S_4$	479.5	59.6	222120010	0.0003566	0.7222
			202122010	---	0.0773
$S_0 \rightarrow S_5$	472.4	60.5	122220100	0.0001327	0.7056
			221211100	---	0.0791
$S_0 \rightarrow S_6$	463.2	61.7	222210010	0.0858212	0.3931
			221220010	---	0.2037
$S_0 \rightarrow S_7$	439.3	65.1	222120001	0.0000514	0.7108
			202122001	---	0.0744
$S_0 \rightarrow S_8$	428.4	66.7	221220010	0.0799110	0.3735
			222210001	---	0.3188
$S_0 \rightarrow S_9$	411.9	69.4	222210001	0.1256711	0.2387
			221220010	---	0.2186
$S_0 \rightarrow S_{10}$	396.2	72.2	222211000	0.0001096	0.7697
			212212000	---	0.0922
$S_0 \rightarrow S_{11}$	389.3	73.4	122221000	0.0146636	0.6323
			122211100	---	0.0868
$S_0 \rightarrow S_{12}$	381.1	75.0	221221000	0.0008472	0.7203
			211222000	---	0.0560
$S_0 \rightarrow S_{13}$	375.2	76.2	222121000	0.1025873	0.4292
			222210001	---	0.1754
$S_0 \rightarrow S_{14}$	351.9	81.2	221220001	0.4703139	0.5884
			212221000	---	0.0772

Table C.1I-1. Compound **1** – CASSCF/QD-NEVPT2. Transitions for the CPCM(THF) phase spectrum. 9o, 10e Active Space – 25 triplet roots, 15 singlet roots. Orbital (in order for CI vector notation below): d(xy), bonding d(x^2-y^2)/C(sp^2), d(yz), d(xz), d(z^2), d(x^2-y^2)/C(sp^2)*, π*(1), π*(2), π*(3).

Transition	**ΔE/nm**	**ΔE/kcal mol^{-1}**	**CI Vector**	f_{osc}	**Contribution**
$S_0 \rightarrow S_1$	671.4	42.6	222210100	0.0008408	0.8161
			202212100	---	0.0876
$S_0 \rightarrow S_2$	604.2	47.3	221220100	0.0622469	0.4193
			222120100	---	0.3382
$S_0 \rightarrow S_3$	546.6	52.3	221220100	0.1520657	0.3722
			222120100	---	0.2674
$S_0 \rightarrow S_4$	444.6	64.3	222120010	0.1043472	0.5270
			221220010	---	0.1267
$S_0 \rightarrow S_5$	440.4	64.9	122220100	0.0001963	0.4135
			222210010	---	0.3424
$S_0 \rightarrow S_6$	437.3	65.4	222210010	0.0003333	0.4320
			122220100	---	0.3239
$S_0 \rightarrow S_7$	407.1	70.2	222121000	0.0002537	0.6733
			221221000	---	0.1149
$S_0 \rightarrow S_8$	401.3	71.3	222211000	0.0305023	0.2808
			221220010	---	0.2155
$S_0 \rightarrow S_9$	399.9	71.5	122221000	0.0329884	0.4648
			222211000	---	0.1385
$S_0 \rightarrow S_{10}$	395.3	72.3	222210001	0.0001302	0.7121
			202212001	---	0.0765
$S_0 \rightarrow S_{11}$	390.1	73.3	221221000	0.0016152	0.5853
			222121000	---	0.1189
$S_0 \rightarrow S_{12}$	371.3	77.0	221220010	0.0139708	0.3376
			222211000	---	0.2166
$S_0 \rightarrow S_{13}$	365.5	78.2	222120001	0.1967238	0.4902
			222211000	---	0.0927
$S_0 \rightarrow S_{14}$	333.9	85.6	221220001	0.4607820	0.6454
			212221000	---	0.0665

Table C.1I-2. Compound **1** – CASSCF/QD-NEVPT2. Spin-orbit corrected absorption transitions for the CPCM(THF) phase spectrum. 9o, 10e Active Space – 25 triplet roots, 15 singlet roots.

Energy/ nm	**Energy/ kcal mol^{-1}**	f_{osc}	**Energy/ nm**	**Energy/ kcal mol^{-1}**	f_{osc}
686.8	41.6	0.0006638	420.9	67.9	0.0026607
681.3	42.0	0.0000492	420.7	68.0	0.0000932
679.1	42.1	0.0014753	413.2	69.2	0.0153295
672.4	42.5	0.0018573	412.5	69.3	0.0001385
641.0	44.6	0.0000800	412.5	69.3	0.0028688
640.3	44.7	0.0022972	405.7	70.5	0.0001127
638.3	44.8	0.0002073	398.7	71.7	0.0002244
602.4	47.5	0.0625017	398.2	71.8	0.0400852
567.6	50.4	0.0000177	397.7	71.9	0.0078340
566.9	50.4	0.0003588	389.3	73.4	0.0017359
566.5	50.5	0.0056594	381.8	74.9	0.0000093
548.2	52.2	0.0000804	381.7	74.9	0.0007565
548.0	52.2	0.0000025	381.7	74.9	0.0000361
547.4	52.2	0.0077188	378.1	75.6	0.0000159
541.3	52.8	0.1271535	377.9	75.6	0.0081108
453.0	63.1	0.0581791	377.2	75.8	0.0001353
446.5	64.0	0.0000000	369.9	77.3	0.0213533
446.4	64.1	0.0013619	364.8	78.4	0.1646061
444.2	64.4	0.0002830	350.5	81.6	0.0000067
437.0	65.4	0.0000814	350.3	81.6	0.0222811
434.5	65.8	0.0442016	350.2	81.6	0.0000361
422.4	67.7	0.0020976	332.2	86.1	0.4457060

Table C.1J. Compound **1** – TDDFT calculated lowest transition energies with CPCM(THF).

State	Root	Multiplicity	ΔE/nm	ΔE/kcal mol^{-1}	Transition	f_{osc}	Contribution
0	0	1	---	---	---	---	---
					---	---	---
1	1	3	858.5	33.3	119a → 123a	---	0.77795
					118a → 123a	---	0.13713
2	2	3	745.4	38.4	117a → 123a	---	0.70862
					118a → 123a	---	0.10691
3	5	3	689.5	41.4	119a → 120a	---	0.86068
					118a → 120a	---	0.09258
4	3	3	677.1	42.2	116a → 123a	---	0.76487
					115a → 123a	---	0.08395
5	8	3	660.6	43.3	118a → 120a	---	0.74196
					117a → 120a	---	0.11865
6	6	3	613.9	46.6	117a → 120a	---	0.81309
					118a → 120a	---	0.12652
7	14	3	593.8	48.1	115a → 120a	---	0.70784
					114a → 120a	---	0.13833
8	1	1	580.6	49.2	119a → 120a	0.0008793	0.85637
					118a → 120a	---	0.08983
9	4	3	530.2	53.9	114a → 123a	---	0.48094
					109a → 123a	---	0.16890
10	7	3	504.4	56.7	116a → 120a	---	0.85548
					115a → 120a	---	0.07395
11	9	3	504.2	56.7	114a → 120a	---	0.76732
					115a → 120a	---	0.16764
12	2	1	486.4	58.8	119a → 123a	0.0149377	0.43727
					117a → 120a	---	0.28572
13	11	1	464.3	61.6	115a → 120a	0.0010048	0.74526
					114a → 120a	---	0.17279
14	10	3	456.9	62.6	113a → 120a	---	0.81346
					114a → 120a	---	0.04189
15	3	1	451.4	63.3	117a → 123a	0.0000160	0.69793
					118a → 123a	---	0.09923
16	17	3	451.4	63.3	118a → 121a	---	0.71600
					117a → 121a	---	0.11668
17	4	1	438.8	65.2	117a → 120a	0.0091056	0.31383
					119a → 123a	---	0.20057
18	5	1	438.8	65.2	118a → 120a	0.0000671	0.34012
					116a → 123a	---	0.33024
19	6	1	432.3	66.1	116a → 123a	0.0006521	0.39229
					118a → 120a	---	0.30750
20	9	1	429.6	66.5	114a → 120a	0.0002344	0.74666
					115a → 120a	---	0.16061

Table C.1K. Compound **1** – TDDFT with CPCM(THF). Transitions corresponding to singlets down to 300 nm.

Root	ΔE/nm	ΔE/kcal mol^{-1}	Transition	f_{osc}	Contribution
1	580.6	49.2	119a → 120a	0.0008793	0.85637
			118a → 120a	---	0.08983
2	486.4	58.8	119a → 123a	0.0149377	0.43727
			117a → 120a	---	0.28572
11	464.3	61.6	115a → 120a	0.0010048	0.74526
			114a → 120a	---	0.17279
3	451.4	63.3	117a → 123a	0.0000160	0.69793
			118a → 123a	---	0.09923
4	438.8	65.2	117a → 120a	0.0091056	0.31383
			119a → 123a	---	0.20057
5	438.8	65.2	118a → 120a	0.0000671	0.34012
			116a → 123a	---	0.33024
6	432.3	66.1	116a → 123a	0.0006521	0.39229
			118a → 120a	---	0.30750
9	429.6	66.5	114a → 120a	0.0002344	0.74666
			115a → 120a	---	0.16061
8	429.3	66.6	116a → 120a	0.0774053	0.73096
			117a → 120a	---	0.11234
7	416.4	68.7	114a → 123a	0.0040780	0.43475
			109a → 123a	---	0.10090
10	411.7	69.4	119a → 121a	0.0002556	0.90253
			118a → 121a	---	0.06081
14	393.7	72.6	118a → 121a	0.0002484	0.74852
			117a → 121a	---	0.13455
13	374.9	76.3	119a → 122a	0.0000090	0.88873
			118a → 122a	---	0.07966
12	372.2	76.8	117a → 121a	0.0103918	0.75836
			118a → 121a	---	0.13533
18	363.5	78.7	118a → 122a	0.0002226	0.72376
			117a → 122a	---	0.11295
21	343.8	83.2	115a → 121a	0.0293580	0.61427
			114a → 121a	---	0.22459
17	341.1	83.8	116a → 121a	0.0253815	0.72971
			117a → 122a	---	0.10940
16	339.9	84.1	112a → 120a	0.0000921	0.96045
			---	---	---
15	335.0	85.4	117a → 122a	0.0228657	0.61108
			116a → 121a	---	0.12381
19	334.8	85.4	114a → 121a	0.0004394	0.68195
			115a → 121a	---	0.24704
25	321.7	88.9	115a → 122a	0.0021238	0.61609
			114a → 122a	---	0.16497

Table C.1L. Compound **1** with Ni–C distance of 3.20 Å – CASSCF/QD-NEVPT2 lowest transition energies in CPCM(THF). 8o, 10e Active Space – 25 triplet roots, 15 singlet roots. Orbitals (in order for CI vector notation below): d(xy), d(yz), d(z^2), d(xz), bonding d(x^2-y^2)/C(sp^2), d(x^2-y^2)/C(sp^2)*, π*(1), π*(2).

State	Root	Multiplicity	ΔE/nm	ΔE/kcal mol^{-1}	CI Vector	f_{osc}	Contribution
0	0	1	---	---	22211110	---	0.5994
					22212010	---	0.1042
					22112110	---	0.0579
1	0	3	9220.8	3.1	22211110	---	0.7413
					22112110	---	0.0631
2	1	3	4238.2	6.8	22121110	---	0.8175
					22122010	---	0.1200
3	1	1	3665.3	7.8	22121110	0.0000056	0.8154
					22122010	---	0.1208
4	2	3	3436.2	8.3	22211110	---	0.7508
					22212010	---	0.0904
5	3	3	2779.3	10.3	22121110	---	0.9893
					12221110	---	0.0030
6	4	3	2465.5	11.6	21221110	---	0.7577
					21222010	---	0.1076
7	2	1	2439.5	11.7	21221110	0.0000012	0.6968
					21222010	---	0.1037
8	5	3	2034.0	14.1	21221110	---	0.8601
					22211110	---	0.0519
9	3	1	1185.6	24.1	22220110	0.0001996	0.7437
					22221010	---	0.0721
10	6	3	1184.1	24.1	22220110	---	0.7898
					22221010	---	0.0749
11	4	1	1117.7	25.6	22211101	0.0501900	0.6199
					22212001	---	0.0954
12	5	1	1102.6	25.9	21212110	0.0046113	0.3668
					12221110	---	0.3589
13	7	3	1070.5	26.7	12221110	---	0.4548
					21212110	---	0.4330
14	8	3	1050.9	27.2	22121101	---	0.8032
					22122001	---	0.1181
15	9	3	1043.3	27.4	22211101	---	0.7337
					22212001	---	0.0821
16	6	1	1042.0	27.4	22121101	0.0000466	0.8118
					22122001	---	0.1196
17	10	3	1008.1	28.4	12221110	---	0.4842
					21212110	---	0.4145
18	11	3	994.2	28.8	22211101	---	0.8211
					22112101	---	0.0703
19	12	3	960.4	29.8	22121101	---	0.9873
					12221101	---	0.0030
20	7	1	896.2	31.9	21221101	0.0028482	0.7468

21222001	---	0.1085

Table C.1M. Compound **1** – CASSCF/QD-NEVPT2 composition of the singlet equilibrium ground state with Ni–C distance of 3.20 Å – CASSCF/QD-NEVPT2 in gas phase. 8o, 10e Active Space – 25 triplet roots, 15 singlet roots. Orbitals (in order for CI vector notation below): d(xy), d(yz), d(z^2), d(xz), bonding d(x^2-y^2)/C(sp^2), d(x^2-y^2)/C(sp^2)*, π*(1), π*(2).

CI Vector	Transition	Contribution
22211110	d(xz) + bonding d(x^2-y^2)/C(sp^2) → d(x^2-y^2)/C(sp^2)* + π*(1)	0.5998
22212010	d(xz) → π*(1)	0.1057
22221100	bonding d(x^2-y^2)/C(sp^2) → d(x^2-y^2)/C(sp^2)*	0.0567
22112110	d(xz) + d(z^2) → d(x^2-y^2)/C(sp^2)* + π*(1)	0.0549
22210210	d(xz) + 2x[bonding d(x^2-y^2)/C(sp^2)] → 2x[d(x^2-y^2)/C(sp^2)*] + π*(1)	0.0472
21221110	d(yz) + bonding d(x^2-y^2)/C(sp^2) → d(x^2-y^2)/C(sp^2)* + π*(1)	0.0434
22211101	d(xz) + bonding d(x^2-y^2)/C(sp^2) → d(x^2-y^2)/C(sp^2)* + π*(2)	0.0273
11222110	d(yz) + d(xy) → d(x^2-y^2)/C(sp^2)* + π*(1)	0.0170
22222000	Closed shell singlet (CSS) d^8	0.0105
21222010	d(yz) → π*(1)	0.0067
22212001	d(xz) → π*(2)	0.0047
22122100	d(z^2) → d(x^2-y^2)/C(sp^2)*	0.0034
21220210	2x[bonding d(x^2-y^2)/C(sp^2)] + d(yz) → 2x[d(x^2-y^2)/C(sp^2)*] + π*(1)	0.0034
12212110	d(xy) + d(xz) → d(x^2-y^2)/C(sp^2)* + π*(1)	0.0032

Table C.1N. Compound **1** – CASSCF/QD-NEVPT2 composition of the singlet equilibrium ground state with Ni–C distance of 3.20 Å – CASSCF/QD-NEVPT2 with CPCM(THF). 8o, 10e Active Space – 25 triplet roots, 15 singlet roots. Orbitals (in order for CI vector notation below): d(xy), d(yz), d(z^2), d(xz), bonding d(x^2-y^2)/C(sp^2), d(x^2-y^2)/C(sp^2)*, π*(1), π*(2).

CI Vector	Transition	Contribution
22211110	d(xz) + bonding d(x^2-y^2)/C(sp^2) → d(x^2-y^2)/C(sp^2)* + π*(1)	0.5994
22212010	d(xz) → π*(1)	0.1042
22112110	d(xz) + d(z^2) → d(x^2-y^2)/C(sp^2)* + π*(1)	0.0579
22221100	bonding d(x^2-y^2)/C(sp^2) → d(x^2-y^2)/C(sp^2)*	0.0560
21221110	d(yz) + bonding d(x^2-y^2)/C(sp^2) → d(x^2-y^2)/C(sp^2)* + π*(1)	0.0463
22210210	d(xz) + 2x[bonding d(x^2-y^2)/C(sp^2)] → 2x[d(x^2-y^2)/C(sp^2)*] + π*(1)	0.0463
22211101	d(xz) + bonding d(x^2-y^2)/C(sp^2) → d(x^2-y^2)/C(sp^2)* + π*(2)	0.0254
11222110	d(yz) + d(xy) → d(x^2-y^2)/C(sp^2)* + π*(1)	0.0169
22222000	Closed shell singlet (CSS) d^8	0.0102
21222010	d(yz) → π*(1)	0.0071
22212001	d(xz) → π*(2)	0.0043
22122100	d(z^2) → d(x^2-y^2)/C(sp^2)*	0.0035
21220210	2x[bonding d(x^2-y^2)/C(sp^2)] + d(yz) → 2x[d(x^2-y^2)/C(sp^2)*] + π*(1)	0.0035
12212110	d(xy) + d(xz) → d(x^2-y^2)/C(sp^2)* + π*(1)	0.0029

Table C.1O. Leadings terms of CI-vector for T_0 (first triplet manifold reached from vertical excitation of singlet ground state) of **1** in Figure 4.4. In the vicinity of the equilibrium geometry, the CI-vector is dominated by ^{3}d-d transitions. Note that using the relaxed, DFT optimized T_d triplet geometries of **1** (surfaces shown in Figure 4.1), the ground state triplet CI-vector is very heavily dominated by the $[d(x^2\text{-}y^2)]^1[d(z^2)/C(sp^2)^*]^1$ ^{3}d-d configuration (65% at the 1.9 Å equilibrium geometry, Figure C.1H). For T_0, at long Ni–C distances, the transition d(xz) → π*(1) is very dominant, but still less so than in the repulsive manifold shown in black, and assigned to the aforementioned transition, in Figure 4.4.

Ni–C Distance (Å)	Weight	Transition
1.60	0.8420	$d(z^2) \rightarrow \pi^*(1)$
	0.0669	$d(xy) \rightarrow \pi^*(1)$
1.80	0.7339	$d(z^2) \rightarrow \pi^*(1)$
	0.0867	$d(xy) \rightarrow \pi^*(1)$
1.89	0.4035	$d(z^2) \rightarrow d(x^2\text{-}y^2)/C(sp^2)^*$
	0.1917	$d(xz) \rightarrow \pi^*(1)$
2.20	0.4499	$d(xz) \rightarrow d(x^2\text{-}y^2)/C(sp^2)^*$
	0.1777	$d(yz) \rightarrow d(x^2\text{-}y^2)/C(sp^2)^*$
2.40	0.5278	$d(z^2) \rightarrow d(x^2\text{-}y^2)/C(sp^2)^*$
	0.2942	$d(z^2)$ + bonding $d(x^2\text{-}y^2)/C(sp^2) \rightarrow 2x[d(x^2\text{-}y^2)/C(sp^2)^*]$
2.60	0.4220	dz2→ π*(1)
	0.4045	$d(z^2)$ + bonding $d(x^2\text{-}y^2)/C(sp^2) \rightarrow d(x^2\text{-}y^2)/C(sp^2)^* + \pi^*(1)$
2.80	0.5427	$d(xz)$ + bonding $d(x^2\text{-}y^2)/C(sp^2) \rightarrow d(x^2\text{-}y^2)/C(sp^2)^* + \pi^*(1)$
	0.2368	$d(xz) \rightarrow \pi^*(1)$
3.00	0.6998	$d(xz)$ + bonding $d(x^2\text{-}y^2)/C(sp^2) \rightarrow d(x^2\text{-}y^2)/C(sp^2)^* + \pi^*(1)$
	0.0650	$d(xz) \rightarrow \pi^*(1)$
3.20	0.7446	$d(xz)$ + bonding $d(x^2\text{-}y^2)/C(sp^2) \rightarrow d(x^2\text{-}y^2)/C(sp^2)^* + \pi^*(1)$
	0.0600	$d(z^2)$ + bonding $d(x^2\text{-}y^2)/C(sp^2) \rightarrow d(x^2\text{-}y^2)/C(sp^2)^* + \pi^*(1)$
3.40	0.7572	$d(xz)$ + bonding $d(x^2\text{-}y^2)/C(sp^2) \rightarrow d(x^2\text{-}y^2)/C(sp^2)^* + \pi^*(1)$
	0.0610	bonding $d(x^2\text{-}y^2)/C(sp^2) \rightarrow d(x^2\text{-}y^2)/C(sp^2)^*$
3.60	0.7627	$d(xz)$ + bonding $d(x^2\text{-}y^2)/C(sp^2) \rightarrow d(x^2\text{-}y^2)/C(sp^2)^* + \pi^*(1)$
	0.0617	bonding $d(x^2\text{-}y^2)/C(sp^2) \rightarrow d(x^2\text{-}y^2)/C(sp^2)^*$

Table C.1P. Spin Contamination Values from BSS Calculation and Yamaguchi Correction[1,2] BSS Energy of **1**. Using $<S^2>$ values and energies for the triplet and BSS solutions for the same geometry, $\alpha = <S^2>_{trip.}/(<S^2>_{trip.} - <S^2>_{BSS})$, $\beta = <S^2>_{BSS}/(<S^2>_{trip.} - <S^2>_{BSS})$, and $E_{Yamaguchi} = \alpha E_{BSS} - \beta E_{trip}$.

Ni–C Dist. (Å)	**$<S^2>$ S=1**	**$<S^2>$ BSS**	**α**	**β**	**Energy S=1/ kcal mol^{-1}**	**Energy BSS/ kcal mol^{-1}**	**Energy Yamaguchi/ kcal mol^{-1}**
1.60	2.01	0.00	1.00	0.00	72.8	22.4	22.4
1.80	2.01	0.00	1.00	0.00	43.6	1.9	1.9
1.89	2.01	0.00	1.00	0.00	38.3	0.0	0.0
2.00	2.01	0.00	1.00	0.00	35.8	1.1	1.1
2.20	2.01	0.00	1.00	0.00	37.2	8.2	8.2
2.40	2.01	0.00	1.00	0.00	42.0	17.8	17.8
2.60	2.02	0.24	1.13	0.13	47.0	27.3	24.7
2.80	2.03	0.51	1.34	0.34	48.1	34.0	29.1
3.00	2.03	0.71	1.53	0.53	47.0	38.2	33.5
3.20	2.03	0.83	1.70	0.70	46.2	40.9	37.1
3.40	2.03	0.92	1.82	0.82	45.5	42.4	39.9
3.60	2.03	0.96	1.91	0.91	45.0	43.3	41.7

Table C.1Q. Compound **1** (S=0) – Decomposition of Leading Configuration in the Singlet Ground State into Specific Spin Arrangements – Ni–C distance of 3.6 Å and 3.4 Å – CASSCF/QD-NEVPT2 in gas phase. 8o, 10e Active Space – 25 triplet roots, 15 singlet roots.

3.6 Å Spin Det.	**Spin Arrangement in Singly Occupied Orbitals**	**Coefficient**	**Weight**
222dduu0	$(d(xz))^{down}(d(x^2-y^2))^{down}(Csp^2)^{*up}(\pi^*(1))^{up}$	-0.486	0.236
222dudu0	$(d(xz))^{down}(d(x^2-y^2))^{up}(Csp^2)^{*down}(\pi^*(1))^{up}$	0.284	0.081
222uddu0	$(d(xz))^{up}(d(x^2-y^2))^{down}(Csp^2)^{*down}(\pi^*(1))^{up}$	0.202	0.041
222duud0	$(d(xz))^{down}(d(x^2-y^2))^{up}(Csp^2)^{*up}(\pi^*(1))^{down}$	0.202	0.041
222udud0	$(d(xz))^{up}(d(x^2-y^2))^{down}(Csp^2)^{*up}(\pi^*(1))^{down}$	0.284	0.081
222uudd0	$(d(xz))^{up}(d(x^2-y^2))^{up}(Csp^2)^{*down}(\pi^*(1))^{down}$	-0.486	0.236
		Total Weight:	0.716

3.4 Å Spin Det.	**Spin Arrangement in Singly Occupied Orbitals**	**Coefficient**	**Weight**
222dduu0	$(d(xz))^{down}(d(x^2-y^2))^{down}(Csp^2)^{*up}(\pi^*(1))^{up}$	0.470	0.221
222dudu0	$(d(xz))^{down}(d(x^2-y^2))^{up}(Csp^2)^{*down}(\pi^*(1))^{up}$	-0.274	0.075
222uddu0	$(d(xz))^{up}(d(x^2-y^2))^{down}(Csp^2)^{*down}(\pi^*(1))^{up}$	-0.196	0.039
222duud0	$(d(xz))^{down}(d(x^2-y^2))^{up}(Csp^2)^{*up}(\pi^*(1))^{down}$	-0.196	0.039
222udud0	$(d(xz))^{up}(d(x^2-y^2))^{down}(Csp^2)^{*up}(\pi^*(1))^{down}$	-0.274	0.075
222uudd0	$(d(xz))^{up}(d(x^2-y^2))^{up}(Csp^2)^{*down}(\pi^*(1))^{down}$	0.470	0.221
		Total Weight:	0.670

Table C.1R. Compound **1** (S=1) – Decomposition of Leading Configuration in the Triplet Ground State into Specific Spin Arrangements – Ni–C distance of 3.6 Å and 3.4 Å – CASSCF/QD-NEVPT2 in gas phase. 8o, 10e Active Space – 25 triplet roots, 15 singlet roots.

3.6 Å Spin Det.	**Spin Arrangement in Singly Occupied Orbitals**	**Coefficient**	**Weight**
222duuu0	$(d(yz))^{down}(d(x^2\text{-}y^2))^{up}(Csp^2)^{*up}(\pi^*(1))^{up}$	0.390	0.152
222uduu0	$(d(yz))^{up}(d(x^2\text{-}y^2))^{down}(Csp^2)^{*up}(\pi^*(1))^{up}$	0.282	0.080
222uudu0	$(d(yz))^{up}(d(x^2\text{-}y^2))^{up}(Csp^2)^{*down}(\pi^*(1))^{up}$	0.048	0.002
222uuud0	$(d(yz))^{up}(d(x^2\text{-}y^2))^{up}(Csp^2)^{*up}(\pi^*(1))^{down}$	-0.720	0.519
		Total Weight:	0.753

3.4 Å Spin Det.	**Spin Arrangement in Singly Occupied Orbitals**	**Coefficient**	**Weight**
222duuu0	$(d(yz))^{down}(d(x^2\text{-}y^2))^{up}(Csp^2)^{*up}(\pi^*(1))^{up}$	0.358	0.128
222uduu0	$(d(yz))^{up}(d(x^2\text{-}y^2))^{down}(Csp^2)^{*up}(\pi^*(1))^{up}$	0.253	0.064
222uudu0	$(d(yz))^{up}(d(x^2\text{-}y^2))^{up}(Csp^2)^{*down}(\pi^*(1))^{up}$	0.085	0.007
222uuud0	$(d(yz))^{up}(d(x^2\text{-}y^2))^{up}(Csp^2)^{*up}(\pi^*(1))^{down}$	-0.696	0.485
		Total Weight:	0.684

C.C. Figures Part 1: Compound *1*

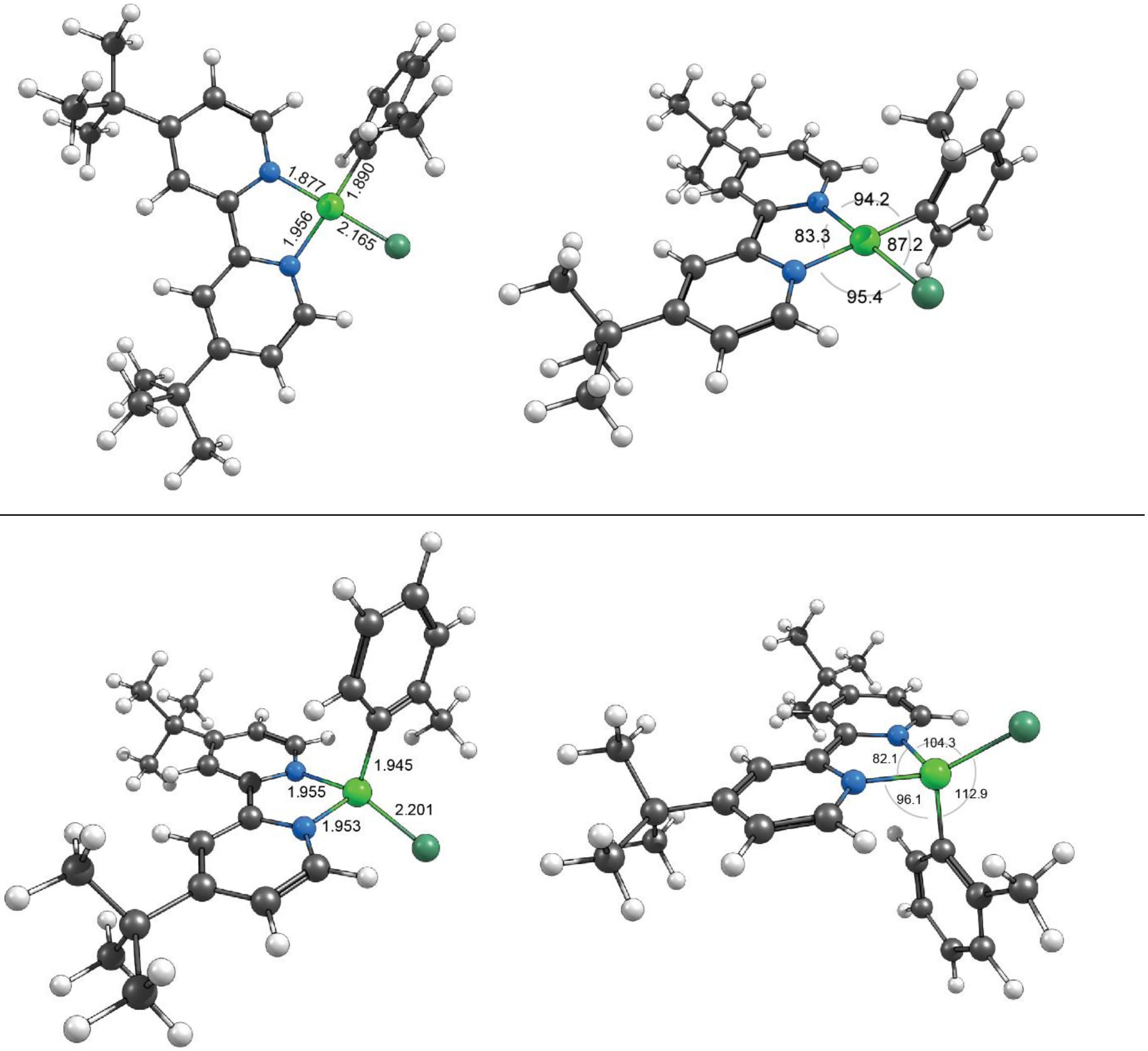

Figure C.1A. Top: square planar equilibrium geometry of compound **1** (S=0), and bottom: tetrahedral equilibrium geometry of **1** (S=1) as calculated by DFT. Selected bond lengths and angles are shown.

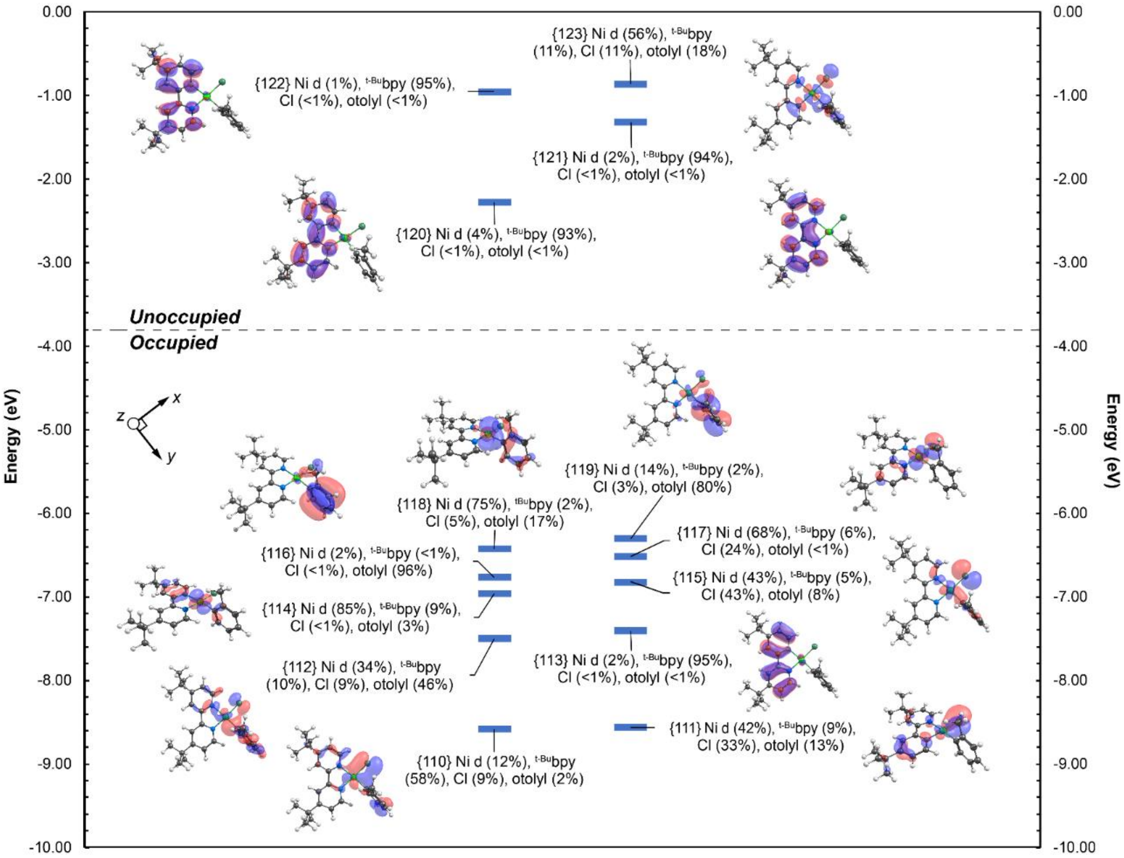

Figure C.1B. Compound 1 (S=0) – Single point DFT frontier molecular orbital diagram. Orbitals are offset for clarity.

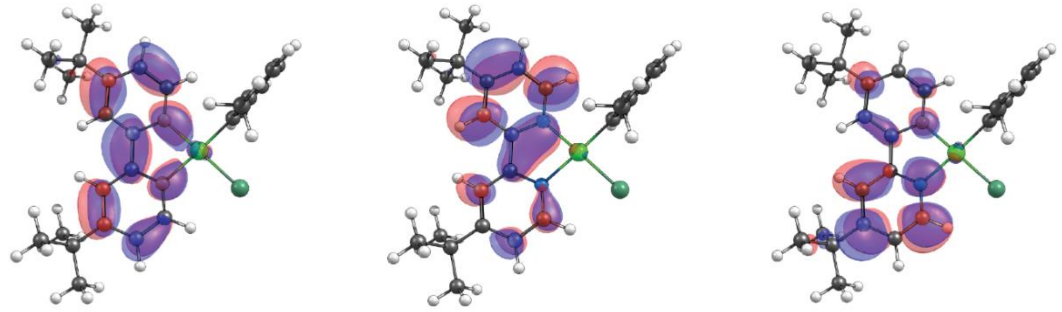

π*(1) *Occ: 0.361*

π*(2) *Occ: 0.184*

π*(3) *Occ: 0.162*

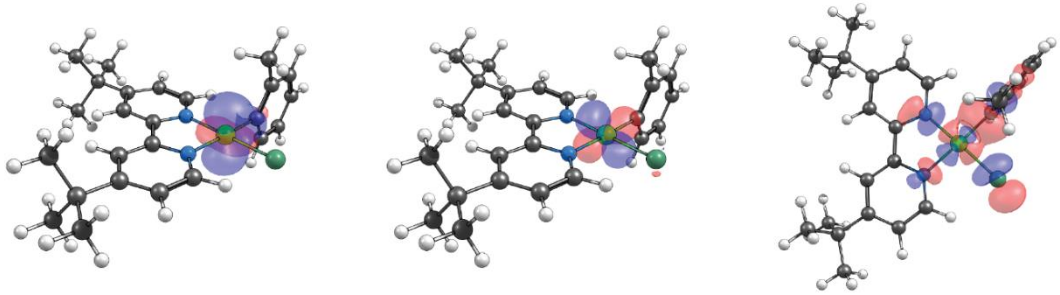

$d(z^2)$ *Occ: 1.688*

$d(xz)$ *Occ: 1.686*

$d(x^2-y^2)/C(sp^2)^*$ *Occ: 0.688*

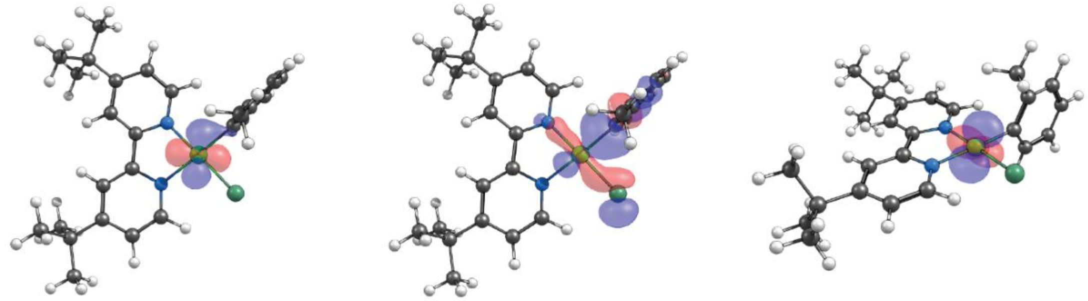

$d(xy)$ *Occ: 1.769*

bonding $d(x^2-y^2)/C(sp^2)$ *Occ: 1.765*

$d(yz)$ *Occ: 1.698*

Figure C.1C. Compound **1** (S=0) – CASSCF/QD-NEVPT2 9o, 10e Active Space.

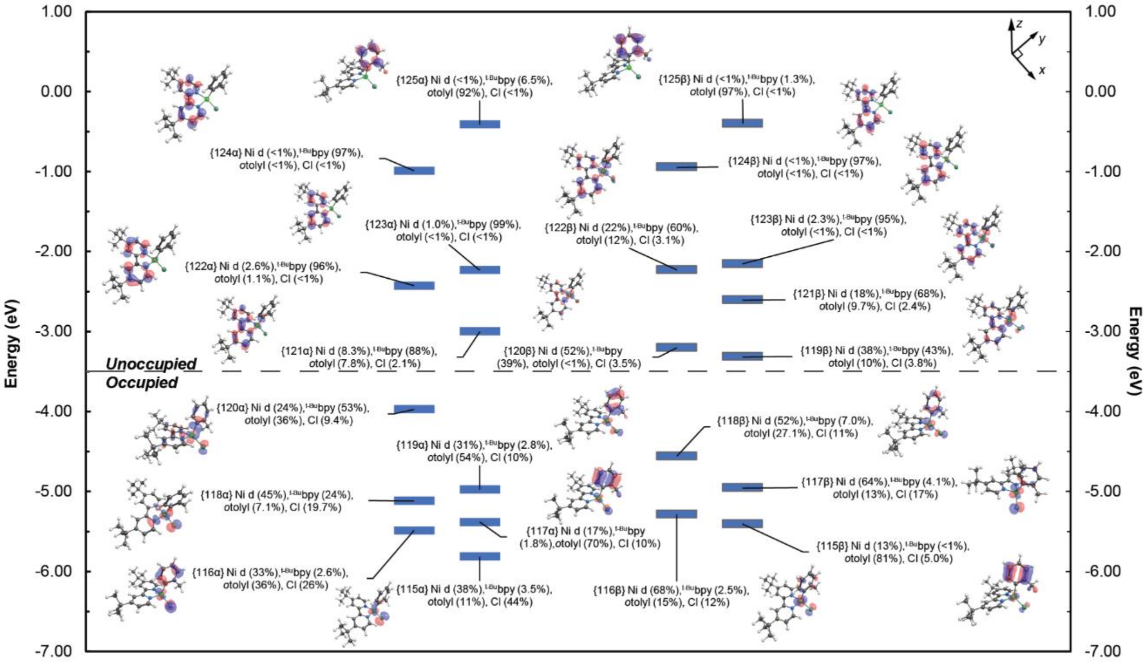

Figure C.1D. Compound 1 (S=1) – Single point DFT frontier molecular orbital diagram, with α orbitals on the left and β orbitals on the right. α and β orbitals are also offset for clarity.

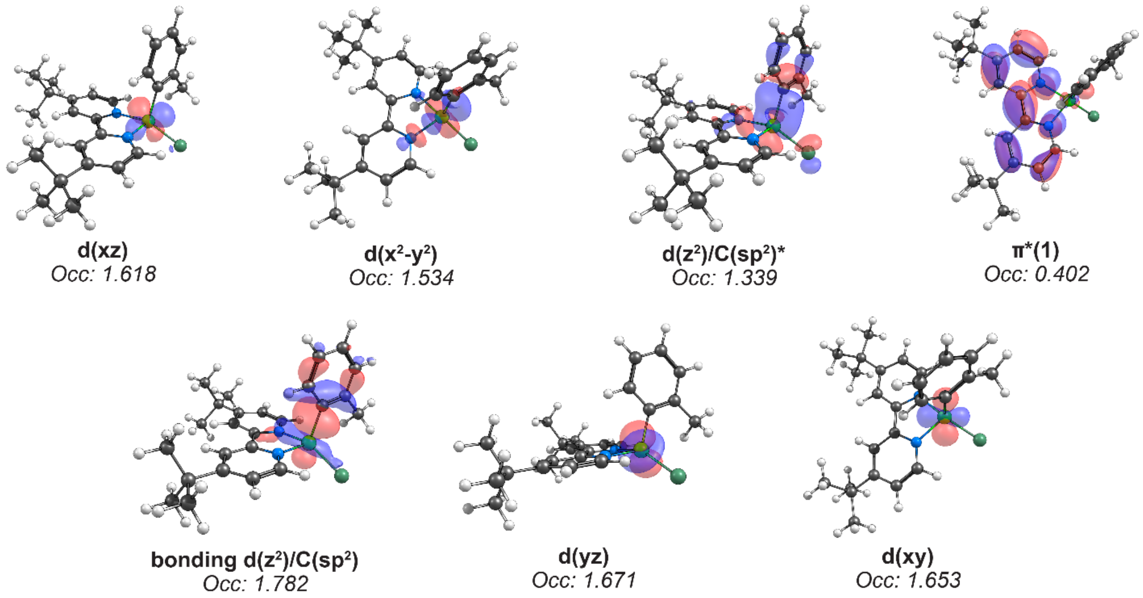

Figure C.1E. Compound **1** (S=1) – CASSCF/QD-NEVPT2 7o, 10e Active Space.

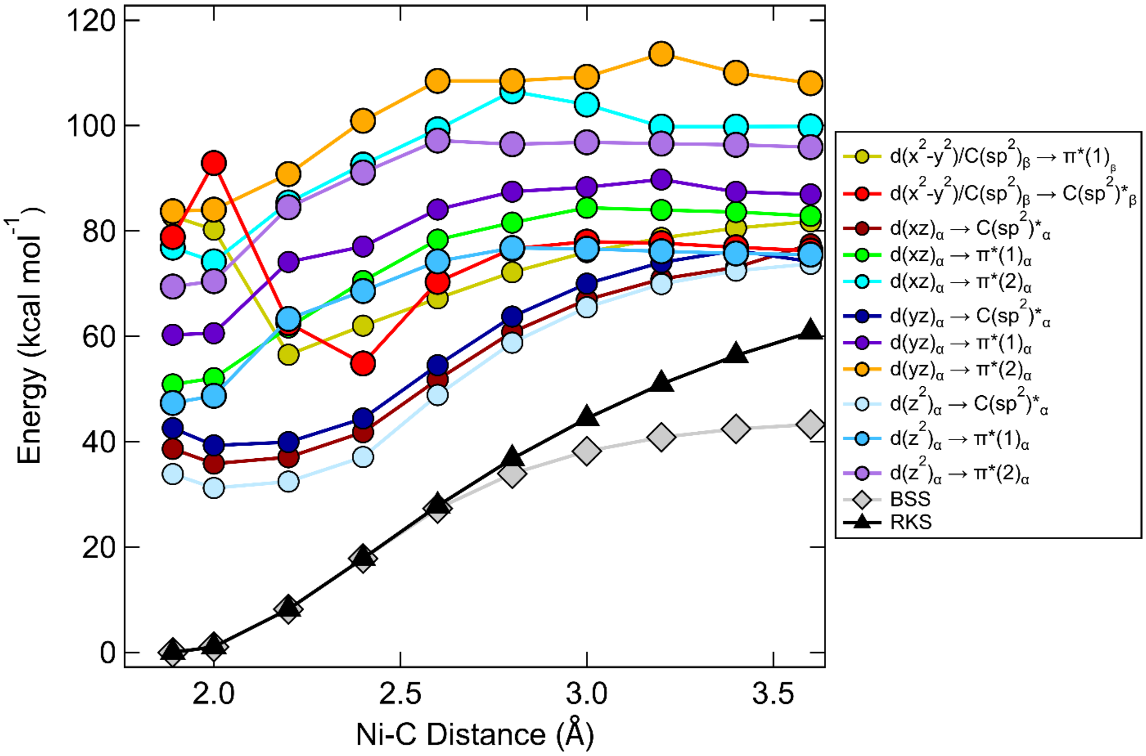

Figure C.1F. Broken symmetry singlet TDDFT excitations along the Ni–C coordinate of **1** show no repulsive excited states. Spin-contaminated BSS calculations gave a Ni–C BDE of 43.3 kcal mol^{-1}, while the Yamaguchi corrected Ni–C BDE is only marginally different, at 41.7 kcal mol^{-1}.

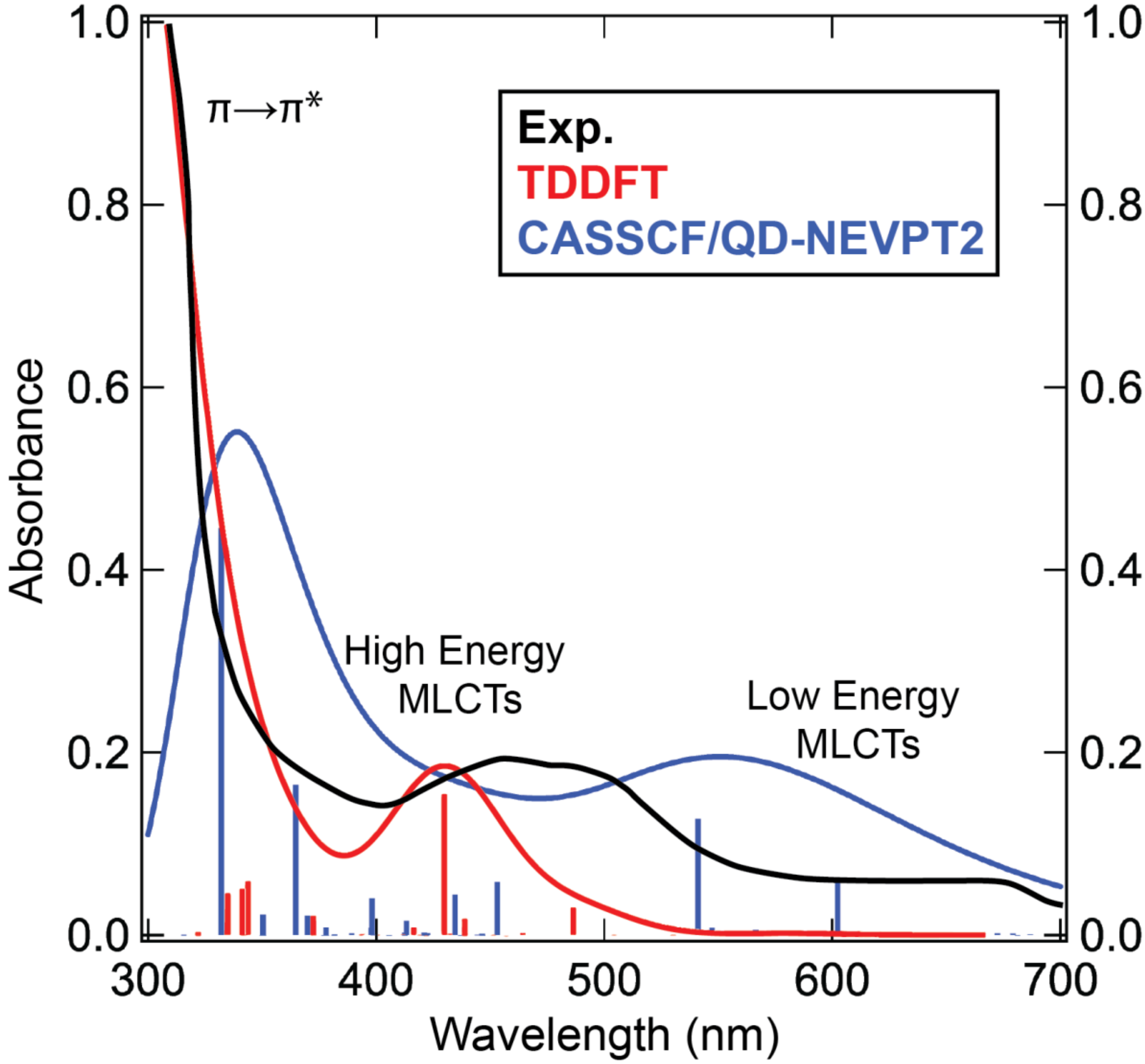

Figure C.1G. Overlay of the experimental (THF) and calculated UV-vis spectrum of the equilibrium structure of **1**. The TDDFT calculated spectrum (CPCM(THF)) in this research aligns well with that previously reported.[3] The CASSCF/QD-NEVPT2 spectrum is spin-orbit coupling corrected with CPCM(THF). Note that the relative oscillator strengths of the lower energy MLCT transitions are partially over-estimated in the CASSCF/QD-NEVPT2 calculated spectrum. This spectrum also does not display the intramolecular bpy-based π→π* transitions, as the π orbitals are not part of the active space.

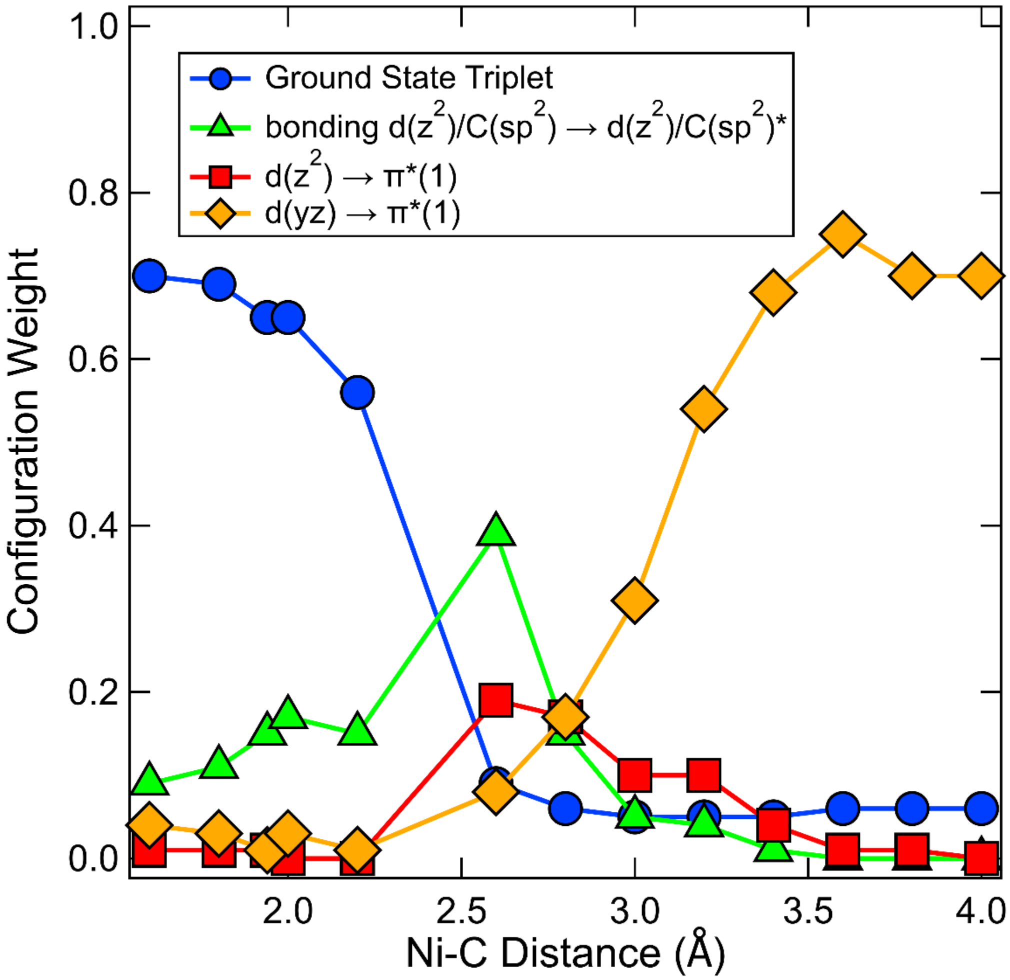

Figure C.1H. Plot of the dominant configurations that contribute to the ground state CI vector along the optimized triplet Ni–C bond elongation surface of **1**. Note that for high spin **1**, the ground state triplet is $[d(x^2\text{-}y^2)]^1[(dz^2)/C(sp^2)^*]^1$, making a d(yz) → π*(1) transition yield an orbital configuration of $[d(yz)]^1[d(x^2\text{-}y^2)]^1[(dz^2)/C(sp^2)^*]^1[\pi^*(1)]^1$.

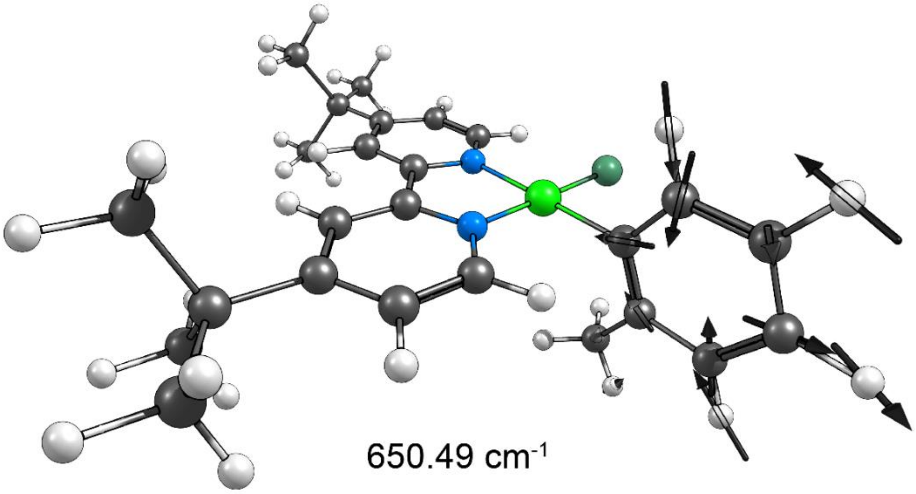

Figure C.1I. Higher energy vibrational frequency in **1** that exhibits a Ni–C bond stretching mode.

C.D. Tables Part 2: Compound *2*

Table C.2A. Compound **2** – TDDFT lowest transition energies with CPCM(THF).

State	Root	Mult.	ΔE/nm	ΔE/kcal mol^{-1}	Transition	f_{osc}	Contribution
0	0	1	---	---	---	---	---
					---	---	---
1	1	3	869.2	32.9	90a → 94a	---	0.88196
					84a → 94a	---	0.03221
2	4	3	840.6	34.0	90a → 91a	---	0.95884
					90a → 92a	---	0.01518
3	2	3	700.1	40.8	88a → 94a	---	0.79230
					87a → 94a	---	0.11738
4	1	1	685.0	41.7	90a → 91a	0.0008022	0.97220
					---	---	---
5	13	3	654.9	43.7	87a → 94a	---	0.76446
					88a → 94a	---	0.09933
6	3	3	647.7	44.1	89a → 91a	---	0.76152
					87a → 91a	---	0.12192
7	8	3	621.1	46.0	88a → 91a	---	0.84342
					87a → 91a	---	0.01896
8	6	3	597.5	47.8	87a → 91a	---	0.80903
					89a → 91a	---	0.09728
9	7	3	561.6	50.9	89a → 94a	---	0.27140
					85a → 94a	---	0.20986
10	5	3	515.1	55.5	88a → 91a	---	0.43424
					90a → 94a	---	0.38209
11	2	1	499.1	57.3	88a → 91a	0.0049816	0.43424
					90a → 94a	---	0.38209
12	10	3	489.4	58.4	90a → 92a	---	0.63866
					85a → 91a	---	0.28025
13	11	3	473.1	60.4	85a → 91a	---	0.56985
					90a → 92a	---	0.32997
14	3	1	471.9	60.6	89a → 91a	0.0019717	0.60213
					88a → 94a	---	0.25483
15	12	3	456.8	62.6	90a → 93a	---	0.97175
					---	---	---
16	9	1	437.6	65.3	90a → 92a	0.0004057	0.93755
					85a → 91a	---	0.02892
17	4	1	436.6	65.5	90a → 94a	0.0042122	0.44811
					87a → 91a	---	0.21201
18	11	1	428.9	66.7	86a → 91a	0.0009630	0.61475
					90a → 93a	---	0.33337
19	5	1	418.4	68.3	88a → 94a	0.0035092	0.61036
					89a → 91a	---	0.28106
20	8	1	414.8	68.9	87a → 91a	0.0473264	0.47012
					88a → 91a	---	0.21114

Table C.2B-1. Compound **2** – CASSCF/QD-NEVPT2 lowest transition energies in the gas phase. 5o, 8e Active Space. 10 triplet roots, 10 singlet roots. Orbitals (in order for CI vector notation below): d(z^2), d(xz), d(yz), d(xy), d(x^2-y^2).

State	**Root**	**Mult.**	**ΔE/nm**	**ΔE/kcal mol^{-1}**	**CI Vector**	f_{osc}	**Contribution**
0	0	1	---	---	22220	---	0.9515
					22022	---	0.0127
1	0	3	1175.9	24.3	12221	---	0.9996
					---	---	---
2	1	3	963.0	29.7	22121	---	0.8786
					21221	---	0.0926
3	2	3	891.6	32.1	21221	---	0.8834
					22121	---	0.0919
4	3	3	627.0	45.6	22211	---	0.9394
					21122	---	0.0578
5	1	1	420.7	68.0	12221	0.0000621	0.9806
					20222		0.0088
6	2	1	407.6	70.1	22121	0.0000131	0.9097
					21221		0.0496
7	3	1	391.7	73.0	21221	0.0001101	0.9245
					22121		0.0488
8	4	1	385.2	74.2	22211	0.0000915	0.9826
					22121		0.0155
9	4	3	293.2	97.5	12212	---	0.9890
					22112	---	0.0055
10	5	3	288.5	99.1	22112	---	0.7613
					21212	---	0.0649

Table C.2B-2. Compound **2** – CASSCF/QD-NEVPT2 lowest transition energies with CPCM(THF). 5o, 8e Active Space – 10 triplet roots, 10 singlet roots. Orbitals (in order for CI vector notation below): d(z^2), d(xz), d(yz), d(xy), d(x^2-y^2).

State	Root	Mult,	ΔE/nm	ΔE/kcal mol^{-1}	CI Vector	f_{osc}	Contribution
0	0	1	---	---	22220	---	0.9510
					02222	---	0.0211
1	0	3	1237.6	23.1	12221	---	0.9992
					---	---	---
2	1	3	1011.0	28.3	22121	---	0.9053
					21221	---	0.0672
3	2	3	941.0	30.4	21221	---	0.9075
					22121	---	0.0668
4	3	3	635.5	45.0	22211	---	0.9379
					21122	---	0.0611
5	1	1	426.9	67.0	12221	0.0000485	0.9796
					20222	---	0.0090
6	2	1	414.6	69.0	22121	0.0000040	0.9339
					21221	---	0.0351
7	3	1	399.8	71.5	21221	0.0001066	0.9353
					22121	---	0.0359
8	4	1	387.0	73.9	22211	0.0000935	0.9944
					22121	---	0.0048
9	4	3	297.1	96.2	12212	---	0.9759
					21212	---	0.0145
10	5	3	293.3	97.5	22112	---	0.7716
					11222	---	0.1477

Table C.2C-1. Compound **2** – CASSCF/QD-NEVPT2 lowest transition energies in the gas phase. 9o, 10e Active Space – 25 triplet roots, 15 singlet roots. Orbitals (in order for CI vector notation below): bonding d(x^2-y^2)/C(sp^2), d(xy), d(xz), d(yz), d(z^2), d(x^2-y^2)/C(sp^2)*, π*(1), π*(2), π*(3).

State	Root	Mult.	ΔE/nm	ΔE/kcal mol^{-1}	CI Vector	f_{osc}	Contribution
0	0	1	---	---	222220000	---	0.5464
					222120100	---	0.1039
					122221000	---	0.0858
1	0	3	970.1	29.5	222211000	---	0.4539
					122212000	---	0.1696
2	1	3	804.6	35.5	222121000	---	0.6017
					212221000	---	0.1400
3	2	3	758.2	37.7	212221000	---	0.5703
					222121000	---	0.1536
4	3	3	737.1	38.8	222210100	---	0.5396
					122220100	---	0.2880
5	1	1	729.4	39.2	222210100	0.0019683	0.5703
					122220100	---	0.2712
6	4	3	642.1	44.5	222120100	---	0.8142
					122112100	---	0.0417
7	2	1	624.3	45.8	222120100	0.0905865	0.6714
					212220100	---	0.0655
8	5	3	592.5	48.3	221221000	---	0.6680
					212122000	---	0.0822
9	6	3	571.6	50.0	212220100	---	0.7675
					212202100	---	0.0438
10	3	1	569.9	50.2	212220100	0.1206524	0.6956
					112212100	---	0.0370
11	4	1	444.4	64.3	221220100	0.0003508	0.7306
					212121100	---	0.0444
12	7	3	433.9	65.9	222210010	---	0.4812
					122220010	---	0.2506
13	5	1	432.7	66.1	222210010	0.0010716	0.4782
					122220010	---	0.2503
14	8	3	429.9	66.5	221220100	---	0.7217
					212121100	---	0.0699
15	6	1	410.4	69.7	222120010	0.0274877	0.3593
					222211000	---	0.1504
16	7	1	404.5	70.7	222120001	0.0141815	0.2505
					222211000	---	0.1880
17	9	3	400.6	71.4	222120010	---	0.7918
					122112010	---	0.0430
18	8	1	399.8	71.5	222121000	0.0076735	0.4769
					222120010	---	0.0742
19	9	1	396.4	72.1	222210001	0.0025346	0.3590
					122220001	---	0.1937
20	10	3	389.0	73.5	222210001	---	0.5095
					122220001	---	0.2709

Table C.2C-2. Compound **2** – CASSCF/QD-NEVPT2 lowest transition energies with CPCM(THF). 9o, 10e Active Space – 25 triplet roots, 15 singlet roots. Orbitals (in order for CI vector notation below): bonding d(x^2-y^2)/C(sp^2), d(xy), d(xz), d(yz), d(z^2), d(x^2-y^2)/C(sp^2)*, π*(1), π*(2), π*(3).

State	**Root**	**Mult.**	**ΔE/nm**	**ΔE/kcal mol^{-1}**	**CI Vector**	f_{osc}	**Contribution**
0	0	1	---	---	222220000	---	0.5730
					222120100	---	0.1468
					122221000	---	0.0958
1	0	3	881.1	32.4	222211000	---	0.7022
					122212000	---	0.1274
2	1	3	794.6	36.0	222210100	---	0.7593
					022212100	---	0.0692
3	1	1	768.5	37.2	222210100	0.0013739	0.7523
					022212100	---	0.0686
4	2	3	747.1	38.3	221221000	---	0.4723
					222121000	---	0.2884
5	3	3	698.1	41.0	222121000	---	0.3430
					221221000	---	0.2101
6	4	3	681.7	41.9	222120100	---	0.5581
					222121000	---	0.1158
7	2	1	645.2	44.3	221220100	0.0410929	0.4915
					222120100	---	0.2839
8	5	3	606.9	47.1	221220100	---	0.7427
					222120100	---	0.0615
9	3	1	577.4	49.5	221220100	0.1644325	0.3046
					222120100	---	0.2834
10	6	3	570.0	50.2	212221000	---	0.7017
					221122000	---	0.0669
11	4	1	461.1	62.0	212220100	0.0001703	0.7321
					221121100	---	0.0719
12	7	3	451.1	63.4	222210010	---	0.3902
					212220100	---	0.3515
13	8	3	449.1	63.7	212220100	---	0.4083
					222210010	---	0.3346
14	5	1	448.7	63.7	222210010	0.0030332	0.6533
					222120010	---	0.0760
15	6	1	439.7	65.0	222120010	0.1016451	0.4437
					221220010	---	0.1562
16	9	3	416.2	68.7	222120010	---	0.7280
					22122010	---	0.0705
17	7	1	413.6	69.1	222210001	0.0097205	0.5953
					222211000	---	0.1138
18	10	3	402.8	71.0	222210001	---	0.7274
					022212001	---	0.0661
19	8	1	397.2	72.0	222121000	0.0315108	0.2618
					222120001	---	0.1434
20	9	1	392.8	72.8	222121000	0.0000160	0.2800
					212221000	---	0.2335

Table C.2C-3. Compound **2** – CASSCF/QD-NEVPT2 lowest transition energies in gas phase 9o, 10e Active Space – 25 triplet roots, 25 singlet roots. Orbitals (in order for CI vector notation below): d(z^2), d(xz), d(xy), d(yz), bonding d(x^2-y^2)/C(sp^2), d(x^2-y^2)/C(sp^2)*, π*(1), π*(2), π*(3).

State	Root	Mult.	ΔE/nm	ΔE/kcal mol^{-1}	CI Vector	f_{osc}	Contribution
0	0	1	---	---	222220000	---	0.5529
					222211000	---	0.1358
					222120100	---	0.0884
1	0	3	1069.5	26.7	122221000	---	0.4330
					222211000	---	0.2996
2	1	3	814.6	35.1	212221000	---	0.4162
					222121000	---	0.3044
3	2	3	776.5	36.8	222121000	---	0.4340
					212221000	---	0.2879
4	3	3	739.2	38.7	122220100	---	0.4187
					222210100	---	0.3986
5	1	1	731.2	39.1	122220100	0.0032771	0.4253
					222210100	---	0.3978
6	4	3	644.6	44.4	222120100	---	0.8188
					122112100	---	0.0443
7	2	1	634.3	45.1	222120100	0.1012976	0.7104
					222211000	---	0.0384
8	5	3	568.6	50.3	212220100	---	0.4565
					221221000	---	0.2881
9	3	1	565.3	50.6	212220100	0.0896286	0.7351
					212202100	---	0.0675
10	6	3	558.8	51.2	221221000	---	0.3895
					212220100	---	0.3283
11	7	3	471.8	60.6	221220100	---	0.6713
					212121100	---	0.0636
12	8	3	467.7	61.1	122220010	---	0.3885
					222210010	---	0.3303
13	4	1	448.0	63.8	221220100	0.0026610	0.7014
					221202100	---	0.0521
14	5	1	436.5	65.5	122220010	0.0021410	0.3993
					222210010	---	0.3394
15	6	1	421.5	67.8	222120010	0.0471175	0.2936
					122221000	---	0.1924
16	9	3	406.0	70.4	222120010	---	0.7977
					122112010	---	0.0460
17	7	1	398.6	71.7	222121000	0.0012705	0.6168
					122122000	---	0.0491
18	8	1	397.8	71.9	222120010	0.0337901	0.2880
					122221000	---	0.1805
19	10	3	390.3	73.3	122220001	---	0.4339
					222210001	---	0.3609
20	9	1	389.5	73.4	221221000	0.0056080	0.5974
					122220001	---	0.0506

Table C.2C-4. Compound **2** – CASSCF/QD-NEVPT2 lowest transition energies with CPCM(THF). 9o, 10e Active Space – 25 triplet roots, 25 singlet roots. Orbitals (in order for CI vector notation below): d(z^2), d(xz), d(xy), d(yz), bonding d(x^2-y^2)/C(sp^2), d(x^2-y^2)/C(sp^2)*, π*(1), π*(2), π*(3).

State	**Root**	**Mult.**	**ΔE/nm**	**ΔE/kcal mol^{-1}**	**CI Vector**	f_{osc}	**Contribution**
0	0	1	---	---	222220000	---	0.5464
					222120100	---	0.1039
					222211000	---	0.0853
1	0	3	970.1	29.5	222211000	---	0.4539
					122221000	---	0.2912
2	1	3	804.6	35.5	222121000	---	0.6017
					212221000	---	0.1400
3	2	3	758.2	37.7	212221000	---	0.5703
					222121000	---	0.1536
4	3	3	737.1	38.8	222210100	---	0.5396
					122220100	---	0.2880
5	1	1	729.4	39.2	222210100	0.0019683	0.5703
					122220100	---	0.2712
6	4	3	642.1	44.5	222120100	---	0.8142
					122112100	---	0.0417
7	2	1	624.3	45.8	222120100	0.0905865	0.6714
					212220100	---	0.0655
8	5	3	592.5	48.3	221221000	---	0.6680
					212122000	---	0.0822
9	6	3	571.6	50.0	212220100	---	0.7675
					112212100	---	0.0416
10	3	1	569.9	50.2	212220100	0.1206524	0.6956
					212202100	---	0.0386
11	4	1	444.4	64.3	221220100	0.0003508	0.7306
					212121100	---	0.0444
12	7	3	433.9	65.9	222210010	---	0.4812
					122220010	---	0.2506
13	5	1	432.7	66.1	222210010	0.0010716	0.4782
					122220010	---	0.2503
14	8	3	429.9	66.5	221220100	---	0.7217
					212121100	---	0.0699
15	6	1	410.4	69.7	222120010	0.0274877	0.3593
					222211000	---	0.1504
16	7	1	404.5	70.7	222120001	0.0141815	0.2505
					222211000	---	0.1880
17	9	3	400.6	71.4	222120010	---	0.7918
					122112010	---	0.0430
18	8	1	399.8	71.5	222120010	0.0076735	0.4769
					222120010	---	0.0742
19	9	1	396.4	72.1	222210001	0.0025346	0.3590
					122220001	---	0.1937
20	10	3	389.0	73.5	222210001	---	0.5095
					122220001	---	0.2709

Table C.2D-1. Compound **2** – CASSCF/QD-NEVPT2 composition of the singlet equilibrium ground state in the gas phase. 9o, 10e Active Space – 25 triplet roots, 15 singlet roots. Orbitals: bonding d(x^2-y^2)/C(sp^2), d(xy), d(xz), d(yz), d(z^2), d(x^2-y^2)/C(sp^2)*, π*(1), π*(2), π*(3).

CI Vector	**Transition**	**Contribution**
222220000	Closed shell singlet (CSS) d^8	0.5509
222120100	d(yz) → π*(1)	0.1282
122221000	bonding d(x^2-y^2)/C(sp^2) → d(x^2-y^2)/C(sp^2)*	0.0888
222210100	d(z^2) → π*(1)	0.0619
221220001	d(xz) → π*(3)	0.0363
222120010	d(yz) → π*(2)	0.0194
222211000	d(z^2) → d(x^2-y^2)/C(sp^2)*	0.0142
022122100	2x[bonding d(x^2-y^2)/C(sp^2)] + d(yz) → 2x[d(x^2-y^2)/C(sp^2)*] + π*(1)	0.0134
221220100	d(xz) → π*(1)	0.0075
222202000	2x[d(z^2)] → 2x[d(x^2-y^2)/C(sp^2)*]	0.0068
022212100	2x[bonding d(x^2-y^2)/C(sp^2)] + d(z^2) → 2x[d(x^2-y^2)/C(sp^2)*] + π*(1)	0.0067
220222000	2x[d(xz)] → 2x[d(x^2-y^2)/C(sp^2)*]	0.0058
122121100	bonding d(x^2-y^2)/C(sp^2) + d(yz) + → d(x^2-y^2)/C(sp^2)* + π*(1)	0.0057
222022000	2x[d(yz)] → 2x[d(x^2-y^2)/C(sp^2)*]	0.0057
222210010	d(z^2) → π*(2)	0.0054
021222001	2x[bonding d(x^2-y^2)/C(sp^2)] + d(xz) → 2x[d(x^2-y^2)/C(sp^2)*] + π*(3)	0.0031
122112100	bonding d(x^2-y^2)/C(sp^2) + d(xz) + d(yz) → 2x[d(x^2-y^2)/C(sp^2)*] + π*(1)	0.0026
Sum of CSS		55%
Sum of all MLCT		26%
Sum of all d-d		12%
Sum of mixed MLCT + d-d		3.1%

Table C.2D-2. Compound **2** – CASSCF/QD-NEVPT2 composition of the singlet equilibrium ground state with CPCM(THF). 9o, 10e Active Space – 25 triplet roots, 15 singlet roots. Orbitals: $d(z^2)$, d(xz), d(xy), d(yz), bonding $d(x^2-y^2)/C(sp^2)$, $d(x^2-y^2)/C(sp^2)^*$, $\pi^*(1)$, $\pi^*(2)$, $\pi^*(3)$.

CI Vector	Transition	Contribution
222220000	Closed shell singlet (CSS) d^8	0.5730
222120100	d(yz) → $\pi^*(1)$	0.1468
122221000	bonding $d(x^2-y^2)/C(sp^2)$ → $d(x^2-y^2)/C(sp^2)^*$	0.0958
221220001	d(xz) → $\pi^*(3)$	0.0359
222120010	d(yz) → $\pi^*(2)$	0.0206
222210100	$d(z^2)$ → $\pi^*(1)$	0.0178
222211000	$d(z^2)$ → $d(x^2-y^2)/C(sp^2)^*$	0.0160
022122100	2x[bonding $d(x^2-y^2)/C(sp^2)$] + d(yz) → 2x[$d(x^2-y^2)/C(sp^2)^*$] + $\pi^*(1)$	0.0155
221220100	d(xz) → $\pi^*(1)$	0.0119
222202000	2x[$d(z^2)$] → 2x[$d(x^2-y^2)/C(sp^2)^*$]	0.0079
122121100	bonding $d(x^2-y^2)/C(sp^2)$ + d(yz) + → $d(x^2-y^2)/C(sp^2)^*$ + $\pi^*(1)$	0.0066
220222000	2x[d(xz)] → 2x[$d(x^2-y^2)/C(sp^2)^*$]	0.0063
222022000	2x[d(yz)] → 2x[$d(x^2-y^2)/C(sp^2)^*$]	0.0059
021222001	2x[bonding $d(x^2-y^2)/C(sp^2)$] + d(xz) → 2x[$d(x^2-y^2)/C(sp^2)^*$] + $\pi^*(3)$	0.0030
122112100	bonding $d(x^2-y^2)/C(sp^2)$ + d(yz) + $d(z^2)$ → 2x[$d(x^2-y^2)/C(sp^2)^*$] + $\pi^*(1)$	0.0025
Sum of CSS		57%
Sum of all MLCT		23%
Sum of all d-d		13%
Sum of mixed MLCT + d-d		2.8%

Table C.2D-3. Compound **2** – CASSCF/QD-NEVPT2 composition of the singlet equilibrium ground state in gas phase. 9o, 10e Active Space – 25 triplet roots, 25 singlet roots. Orbitals: $d(z^2)$, d(xz), d(xy), d(yz), bonding $d(x^2-y^2)/C(sp^2)$, $d(x^2-y^2)/C(sp^2)^*$, $\pi^*(1)$, $\pi^*(2)$, $\pi^*(3)$.

CI Vector	Transition	Contribution
222220000	Closed shell singlet (CSS) d^8	0.5529
222211000	bonding $d(x^2-y^2)/C(sp^2)$ → $d(x^2-y^2)/C(sp^2)^*$	0.1358
222120100	d(yz) → $\pi^*(1)$	0.0884
122221000	$d(z^2)$ → $d(x^2-y^2)/C(sp^2)^*$	0.0547
212220100	d(xz) → $\pi^*(1)$	0.0274
222120010	d(yz) → $\pi^*(2)$	0.0265
212220001	d(xz) → $\pi^*(3)$	0.0246
122212000	$d(z^2)$ + bonding $d(x^2-y^2)/C(sp^2)$ → 2x[$d(x^2-y^2)/C(sp^2)^*$]	0.0122
202222000	2x[d(xz)] → 2x[$d(x^2-y^2)/C(sp^2)^*$]	0.0070
222022000	2x[d(yz)] → 2x[$d(x^2-y^2)/C(sp^2)^*$]	0.0069
222102100	d(yz) + 2x[bonding $d(x^2-y^2)/C(sp^2)$] → 2x[$d(x^2-y^2)/C(sp^2)^*$] + $\pi^*(1)$	0.0058
122220100	$d(z^2)$ → $\pi^*(1)$	0.0056
122112100	$d(z^2)$ + d(yz) + bonding $d(x^2-y^2)/C(sp^2)$ → 2x[$d(x^2-y^2)/C(sp^2)^*$] + $\pi^*(1)$	0.0052
222120001	d(yz) → $\pi^*(3)$	0.0051
222210100	bonding $d(x^2-y^2)/C(sp^2)$ → $\pi^*(1)$	0.0039
022222000	2x[$d(z^2)$] → 2x[$d(x^2-y^2)/C(sp^2)^*$]	0.0025
Sum of CSS		55%
Sum of all MLCT		18%

Sum of all d-d	21%
Sum of mixed MLCT + d-d	2.3%

Table C.2D-4. Compound **2** – CASSCF/QD-NEVPT2 composition of the singlet equilibrium ground state with CPCM(THF). 9o, 10e Active Space – 25 triplet roots, 25 singlet roots. Orbitals: d(z^2), d(xz), d(xy), d(yz), bonding d(x^2-y^2)/C(sp^2), d(x^2-y^2)/C(sp^2)*, π*(1), π*(2), π*(3).

CI Vector	Transition	Contribution
222220000	Closed shell singlet (CSS) d^8	0.5464
222120100	d(yz) → π*(1)	0.1039
122221000	d(z^2) → d(x^2-y^2)	0.0858
222211000	bonding d(x^2-y^2)/C(sp^2) → d(x^2-y^2)/C(sp^2)*	0.0853
212220100	d(xz) → π*(1)	0.0373
212220001	d(xz) → π*(3)	0.0290
222120010	d(yz) → π*(2)	0.0236
122212000	d(z^2) + bonding d(x^2-y^2)/C(sp^2) → 2x[d(x^2-y^2)/C(sp^2)*]	0.0122
202222000	2x[d(xz)] → 2x[d(x^2-y^2)/C(sp^2)*]	0.0069
222022000	2x[d(yz)] → 2x[d(x^2-y^2)/C(sp^2)*]	0.0066
122112100	d(z^2) + d(yz) + bonding d(x^2-y^2)/C(sp^2) → 2x[d(x^2-y^2)/C(sp^2)*] + π*(1)	0.0063
222120001	d(yz) → π*(3)	0.0056
022122100	d(z^2) + d(yz) → d(x^2-y^2) + π*(1)	0.0054
222210100	bonding d(x^2-y^2)/C(sp^2) → π*(1)	0.0053
222102100	d(yz) + bonding d(x^2-y^2)/C(sp^2) → d(x^2-y^2)/C(sp^2)* + π*(1)	0.0030
Sum of CSS		55%
Sum of all MLCT		20%
Sum of all d-d		20%
Sum of mixed MLCT + d-d		1.5%

Table C.2E-1. Compound **2** – CASSCF/QD-NEVPT2 lowest transition energies in the gas phase. 10o, 12e Active Space – 20 triplet roots, 10 singlet roots. Orbitals (in order for CI vector notation below): bonding d(xy)/C(π), bonding d(x^2-y^2)/C(sp^2), d(xz), d(xy), d(yz), d(z^2), d(x^2-y^2)/C(sp^2)*, π*(1), π*(2), π*(3).

State	**Root**	**Mult.**	**ΔE/nm**	**ΔE/kcal mol^{-1}**	**CI Vector**	f_{osc}	**Contribution**
0	0	1	---	---	2222220000	---	0.6318
					2222120100	---	0.1391
					2122221000	---	0.0531
1	0	3	1000.6	28.6	2222210100	---	0.8429
					2022212100	---	0.0675
2	1	1	960.9	29.8	2222210100	0.0021210	0.8218
					2022212100		0.0667
3	1	3	846.1	33.8	2222120100	---	0.7748
					2022122100	---	0.0698
4	2	1	775.8	36.9	2212220100	0.0192175	0.5127
					2222120100		0.2761
5	2	3	738.0	38.7	2212220100	---	0.7239
					2012222100	---	0.0538
6	3	3	714.1	40.0	2222211000	---	0.7712
					2122212000	---	0.0802
7	4	3	626.0	45.7	2212221000	---	0.5501
					2222121000	---	0.2572
8	3	1	619.0	46.2	2222120100	0.2167547	0.3590
					2212220100		0.2585
9	5	3	577.6	49.5	2222121000	---	0.5793
					2212221000	---	0.2374
10	4	1	560.2	51.0	2221220100	0.0023581	0.7622
					2212121100		0.0553
11	6	3	541.8	52.8	2221220100	---	0.7308
					2212121100	---	0.0550
12	7	3	524.8	54.5	2221221000	---	0.6806
					2221121100	---	0.0483
13	8	3	455.1	62.8	2222210010	---	0.4270
					2222210001	---	0.4167
14	5	1	433.8	65.9	2222210010	0.0146952	0.7914
					2022212010		0.0650
15	9	3	432.4	66.1	2222210001	---	0.4282
					2222210010	---	0.4100
16	10	3	405.7	70.5	2222120010	---	0.5858
					2212220010	---	0.1251
17	6	1	391.2	73.1	2221221000	0.0017318	0.6850
					2222211000		0.0873
18	7	1	373.8	76.5	2222211000	0.0037102	0.7321
					2221221000		0.0891
19	8	1	364.5	78.4	2222121000	0.0007688	0.4732
					2212221000		0.3645

20	11	3	357.3	80.0	2212220010	---	0.4398
					2222120001	---	0.1767

Table C.2E-2. Compound **2** – CASSCF/QD-NEVPT2 lowest transition energies in the gas phase. 10o, 12e Active Space – 25 triplet roots, 15 singlet roots. Orbitals (in order for CI vector notation below): bonding d(xy)/C(π), bonding d(x^2-y^2)/C(sp^2), d(xy), d(xz), d(yz), d(z^2), d(x^2-y^2)/C(sp^2)*, π*(1), π*(2), π*(3).

State	Root	Mult.	ΔE/nm	ΔE/kcal mol^{-1}	CI Vector	f_{osc}	Contribution
0	0	1	---	---	2222220000	---	0.5796
					2222120100	---	0.1775
					2122221000	---	0.0644
1	0	3	922.3	31.0	2222210100	---	0.8168
					2022212100	---	0.0659
2	1	1	890.7	32.1	2222210100	0.00179	0.7846
					2022212100	---	0.0631
3	1	3	809.4	35.3	2222211000	---	0.4160
					2222120100	---	0.3302
4	2	3	778.7	36.7	2222120100	---	0.4159
					2222211000	---	0.3457
5	2	1	720.5	39.7	2221220100	0.03340	0.5256
					2222120100	---	0.2310
6	3	3	686.7	41.6	2221221000	---	0.4526
					2222121000	---	0.3029
7	4	3	675.3	42.3	2221220100	---	0.7063
					2021222100	---	0.0498
8	5	3	638.2	44.8	2222121000	---	0.4856
					2221221000	---	0.3037
9	3	1	632.0	45.2	2222120100	0.17525	0.3036
					2221220100	---	0.2534
10	6	3	549.5	52.0	2212221000	---	0.6054
					2212121100	---	0.0685
11	4	1	517.8	55.2	2212220100	0.00051	0.7254
					2221121100	---	0.0611
12	7	3	509.9	56.1	2212220100	---	0.7244
					2221121100	---	0.0600
13	8	3	489.3	58.4	2222210010	---	0.7691
					2022212010	---	0.0670
14	5	1	487.5	58.6	2222210010	0.00192	0.7185
					2022212010	---	0.0627
15	6	1	458.8	62.3	2222120010	0.09519	0.4058
					2221220010	---	0.1885
16	9	3	452.2	63.2	2222120010	---	0.7398
					2022122010	---	0.0698
17	7	1	442.8	64.6	2222210001	0.01268	0.7254
					2022212001	---	0.0617
18	10	3	430.1	66.5	2222210001	---	0.7692
					2022212001	---	0.0651
19	8	1	430.0	66.5	2221220010	0.00571	0.5576
					2222120010	---	0.1065

20	11	3	409.9	69.7	2221220010	---	0.6892
					2221220001	---	0.0620

Table C.2E-3. Compound **2** – CASSCF/QD-NEVPT2 Lowest transition energies with CPCM(THF). 10o, 12e Active Space – 25 triplet roots, 15 singlet roots. Orbitals (in order for CI vector notation below): bonding d(xy)/C(π), bonding d(x^2-y^2)/C(sp^2), d(xy), d(xz), d(yz), d(z^2), d(x^2-y^2)/C(sp^2)*, π*(1), π*(2), π*(3).

State	**Root**	**Mult.**	**ΔE/nm**	**ΔE/kcal mol^{-1}**	**CI Vector**	f_{osc}	**Contribution**
0	0	1	---	---	2222220000	---	0.6012
					2222120100	---	0.1574
					2122221000	---	0.0715
1	0	3	907.8	31.5	2222210100	---	0.7864
					2022212100	---	0.0647
2	1	3	816.4	35.0	2222211000	---	0.7763
					2122212000	---	0.0980
3	1	1	805.7	35.5	2222210100	0.0015632	0.7932
					2022212100	---	0.0651
4	2	3	717.2	39.9	2222120100	---	0.7553
					2022122100	---	0.0679
5	2	1	666.5	42.9	2221220100	0.0318143	0.5075
					2222120100	---	0.2601
6	3	3	656.2	43.6	2222121000	---	0.3972
					2221221000	---	0.3808
7	4	3	652.4	43.8	2222121000	---	0.4020
					2221221000	---	0.3910
8	5	3	633.5	45.1	2221220100	---	0.7386
					2222120100	---	0.0451
9	3	1	584.7	48.9	2222120100	0.1984600	0.3109
					2221220100	---	0.2682
10	6	3	547.0	52.3	2212221000	---	0.6240
					2221122000	---	0.0672
11	4	1	487.9	58.6	2212220100	0.0005989	0.7323
					2221121100	---	0.0615
12	7	3	477.5	59.9	2212220100	---	0.7351
					2221121100	---	0.0610
13	8	3	460.5	62.1	2222210010	---	0.6676
					2222210001	---	0.1412
14	5	1	456.2	62.7	2222210010	0.0029045	0.7120
					2022212010	---	0.0633
15	6	1	443.5	64.5	2222120010	0.1027144	0.4285
					2221220010	---	0.1113
16	9	3	429.7	66.5	2222210001	---	0.6684
					2222210010	---	0.1350
17	10	3	424.1	67.4	2222120010	---	0.7429
					2122121010	---	0.0501
18	7	1	410.1	69.7	2222210001	0.0097454	0.6190
					2222211000	---	0.0582
19	8	1	398.6	71.7	2212221000	0.0169288	0.3458
					2222210001	---	0.1354
20	11	3	391.6	73.0	2221220010	---	0.7063
					2221220001	---	0.0557

Table C.2E-4. Compound **2** – CASSCF/QD-NEVPT2 lowest transition energies in the gas phase. 10o, 12e Active Space – 40 triplet roots, 25 singlet roots. Orbitals (in order for CI vector notation below): bonding d(xy)/C(π), bonding d(x^2-y^2)/C(sp^2), d(xz), d(yz), d(z^2), d(xy), d(x^2-y^2)/C(sp^2)*, π*(1), π*(2), π*(3).

State	Root	Mult.	ΔE/nm	ΔE/kcal mol^{-1}	CI Vector	f_{osc}	Contribution
0	0	1	---	---	2222220000	---	0.6252
					2221220100	---	0.0660
					2212220100	---	0.0637
1	0	3	846.7	33.8	2222121000	---	0.5072
					2122221000	---	0.1444
2	1	3	791.3	36.1	2222120100	---	0.5010
					2222210100	---	0.1672
3	1	1	770.4	37.1	2222120100	0.0024769	0.5080
					2222210100	---	0.1611
4	2	3	754.4	37.9	2221221000	---	0.7900
					2121222000	---	0.0728
5	3	3	706.9	40.4	2212221000	---	0.6698
					2122221000	---	0.0929
6	4	3	691.6	41.3	2221220100	---	0.7037
					2212220100	---	0.0610
7	2	1	660.5	43.3	2221220100	0.0915113	0.6732
					2222220000	---	0.0387
8	5	3	622.2	46.0	2212220100	---	0.6105
					2122220100	---	0.0586
9	3	1	598.3	47.8	2212220100	0.0987239	0.5993
					2122220100	---	0.0634
10	6	3	573.0	49.9	2222211000	---	0.4666
					2222121000	---	0.1321
11	4	1	476.0	60.1	2222210100	0.0009262	0.4903
					2222120100	---	0.2030
12	7	3	473.2	60.4	2222210100	---	0.5038
					2222120100	---	0.2033
13	8	3	456.7	62.6	2222120010	---	0.4563
					2222210010	---	0.1511
14	5	1	454.8	62.9	2222120010	0.0020837	0.4470
					2222210010	---	0.1435
15	6	1	428.3	66.8	2221220010	0.0399342	0.4974
					2221220001	---	0.2063
16	9	3	424.5	67.4	2221220010	---	0.6741
					2212220010	---	0.0759
17	7	1	407.4	70.2	2222120001	0.0152654	0.4264
					2122220001	---	0.1124
18	10	3	403.2	70.9	2222120001	---	0.4598
					2222210001	---	0.1477
19	8	1	399.7	71.5	2221220001	0.1277239	0.2755
					2212220001	---	0.1806

20	9	1	395.7	72.3	2221221000	0.0091248	0.3478
					2212220010	---	0.1772

Table C.2F-1. Compound **2** – CASSCF/QD-NEVPT2 composition of the singlet equilibrium ground state in the gas phase. 10o, 12e Active Space – 20 triplet roots, 10 singlet roots. Orbitals: bonding d(xy)/C(π), bonding d(x^2-y^2)/C(sp^2), d(xz), d(xy), d(yz), d(z^2), d(x^2-y^2)/C(sp^2)*, π*(1), π*(2), π*(3).

CI Vector	Transition	Contribution
2222220000	Closed shell singlet (CSS) d^8	0.6318
2222120100	d(yz) → π*(1)	0.1391
2122221000	bonding d(x^2-y^2)/C(sp^2) → d(x^2-y^2)/C(sp^2)*	0.0531
2212220100	d(xz) → π*(1)	0.0283
2222120001	d(yz) → π*(3)	0.0237
2022122100	2x[bonding d(x^2-y^2)/C(sp^2)] + d(yz)→ 2x[d(x^2-y^2)/C(sp^2)*] + π*(1)	0.0149
2122121100	bonding d(x^2-y^2)/C(sp^2) + d(yz) → d(x^2-y^2)/C(sp^2)* + π*(1)	0.0142
2212220010	d(xz) → π*(2)	0.0134
2222202000	2x[d(z^2)] → 2x[d(x^2-y^2)/C(sp^2)*]	0.0088
2222210100	d(z^2) → π*(1)	0.0088
2202222000	2x[d(xz)] → 2x[d(x^2-y^2)/C(sp^2)*]	0.0055
2222022000	2x[d(yz)] → 2x[d(x^2-y^2)/C(sp^2)*]	0.0050
2122121001	bonding d(x^2-y^2)/C(sp^2) + d(yz) + → d(x^2-y^2)/C(sp^2)* + π*(3)	0.0045
2022122001	2x[bonding d(x^2-y^2)/C(sp^2)] + d(yz)→ 2x[d(x^2-y^2)/C(sp^2)*] + π*(3)	0.0036
2222120010	d(yz) → π*(2)	0.0031
2222111100	d(yz) + d(z^2) → d(x^2-y^2)/C(sp^2)* + π*(1)	0.0029
2112221100	bonding d(x^2-y^2)/C(sp^2) + d(xz) → d(x^2-y^2)/C(sp^2)* + π*(1)	0.0028
2012222100	2x[bonding d(x^2-y^2)/C(sp^2)] + d(xz)→ 2x[d(x^2-y^2)/C(sp^2)*] + π*(1)	0.0027
Sum of CSS		**63%**
Sum of all MLCT		**22%**
Sum of all d-d		**7.2%**
Sum of mixed MLCT + d-d		**4.6%**

Table C.2F-2. Compound **2** – CASSCF/QD-NEVPT2 composition of the singlet equilibrium ground state in the gas phase. 10o, 12e Active Space – 25 triplet roots, 15 singlet roots. Orbitals: bonding d(xy)/C(π), bonding d(x^2-y^2)/C(sp^2), d(xy), d(xz), d(yz), d(z^2), d(x^2-y^2)/C(sp^2)*, π*(1), π*(2), π*(3).

CI Vector	Transition	Contribution
2222220000	Closed shell singlet (CSS) d^8	0.5796
2222120100	d(yz) → π*(1)	0.1775
2122221000	bonding d(x^2-y^2)/C(sp^2) → d(x^2-y^2)/C(sp^2)*	0.0644
2222120010	d(yz) → π*(2)	0.0235
2221220001	d(xz) → π*(3)	0.0218
2022122100	2x[bonding d(x^2-y^2)/C(sp^2)] + d(yz) → 2x[d(x^2-y^2)/C(sp^2)*] + π*(1)	0.0174
2222210100	d(z^2) → π*(1)	0.0143
2221220100	d(xz) → π*(1)	0.0121
2122121100	bonding d(x^2-y^2)/C(sp^2) + d(yz) → d(x^2-y^2)/C(sp^2)* + π*(1)	0.0121
2222202000	2x[d(z^2)] → 2x[d(x^2-y^2)/C(sp^2)*]	0.0083
2222211000	d(z^2) → d(x^2-y^2)/C(sp^2)*	0.0079
2220222000	2x[d(xz)] → 2x[d(x^2-y^2)/C(sp^2)*]	0.0056
2222022000	2x[d(yz)] → 2x[d(x^2-y^2)/C(sp^2)*]	0.0052
2222111100	d(yz) + d(z^2) → d(x^2-y^2)/C(sp^2)* + π*(1)	0.0031
2212221000	d(xy) → d(x^2-y^2)/C(sp^2)*	0.0029
2022122010	2x[bonding d(x^2-y^2)/C(sp^2)] + d(yz) → d(x^2-y^2)/C(sp^2)* + π*(2)	0.0025
Sum of CSS		**58%**
Sum of all MLCT		**25%**
Sum of all d-d		**9.4%**
Sum of mixed MLCT + d-d		**3.5%**

Table C.2F-3. Compound **2** – CASSCF/QD-NEVPT2 composition of the singlet equilibrium ground state with CPCM(THF). 10o, 12e Active Space – 25 triplet roots, 15 singlet roots. Orbitals: bonding d(xy)/C(π), bonding d(x^2-y^2)/C(sp^2), d(xy), d(xz), d(yz), d(z^2), d(x^2-y^2)/C(sp^2)*, π*(1), π*(2), π*(3).

CI Vector	Transition	Contribution
2222220000	Closed shell singlet (CSS) d^8	0.6012
2222120100	d(yz) → π*(1)	0.1574
2122221000	bonding d(x^2-y^2)/C(sp^2) → d(x^2-y^2)/C(sp^2)*	0.0715
2222120010	d(yz) → π*(2)	0.0222
2221220001	d(xz) → π*(3)	0.0195
2022122100	d(xz) → π*(1)	0.0165
2222210100	2x[bonding d(x^2-y^2)/C(sp^2)] + d(yz) → 2x[d(x^2-y^2)/C(sp^2)*] + π*(1)	0.0157
2221220100	bonding d(x^2-y^2)/C(sp^2) + d(yz) → d(x^2-y^2)/C(sp^2)* + π*(1)	0.0112
2122121100	d(z^2) → π*(1)	0.0099
2222202000	2x[d(z^2)] → 2x[d(x^2-y^2)/C(sp^2)*]	0.0090
2222211000	d(z^2) → d(x^2-y^2)/C(sp^2)*	0.0085
2220222000	2x[d(xz)] → 2x[d(x^2-y^2)/C(sp^2)*]	0.0062
2222022000	2x[d(yz)] → 2x[d(x^2-y^2)/C(sp^2)*]	0.0057
2222111100	d(yz) + d(z^2) → d(x^2-y^2)/C(sp^2)* + π*(1)	0.0028
Sum of CSS		**60%**
Sum of all MLCT		**23%**
Sum of all d-d		**10%**
Sum of mixed MLCT + d-d		**3.0%**

Table C.2F-4. Compound **2** – CASSCF/QD-NEVPT2 composition of the singlet equilibrium ground state in the gas phase. 10o, 12e Active Space – 40 triplet roots, 25 singlet roots. Orbitals: bonding d(xy)/C(π), bonding d(x^2-y^2)/C(sp^2), d(xz), d(yz), d(z^2), d(xy), d(x^2-y^2)/C(sp^2)*, π*(1), π*(2), π*(3).

CI Vector	Transition	Contribution
2222220000	Closed shell singlet (CSS) d^8	0.6252
2221220100	d(yz) → π*(1)	0.0660
2212220100	d(xz) → π*(1)	0.0637
2122221000	bonding d(x^2-y^2)/C(sp^2) → d(x^2-y^2)/C(sp^2)*	0.0441
2212220001	d(xz) → π*(3)	0.0200
2221220010	d(yz) → π*(2)	0.0188
2222121000	d(z^2) → d(x^2-y^2)/C(sp^2)*	0.0150
2221220001	d(yz) → π*(3)	0.0127
2222211000	d(xy) → d(x^2-y^2)/C(sp^2)*	0.0104
2122220100	bonding d(x^2-y^2)/C(sp^2)* → π*(1)	0.0098
2212220010	d(xz) → π*(2)	0.0077
2220222000	2x[d(yz)] → 2x[d(x^2-y^2)/C(sp^2)*]	0.0061
2221121100	d(yz) + d(z^2) → d(x^2-y^2)/C(sp^2)* + π*(1)	0.0055
2202222000	2x[d(xz)] → 2x[d(x^2-y^2)/C(sp^2)*]	0.0055
2222022000	2x[d(z^2)] → 2x[d(x^2-y^2)/C(sp^2)*]	0.0047
2122220001	bonding d(x^2-y^2)/C(sp^2) → π*(3)	0.0046
2021222100	2x[bonding d(x^2-y^2)/C(sp^2)] + d(yz) → 2x[d(x^2-y^2)/C(sp^2)*] + π*(1)	0.0045
2212221000	d(xz) → d(x^2-y^2)/C(sp^2)*	0.0041
2012222100	2x[bonding d(x^2-y^2)/C(sp^2)] + d(xz) → 2x[d(x^2-y^2)/C(sp^2)*] + π*(1)	0.0036
2121221100	bonding d(x^2-y^2)/C(sp^2) + d(yz) → d(x^2-y^2)/C(sp^2)* + π*(1)	0.0034
2222120100	d(z^2) → π*(1)	0.0032
2112221100	bonding d(x^2-y^2)/C(sp^2) + d(xz) → d(x^2-y^2)/C(sp^2)* + π*(1)	0.0030
2222210100	d(xy) → π*(1)	0.0026
1222221000	bonding d(xy)/C(π) → d(x^2-y^2)/C(sp^2)*	0.0026
Sum of CSS		**63%**
Sum of all MLCT		**21%**
Sum of all d-d		**9.3%**
Sum of mixed MLCT + d-d		**2.0%**

Table C.2G. Compound **2** –CASSCF/QD-NEVPT2 composition of the singlet equilibrium ground state while varying number roots. 9o, 10e Active Space – 25 triplet roots, *X* singlet roots (where *X* ranged from 15 to 25). Orbitals: bonding d(x^2-y^2)/C(sp^2), d(xy), d(xz), d(yz), d(z^2), d(x^2-y^2)/C(sp^2)*, π*(1), π*(2), π*(3). 10o, 12e Active Space – *X* triplet roots, *Y* singlet roots where *X* ranged from 20 to 40, and *Y* ranged from 10 to 25. Orbitals: bonding d(xy)/C(π), bonding d(x^2-y^2)/C(sp^2), d(xy), d(xz), d(yz), d(z^2), d(x^2-y^2)/C(sp^2)*, π*(1), π*(2), π*(3).

Weights of Three Most Dominant Terms in CI-Vector (# Triplets / # Singlets)

Active Spaces:	**9 orbitals, 10 electrons**				**10 orbitals, 12 electrons**			
Configuration	**25/15 Gas**	**25/15 CPCM**	**25/25 Gas**	**25/25 CPCM**	**20/10 Gas**	**25/15 Gas**	**25/15 CPCM**	**40/25 Gas**
CSS	0.5509	0.5730	0.5529	0.5464	0.6318	0.5796	0.6012	0.6252
d(yz) → π*(1)	0.1282	0.1468	0.0884	0.1039	0.1391	0.1775	0.1574	0.0660[†]
d(x^2-y^2)/C(sp^2) → d(x^2-y^2)/C(sp^2)*	0.0888	0.0958	0.1358	0.0853[‡]	0.0531	0.0644	0.0715	0.0441

Sums of Weights

Active Spaces:	**9 orbitals, 10 electrons**				**10 orbitals, 12 electrons**			
Configuration	**25/15 Gas**	**25/15 CPCM**	**25/25 Gas**	**25/25 CPCM**	**20/10 Gas**	**25/15 Gas**	**25/15 CPCM**	**40/25 Gas**
CSS	55%	57%	55%	55%	63%	58%	60%	63%
Sum of MLCT	26%	23%	18%	20%	22%	25%	23%	21%
Sum of d-d	12%	13%	21%	20%	7.2%	9.4%	10%	9.3%
Sum of MLCT+d-d	3.1%	2.8%	2.3%	1.5%	4.6%	3.5%	3.0%	2.0%

Singlet → Singlet Transition Energies (kcal mol^{-1})

Active Spaces:	**9 orbitals, 10 electrons**				**10 orbitals, 12 electrons**			
Transition	**25/15 Gas**	**25/15 CPCM**	**25/25 Gas**	**25/25 CPCM**	**20/10 Gas**	**25/15 Gas**	**25/15 CPCM**	**40/25 Gas**
$S_0 \rightarrow S_1$	33.3	37.2	39.1	39.2	29.8	32.1	35.5	37.1
$S_0 \rightarrow S_2$	40.6	44.3	45.1	45.8	36.9	39.7	42.9	43.3
$S_0 \rightarrow S_3$	45.5	49.5	50.6	50.2	46.2	45.2	48.9	47.8
$S_0 \rightarrow S_4$	58.1	62.0	63.8	64.3	51.0	55.2	58.6	60.1
$S_0 \rightarrow S_5$	59.3	63.7	65.5	66.1	65.9	58.6	62.7	62.9
$S_0 \rightarrow S_6$	63.7	65.0	67.8	69.7	73.1	62.3	64.5	66.8
$S_0 \rightarrow S_7$	66.3	69.1	71.7	70.7	76.5	64.6	69.7	70.2
$S_0 \rightarrow S_8$	68.2	72.0	71.9	71.5	78.4	66.5	71.7	71.5
$S_0 \rightarrow S_9$	69.2	72.8	73.4	72.1	81.4	71.4	73.7	72.3
$S_0 \rightarrow S_{10}$	73.0	74.1	73.5	74.3	---	75.5	74.7	72.7
$S_0 \rightarrow S_{11}$	74.6	75.3	75.2	74.8	---	76.9	76.5	74.2
$S_0 \rightarrow S_{12}$	75.9	77.7	77.2	75.7	---	78.7	78.7	76.9

$S_0 \rightarrow S_{13}$	79.0	80.4	79.8	77.5	---	80.2	81.2	77.2
$S_0 \rightarrow S_{14}$	82.6	86.3	84.2	87.1	---	112.7	116.2	84.2

[†] d(xz) → π*(1) is 0.0637. [‡] d(z^2) → d(x^2-y^2) is slightly higher at 0.0858.

Table C.2H-1. Compound **2** with Ni–C distance of 3.14 Å – CASSCF/QD-NEVPT2 lowest transition energies in the gas phase. 8o, 10e Active Space – 25 triplet roots, 15 singlet roots. Orbitals (in order for CI vector notation below): d(xz), d(yz), d(xy), d(z^2), d(x^2-y^2), C(sp^2)*, π*(1), π*(2). †The lowest singlet and triplet roots are essentially isoenergetic.

State	Root	Mult.	ΔE/nm	ΔE/kcal mol^{-1}	CI Vector	f_{osc}	Contribution
0	0	3†	---	---	12221110	---	0.4414
					22211110	---	0.0777
					21221110	---	0.0769
1	0	1†	1.35E+05	0.2	12221110	---	0.4544
					22220110	---	0.1621
2	1	3	11691.9	2.4	22211110	0.0000185	0.5698
					22211200	---	0.1445
3	1	1	6953.1	4.1	22211110	---	0.7473
					21221110	---	0.0745
4	2	3	6042.1	4.7	22211110	0.0000044	0.5075
					21221110	---	0.1900
5	3	3	5510.1	5.2	22211110	0.0000638	0.3270
					21221110	---	0.3178
6	2	1	4415.9	6.5	22220110	---	0.4317
					12221110	---	0.2298
7	4	3	3990.5	7.2	12221110	0.0000214	0.4491
					22220110	---	0.1777
8	5	3	3896.3	7.3	21221110	0.0000363	0.6461
					22220110	---	0.1142
9	3	1	3858.7	7.4	21221110	---	0.7457
					12221110	---	0.0583
10	6	3	3537.3	8.1	22220110	0.0000600	0.4848
					12221110	---	0.2458
11	7	3	1142.4	25.0	22121110	0.0000216	0.4116
					22121200	---	0.1173
12	4	1	1063.8	26.9	22121110	---	0.5493
					11222110	---	0.2679
13	8	3	1042.4	27.4	22121110	0.0000031	0.5686
					11222110	---	0.2627
14	9	3	966.1	29.6	21221101	0.0536947	0.4585
					12221101	---	0.1746
15	5	1	953.6	30.0	22211101	---	0.4312
					21221101	---	0.2753
16	10	3	947.7	30.2	22211101	0.0008840	0.7957
					22211011	---	0.0538
17	6	1	916.4	31.2	22211101	---	0.3968
					21221101	---	0.2779
18	11	3	887.2	32.2	22211101	0.0003050	0.7210
					21221101	---	0.1448
19	12	3	847.2	33.7	21221101	0.0000199	0.8183
					21221011	---	0.0548
20	13	3	825.5	34.6	12221101	0.0035754	0.7783

					22121101	---	0.0461

Table C.2H-2. Compound **2** with Ni–C distance of 3.14 Å – CASSCF/QD-NEVPT2 lowest transition energies with CPCM(THF). 8o,10e Active Space – 25 triplet roots, 15 singlet roots. Orbitals (in order for CI vector notation below): d(xy), d(xz), d(z^2), d(yz), d(x^2-y^2), C(sp^2)*, π*(1), π*(2). †The lowest singlet and triplet roots are essentially isoenergetic.

State	Root	Multiplicity	ΔE/nm	ΔE/kcal mol^{-1}	CI Vector	f_{osc}	Contribution
0	0	3†	---	---	21221110	---	0.4372
					22121110	---	0.1725
					22211110	---	0.0831
1	0	1†	5.9E+04	0.5	21221110	---	0.4877
					22220110	---	0.1626
2	1	3	13662.2	2.1	22121110	0.0000327	0.5328
					22211110	---	0.1036
3	1	1	7957.3	3.6	22121110	---	0.8617
					21221110	---	0.0331
4	2	3	6570.1	4.4	22121110	0.0000085	0.6242
					22211110	---	0.1966
5	3	3	5735.6	5.0	22211110	0.0000302	0.3595
					22121110	---	0.2485
6	2	1	4184.7	6.8	22220110	---	0.5189
					21221110	---	0.1758
7	4	3	4034.3	7.1	21221110	0.0000046	0.6509
					22220110	---	0.0728
8	5	3	3982.8	7.2	22211110	0.0000565	0.7504
					21221110	---	0.0852
9	3	1	3963.4	7.2	22211110	---	0.7430
					21221110	---	0.1371
10	6	3	3416.6	8.4	22220110	0.0000134	0.7020
					21221110	---	0.1408
11	7	3	1144.3	25.0	12221110	0.0000176	0.5107
					21212110	---	0.2185
12	4	1	1068.5	26.8	12221110	---	0.6071
					21212110	---	0.2776
13	8	3	1043.9	27.4	12221110	0.0000045	0.6244
					21212110	---	0.2658
14	5	1	1007.8	28.4	22121101	---	0.7969
					21221101	---	0.0324
15	9	3	989.2	28.9	22121101	0.0042687	0.6679
					22211101	---	0.1223
16	10	3	975.5	29.3	22121101	0.0457152	0.4067
					22211101	---	0.3207
17	6	1	953.3	30.0	22211101	---	0.6362
					21221101	---	0.1400
18	11	3	925.9	30.9	22121101	0.0001487	0.6010
					22211101	---	0.3172
19	12	3	883.5	32.4	22211101	0.0000838	0.8077

					21122101	---	0.0425
20	7	1	862.1	33.2	21221101	---	0.6712
					22211101		0.1758

Table C.2I-1. Compound **2** – CASSCF/QD-NEVPT2 composition with Ni–C distance of 3.14 Å – CASSCF/QD-NEVPT2 composition of the lowest singlet root in the gas phase. 8o, 10e Active Space – 25 triplet roots, 15 singlet roots. Orbitals (in order for CI vector notation below): d(xz), d(yz), d(xy), d(z^2), d(x^2-y^2), C(sp^2)*, π*(1), π*(2).

CI Vector	Transition	Contribution
12221110	d(xz) + d(x^2-y^2) → C(sp^2)* + π*(1)	0.4544
22220110	2x[d(x^2-y^2)] → C(sp^2)* + π*(1)	0.1621
22211110	d(z^2) + d(x^2-y^2) → C(sp^2)* + π*(1)	0.0698
22220200	2x[d(x^2-y^2)] → 2x[C(sp^2)*]	0.0422
21221110	d(yz) + d(x^2-y^2) → C(sp^2)* + π*(1)	0.0279
22220020	2x[d(x^2-y^2)] → 2x[π*(1)]	0.0270
12222010	d(xz) → π*(1)	0.0157
21122110	d(yz) + d(xy) → C(sp^2)* + π*(1)	0.0151
21221101	d(yz) + d(x^2-y^2) → C(sp^2)* + π*(2)	0.0149
21212110	d(yz) + d(z^2) → C(sp^2)* + π*(1)	0.0144
22121110	d(xy) + d(x^2-y^2) → C(sp^2)* + π*(2)	0.0105
12220210	d(xz) + 2x[d(x^2-y^2)] → 2x[C(sp^2)*] + π*(1)	0.0092
12222100	d(xz) → C(sp^2)*	0.0067
12221101	d(xz) + d(x^2-y^2) → C(sp^2)* + π*(2)	0.0065
22202110	2x[d(z^2)] → C(sp^2)* + π*(1)	0.0056
20222110	2x[d(yz)] → C(sp^2)* + π*(1)	0.0039
02222110	2x[d(xz)] → C(sp^2)* + π*(1)	0.0038

Table C.2I-2. Compound **2** – CASSCF/QD-NEVPT2 composition with Ni–C distance of 3.14 Å – CASSCF/QD-NEVPT2 composition of the lowest singlet root with CPCM(THF). 8o, 10e Active Space – 25 triplet roots, 15 singlet roots. Orbitals (in order for CI vector notation below): d(xy), d(xz), d(z^2), d(yz), d(x^2-y^2), C(sp^2)*, π*(1), π*(2).

CI Vector	Transition	Contribution
21221110	d(yz) + d(x^2-y^2) → C(sp^2)* + π*(1)	0.4877
22220110	2x[d(x^2-y^2)] → C(sp^2)* + π*(1)	0.1626
22211110	d(z^2) + d(x^2-y^2) → C(sp^2)* + π*(1)	0.0842
22221100	d(x^2-y^2) → C(sp^2)*	0.0671
22121110	d(xy) + d(x^2-y^2) → C(sp^2)* + π*(1)	0.0307
22220200	2x[d(x^2-y^2)] → 2x[C(sp^2)*]	0.0273
22112110	d(xy) + d(z^2) → C(sp^2)* + π*(1)	0.0189
22220020	2x[d(x^2-y^2)] → 2x[π*(1)]	0.0149
12212110	d(xz) + d(z^2) → C(sp^2)* + π*(1)	0.0136
21222010	d(yz) → π*(1)	0.0123
22211101	d(z^2) + d(x^2-y^2) → C(sp^2)* + π*(2)	0.0102
12221110	d(xz) + d(x^2-y^2) → C(sp^2)* + π*(1)	0.0087
21220210	d(yz) + 2x[d(x^2-y^2)] → 2x[C(sp^2)*] + π*(1)	0.0071
22022110	2x[d(xy)] → C(sp^2)* + π*(1)	0.0064
21222100	d(xz) → C(sp^2)*	0.0060
22121101	d(xy) + d(x^2-y^2) → C(sp^2)* + π*(2)	0.0053
20222110	2x[d(yz)] → C(sp^2)* + π*(1)	0.0044
22202110	2x[d(z^2)] → C(sp^2)* + π*(1)	0.0038

21221101	d(yz) + $d(x^2-y^2)$ → $C(sp^2)^*$ + π*(2)	0.0028

Table C.2J. Compound **2** – CASSCF/QD-NEVPT2 composition of the formal Ni(I) ground state while varying number of doublet roots. 8o, 9e Active Space – 25 quartet roots, *X* doublet roots (where *X* ranged from 15 to 45).

CI-Vector Weights (# Quartets / # Doublets)					
Transition	**25/15 CPCM**	**25/15 Gas**	**25/25 Gas**	**25/35 Gas**	**25/45 Gas**
d(xz) → π*(1)	0.6210	0.6788	0.6610	0.6567	0.6650
$d(x^2-y^2)$ → π*(1)	0.0887	0.0995	0.1219	0.1153	0.1245
formal Ni(I)	0.0671	0.0691	0.0680	0.0707	0.0693
Doublet→Doublet Transition Energies (kcal mol^{-1})					
Transition	**25/15 CPCM**	**25/15 Gas**	**25/25 Gas**	**25/35 Gas**	**25/45 Gas**
1	5.1	6.1	6.3	6.6	6.6
2	7.4	7.7	7.8	8.0	8.0
3	9.6	9.3	8.6	8.9	8.6
4	26.8	27.0	25.8	26.2	26.3
5	28.8	29.1	29.2	29.4	29.5
6	32.4	33.3	33.7	34.0	34.1
7	35.2	35.6	35.4	35.9	35.6
8	37.0	37.9	35.8	36.2	36.3
9	38.6	39.0	38.2	38.5	38.6
10	41.2	41.3	39.3	39.6	39.6
11	49.7	50.6	39.4	39.8	39.7
12	50.8	51.7	41.6	42.0	42.1
13	55.1	56.1	49.7	49.9	49.9
14	57.3	58.7	50.8	51.1	50.9

Table C.2K. Leadings terms of CI-vector for the T_0 (first triplet manifold reached from vertical excitation of singlet ground state) of **2** in Figure C.2J. Just past the equilibrium geometry, the CI-vector is dominated by ^{3}d-d transitions. Note that using the relaxed, DFT optimized C_{4v} triplet geometries of **2** (surfaces shown in Figure C.2G) the ground state triplet CI-vector is very heavily dominated by the $[d(x^2\text{-}y^2)]^1[d(z^2)/C(sp^2)^*]^1$ ^{3}d-d transition (64% at the 1.95 Å equilibrium geometry, Figure C.2I bottom). At long Ni–C distances, the transition d(xz) → π*(1) becomes dominant, making for a $[d(xz)]^1[d(x^2\text{-}y^2)]^1[(dz^2)/C(sp^2)^*]^1[\pi^*(1)]^1$ configuration.

Ni–C Distance (Å)	**Weight**	**Transition**
1.89 (equil.)	0.8168	d(z^2) → π*(1)
	0.0659	2x[bonding d(x^2-y^2)/C(sp^2)] + d(z^2) → 2x[d(x^2-y^2)/C(sp^2)*] + π*(1)
2.02	0.4339	d(z^2) → d(x^2-y^2)/C(sp^2)*
	0.2551	bonding d(x^2-y^2)/C(sp^2) → d(x^2-y^2)/C(sp^2)*
2.21	0.3666	bonding d(x^2-y^2)/C(sp^2) → d(x^2-y^2)/C(sp^2)*
	0.2786	d(z^2) → d(x^2-y^2)/C(sp^2)*
2.40	0.5334	d(z^2) → d(x^2-y^2)/C(sp^2)*
	0.3130	d(z^2) + bonding d(x^2-y^2)/C(sp^2) → 2x[d(x^2-y^2)/C(sp^2)*]
2.60	0.4218	d(z^2) →π*(1)
	0.3788	d(z^2) + bonding d(x^2-y^2)/C(sp^2) → d(x^2-y^2)/C(sp^2)* + π*(1)
2.91	0.6157	d(z^2) + bonding d(x^2-y^2)/C(sp^2) → d(x^2-y^2)/C(sp^2)* + π*(1)
	0.2267	d(z^2) →π*(1)
3.14	0.4414	d(xz) + bonding d(x^2-y^2)/C(sp^2) → d(x^2-y^2)/C(sp^2)* + π*(1)
	0.0777	d(z^2) + bonding d(x^2-y^2)/C(sp^2) → d(x^2-y^2)/C(sp^2)* + π*(1)
3.31	0.5253	d(xz) + bonding d(x^2-y^2)/C(sp^2) → d(x^2-y^2)/C(sp^2)* + π*(1)
	0.1070	2x[bonding d(x^2-y^2)/C(sp^2)] → d(x^2-y^2)/C(sp^2)* + π*(1)
3.49	0.6173	d(xz) + bonding d(x^2-y^2)/C(sp^2) → d(x^2-y^2)/C(sp^2)* + π*(1)
	0.1150	2x[bonding d(x^2-y^2)/C(sp^2)] → d(x^2-y^2)/C(sp^2)* + π*(1)
3.71	0.2595	d(yz) + bonding d(x^2-y^2)/C(sp^2) → d(x^2-y^2)/C(sp^2)* + π*(1)
	0.1641	2x[bonding d(x^2-y^2)/C(sp^2)] → d(x^2-y^2)/C(sp^2)* + π*(1)
3.94	0.2298	d(yz) + bonding d(x^2-y^2)/C(sp^2) → d(x^2-y^2)/C(sp^2)* + π*(1)
	0.2117	d(xz) + bonding d(x^2-y^2)/C(sp^2) → d(x^2-y^2)/C(sp^2)* + π*(1)

Table C.2L. Spin Contamination Values From BSS Calculation and Yamaguchi Correction[1,2] BSS Energy of **2**. Using $<S^2>$ values and energies for the triplet and BSS solutions for the same geometry, $\alpha = <S^2>_{trip.}/(<S^2>_{trip.} - <S^2>_{BSS})$, $\beta = <S^2>_{BSS}/(<S^2>_{trip.} - <S^2>_{BSS})$, and $E_{Yamaguchi} = \alpha E_{BSS} - \beta E_{trip}$.

Ni–C Dist. (Å)	$<S^2>$ S=1	$<S^2>$ BSS	α	β	Energy S=1/ kcal mol^{-1}	Energy BSS/ kcal mol^{-1}	Energy Yamaguchi/ kcal mol^{-1}
1.89	2.01	0.00	1.00	0.00	37.5	0.0	0.0
2.02	2.01	0.00	1.00	0.00	34.6	1.5	1.5
2.21	2.01	0.00	1.00	0.00	36.7	8.8	8.8
2.40	2.01	0.00	1.00	0.00	41.7	18.3	18.3
2.60	2.01	0.03	1.02	0.02	47.0	27.6	27.2
2.91	2.04	0.50	1.33	0.33	51.7	39.6	35.6
3.14	2.04	0.94	1.86	0.86	42.9	44.5	45.9
3.31	2.04	0.98	1.93	0.93	44.3	45.4	46.4
3.49	2.03	1.00	1.98	0.98	44.8	45.5	46.2
3.71	2.03	1.02	2.00	1.00	44.8	45.3	45.7
3.94	2.03	1.02	2.02	1.02	44.6	44.9	45.1

Table C.2M. Compound **2** (S=0) – Decomposition of Leading Configuration in the Singlet Ground State into Specific Spin Arrangements – Ni–C distance of 3.5 Å and 3.3 Å – CASSCF/QD-NEVPT2 in gas phase. 8o, 10e Active Space – 25 triplet roots, 15 singlet roots.

3.5 Å Spin Det.	Spin Arrangement in Singly Occupied Orbitals	Coefficient	Weight
d222duu0	$(d(xz))^{down}(d(x^2\text{-}y^2))^{down}(Csp^2)^{*up}(\pi^*(1))^{up}$	-0.449	0.202
d222udu0	$(d(xz))^{down}(d(x^2\text{-}y^2))^{up}(Csp^2)^{*down}(\pi^*(1))^{up}$	0.253	0.064
u222ddu0	$(d(xz))^{up}(d(x^2\text{-}y^2))^{down}(Csp^2)^{*down}(\pi^*(1))^{up}$	0.197	0.039
d222uud0	$(d(xz))^{down}(d(x^2\text{-}y^2))^{up}(Csp^2)^{*up}(\pi^*(1))^{down}$	0.197	0.039
u222dud0	$(d(xz))^{up}(d(x^2\text{-}y^2))^{down}(Csp^2)^{*up}(\pi^*(1))^{down}$	0.253	0.064
u222udd0	$(d(xz))^{up}(d(x^2\text{-}y^2))^{up}(Csp^2)^{*down}(\pi^*(1))^{down}$	-0.449	0.202
		Total Weight:	0.608

3.3 Å Spin Det.	Spin Arrangement in Singly Occupied Orbitals	Coefficient	Weight
d222duu0	$(d(xz))^{down}(d(x^2\text{-}y^2))^{down}(Csp^2)^{*up}(\pi^*(1))^{up}$	-0.415	0.172
d222udu0	$(d(xz))^{down}(d(x^2\text{-}y^2))^{up}(Csp^2)^{*down}(\pi^*(1))^{up}$	0.229	0.052
u222ddu0	$(d(xz))^{up}(d(x^2\text{-}y^2))^{down}(Csp^2)^{*down}(\pi^*(1))^{up}$	0.186	0.035
d222uud0	$(d(xz))^{down}(d(x^2\text{-}y^2))^{up}(Csp^2)^{*up}(\pi^*(1))^{down}$	0.186	0.035
u222dud0	$(d(xz))^{up}(d(x^2\text{-}y^2))^{down}(Csp^2)^{*up}(\pi^*(1))^{down}$	0.229	0.052
u222udd0	$(d(xz))^{up}(d(x^2\text{-}y^2))^{up}(Csp^2)^{*down}(\pi^*(1))^{down}$	-0.415	0.172
		Total Weight:	0.518

Table C.2N. Compound **2** (S=1) – Decomposition of Leading Configuration in the Triplet Ground State into Specific Spin Arrangements – Ni–C distance of 3.6 Å and 3.3 Å – CASSCF/QD-NEVPT2 in gas phase. 9o, 10e Active Space – 25 triplet roots, 15 singlet roots.

3.6 Å Spin Det.	**Spin Arrangement in Singly Occupied Orbitals**	**Coefficient**	**Weight**
2d22uuu00	$(d(xz))^{down}(d(x^{2}-y^{2}))^{up}(Csp^{2})*^{up}(\pi*(1))^{up}$	-0.353	0.125
2u22duu00	$(d(xz))^{up}(d(x^{2}-y^{2}))^{down}(Csp^{2})*^{up}(\pi*(1))^{up}$	-0.245	0.060
2u22udu00	$(d(xz))^{up}(d(x^{2}-y^{2}))^{up}(Csp^{2})*^{down}(\pi*(1))^{up}$	-0.015	0.000
2u22uud00	$(d(xz))^{up}(d(x^{2}-y^{2}))^{up}(Csp^{2})*^{up}(\pi*(1))^{down}$	0.613	0.376
		Total Weight:	0.561

3.3 Å Spin Det.	**Spin Arrangement in Singly Occupied Orbitals**	**Coefficient**	**Weight**
2d22uuu00	$(d(xz))^{down}(d(x^{2}-y^{2}))^{up}(Csp^{2})*^{up}(\pi*(1))^{up}$	0.327	0.107
2u22duu00	$(d(xz))^{up}(d(x^{2}-y^{2}))^{down}(Csp^{2})*^{up}(\pi*(1))^{up}$	0.228	0.052
2u22udu00	$(d(xz))^{up}(d(x^{2}-y^{2}))^{up}(Csp^{2})*^{down}(\pi*(1))^{up}$	0.030	0.001
2u22uud00	$(d(xz))^{up}(d(x^{2}-y^{2}))^{up}(Csp^{2})*^{up}(\pi*(1))^{down}$	-0.585	0.343
		Total Weight:	0.502

C.E. Figures Part 2: Compound *2*

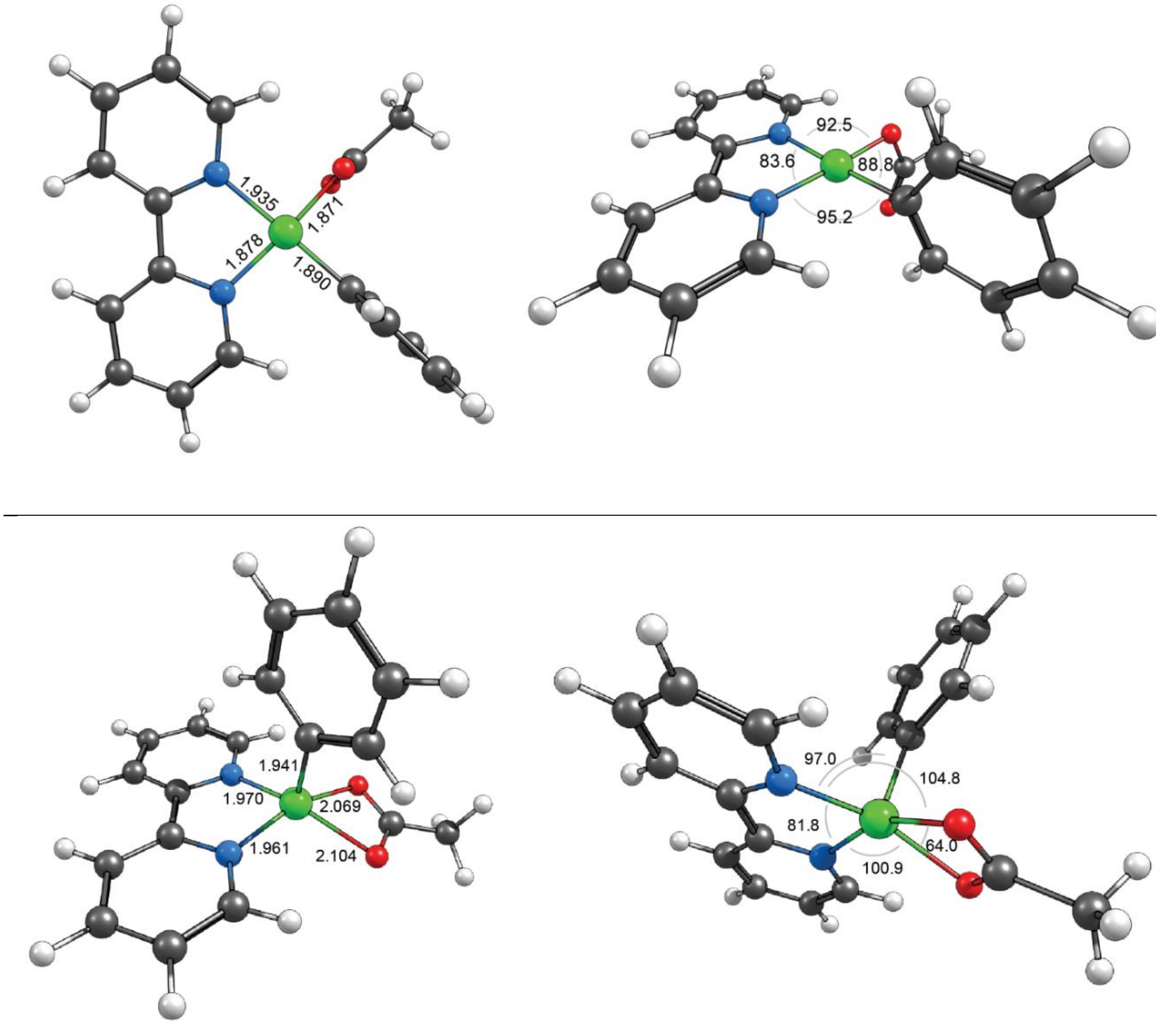

Figure C.2A. Top: square planar equilibrium geometry of compound **2** (S=0), and bottom: square pyramidal equilibrium geometry of **2** (S=1) as calculated by DFT. Selected bond lengths and angles are shown.

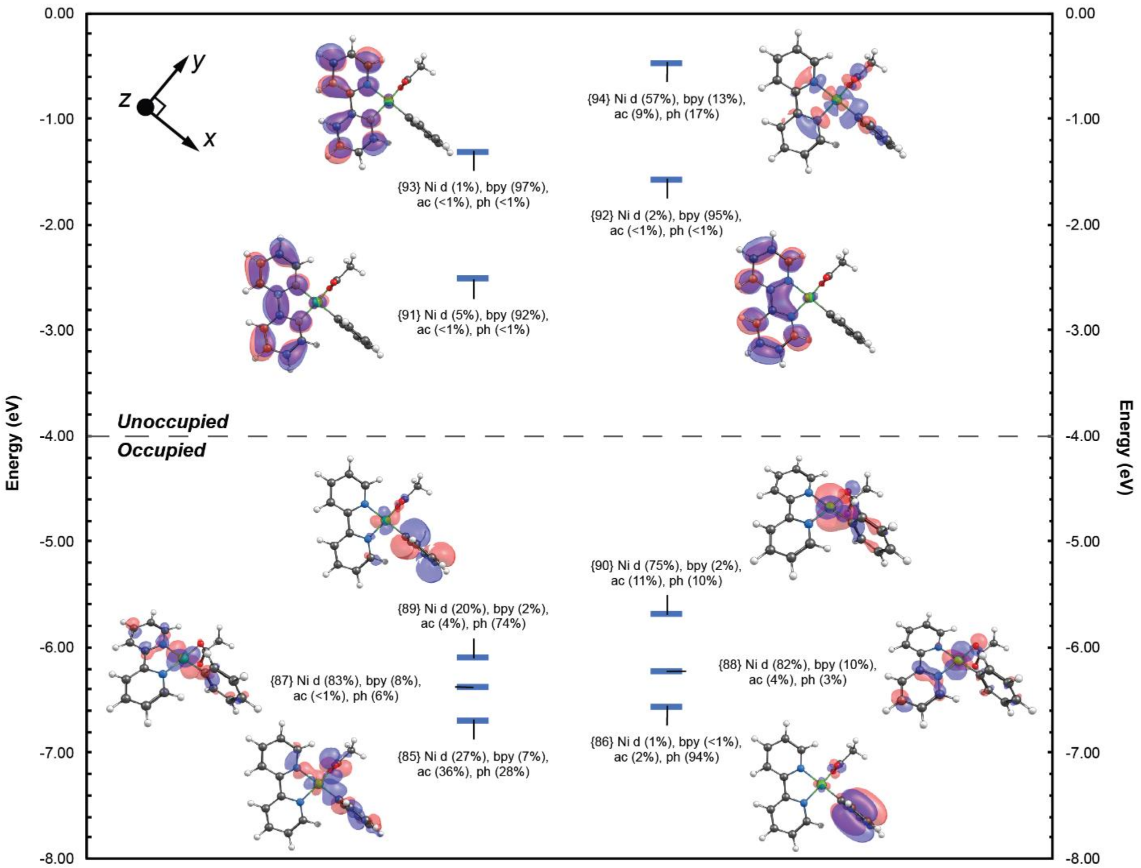

Figure C.2B. Compound **2** (S=0)– Single point DFT Frontier molecular orbital diagram. Orbitals are offset for clarity.

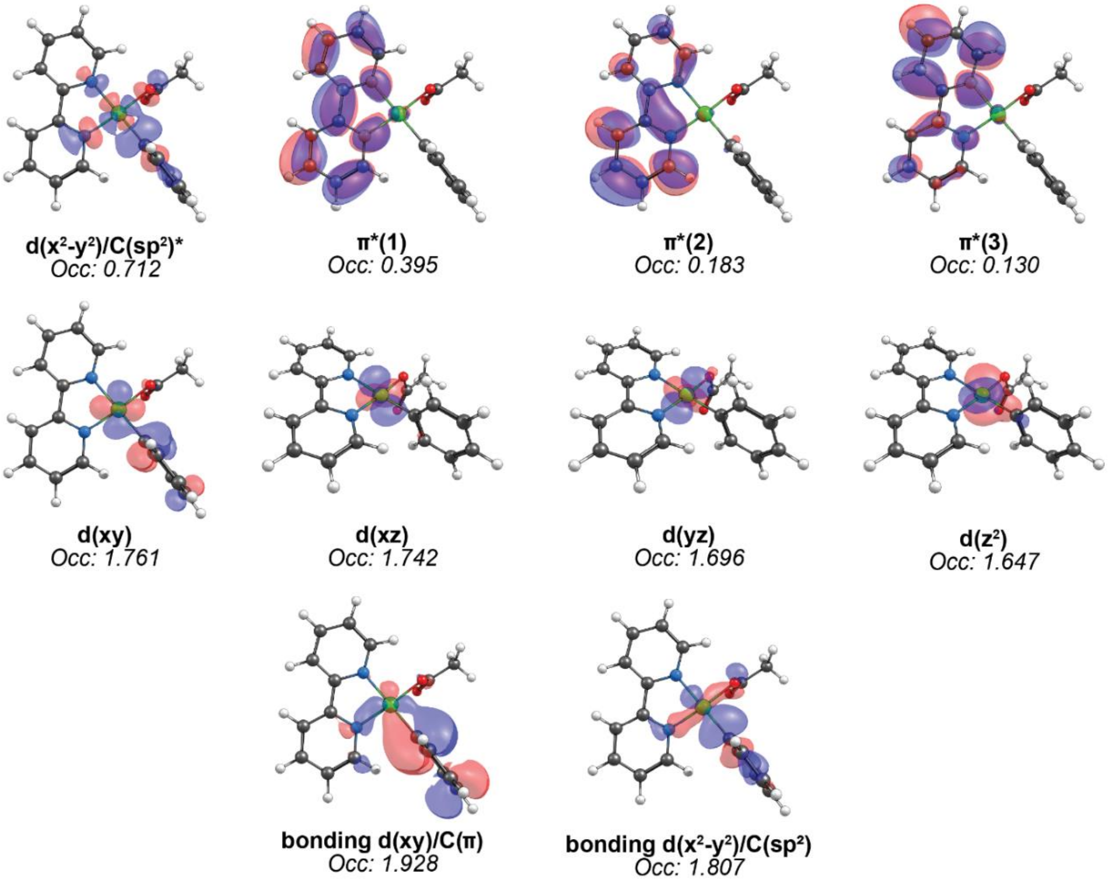

Figure C.2C. Compound **2** (S=0)– CASSCF/QD-NEVPT2 10o, 12e Active Space.

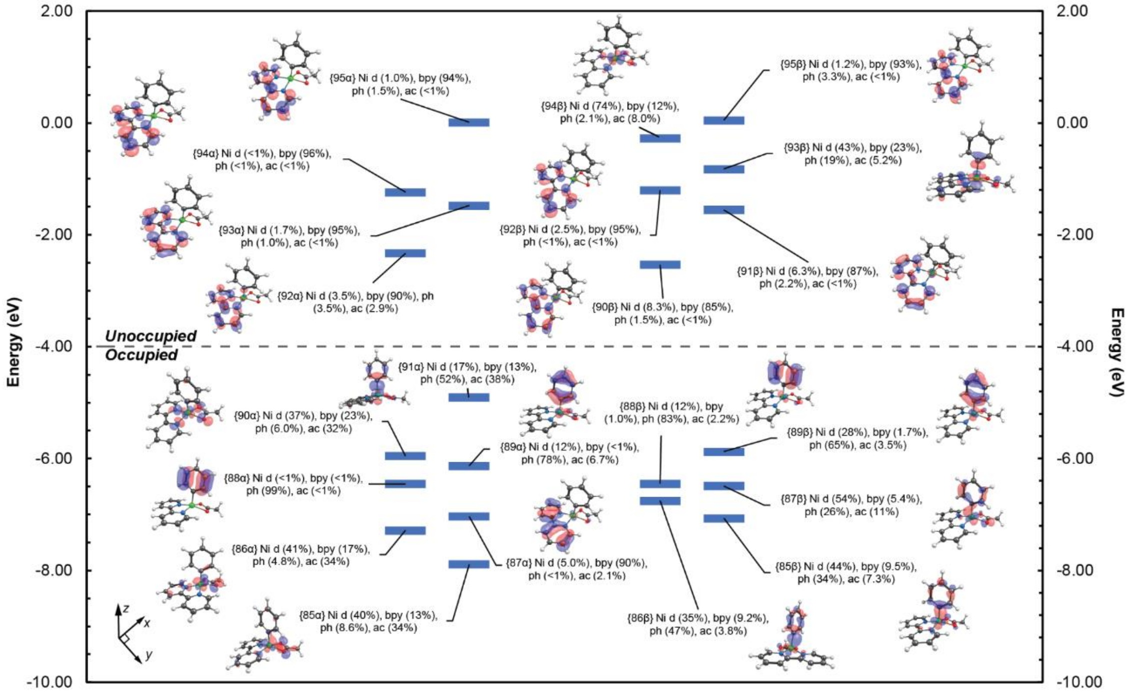

Figure C.2D. Compound 2 (S=1) – Single point DFT Frontier molecular orbital diagram, with α orbitals on the left and β orbitals on the right. α and β orbitals are also offset for clarity.

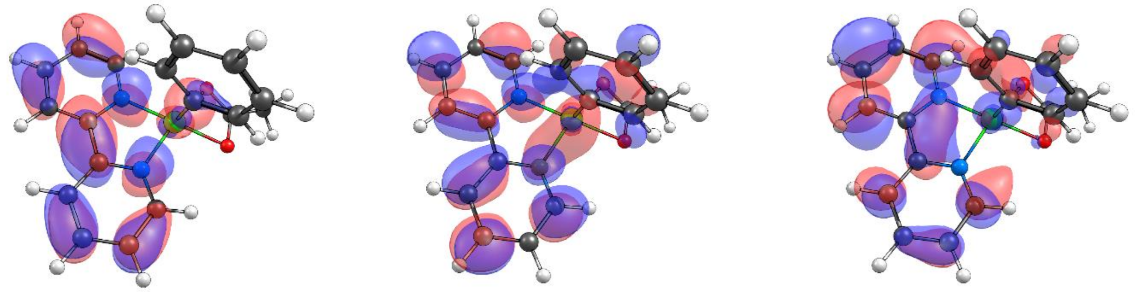

π^*(1) *Occ: 0.509*

π^*(2) *Occ: 0.066*

π^*(3) *Occ: 0.059*

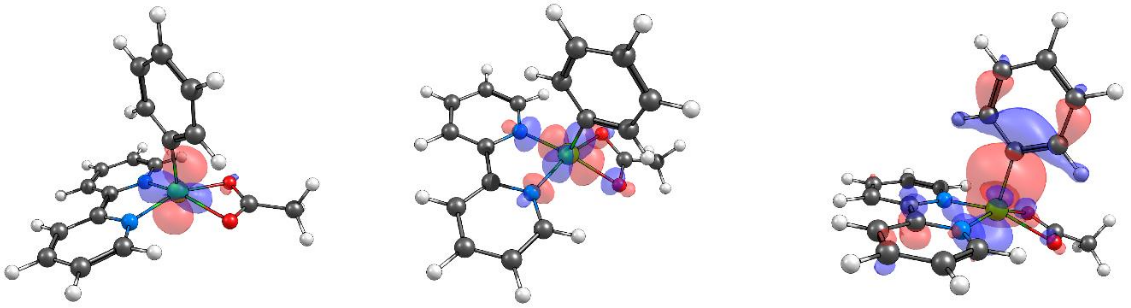

d(yz) *Occ: 1.698*

d(x^2-y^2) *Occ: 1.385*

d(z^2)/C(sp^2)* *Occ: 0.143*

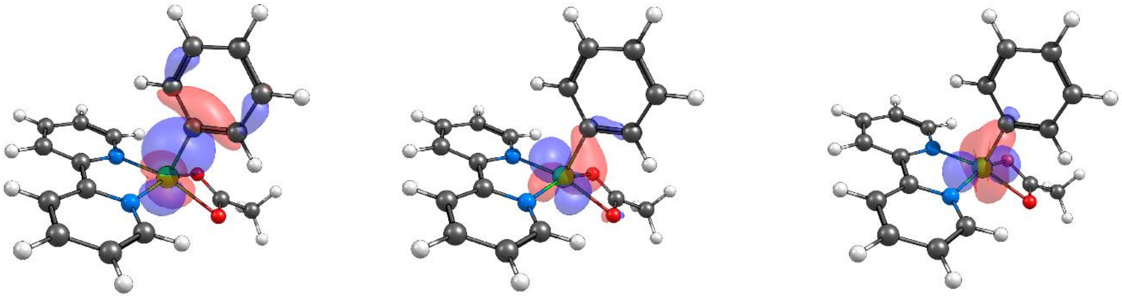

bonding d(z^2)/C(sp^2) *Occ: 1.726*

d(xz) *Occ: 1.710*

d(xy) *Occ: 1.703*

Figure C.2E. Compound **2** (S=1) – CASSCF/QD-NEVPT2 9o, 10e Active Space.

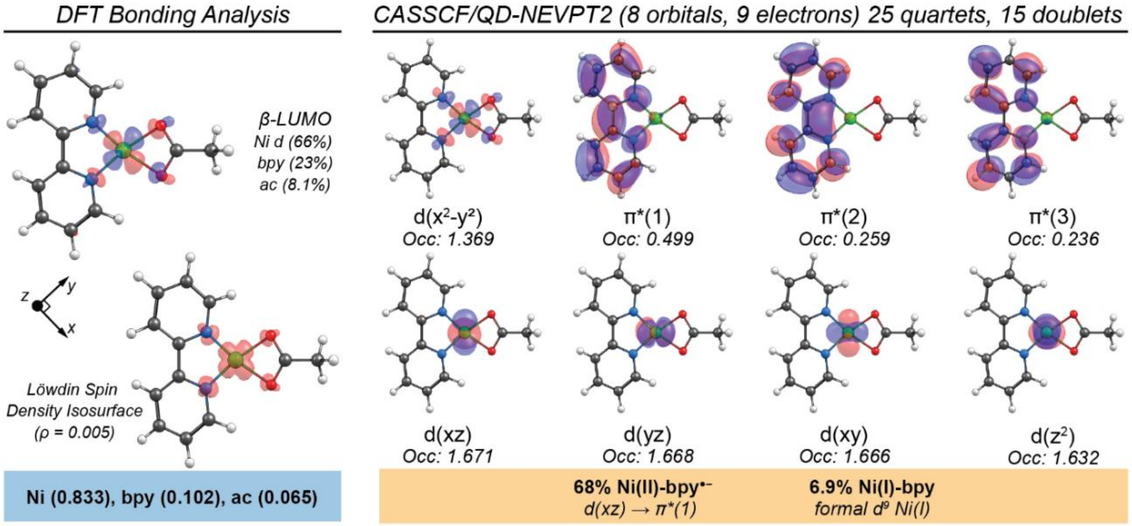

Figure C.2F. Comparison between the description given by DFT vs CASSCF/QD-NEVPT2 of the formal Ni(I) product of **2** that results after Ni–C bond cleavage.

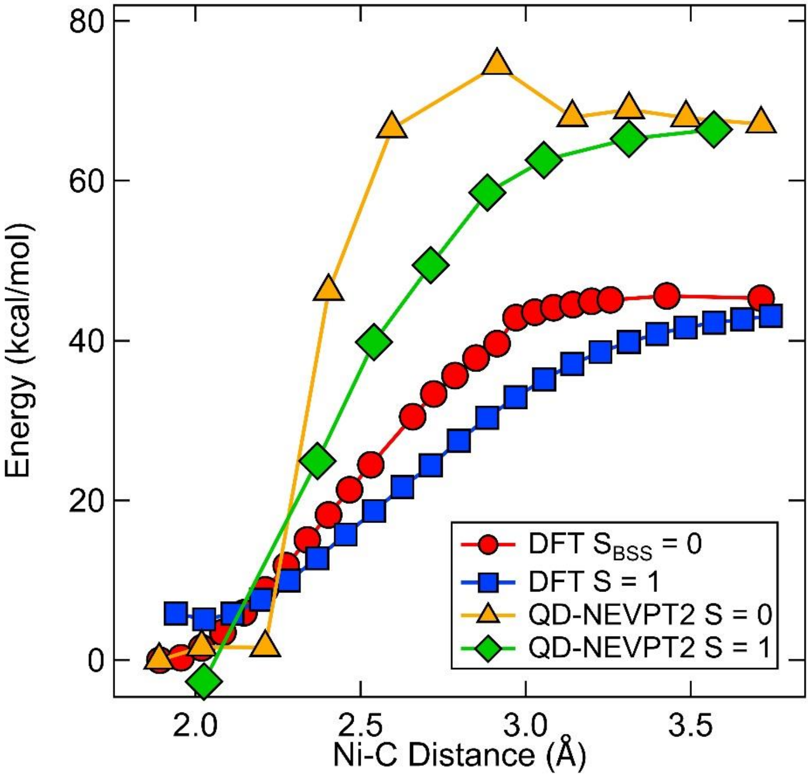

Figure C.2G. Thermodynamics (DFT and CASSCF/QDNEVPT2) along Ni–C coordinate for **2**.

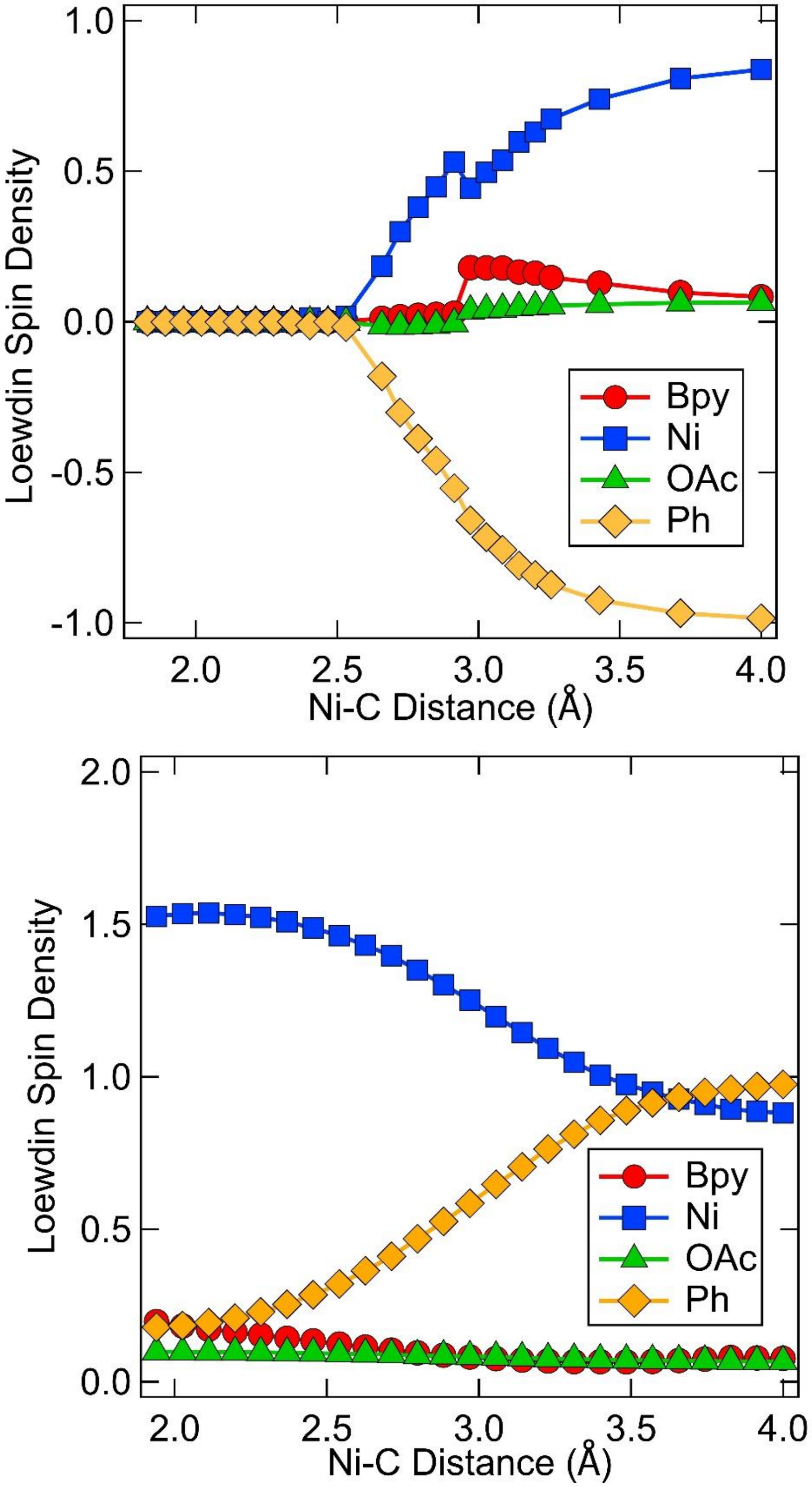

Figure C.2H. DFT Loewdin spin density per group along the Ni–C coordinate for **2**: (top) BSS and (bottom) UKS S=1.

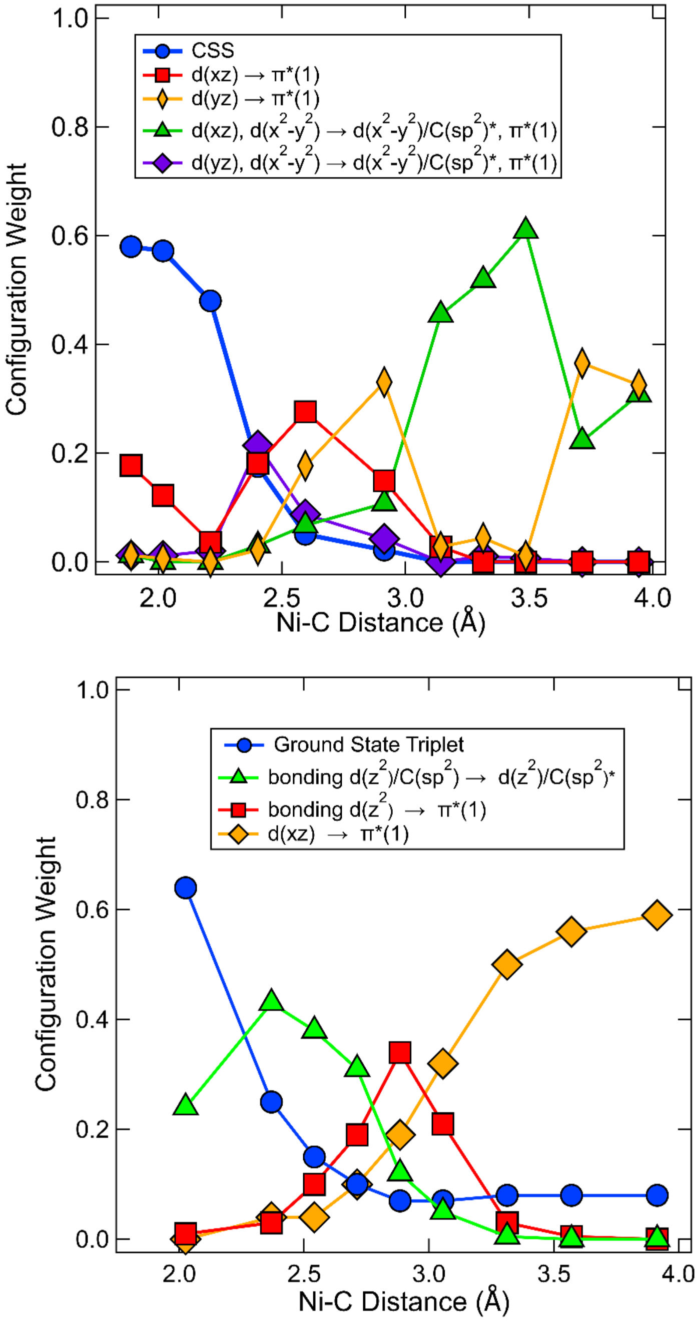

Figure C.2I. Dominant CASSCF/QD-NEVPT2 CI vectors along the Ni–C coordinate for **2**: (top) S=0 and (bottom) S=1. Note that for high spin **2**, the ground state triplet is $[d(x^2-y^2)]^1[(dz^2)/C(sp^2)^*]^1$, making a d(xz) → π*(1) transition yield a configuration of $[d(xz)]^1[d(x^2-y^2)]^1[(dz^2)/C(sp^2)^*]^1[\pi^*(1)]^1$.

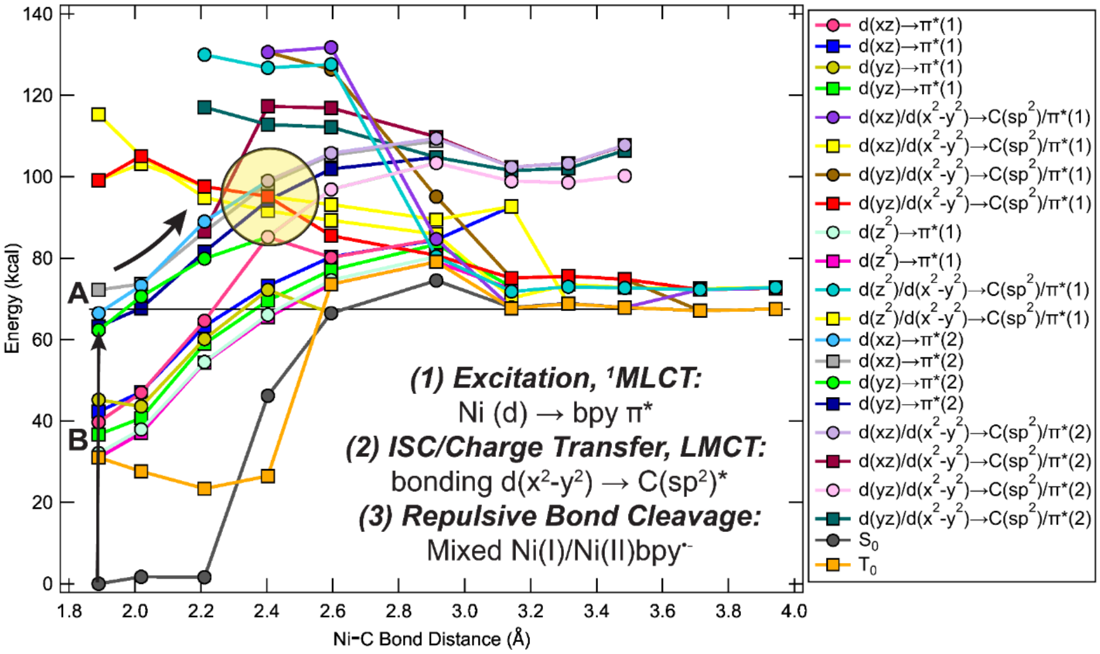

Figure C.2J. CASSCF/QD-NEVPT2 calculated relaxed ground and excited state PESs along the Ni–C coordinate of 2, with depictions of vertical excitation (black vertical arrow), the higher (A) and lower energy (B) manifolds of MLCTs, and the crossings between the higher energy MLCTs and the repulsive triplet surfaces (circled). Singlet states are shown with circles, triplets with squares.

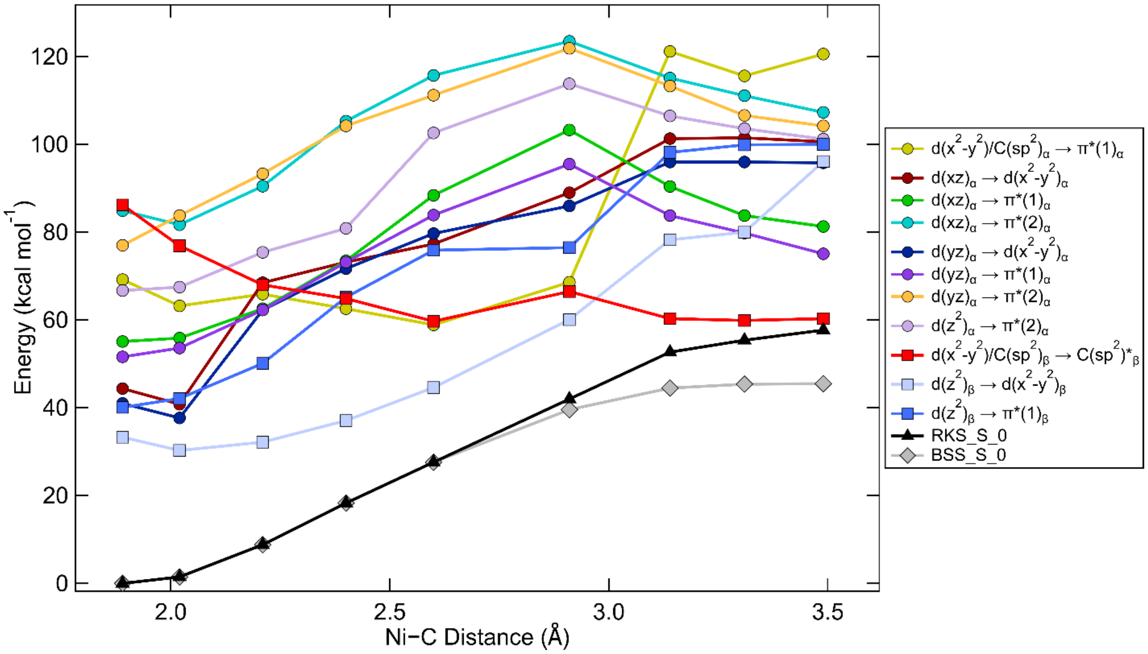

Figure C.2K. Broken symmetry singlet TDDFT (CPCM(THF)) excitations along the Ni–C coordinate of **2** show a possible high energy repulsive state (red line) which is ~86 kcal mol^{-1} above the equilibrium ground state. Spin-contaminated BSS calculations gave a Ni–C BDE of 45.1 kcal mol^{-1}, while the Yamaguchi corrected Ni–C BDE is essentially identical, at 44.9 kcal mol^{-1}.

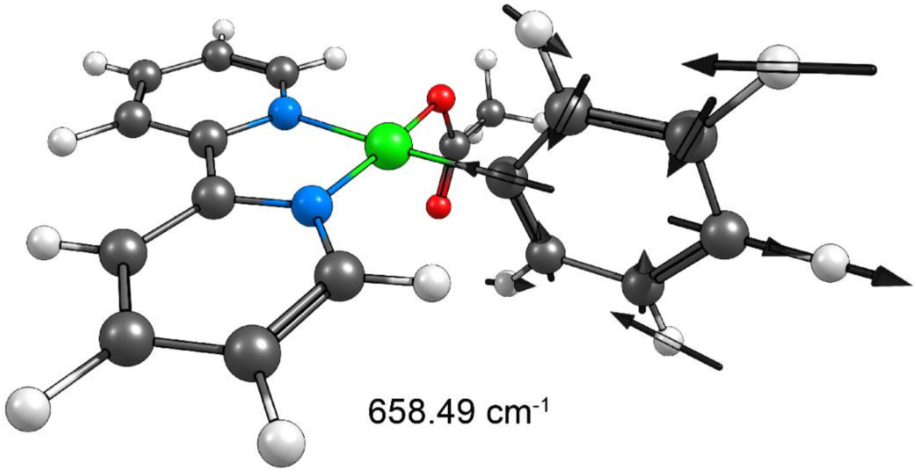

Figure C.2L. Higher energy vibrational frequency in **2** that exhibits a Ni–C bond stretching mode.

REFERENCES

(1) Yamaguchi, K.; Takahara, Y.; Fueno, T.; Houk, K. N. Extended Hartree-Fock (EHF) Theory of Chemical Reactions. *Theor. Chim. Acta* **1988**, *73* (5), 337–364. https://doi.org/10.1007/BF00527740.

(2) Kitagawa, Y.; Saito, T.; Nakanishi, Y.; Kataoka, Y.; Matsui, T.; Kawakami, T.; Okumura, M.; Yamaguchi, K. Spin Contamination Error in Optimized Geometry of Singlet Carbene ($^1A_1$) by Broken-Symmetry Method. *J. Phys. Chem. A* **2009**, *113* (52), 15041–15046. https://doi.org/10.1021/jp905125g.

(3) Shields, B. J.; Kudisch, B.; Scholes, G. D.; Doyle, A. G. Long-Lived Charge-Transfer States of Nickel(II) Aryl Halide Complexes Facilitate Bimolecular Photoinduced Electron Transfer. *J. Am. Chem. Soc.* **2018**, *140* (8), 3035–3039. https://doi.org/10.1021/jacs.7b13281.

Appendix D

EXAMPLE ORCA SCRIPTS AND COMMENTARY

D.A. Example ORCA Input Script for DFT Optimization-Frequency Job

```
#
# Opt+Freq Calc. of Pentacene
#
! RKS BP86 6-31G(d) OPT FREQ RI TIGHTSCF GRID7 NOFINALGRID PrintBasis

%basis
auxJ "AutoAux"
end

%pal nprocs 16
end
%maxcore 18000

%method
Z_solver Pople
end

*xyz 0 1
C     1.93200    2.20657    8.17285
C    -0.19393    1.27313    7.46480
C     2.56375    2.19304   10.54130
C     0.43095    1.27163    9.83566
C     1.31635    2.19171    5.80017
C    -0.47867    0.97197    8.80744
C     0.15243    0.95478   11.17612
C    -0.80631    1.24630    5.09172
C     1.02691    1.89746    7.14345
C    -1.09762    0.95891    6.43553
C     1.65110    1.89739    9.51445
C     1.06733    1.24286   12.20241
C     3.20565    2.15656   12.90638
C     0.41738    1.87054    4.76966
C     0.79445    0.91620   13.54118
C    -1.70425    0.92217    4.06112
C     0.71141    2.15336    3.42540
C     2.28917    1.87092   11.88074
C    -1.39688    1.20779    2.72997
C    -0.18987    1.82266    2.41233
C     1.71625    1.20431   14.54880
C     2.92082    1.82422   14.23167
H    -0.14124    0.43049   13.80888
H     4.15305    2.63978   12.67829
H     1.65015    2.63277    3.15703
H    -1.42184    0.48848    9.05572
H    -0.78993    0.47011   11.42465
H    -2.04133    0.47655    6.68348
H     2.87551    2.68933    7.92448
H    -2.65228    0.44023    4.28926
H     2.26025    2.67322    5.55131
H     3.50682    2.67669   10.29345
H     3.64041    2.04888   15.01456
H     1.49287    0.94347   15.57995
H     0.05219    2.04473    1.37633
H    -2.09989    0.94868    1.94266
*
```

D.B. Example ORCA Input Script for CASSCF Single Point Energy Calculation

```
# CASSCF Free-Carbene Example

! 6-311G(d) TIGHTSCF LargePrint PrintBasis

%casscf
nel 2
norb 2
mult 1
nroots 2
etol 1e-7
printwf det
end

%maxcore 144000

*xyz 0 1
 C  -0.00781837672941   -1.43586261424484    3.32033592257988
 C  -1.35319259365582   -1.20033328551954    3.98778114273479
 C  0.11567135133220    0.97108844418197   -0.99859717177681
 C  -0.14143531493726   -0.18548820254101   -0.13400807883545
 C  -0.03821028317116   -0.14162826193536    1.31958158482758
 O  0.09657455559851    0.89414947123754    1.94962736525179
 O  -0.11214819087619   -1.36642597610828    1.87729367422681
 H  -2.10287135437343   -1.89789785281239    3.60620051926157
 H  -1.26485198181623   -1.35090481482347    5.06806149388776
 H  -1.70084530454022   -0.18042810185983    3.81461614863469
 H  0.73415507813258   -0.70977670769190    3.65698310989852
 H  0.36251883697207   -2.44386644796001    3.50991554588733
 H  -0.22637909771278    0.81076400371095   -2.02384043494263
 H  -0.36983034405700    1.86987423608222   -0.59216209670185
 H  1.19286180883415    1.19991272328394   -1.03651859193396
*
```

D.C. Additional Considerations and Comments Related to Input Examples

When performing a DFT geometry optimization followed by frequency calculations, using fine grids may help prevent obtaining small imaginary frequencies due to numerical noise. While the example for pentacene applies the ‘Pople’-solver for the CP-SCF equations (under the %method block), the ‘DIIS’ solver (often applied with a level-shift) is, from experience, very robust for successfully obtaining frequencies for transition metal complexes. Regarding determination of the requested amount of memory (specified in %maxcore), a common rule of thumb is to request only about 75% of the memory available from the requested computational resources. The CASSCF example is a state-averaged single point calculation on a free carbene using a two electrons in two orbitals active space (described in detail in Chapter 3 and Appendix B).